The Impact of Energetic Electron Precipitation on Mesospheric Hydroxyl Radical

Annet Eva Zawedde

Thesis for the Degree of Philosophiae Doctor (PhD)
University of Bergen, Norway
2018

UNIVERSITY OF BERGEN

The Impact of Energetic Electron Precipitation on Mesospheric Hydroxyl Radical

Annet Eva Zawedde

Thesis for the Degree of Philosophiae Doctor (PhD)
at the University of Bergen

2018

Date of defence: 12.12.2018

Year: 2018

Title: The Impact of Energetic Electron Precipitation on Mesospheric Hydroxyl Radical

Name: Annet Eva Zawedde

Print: Skipnes Kommunikasjon / University of Bergen

Preface

Paper I A. E. Zawedde, H. Nesse-Tyssøy, R. Hibbins, P. J. Espy, L. K. G. Ødegaard, M. I. Sandanger, and J. Stadsnes, The impact of energetic electron precipitation on mesospheric hydroxyl during a year of solar minimum, *Journal of Geophysical Research: Space Physics*, Vol. 121, doi:10.1002/2016JA022371, 2016

Paper II A. E. Zawedde, H. Nesse-Tyssøy, J. Stadsnes, and M. I. Sandanger, The impact of energetic particle precipitation on mesospheric OH – Variability of the sources and the background atmosphere, *Journal of Geophysical Research: Space Physics*, Vol. 123, doi:10.1029/2017JA025038, 2018

Paper III A. E. Zawedde, H. Nesse-Tyssøy, J. Stadsnes, and M. I. Sandanger, Are EEP events Important for the Tertiary Ozone Layer?, To be submitted to *the Journal of Geophysical Research: Space Physics*

During my PhD studies, I have also contributed to this paper.

A H. Nesse Tyssøy, M. I. Sandanger, L.-K. G. Ødegaard, and J. Stadsnes, A. Aasnes and A. E. Zawedde, Energetic electron precipitation into the middle atmosphere—Constructing the loss cone fluxes from MEPED POES, *Journal of Geophysical Research*, Vol. 121, doi:10.1002/2016JA022752, 2016

Contents

Acknowledgements

This work would not have been possible without the financial support of the Norwegian State Education Loan Fund quota scheme and the Research Council of Norway under contract 223252/F50. For the last year of this study, I am grateful to the Birkeland Centre for Space Science (BCSS) for accepting and supporting me through that year.

I am grateful to my supervisor Dr. Hilde Nesse Tyssøy for all the invaluable knowledge, discussions and time we shared during the course of this work. Always encouraging me to attend short courses, seminars and conferences to improve on my knowledge of the subject matter of this study. Your contribution to this phase of my life shall forever be appreciated.

I am also very grateful to all the co-authors: Hilde Nesse-Tyssøy, Robert Hibbins, Patrick. J. Espy, Linn-Kristine Glesnes Ødegaard, Marit Irene Sandanger, and Johan Stadsnes, with whom I worked to make what is presented in this thesis possible and successful. Thank you so much for your respective contributions to my PhD studies.

With the Q-3 team, many of my programming dilemmas were resolved. My supervisor sometimes had to transcribe codes from IDL to MATLAB. I wish to thank Linn-Kristine Glesnes Ødegaard, Marit Irene Sandanger and my supervisor who unrelentingly did those long code runs of the raw POES data. It is not common that one gets to use "clean" POES data. Thank you so much for laying such a firm and warm foundation for my research work.

Without the entire BCSS team at UiB, my studies in Bergen would not have been successful. There is always a solution for anything within this team. One just needs to ask. For proofreading this thesis, I would like to thank my supervisor Dr. Hilde Nesse Tyssøy, Prof. Emeritus Johan Stadsnes, Dr. Christine Smith-Johnsen and Dr. Marit Irene Sandanger.

Finally to Daniel and Harmony, thank you so much for the moral and motivational support, I hope the wait was worthwhile.

Chapter 1

Introduction

The general motivation for this thesis is to understand the effects of energetic particle precipitation (EPP), in particular energetic electron precipitation (EEP), on the atmospheric system. It is well known that EPP through Solar Proton Events (SPEs) and EEP events can affect the chemical composition in the polar regions. EPP will, through dissociation, dissociative ionization and ionization of the most abundant chemical species (N_2 and O_2) in the atmosphere, initiate reactions that increase the production of odd nitrogen (NO_X: N, NO, NO_2) and odd hydrogen (HO_X: H, OH, HO_2). HO_X and NO_X can catalytically destroy ozone (O_3) and subsequently affect the atmospheric energy budget. EPP-induced chemical changes can be transported through large scale atmospheric patterns to lower altitudes, where they can lead to long lasting loss of stratospheric O_3. The EPP effects on atmospheric chemistry and their potential links to the atmospheric dynamics are illustrated by Figure 1.1.

Being that SPEs precipitate large fluxes of high energy protons directly over a wide area at the polar cap and the associated impact on the atmospheric composition is strong and easily detected, SPEs have been extensively studied. The electrons, on the other hand, are first trapped in the magnetosphere, where some are accelerated to relativistic energies before they precipitate into the atmosphere at magnetic latitudes connected to the Earth's outer radiation belt. Partly due to the complexity of the processes, and partly due to instrumental challenges, the total impact of energetic electrons on the chemistry of the middle atmosphere is still an open question. Though generally weak, the high frequency of occurrence of EEP events is speculated to lead to variability in mesospheric OH and subsequently O_3 over solar cycle timescales [Andersson et al., 2014a; Daae et al., 2012]. Hence, since EEP might be an important (missing) part of the solar input in climate models, more research should be directed to better understand the potential effects of EEP in order to understand the overall solar influence on climate [Andersson et al., 2014a].

In the mesosphere, the HO_X species are the important chemical family for catalytic reduction of O_3. However, space-borne observations of HO_X species only started re-

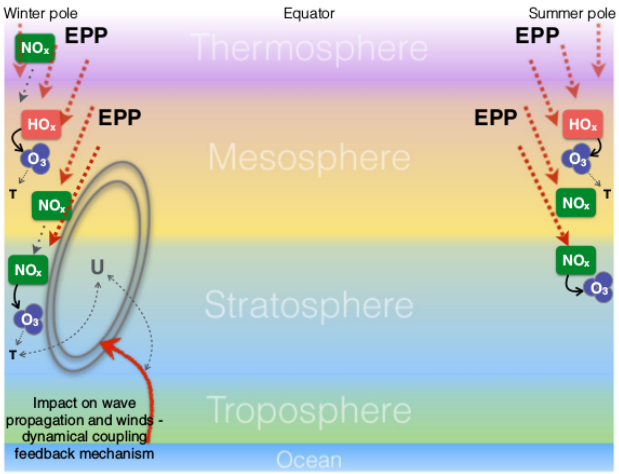

Figure 1.1: A schematic diagram showing energetic particle precipitation (EPP) impact on the atmospheric system, illustrating regions where HO_X and NO_X species are important for the chemistry. EPP initiates processes that lead to enhanced levels of HO_X and NO_X species, which catalytically destroy O_3. The EPP effects on atmospheric chemistry can be transported to the stratosphere where they can lead to long lasting O_3 loss. Transport processes are shown with grey dotted lines, while coupling mechanisms are indicated with grey dashed lines. Direct chemical impacts are shown with black arrows. Taken from Seppälä et al. [2014].

cently with the Aura MLS (Microwave Limb Sounder) satellite measurements. It is hence, the only space-borne instrument to measure both OH and O_3 together. Covering the declining phase of solar cycle 23, Aura MLS observations give us an opportunity to observe the effects on the atmospheric OH and O_3 species due to the weak, but frequent and recurring electron precipitation. This has given impetus to various studies during the last decade [e.g. Andersson et al., 2014a,b, 2012; Verronen et al., 2011].

The EPP-OH production depends on the ionization rate and the H_2O density which modulates the formation of water cluster ions, from which HO_X is formed through dissociative recombination with electrons [see Crutzen and Solomon, 1980; Sinnhuber et al., 2012; Solomon et al., 1981]. The catalytic O_3 reduction requires atomic oxygen, that is abundant only during sunlit hours [Turunen et al., 2016]. Therefore to observe the direct EEP-OH effect on O_3, electron precipitation must take place within the latitude extent of tertiary O_3 layer preferably at twilight (and/or sunlit) conditions.

The precipitating particle observations are available from the Medium Energy Electron and Proton Detectors (MEPED) instruments on board the National Oceanic and Atmospheric Administration Polar Orbiting Environmental Satellites (NOAA POES). The NOAA-16 and NOAA-18 satellites during the years 2005 and 2006 to 2009 respectively, make observations at approximately the same spatial and solar local time locations as the atmospheric observations made by Aura MLS. The known MEPED

data challenges in regard to proton detector degradation due to radiation damage, low energy proton contamination of the electron fluxes and insufficient information on the loss cone, are catered for as described in Nesse Tyssøy et al. [2016]. The Nesse Tyssøy et al. [2016] method accounting for a complete bounce loss cone (BLC) gives a novel possibility to better monitor the impact of the weaker geomagnetic storms.

With the overarching goal of revealing the total EEP impact on OH mixing ratios and the subsequent impact on the tertiary O_3 layer, this thesis is made up of three separate papers: The first paper aims to estimate and understand the impact of EEP events on OH production during a year of solar minimum. We target year 2008, during which a sequence of weak to moderate storms triggered by High Speed Solar Wind Streams (HSSWS) occurred. The low strength of the recurrent storms implies that we need to carefully consider the role of the changing background dynamics in order to isolate and estimate the contribution of EEP from the background OH production. This requires a method that can simultaneously take into consideration the available probable sources of OH variability, including for example the production through photolysis of water vapor (H_2O), temperature that can account for the dynamical variability, and the energy deposition associated with EEP events.

The aim of the study that follows is to model the temporal OH variability and identify the role of probable sources during the declining phase of solar cycle 23 (2005-2009). The proposed background predictors to OH variability are: temperature, geopotential height (GPH), H_2O mixing ratios and solar Lyman alpha (Ly-α) radiation with a dependence on the solar zenith angle (SZA). The proposed EPP predictors are: the electron and proton energy deposition. We use multiple linear regression analysis to find the contribution of each predictor variable when the other variables are held constant, and subsequently calculate the relative contribution of each predictor variable.

The last paper investigates the EPP-OH impact on O_3 mixing ratios in the northern hemisphere (NH) winter. Most recent studies focus on either EEP and OH mixing ratios or EEP and O_3 mixing ratios [see e.g. Andersson et al., 2014a,b, 2012; Verronen et al., 2011]. The Aura MLS, however, observes both species and hence, allow for studies of whether apparent O_3 mixing ratio changes are correlated with EEP-produced OH. We investigate when and where maximum intersection between the auroral zone and the tertiary O_3 layer exists, focusing on SZA $>95^\circ$ when twilight to nighttime conditions are expected. By identifying two sets of SPEs and EEP events during the same NH winter months, we study the EPP-OH link to O_3 reduction. We further investigate whether linear relationships exist between O_3 mixing ratios and the proposed predictors: OH mixing ratios, electron energy deposition, proton energy deposition, H_2O mixing ratios and temperature at different SZA bands, using correlation analysis. Finally, a superposed epoch analysis is applied, identifying EEP events exclusively occurring in winter time, investigating both the response in OH and O_3 mixing ratios.

The title of this thesis indicates three main areas of consideration; EPP, the background atmosphere where the precipitation occurs and the effects on the chemical composition of the atmosphere. Chapter 2 describes the physical processes relating to the atmosphere and its composition, as well as the energization and deposition of particle energy in the atmosphere. The mesospheric OH and O_3 variability are given a particular focus, followed by a description of the recent research regarding the effects of SPE and EEP on OH and O_3, and open questions. In chapter 3, the measurements of EPP, atmospheric parameters (OH, O_3, temperature, geopotential height (GPH), H_2O, solar Lyman alpha radiation), magnetic indices and solar wind parameters used in this thesis and their sources are discussed with emphasis on the particle observations. In chapter 4, a summary and discussion of the papers comprising this thesis is given. This is followed by an appendix with abbreviations and some definitions.

Chapter 2

Theory and Background

This chapter starts with a rudimentary description of the Sun-Space-Earth connection and the atmospheric structure, before embarking on the more specific OH and O_3 variability in the atmosphere and chemical processes associated with the particles precipitating into the atmosphere. Finally, a summary of the recent research regarding EPP effects on OH and O3 is given.

2.1 Basic Concepts on the Sun-Earth Connections

The Sun-Earth connections includes how the solar particles enter the Earth's magnetosphere, how they are stored and some are accelerated to relativistic energies before being lost to the Earth's atmosphere.

2.1.1 Solar Sources of Geomagnetic Activity

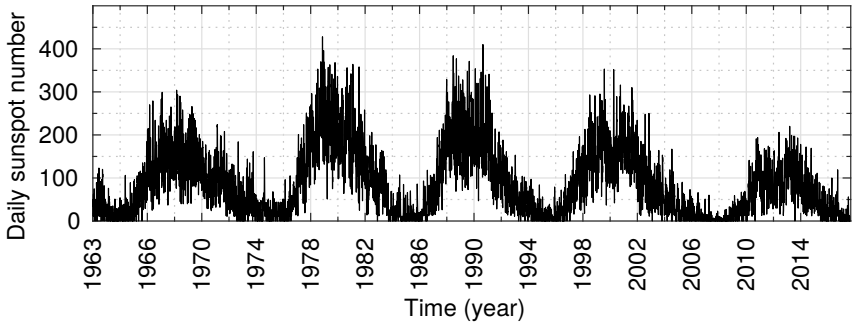

Figure 2.1: The 11 year sunspot cycle showing solar minimum and maximum during solar cycles 20-24. The data is obtained from the Coordinated Data Analysis Web (CDAWeb) [https://cdaweb.sci.gsfc.nasa.gov/index.html/].

The Sun's magnetic activity varies over a period of approximately 11 years. This is known as the solar cycle, represented by the relative sunspot number (equation 6 in Appendix). Sunspots are dark regions on the Sun associated with high magnetic field strength. Figure 2.1 shows the relative sunspot numbers during recent five solar cycles exhibiting the 11 year periodicity. Coronal mass ejections (CMEs) originate on closed field lines on the Sun associated with sunspot activity, hence predominantly occur during solar maximum.

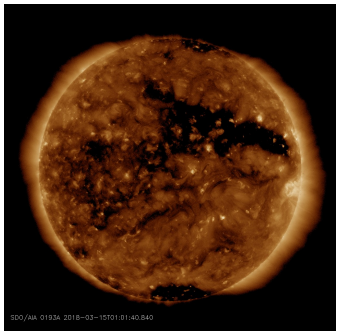

Figure 2.2: Coronal hole (dark region) on the Sun on 15/03/2018. Credit:SDO/AIA [http://spaceweather.com/]

The Sun with its features spin about its axis with a periodicity of about 27 days. This is the synodic rotation period, which is the time for a fixed feature on the Sun to rotate to the same apparent position as viewed from the Earth. Coronal Holes (CHs) are active regions on the Sun's surface which spew high speed, low density solar wind on open magnetic field lines [Billings and Roberts, 1964]. The stable long lasting CHs will re-appear for several solar rotations, giving recurrent solar wind streams and hence recurrent geomagnetic activity at 27 days intervals [Neupert and Pizzo, 1974]. This kind of recurrent activity is predominant during the declining phase of the solar cycle. Figure 2.2 shows a coronal hole on the solar disk (dark region) on 15/03/2018. Both the solar cycle (and its different phases) and the 27 days solar rotation period influence geomagnetic activity [see e.g Sheeley et al., 1976; Webb, 1995].

The Sun continuously emits a stream of highly conducting plasma consisting of mainly protons and electrons at supersonic speeds ($\sim$500 km/s) into the interplanetary space, known as solar wind, which carries the Sun's magnetic field with it. During solar minimum, the solar wind is mainly of two types depending on its source location on the solar surface. The fast, tenuous and relatively homogeneous solar wind emanates from large polar CHs located at high heliolatitudes, while the slower, denser and highly variable solar wind comes from lower latitudes [McComas et al., 2008, and references therein]. Unlike the well-ordered steady solar wind observed during solar minimum (Figure

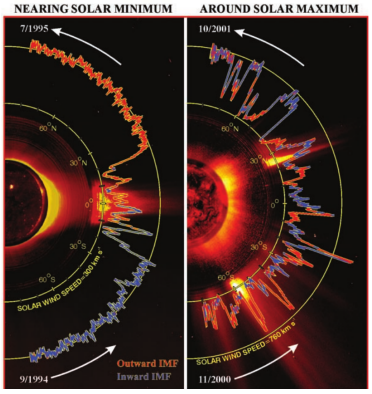

Figure 2.3: Comparison of solar wind speed during solar minimum and maximum. Taken from McComas et al. [2002].

2.3, left panel), the solar wind during solar maximum is an irregularly structured mixture of slow and intermediate-speed flows as shown in Figure 2.3 right panel, which arise from a mixture of sources including CMEs, small low latitude CHs, and possibly other active regions [see McComas et al., 2002, 2003, and references therein].

When the solar wind magnetic field reconnects with the Earth's magnetic field, solar particles are injected into the ring current resulting in a decrease in the Earth's magnetic field measured at the ground at equatorial latitudes. This is known as a geomagnetic storm. In particular, storms can be classified based on their intensity using the horizontal component of the Earth's magnetic field represented by the Dst index [Sugiura, 1964] as shown in Table 2.1 [see Gonzalez et al., 1994; Loewe and Prölss, 1997]. There are mainly two broad categories of interplanetary structures that cause geomagnetic storms: corotating interaction regions (CIRs) and interplanetary coronal mass ejections (ICMEs).

Type of storm	Intensity
Weak	$-30 \geq Dst > -50nT$
Moderate	$-50 \geq Dst > -100nT$
Strong	$-100 \geq Dst > -200nT$
Severe	$-200 \geq Dst > -350nT$
Great	$Dst \leq -350nT$

Table 2.1: Classification of magnetic storms by Loewe and Prölss [1997].

CME Driven Storms

CMEs are large magnetized plasma structures expelled from the active regions on the Sun into the heliosphere with velocities (>1000 km s^{-1}) faster than the background solar wind [Moldwin, 2008]. Many of these fast CMEs create shock waves in front of them as they stream away from the Sun, which accelerate energetic particles to penetrate the Earth's magnetosphere. The ICME are the interplanetary remnants from a CME.

Figure 2.4 (top) shows the main features of a CME-driven geomagnetic storm. Fast moving interplanetary shocks associated with ICMEs compress the solar wind plasma and magnetic fields upon impinging on the magnetosphere, leading to the storm sudden commencement (SSC) [see e.g Gopalswamy, 2008; Tsurutani et al., 2006]. The storm main phase is characterized by a decrease in the Dst index. In the recovery phase, the Earth's magnetic field returns to its pre-storm condition because the newly injected particles are lost to either the magnetopause or to the atmosphere.

CIR Driven Storm

The study by Burlaga and Lepping [1977] identifies two stages of a CIR-driven geomagnetic storm; the first stage is associated with the passage of the CIR (large B_Z fluctuations) while the second stage is associated with the passage of the high speed solar wind stream (HSSWS). As the solar wind from the CHs propagates through the interplanetary space, the fast plasma can overtake the slow plasma and forms an interaction region. The density, strength of the magnetic field and the B_Z fluctuations are compressed and magnified within the interaction region which corotates with the Sun. The amplified B_Z fluctuations together with the slowly increasing stream flow speed produce large fluctuating electric fields which drive the first phase of the geomagnetic storm. Figure 2.4 (bottom panel) shows a schematic representation of the features of a CIR-driven storm. There are typically no shocks at the leading edges of CIRs, therefore, the storm initial phase evolves gradually without the SSC. The ram pressure increase, which is associated with the high density and low velocity plasma, compresses the magnetosphere. This is causes an increase in the horizontal component of the Earth's magnetic field, and the storm initial phase starts [Tsurutani et al., 2006].

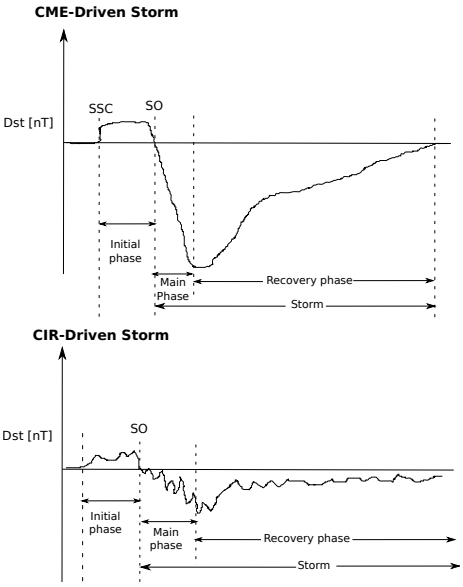

Figure 2.4: A schematic diagram showing geomagnetic storms driven by CMEs and CIRs. Although both profiles are qualitatively similar, the physical causes and characteristics of the different storm phases are different. Adopted from Tsurutani et al. [2006].

The second stage, the storm main phase, is mainly driven by the HSSWS. The amplitude of the B_Z fluctuations in the HSSWS is moderate, sustaining the non uniform quasi stationary electric field. This drives geomagnetic activity, causing the long recovery phase of several days.

The presence of Alfvén waves in the HSSWS is the cause of the B_Z fluctuations within CIRs. The highly fluctuating IMF B_Z leads to continuous fluctuating low intensity particle injections into the ring current and, therefore, causing weak to moderate geomagnetic storms (see Table 2.1) when CIRs impinge on the Earth's magnetosphere. HSSWS/CIRs driven storms are the most common storm types during the declining and minimum phases of the solar cycle. The 27 days recurrent nature of HSSWS leads to a repetitive geomagnetic impact on the magnetosphere and hence on the atmospheric composition.

2.1.2 The Earth's Magnetosphere

In the near-Earth space, the solar wind plasma is generally deflected by a region dominated by the Earth's magnetic field, called the magnetosphere. The interplanetary magnetic field (IMF) is frozen in with the solar wind and can not penetrate the Earth's magnetic field. The solar wind kinetic pressure compresses the magnetosphere on the dayside while the nightside is stretched into a long magnetotail.

Magnetic Merging and Reconnection

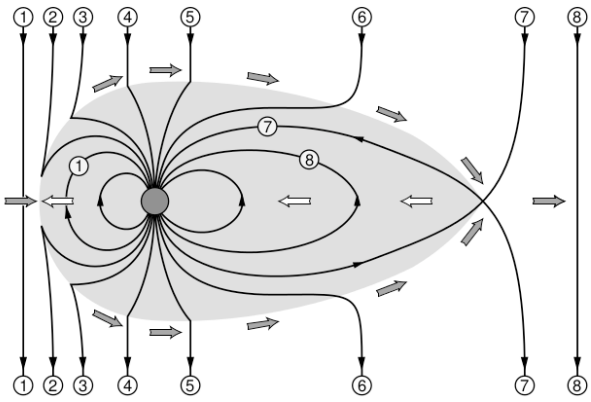

Figure 2.5: Magnetic field line merging and reconnection at the magnetopause. Taken from Baumjohann and Treumann [1996].

On impinging the magnetosphere, the IMF carried by the solar wind will connect (or merge) with the Earth magnetic field if the two fields are of opposite polarity. This mechanism transfers solar wind energy into the magnetosphere, illustrated by Figure 2.5, as first proposed by Dungey [1961]. If the IMF is southward ($Bz<0$) at the dayside magnetopause, it will effectively merge with the northward directed Earth's magnetic field, forming open magnetic field lines. The newly opened field lines are driven by the solar wind pressure to the nightside where they meet again and reconnect, forming closed stretched field lines. The magnetic tension along the stretched closed field lines will lead to relaxation and shortening in the Earthward direction resulting in transportation of plasma toward the Earth since the magnetic field is frozen in with the plasma.

This process is repetitive as long as there is a southward component of the IMF. This process initiates the three basic types of charged particle motion and hence the trapping of particles in the magnetosphere illustrated in Figure 2.6.

The Earth's Radiation Belts

In the presence of a magnetic field, charged particles are constrained to gyrate along the field lines. Conservation of magnetic momentum in a converging magnetic field increases the angle between the particle's velocity vector and the local magnetic field line. When this angle, called pitch angle, approaches 90°, the particle will bounce back along the field line and it is consequently trapped on closed field lines as shown in Figure 2.6.

The trapped populations of energetic particles form the Earth's radiation belts. The inner radiation belt, located at L=1.2-2.5, consists of energetic protons (>100 MeV) stably trapped over scales greater than the solar cycle. It also contains energetic electrons, centered near 1.5 Earth radii (R_E) [Li and Temerin, 2001]. The outer radiation belt, centered around L=4-5 R_E, consists of mainly electrons. The lower energy electrons show more frequent variations associated with substorms (AE) while higher energies vary more with geomagnetic storms associated with the Dst index [Li and Temerin, 2001].

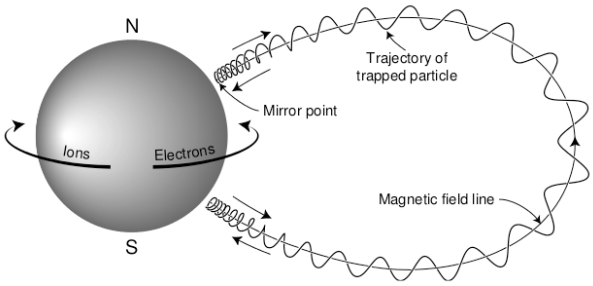

Figure 2.6: Trajectories of particles trapped on closed field lines. Taken from Baumjohann and Treumann [1996].

The trapped particles undergo an azimuthal drift, whereby ions drift westward while electrons drift eastward around the Earth, forming the ring current. The injection of moderate energy (10s to 100s of keV) electrons and ions into the ring current during geomagnetic storms intensifies the ring current, providing a source of energy for electromagnetic waves as well as a seed population for electron acceleration [e.g. Summers et al., 1998]. During geomagnetic storms, significant increases or decreases in the trapped electron flux can occur depending on whether the acceleration or loss processes dominate [Reeves et al., 2003]. There are various wave particle interactions that play a dominant role in the acceleration/energization and loss mechanism in the Earth's radiation belts [see e.g. Reeves et al., 2003]. The three basic particle motions shown in Figure 2.6 are associated with respective adiabatic invariants defined in the Appendix.

2.1.3 Particle Acceleration and Loss in the Radiation Belts

The source mechanisms for accelerating outer radiation belt electrons can be broadly categorized into global or local acceleration; inward radial diffusion by violation of one or more of the adiabatic invariants and cyclotron-resonant wave particle interactions (WPI) for example with whistler mode chorus waves [Friedel et al., 2002; Reeves et al., 2013; Turner et al., 2014a]. Electrons experience an increasing magnetic field when they are transported radially towards the Earth and gain energy if the first and second adiabatic invariants are conserved [Reeves et al., 2013]. Therefore, the flux of relativistic electrons produced by an acceleration event will be a function of the low energy source population (and WPI) as well as the amount of radial transport [Reeves et al., 2003]. For detailed explanations and descriptions of particular acceleration mechanisms within the two broad categories see for example Friedel et al. [2002] and Turner et al. [2013].

The loss mechanisms in the radiation belts can also be broadly categorized in two types: the adiabatic (reversible) and the non adiabatic (irreversible) processes. For the reversible processes, the flux dropouts return to the pre-storm flux level on magnetic field recovery [see e.g Friedel et al., 2002; Turner et al., 2012]. While the irreversible processes lead to true particle loss to either the atmosphere or the magnetosphere's outer boundary, called the magnetopause. The true particles losses occur through scattering into the atmospheric loss cone (drift or bounce loss cone) and through magnetopause shadowing. For detailed studies on magnetopause shadowing see for example Turner et al. [2014b, 2013, 2012]. In the next subsection, are short descriptions of WPI as an acceleration and loss mechanism in the radiation belts, leading to precipitation of particles into the atmosphere.

Local Acceleration by Wave Particle Interactions

Whistler mode chorus waves are electromagnetic emissions resulting from cyclotron instabilities of energetic electrons, with frequencies in the range of $\sim$0.1-0.8 of the electron cyclotron frequency (f_{ce}), typically ranging from 0.1 to 10 kHz throughout the outer radiation belt [Turner et al., 2014a]. Chorus emissions can interact with electrons of energies 10-100 keV resulting in energy diffusion that can accelerate electrons to relativistic energies (MeV) in a few days [Summers et al., 1998]. The seed population of 10-100s keV electrons can be introduced into the inner magnetosphere from the near-Earth plasma sheet during periods of enhanced convection and (or) energetic particle injections or through substorm activity [see e.g. Foster et al., 2014]. This seed population can act as a source population/energy source for chorus waves that interact with the seed population of electrons, accelerating them to relativistic energies. Electron acceleration can be effective over a range of energies (100s of keV to >5MeV)

and a range of pitch angles [Turner et al., 2014a].

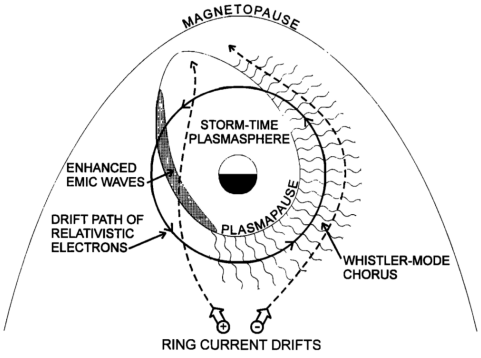

Figure 2.7: Schematic diagram showing spatial distribution of whistler mode chorus and Electromagnetic Ion Cyclotron (EMIC) waves during magnetic storms in relation to the position of the plasmapause and the drift paths of ring current (10-100 keV) electrons and ions and relativistic ($>\sim$ 1 MeV) electrons. Taken from Summers et al. [1998].

Although chorus wave interaction with the seed population (10-100 keV) can lead to scattering into the loss cone, energy diffusion dominates over pitch angle diffusion for relativistic electrons, resulting in energization and scattering towards higher pitch angles [Turner et al., 2014a]. The most significant electron energy diffusion occurs during resonant interactions with whistler mode waves in regions of relatively low plasma density, producing a relativistic electron population with a distribution peaking at pitch angles near 90° [Summers et al., 1998]. This anisotropic electron distribution is reduced through pitch angle scattering by EMIC waves while conserving the electron energy. EMIC waves are pulsations in the frequency range of 0.1-5 Hz, generated by unstable ion distributions in the ring current [Turner et al., 2014a]. They occur throughout the magnetosphere, but most often on the dusk and day-side at high L-shells as shown in Figure 2.7. Relativistic electrons (>1 MeV) can interact with whistler mode waves for over 50% of their drift orbit, but only pass briefly through the duskside region of intense EMIC waves (see Figure 2.7). Therefore, interaction of the relativistic electrons with chorus in the region outside the plasmapause can cause further diffusion toward pitch angles near 90° and hence lead to additional acceleration.

Loss by Wave Particle Interactions

Pitch angle diffusion and scattering by WPI can result in loss of electrons to the Earth's atmosphere [Turner et al., 2013]. It is dependent on electron energy, equatorial pitch angle and magnetic latitude [Turner et al., 2014a]. VLF chorus, plasmaspheric ELF hiss, and EMIC waves can each separately, or in combination, cause effective scattering loss of MeV electrons from the outer zone, under suitable conditions [Summers et al., 2007]. Hence, they can contribute significantly to the depletion of relativistic electrons from the outer radiation belt over the course of a magnetic storm. Chorus and hiss also scatter electrons and cause precipitation at sub-relativistic energies (10s to 100s keV)

[Li et al., 2013, 2014].

Although whistler mode chorus waves preferentially accelerate electrons, they can also scatter them into the loss cone at high latitudes resulting in MeV microbusts of precipitation [Summers et al., 2007; Turner et al., 2013, and references therein].

Plasmaspheric hiss is a broadband ELF whistler mode emission with frequency in the range 100s Hz to kHz, occurring particularly in the equatorial and mid-latitude zones on the dayside [Summers et al., 2007]. Hiss can be excited from anisotropic distributions of electrons injected into the inner magnetosphere from the plasmasheet during substorms. Hiss contribute to pitch angle scattering loss of relativistic electrons ($>$1 MeV) to the atmosphere during the recovery phase of magnetic storms and can explain the formation of the quiet-time slot region that separates the inner and outer radiation belts [Summers et al., 2007, and references therein].

EMIC waves interact resonantly with relativistic electrons causing strong pitch angle diffusion and rapid precipitation of electrons with equatorial pitch angles $<\sim$40-60° into the atmospheric loss cone [Turner et al., 2014a]. Particle injections can also introduce energetic ions which can generate EMIC waves near the plasmapause as particles drift through the dusk magnetic local time (MLT) sector. Only relativistic electrons ($>\sim$2 MeV) can resonate with EMIC waves, but the energy limit might drop to $\sim$400 keV during very active conditions and in regions of high plasma density like the plasmapause [Turner et al., 2014b, and references therein].

2.1.4 Energetic Particle Precipitation

In this study, we focus on two classes of precipitating particles that deposit their energy in the mesosphere: solar protons ($>$1 MeV) and energetic electrons ($>$ 30 keV) which are associated with SPEs and EEP respectively. Solar protons can precipitate on open field lines in the polar cap. Depending on their energy/rigidity, some will also penetrate the closed field lines. The electrons are first stored in the radiation belts, where they, through inward radial diffusion and wave-particle-interactions, are accelerated and lost to the atmosphere along geomagnetic latitudes connected to the Earth's radiation belts: 55°-72° [see e.g Andersson et al., 2014b]. Figure 2.8 shows the dominant regions in the magnetosphere where energetic particles precipitate. Auroral electron precipitation occurs at altitudes $>$100 km and is an important source of mesospheric NO_X, but not for the short lived HO_X.

As the precipitating particles propagate through the dense atmosphere, they collide with either free or bound electrons. They loose energy and hence are slowed down until they reach the energy of the ambient atmospheric air. In that process, they produce large fluxes of secondary electrons which in turn transfer a major portion of the incident energy to the atmosphere [Thorne, 1980]. Protons of energies 1-1000 MeV and

electrons of energies 4-4000 Kev precipitating in the atmosphere will produce energy deposition profiles as shown in Figure 2.9 [Turunen et al., 2009].

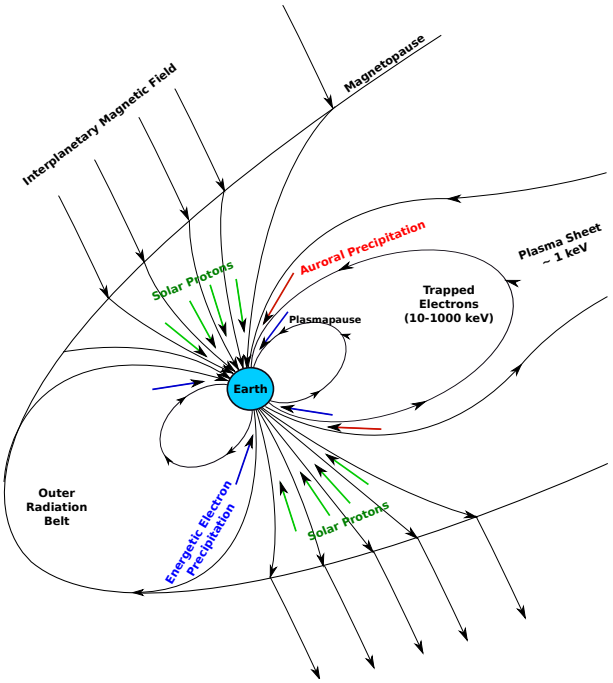

Figure 2.8: A schematic diagram showing the Earth's magnetosphere illustrating the dominant zones of particle precipitation. Adopted from Thorne [1980].

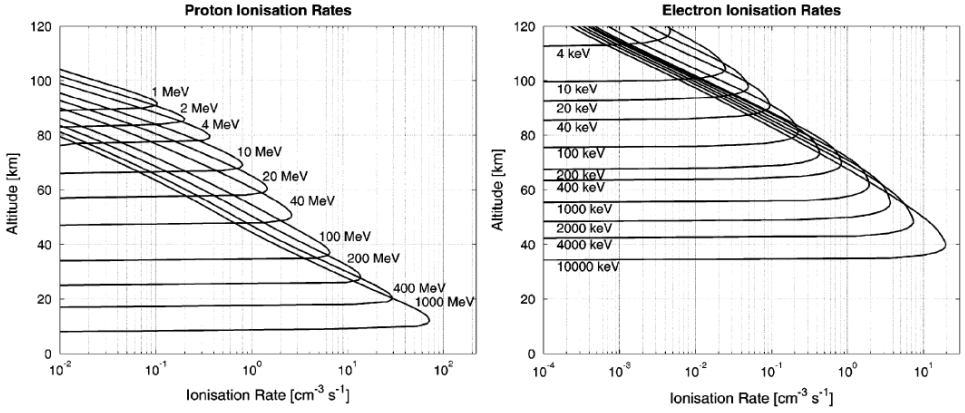

Figure 2.9: Altitude versus ionization rates for monoenergetic beams of protons 1–1000 MeV (left) and electrons 4–10000 keV (right). [see Turunen et al., 2009].

2.2 The Atmosphere

Knowing the basic properties of the region in the atmosphere where the solar energetic particles are expected to precipitate is an important step in understanding the effects thereof. Apart from the direct photoionization processes, there are various dynamical mechanisms that may influence the composition of the atmosphere. In this thesis, the region of interest is as mentioned mainly the mesosphere. The other regions are described to give a complete picture.

2.2.1 Structure

By considering the mixing ratios of gases, the atmosphere can generally be divided into two parts: the homosphere and heterosphere. The homosphere is the region from the ground up to about 100 km, characterized by constant mixing of the most abundant species in the atmosphere namely N_2 and O_2. Above 100 km is the heterosphere where the relative abundance of the atmospheric constituents depends on diffusion separation between the light and heavier constituents.

The atmosphere is to the first order horizontally stratified due to the influence of gravity, and can be divided into layers based on the atmospheric mean temperature gradients as illustrated in Figure 2.10. In the lowest layer, the troposphere, the temperature decreases with altitude. At the tropopause ($\sim$10 km), the temperature gradient reverses. In the stratosphere, the temperature increases with altitude primarily due to absorption of solar ultraviolet (UV) radiation wavelengths by ozone (O_3). The temperature trend again reverses at the stratopause (50 km). This is followed by a very sharp decrease in temperature in the mesosphere to a minimum at the mesopause ($\sim$85-100 km depending on season and latitude), created by radiative cooling which can occur through infrared emission associated with the vibrational relaxation of CO_2 , H_2O, and O_3 as well as dynamics. The absorption of UV radiation by O_3 and to a lesser extent

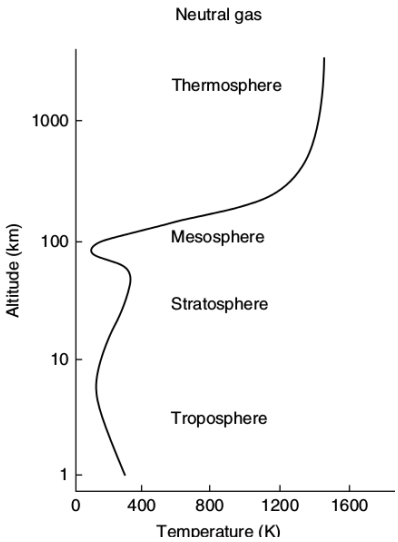

Figure 2.10: Typical mid-latitude profile of the neutral atmospheric temperature showing the different layers. Taken from Kelley [2009].

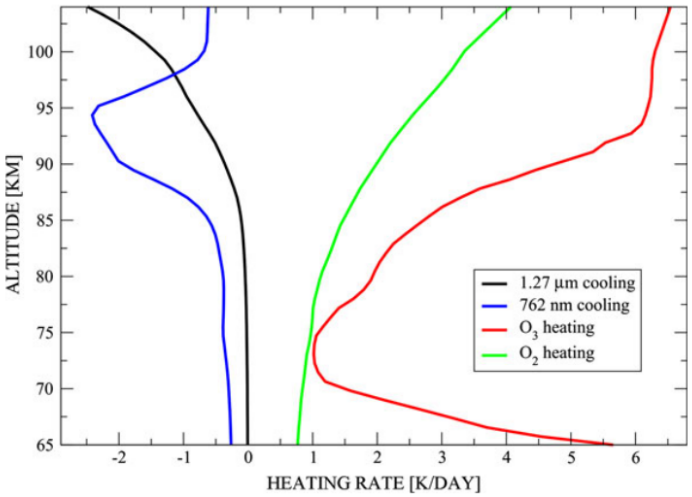

Figure 2.11: Heating effects due to solar absorption by O_2 (Lyman-α, Schumann-Runge bands and continuum) and O_3 (Hartley, Huggins and Chappuis bands). Cooling rates in the 1.27 μm and 762 nm bands estimated from the corresponding volume emission rates measured by the METEORS experiment [Feofilov and Kutepov, 2012, see].

by O_2 is the dominant source of heat in the mesosphere. Figure 2.11 shows the heating rates due to absorption of solar radiation by O_3 and O_2 as well as cooling in the O_2 bands. This illustrates the link between the chemical species, the temperature profile and the radiation budget.

2.2.2 Photoionization Sources

The chemical composition of the atmosphere is modified by solar radiation during daytime resulting in diurnal variability of most chemical species in the atmosphere. Figure 2.12 shows the depth of penetration of solar radiation as function of wavelength. Of importance to the mesospheric chemistry are wavelengths in the range of 185-242 nm that photodissociate O_2, eventually leading to O_3 formation and the Lyman-α which photodissociates H_2O resulting in formation of OH.

2.2.3 Atmospheric Dynamics

The zonal (longitudinal directed) wind speed is one of the most important quantities in atmospheric dynamics. In the stratosphere and mesosphere, the background zonal winds are eastward (positive) and westward (negative) during winter and summer respectively. The zonal mean flow is strongly influenced by the seasonal variation in the solar heating, as well as local variations in the wind speed and direction associated with atmospheric waves. The basic state of the atmospheric fluid determines the prop-

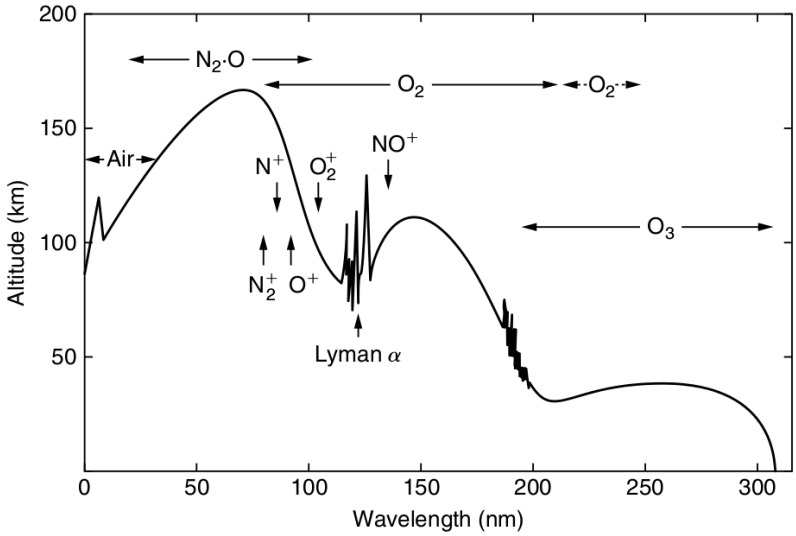

Figure 2.12: Depth of penetration of solar radiation as a function of wavelength. Altitudes correspond to an attenuation of 1/e. The principal absorbers and ionization limits are indicated. Taken from Kelley [2009].

agation of these waves which in turn modify the basic state through wave dissipation [Brasseur and Solomon, 2005]. The atmospheric wind structure is also strongly coupled to the temperature gradients, implying that changes in the winds will have effects on the atmospheric temperature.

The temperature in the polar summer mesosphere is colder than the temperature in the polar winter counterpart with a difference of about 100 K. The cold summer and the warm winter mesopause is a result of the seasonal filtering of gravity waves and their associated momentum deposition. Moreover, there are also unusual temperature variability during winter that are associated with planetary wave activity. The level of temperature fluctuations is higher in winter than in the summer mesosphere [Kelley, 2009]. Therefore, in order to understand the seasonal temperature structure, the dynamics, including the role of atmospheric waves, must be considered.

Gravity Waves

Gravity waves provide the major source of dynamical variability in the mesosphere. Gravity waves are oscillations with typical horizontal wavelengths of 10-1000 km that arise in a stably stratified fluid when air parcels are being displaced vertically [Brasseur and Solomon, 2005]. The sources of these waves are surface wind flow over orographic features, frontal systems and thunderstorms, earthquakes and tsunamis [see e.g. Kelley, 2009]. The propagation of gravity waves through the atmosphere depends on the wind

distribution and thermal structure, which in turn varies with season and the static stability. When the phase speed of a wave is equal to the background zonal wind speed, the wave is absorbed. Hence, the background stratospheric winds cause a filtering process resulting in predominantly westward propagating gravity waves in winter and eastward propagating waves in summer. The amplitude of gravity waves grows exponentially with altitude until its temperature perturbations produce a super-adiabatic lapse rate and the wave become convectively unstable, breaks and deposit its momentum to the background wind.

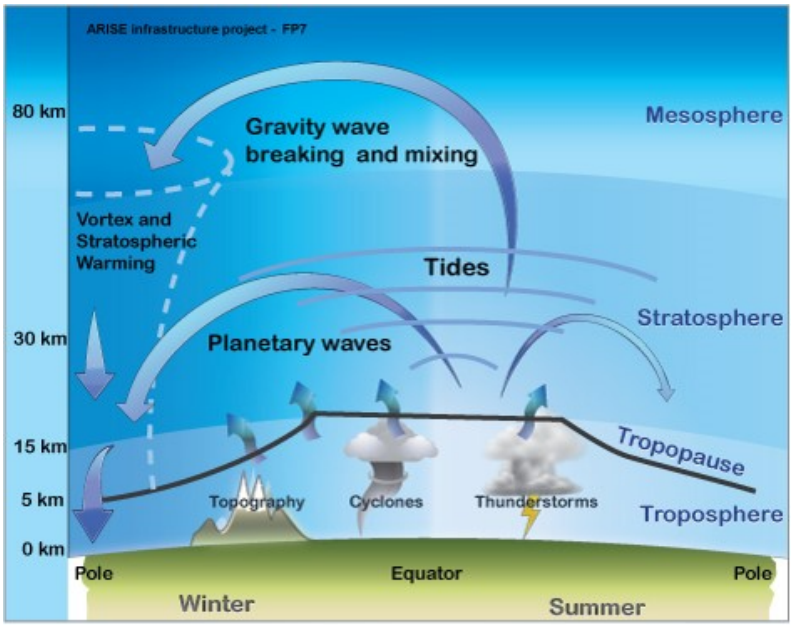

Figure 2.13: Meridional Circulation for solstice conditions
[http://lasp.colorado.edu/home/mag/files/2013/12/mer_cir.jpg].

This implies that during during winter the gravity waves will deposit westward angular momentum to the mean flow in the mesosphere which subsequently spins and give rise to a poleward wind component. To conserve mass, there is downward flow of air at high latitudes resulting in adiabatic heating. At the summer pole, there is a net upward flow of mass resulting in adiabatic cooling, hence the cold summer mesosphere. This results in a meridional circulation pattern, with upwelling at the summer pole, pole-to-pole flow and downwelling at the winter pole shown in Figure 2.13 [see e.g. Brasseur and Solomon, 2005; Kelley, 2009].

Planetary Waves

Planetary-scale (Rossby) waves exist due to meridional gradients in potential vorticity [Brasseur and Solomon, 2005]. They are produced by stationary sources like large-scale orography and land-sea contrasts. Hence these waves are quasi-stationary, propagate upwards and equator-wards in the middle atmosphere. Planetary waves are westward propagating relative to the mean flow. Hence, planetary waves normally propagate into the stratosphere during winter, causing variability with profound effects on temperature, winds and the composition of the wintertime stratosphere and mesosphere.

Critical layer absorption and breaking of planetary waves will result in deposition of westward angular momentum to the mean flow. This will decelerate the flow which in turn modifies the propagation of planetary waves and produces an even stronger deceleration of the mean zonal wind at a lower altitude. As a result, the polar night jet might decrease in strength and on certain occasions even reverses leading to the breakdown of polar vortex [see e.g. Damiani et al., 2014; Manney et al., 2009]. As a result, large temperature enhancements are occasionally observed to occur in the stratosphere, accompanied by cooling in the mesosphere [see e.g. Damiani et al., 2010b; Wang and Alexander, 2009]. Such dynamical phenomenons are called sudden stratospheric warmings (SSWs). A major SSW implies that the zonal wind reverses in the region poleward of 60° and above the height corresponding to 10 hPa [Brasseur and Solomon, 2005].

Tides

Atmospheric solar tides are global-scale oscillations with periods that are harmonics of a 24-hour day, that are driven primarily by the periodic absorption of solar ultraviolet radiation by O_3 in the middle atmosphere and of solar infrared radiation by H_2O in the troposphere. Tides can be either migrating propagating westward with the apparent motion of the Sun or non-migrating, meaning stationary, or propagate either eastward or westward. The dominant source of non-migrating tides is latent heat release in the troposphere, and thus related to meteorological processes in the lower atmosphere. A small semi-diurnal tide is also forced by the gravitational attraction of the Moon.

In the mesosphere, the tidal amplitudes increase with height due to decreasing air density and the tidal wind may have a strong impact on gravity wave breaking and hence on local heating/cooling [Brasseur and Solomon, 2005, and references therein]. The tidal waves in the vertical wind produces strong variations in the concentration of chemical species that exhibit large vertical concentration gradients (e.g., atomic oxygen, nitric oxide) [Brasseur and Solomon, 2005, and references therein]. Tides break above approximately 80 km altitude, where they deposit their momentum and cause turbulence.

2.3 OH Variability

This section describes the main processes involved in OH production and loss. It addresses the variability of background OH on spatial and temporal scales, which is strongly relevant for the research in paper I and II. This is followed by a discussion of recent studies and some open questions .

2.3.1 Background OH Production

For EPP-effects on OH to be detected, the EPP-OH production must overcome the background production. A major portion of the mesospheric background OH comes from photolysis of H_2O. Further, dynamical processes especially during winter, impact the density of H_2O, as well as other constituents relevant for the OH production and loss.

Photolysis Processes

The Hydroxyl radical (OH) belongs to a family of chemical species known as odd hydrogen (HO_X: H + OH + HO_2). In the stratosphere, photolysis of O_3, mainly in the Hartley and Huggins bands (200-330 nm), leads to production of metastable atomic oxygen ($O(^1D)$) by the reaction [Brasseur and Solomon, 2005]:

$$O_3 + h\nu \rightarrow O_2 + O(^1D) \tag{2.1}$$

The $O(^1D)$ oxidizes H_2O forming OH by the reaction:

$$H_2O + O(^1D) \rightarrow 2OH \tag{2.2}$$

In the mesosphere, the main source of OH is through photolysis of H_2O in the Schumann-Runge band region (175-205 nm) for altitudes 60-68 km and Lyman alpha line (121 nm) for altitudes above 68 km:

$$H_2O + h\nu \rightarrow OH + H \tag{2.3}$$

Dynamical Production

HO_X (mainly H) is normally produced at the sunlit latitudes and transported by the meridional circulation pattern (above 85 km) toward the winter pole and downward to altitudes below 80 km. In this region, the pressure level is sufficient to allow a third body (either N_2 or O_2) reaction of O_2 with O, creating O_3:

$$O + O_2 + M \rightarrow O_3 + M \tag{2.4}$$

which in turn reacts with H at night, forming vibrational excited OH (OH^*) [Pickett et al., 2006; Winick et al., 2009]:

$$H + O_3 \rightarrow OH^* + O_2 \tag{2.5}$$

The OH^* is quenched by either spontaneous photon emissions in the Meinel bands or by collisional relaxation [Brasseur and Solomon, 2005; Pickett et al., 2006]. This process leads to the formation of the nighttime OH layer near 82 km [Pickett et al., 2006].

Moreover during some winters, especially in the northern hemisphere, planetary wave activity is known to enhance the downwelling of thermospheric dry air [see e.g. Damiani et al., 2010b; Winick et al., 2009]. The downward motion of air is associated with adiabatic heating. The descent brings along H and O, which are important for the third body reaction shown in equation 2.4, and subsequently creating OH by reaction 2.5. As a consequence, the OH-layer is formed deeper into the atmosphere during February-March 2006 in the NH, as seen in Figure 2.14.

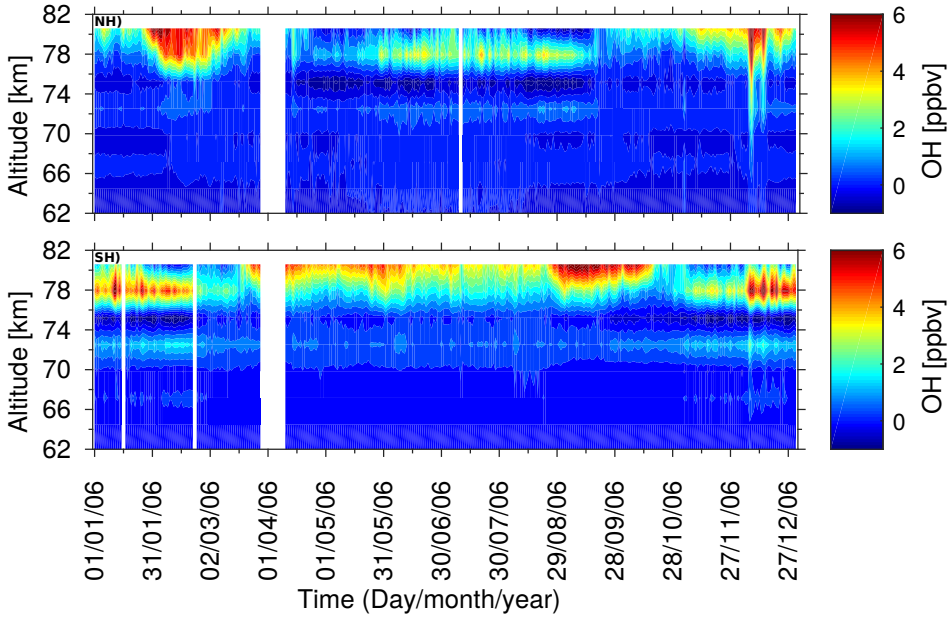

Figure 2.14: The daily mean OH volume mixing ration (VMR) variation during year 2006 at 62-81 km altitudes for the NH (top panel) and the SH (bottom panel), measured by the Aura MLS instrument. OH enhancements are evident during February-March 2006 in the NH, but not in the SH. The OH enhancements due to the December 2006 EPP events are evident in both hemispheres.

2.3.2 EPP Induced OH Production

Although both NO_X and HO_X species are formed as a result of particle precipitation, in this thesis we focus on HO_X species that are important for mesospheric chemistry. The NO_X species are more important in the stratosphere and are therefore only mentioned for completeness.

Primary Processes

As described in section 2.1.4, energetic particles precipitating into the atmosphere lose their energy through collisions causing dissociation, dissociative ionization and ionization of N_2 and O_2 by the reactions 2.6, 2.8 and 2.7 [Sinnhuber et al., 2012]:

$$X_2 + p \rightarrow X + X + p \tag{2.6}$$

$$N_2 + p \rightarrow N^+ + N + p + e^- \tag{2.7}$$

$$X_2 + p \rightarrow X_2^+ + p + e^- \tag{2.8}$$

where X is either N_2 or O_2 and p is the incident particle which can be a primary proton, electron or ion, or a secondary electron.

The above processes can form excited states of the products (N, O, N_2^+, O_2^+, N^+, O^+). Although both N_2^+ and O_2^+ are formed in the ionization process at mesospheric altitudes, the majority of the N_2^+ exchanges charge with O_2 to form O_2^+, adding to that already produced by direct ionization [Aikin and Smith, 1999; Solomon et al., 1981].

Positive Ion chemistry of Odd Hydrogen Production

The O_2^+ ion combines with O_2 to form O_4^+ which reacts with H_2O to form $O_2^+H_2O^+$. This is followed by a series of cluster reactions involving uptake of H_2O, forming progressively larger water cluster ions. This cascade of reactions is stopped when the water cluster ions dissociatively recombine with electrons forming odd hydrogen [see Crutzen and Solomon, 1980; Solomon et al., 1981]. One of the possible pathways for the above mentioned water cluster reaction is:

$$\begin{array}{ll} & O_2^+ + O_2 + M \rightarrow O_4^+ + M \\ & O_4^+ + H_2O \rightarrow O_2^+.H_2O + O_2 \\ & O_2^+.H_2O + H_2O \rightarrow H_3O^+.OH + O_2 \\ & H_3O^+.OH + H_2O \rightarrow H_3O^+.H_2O + OH \\ & H_3O^+.H_2O + e^- \rightarrow 2H_2O + H \\ \hline \text{Net:} & O_2^+ + H_2O + e^- \rightarrow O_2 + H + OH \end{array}$$

The water cluster reactions result in formation of $\sim 2HO_X$ (OH+H) radicals per ionization through dissociation of H_2O. Above 65 km altitude, HO_X production depends

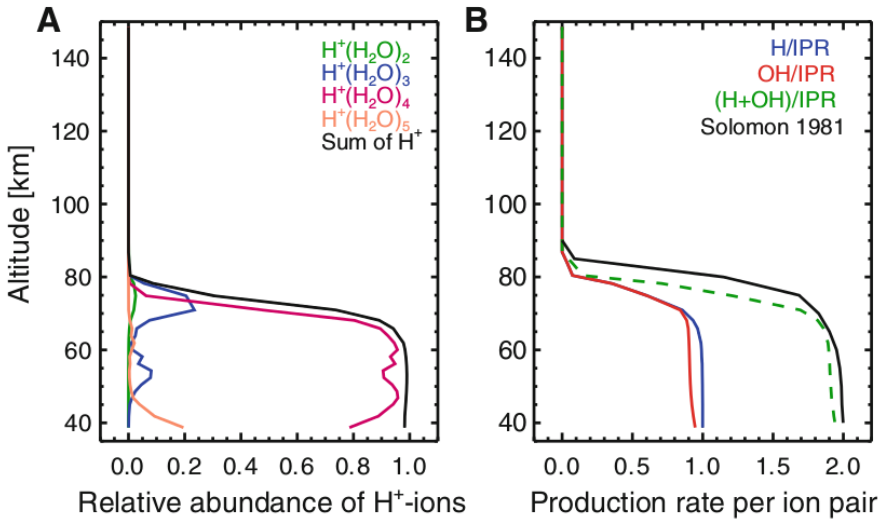

Figure 2.15: **A** Abundance of protonised water cluster ions relative to the total ion density. Colored lines represent water cluster ions with 2, 3, 4, and 5 water molecules attached; black line sum of all protonised water cluster ions. **B** Production of H, OH, and HO_X per ion pair. Blue H production per ion pair; red: OH production per ion pair; green dashed H+OH per ion pair, and black H+OH per ion pair using the parameterization of Solomon et al. [1981]. [Sinnhuber et al., 2012].

on the ionization rate, the atomic oxygen density, H_2O density, and pressure, which forms a rather sharp production cutoff around 80 km [Solomon et al., 1981]. This relationship is also depicted in Figure 2.15.B.

Figure 2.15.A shows the relative abundance of some selected water cluster ions in the mesosphere. The water cluster ions, which are important for EPP induced HO_X formation, are the most abundant positive ions in the stratosphere and lower mesosphere but do not form above ∼80 km. The formation of water cluster ions (e.g. $NO^+(H_2O)n$) that do not contribute to HO_X formation may result in a slightly lower HO_X production rate [see Sinnhuber et al., 2012]. During very elevated ionization periods, water cluster reactions are cut off by dissociative recombination of intermediates (e.g. O^+) with electrons [Crutzen and Solomon, 1980, and references therein].

The increased abundance of negative ions relative to electrons below ∼70 km implies a higher probability that positive ions will recombine with negative ions. This is an additional pathway that leads to HO_X formation in the lower mesosphere due to the reaction of water cluster ions with negative ions containing NO_3^+ [see Sinnhuber et al., 2012; Solomon et al., 1981].

2.3.3 OH Loss

Mesospheric HO_X, regardless of its source, is lost through self-destruction reactions given by [see e.g. Crutzen and Solomon, 1980]:

$$OH + HO_2 \rightarrow H_2O + O_2 \tag{2.9}$$

$$H + HO_2 \rightarrow H_2 + O_2 \tag{2.10}$$

The reaction given by equation 2.10 is responsible for reduced H_2O concentration in the upper mesosphere where photolysis of H_2O by Ly-α radiation lead to HO_X formation. Hence, particle precipitation events add to this process, most pronounced above 70 km in the mesosphere, leading to temporally enhanced conversion of H_2O to H_2 during and after an event. The reduction in H_2O mixing ratios even by a few parts per billion (ppb) may facilitate even the natural electron concentrations to reduce the efficiency of the water cluster reactions [Crutzen and Solomon, 1980].

During winter at high latitudes near the polar night terminator at altitudes near 72 km, the solar radiation responsible for generating OH is cut off because the atmosphere is optically thick at those wavelengths. This results in low OH abundances at altitudes close to 72 km under such conditions.

2.3.4 Temporal and Spatial Distribution of Background OH

Diurnal Variability

The main source of mesospheric OH is through photolysis of H_2O by solar radiation, whose efficiency at a specific altitude and latitude depends on the SZA. Figure 2.16 shows the variation of OH mixing ratio with SZA during December 2006 at 73 km at latitudes 40-80°N. Moreover, the diurnal variations in OH can be expressed as an exponential function of the secant of the SZA [Minschwaner et al., 2011]:

$$[OH] = [OH]_0 exp[-\beta sec(SZA)] \tag{2.11}$$

where $[OH]_0$ and β are altitude dependent fit parameters. β is related to the optical depths of ultraviolet absorption by O_3 and O_2.

Since HO_X production is dependent on solar radiation, nighttime HO_X production is limited, but depending on the chemical lifetime, HO_X produced during the daytime can survive after sunset. The chemical lifetime of HO_X is of the order of 0.1 to 1 day within the mesosphere (60-80 km) [Pickett et al., 2006]. The short lifetime below 80 km limits the impact of transport on HO_X abundances, making it more susceptible to the diurnal cycle. Above 80 km, however, the lifetime increases dramatically reaching $\sim$30 days at 85 km above which transport processes become an important part of the

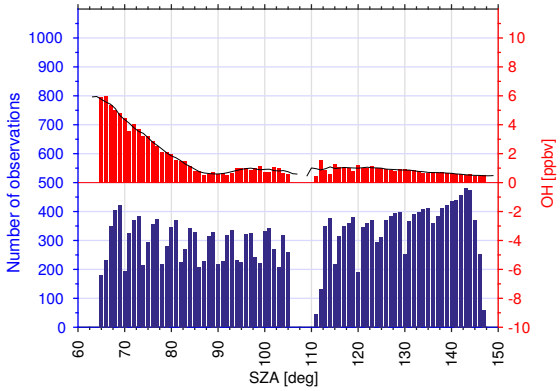

Figure 2.16: (red) Variation of OH with SZA during December 2006 at 73 km within the geographical latitude band of 40-80°N, measured by the Aura MLS instrument. (black) Running mean over a window of 5°. (blue) The number of observations comprising each mean value.

HO_X chemistry [Pickett et al., 2006].

Seasonal Distribution

During winter, the modest levels of photolysis together with lack of transport from the mid latitudes (where most of the HO_X is produced) to the inner polar vortex, lead to low OH concentrations compared to summer at high latitudes [Damiani et al., 2010a]. Figure 2.17 shows the daily mean OH at 78 km within the geographic latitude band of 40-80°N/S during year 2006, illustrating the seasonal variability of OH. The wintertime OH background is, however, sometimes enhanced by downwelling processes that are driven by planetary wave activity as described in subsection 2.3.1, illustrated in Figure 2.17 by the vertical dashed line on 31^{st} January 2006.

As such, EPP related changes in OH are easily detectable when OH background production is low, for example during wintertime as can be seen by the dotted-dashed lines in December 2006 for the NH. During weaker geomagnetic activity, as is the case with most EEP events especially during solar minimum, the EEP-OH can be masked by both the seasonal trends in photolysis of H_2O and by dynamical variability.

Geographic Distribution

The geographic distribution of the background OH is modulated by the seasonal variation of H_2O volume mixing ratio (VMR) which in turn are modulated by the atmospheric dynamics. Higher OH VMR is observed at high latitudes compared to low and mid-latitudes in the mesosphere, though there is more solar irradiation at low and mid-latitudes [see e.g. Andersson et al., 2014b; Damiani et al., 2010b]. The mean meridional circulation pattern described briefly in subsection 2.2.3 and illustrated moves H_2O from

the summer to the winter hemisphere pole, leading to an asymmetry in the distribution also of OH VMR which depends on H_2O VMR.

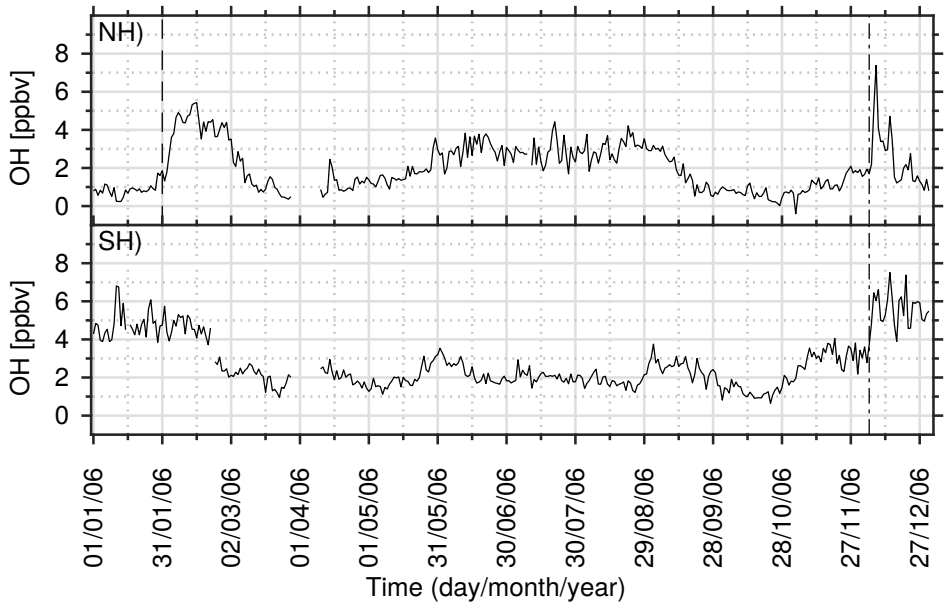

Figure 2.17: Daily mean OH at 78 km for the geographic latitude band of 45-80°N/S during year 2006, illustrating the seasonal variability in both hemispheres. A wintertime OH enhancement denoted by the vertical dashed line represents the 2006 SSW [see Damiani et al., 2010b]. The vertical dotted-dashed lines show the series of EPP activity in December 2006, visible in both hemispheres.

2.3.5 Recent Studies: Observation of SPEs Effects on OH

Theoretical, modelling and simulation studies of the effects of EPP on the atmospheric chemistry (OH and subsequently O_3) have been done since the 1970s [e.g. Crutzen and Solomon, 1980; Sinnhuber et al., 2012; Solomon et al., 1981; Swider and Keneshea, 1973]. Although rocket experimental studies on O_3 response to SPEs were possible [e.g. Weeks et al., 1972], global measurements of the HO_X species only started recently with the Aura MLS satellite.

In the first direct confirmation of the theories of HO_X production by ion chemistry, Verronen et al. [2006] use OH and O_3 measurements from the Aura MLS and GOMOS/Envisat instruments respectively, together with a 1-dimensional ion and neutral chemistry model to study the changes in HO_X and O_X during the January 2005 SPE. They report increases in the OH concentrations of up to one order of magnitude in the middle mesosphere and greater than 100% in the stratosphere, with model predictions

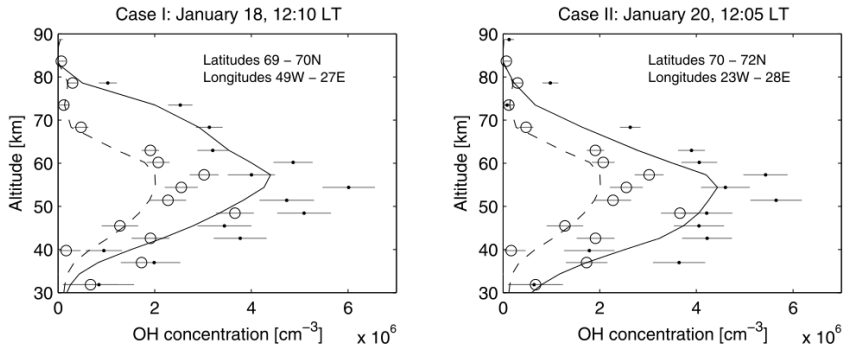

Figure 2.18: (top) Comparisons of OH concentrations. MLS values, which are error weighted averages for the latitude and longitude regions indicated in the panels, are marked by dots, with the statistical error estimates shown with horizontal lines. The solid lines mark the model results from the SPE run. The dashed lines and the circles present reference values, i.e., the modeled and observed OH concentrations for January 15 before the onset of the SPE, respectively. [Verronen et al., 2006].

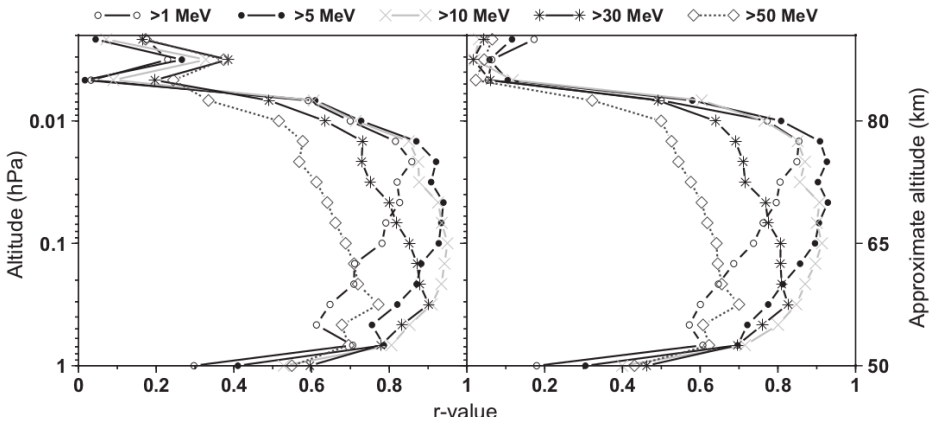

Figure 2.19: Correlation coefficients (r-values) of proton flux vs. OH mixing ratio for various altitudes and energies. Left side: proton flux vs. OH increment (i.e., the difference between the daily OH mixing ratio of SEP influenced days and the daily OH mixing ratio of the pre-event day) induced by SEP events. Right side: proton flux vs. actual daily OH of SEP influenced days [Damiani et al., 2010a].

in reasonable agreement with the observations as shown in Figure 2.18. They point out that using the P_{HO_X}/Q parametrization (HO_X production per each SPE-induced ion-pair) can lead to an underestimation of the HO_X production and O_3 depletion [see also Sinnhuber et al., 2012].

Damiani et al. [2010a] discuss the possibility of using the mesospheric OH observations recorded in the polar nighttime conditions as an indicator of solar energetic particles or SPEs. Figure 2.19 shows the correlation between OH mixing ratios from the Aura MlS and particle fluxes from the Geostationary Operations Environmental satellite (GOES) proton channels at energies >1, >5, >10, >30, and >50 MeV. They found the best correlation of r∼0.90-0.95 for energies >5 MeV and >10 MeV at approximately 65-70 km altitudes while the most energetic channels exhibited high correlations at lower altitudes. They speculate that it is possible to estimate SPE proton fluxes from OH values and vise-versa at approximately 50-86 km altitudes. Such could be useful in studying periods with data gaps.

More of the review of recent studies is given in subsection 2.4.4 where the SPEs effects on OH are linked to O_3 variability.

2.3.6 Recent Studies: Observations of EEP Effects on OH

EEP Impact on the Geographic Distribution of OH

Since medium energy electrons (> 30 keV) typically precipitate from the Earth's radiation belts, the effects thereof are expected in magnetic latitudes connected to the outer radiation belt. Verronen et al. [2011] see OH enhancement at magnetic latitudes 55-65° at altitudes 71 to 78 km. By considering the latitude extent of the electron forcing, Andersson et al. [2012] find clear EEP effects on OH at a wider magnetic latitude band covering 55-72°. Hence the OH density at high latitudes follows magnetic rather than geographic latitudes during EEP events.

EEP not only affects the latitude distribution of OH, but also the longitudinal distribution. Andersson et al. [2014b] analyze the EEP-induced longitudinal OH variations by calculating spatial distributions of nighttime medians between 70 and 78 km during years 2005 to 2009 for two data sets with different strength of EEP forcing: high EEP for which the daily mean electron count rate (ECR) is >100 counts/s (51 days) and low EEP for which the daily mean ECR is <5 counts/s (1340 days). Their results show that the EEP-induced OH variations exhibits local maxima over North America and North Asia in the NH, and a region of high OH mixing ratios over the Antarctic Peninsula (longitudes 150°W-30°E) in the SH as illustrated in Figure 2.20. The Antarctic OH enhancement is attributed to the strong regional EEP forcing, although they speculate that atmospheric conditions also might play a role. This OH signature is also seen during periods of low geomagnetic activity which is attributed to a steady drizzle of radiation

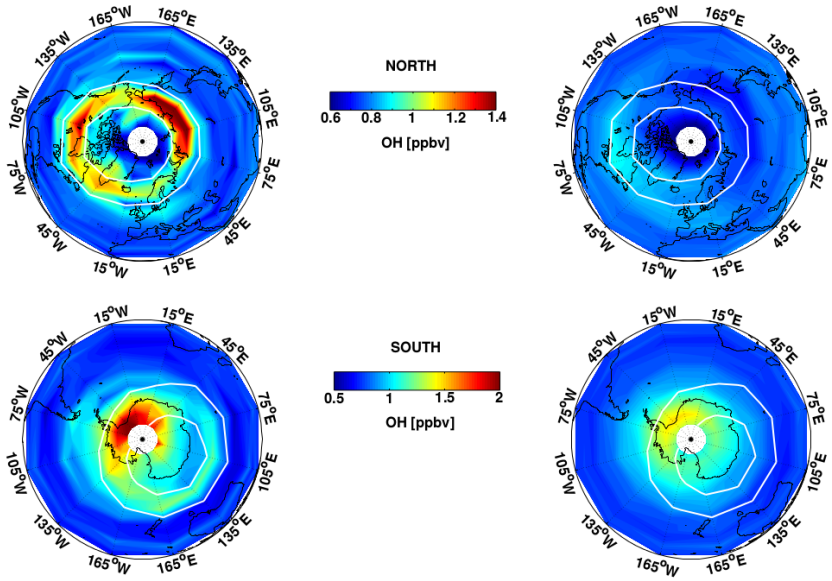

Figure 2.20: Spatial distribution of OH medians in the NH (upper panel) and SH (lower panel) calculated for the days with: (1) electron count rate (ECR)> 100 counts/s (left panels) and (2) ECR< 5 counts/s (right panels) for the time period January 2005–December 2009 and altitude range 70–78 km. Median values were calculated for each 5 (latitude) by 30 (longitude) degree bin between latitudes 82°N to 82°S and longitudes 180°W to 180°E. Approximate geomagnetic latitudes 55–72°N/S are indicated by superimposed white lines. Taken from Andersson et al. [2014b].

belt electrons affecting the atmospheric composition in that region with low magnetic field strength.

Quantification of the Contribution of EEP to OH Variability

Before satellite observations of OH were available, the studies conducted were mainly modeling and numerical simulations giving a measure on the impact of EEP on OH [e.g Aikin and Smith, 1999]. With OH observations from the Aura MLS, it is possible to compare the model predictions with observations.

The Aura MLS provides observations of the perhydroxyl radical (HO_2) but these observations are not suitable for scientific use for altitudes approximately above 70 km [Livesey et al., 2015]. Hence most studies focus on OH as a member of the HO_X to study EEP effects on the HO_X species since the behavior of OH and HO_2 is generally similar [Crutzen and Solomon, 1980].

In the first observational study of the EEP impact on OH, Verronen et al. [2011] select two cases studies: March 2005 and April 2006 to demonstrate the link between 100-300 keV ECRs observed in the outer radiation belt and nighttime OH concentrations in the middle atmosphere at altitudes 71-78 km. They utilize the NOAA/POES

MEPED 0° electron telescope observations from NOAA-15, NOAA-16 and NOAA-17 at magnetic latitudes 55-65°, and OH observations from Aura/MLS. By assuming that the nighttime HO_X production rate is proportional to the ECR and that the loss is due to the HO_X+HO_X reactions so that the loss rate is proportional to $[HO_X][HO_X]$, then the concentration of odd hydrogen $[HO_X]$ is proportional to $\sqrt{ECR}$ by the equation:

$$[OH] = (a * \sqrt{ECR} + b) * 10^5 cm^{-3} \tag{2.12}$$

where a and b are line fit coefficients. They found a low correlation at 81-82 km altitude due to the formation of the nighttime OH layer that masks EEP effects and the lack of H_2O above implying absence water cluster ions. They found that at 71-78 km altitude the correlation between the count rate and OH data was positive and high such that 56-87% of the OH variation can be explained by EEP. This percentage depends on the background OH concentration which determines the threshold flux of electrons that must be exceeded for EEP-OH production to significantly exceed the background production. They also investigated the possible role of H_2O and temperature in the observed OH observations. They found that in March 2005 both EEP and the monthly trend in H_2O need to be considered in order to understand the OH variations. The negative correlation with temperature is because temperature is dynamically connected with H_2O.

In a following study, Andersson et al. [2012] study variations of nighttime EEP induced OH using Aura MLS measurements and the MEPED 0° detector observations from all available NOAA POES satellites located inside the L-shell 3-5.5 (magnetic latitudes 55-65°) in either hemispheres during years 2004 to 2009. By assuming a linear relationship, they calculated Pearson's product-moment correlation coefficients using daily mean ECR and OH for each month separately for altitudes 38-85 km in both hemispheres, the results of which are shown in Figure 2.21. Although Verronen et al. [2011] show that OH mixing ratios do not increase linearly with electron flux, they increase monotonically such that linear correlation analysis can be used to study the EEP-OH relationship. For months with daily mean 100-300 kev ECR>150 counts/s, they find a strong correlation of r$\geq$0.6 between OH mixing ratios at 70-78 km and precipitating electrons. For altitudes 52-70 km, the correlation is at least $\geq$0.35. They point out that the correlation does not always increase linearly with the amount of precipitating electrons, because it is also affected by background atmospheric conditions like the amount of background OH and to a lesser extent day to day variations in H_2O VMR, I_α^{SZA} and temperature. Using the Sodankylä Ion and Neutral Chemistry (SIC) model, they find that the OH concentration is more sensitive to changes in temperature than those in H_2O VMR (during March 2008 at 60°N/S and 0°E), which is related to the changes in chemical reaction rates. Moreover for both H_2O VMR and temperature,

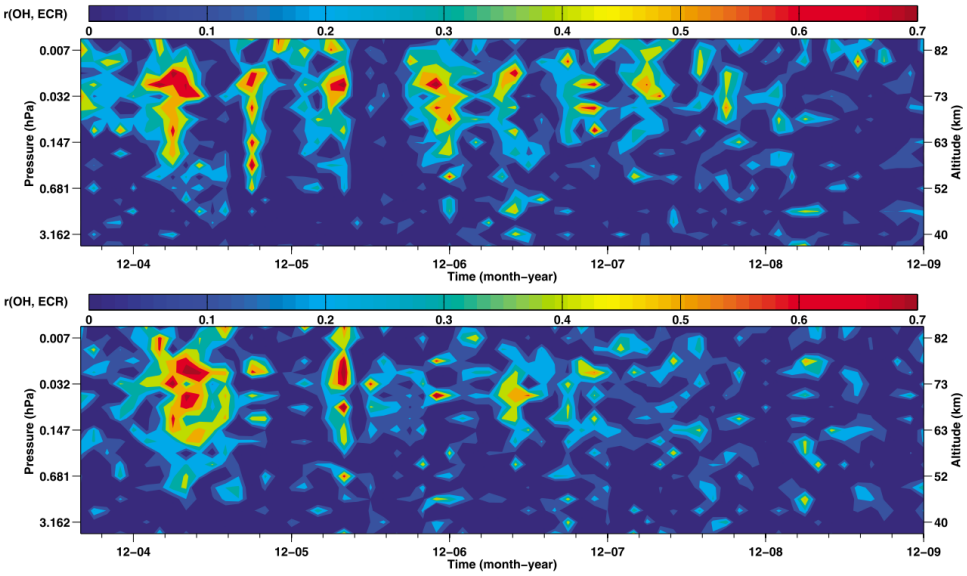

Figure 2.21: Correlation coefficient r between daily mean OH mixing ratio and daily mean ECR. Altitudes 38–85 km (4.642–0.005 hPa) are shown between August 2004–December 2009 at geomagnetic latitudes (top) 55–65°N and (bottom) 55–65°S. Taken from Andersson et al. [2012].

at nighttime the sensitivity is modest compared to daytime, which indicates a better possibility of identifying EEP effects at night.

Verronen et al. [2013] use the SIC Model to study the effects of radiation belt electrons on mesospheric OH and O_3 observed by Aura MLS. They use a combination of electron fluxes from the POES MEPED 0° detector and IDP/DEMETER satellite instruments to model the electrons' energy spectra and atmospheric ionization rates. By considering the four strongest EEP events (January, March, May 2005 and April 2006) that occurred during the period 2004-2009, their results show the magnitude of the relative enhancement in OH depends on SZA and the level of background OH production. They report O_3 depletion of up to several tens of percent, comparable to the effects previously reported in cases of SPEs. Generally, the model was able to reproduce the daily variability of OH and O_3, especially at 70-80 km latitudes as shown in Figure 2.22 for the January EEP 2005 event. However, they can not make strong conclusions for altitudes below 70 km where >300 keV electrons precipitate. The uncertainty might be because the MEPED 0° detector only covers a fraction of the BLC and the electron measurements can be contaminated by protons, which limitations are not catered for.

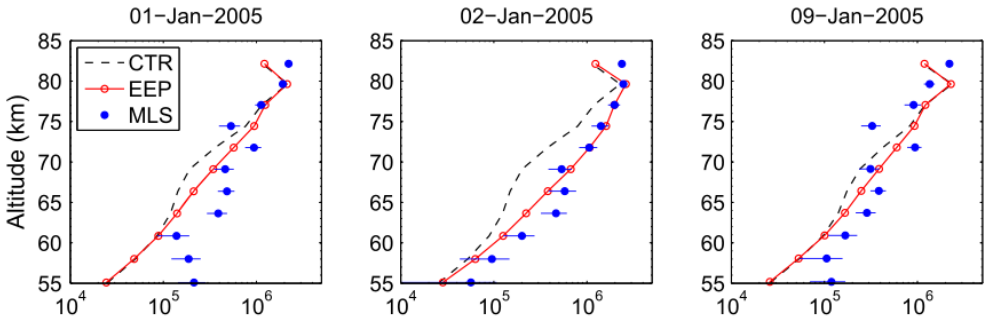

Figure 2.22: Comparison of NH modeled and observed nighttime OH concentrations (left) before, (middle) during, and (right) after the peak EEP day for January 2005. Black, red, and blue colors mark the data from SIC CTR run, SIC EEP run, and MLS observations, respectively. Adopted from Verronen et al. [2013].

2.3.7 Outstanding Questions

Andersson et al. [2014b] point out the relatively high OH mixing ratios over North America during periods of low EEP, but provide no explanation for it. Further, the EEP impacted OH maps are based on only ∼50 days, which during wintertime could be influenced by planetary waves. Therefore, it is important investigate the EEP role in the longitudinal distribution of OH together with the atmospheric conditions that may lead to longitudinal structures in the observed OH enhancement in the two hemispheres.

Andersson et al. [2014b, 2012] and Verronen et al. [2011] point out that the background atmosphere has an undeniable important effect on the OH background, which may affect the detection and assessment of contribution of EEP to OH variability. Therefore in order to separate, quantify and understand the contribution of EEP to OH variability, we need to consider all the possible sources of variability. As already seen, correlation analysis accounts for each predictor variable separately. A method is required that can take into consideration all the predictors together and also account for the nonlinear relationship pointed out in Verronen et al. [2011]. One possible method is multiple linear regression, which gives the contribution of a predictor variable when other variables are held constant.

2.4 Ozone Variability

In this section, the production of O_3 at different atmospheric altitudes and seasonal conditions are described with focus on the wintertime nighttime O_3 variability. The O_3 loss mechanisms are also described with emphasis on the catalytic reactions driven by the HO_X species. This chapter concludes with a discussion of the spatial and temporal

variability of the tertiary O_3 layer and a summary of recent studies.

2.4.1 Ozone Production

The Primary and Secondary Ozone Layer

O_3 belongs to the family of chemical species known as odd oxygen (O_X: O + O_3). An O_3 maximum occurs at altitudes 30 to 35 km in the stratosphere as a result of absorption of UV radiation in the Herzberg continuum (185 - 242 nm) leading to production of O_3 through photolysis of O_2 [Chapman, 1930].

$$O_2 + h\nu \rightarrow O + O \tag{2.13}$$

The resulting atomic oxygen, in turn reacts with O_2 to form O_3 by a reaction which is the same as equation 2.4. In the mesosphere, the rapid photolysis leads to low O_3 concentrations during the daytime compared to nighttime as shown in Figure 2.23.

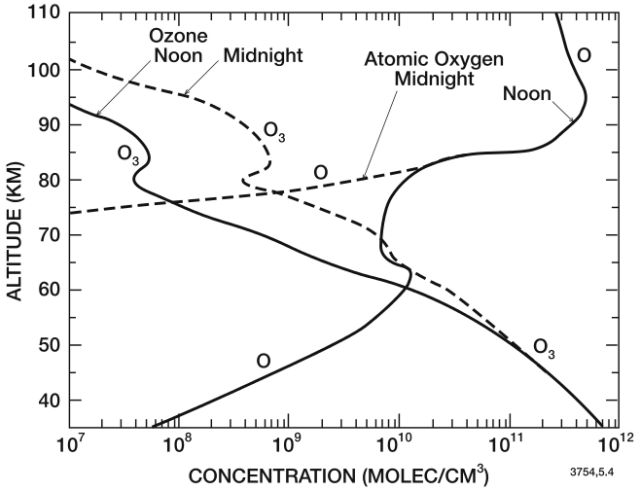

Figure 2.23: Calculated vertical distribution of O_3 and O at noon and midnight. Taken from Brasseur and Solomon [2005].

The downward transport of atomic oxygen from the thermosphere above 100 km caused by photodissociation of O_2 in the Schumann-Runge bands (137-200 nm) results in the formation of the secondary O_3 maximum which is found near the mesopause. The formation reactions are the same as in equation 2.4 in subsection 2.3.1.

The Tertiary Ozone Layer

In the wintertime hemisphere at high latitudes near 72 km, there exists a local maximum in O_3 near the polar night terminator which Marsh et al. [2001] called the tertiary ozone maximum , hereafter called the tertiary O_3 layer. This layer is created near the polar night terminator where the atmosphere is optically thick to wavelengths below 185 nm (primarily Lyman alpha) that are responsible for photolysis of H_2O. At nearly grazing incidence (large SZA) conditions, the solar radiation that dissociates H_2O is almost completely absorbed, resulting in reduced production and low concentrations of HO_X[Marsh et al., 2001; Sonnemann et al., 2006]. The radiation in the Schumann-Runge bands and Herzberg continuum (185-242 nm), however, continues to penetrate the high latitudes near the polar night terminator and thus photolysis of O_2 continues and subsequent production of O_3. Therefore, without the HO_X catalytic losses, O_3 concentrations increase and persist throughout the night since the chemical lifetime of O_X is of the order of $\sim$0.1 to 1 day at 72 km in the polar night depending on the latitude [see Smith et al., 2009]. The altitude-O_3 profiles in Figure 2.23 show the elevated O_3 concentrations during nighttime in the mesosphere.

2.4.2 Ozone Loss

The Chapman [1930] cycle also accounts for O_3 loss by the reaction with atomic oxygen and by photolysis at wavelengths less than 238 nm by the reactions:

$$O_3 + O \rightarrow O_2 + O_2 \tag{2.14}$$

$$O_3 + h\nu \rightarrow O + O_2 \tag{2.15}$$

The Chapman model, however, can only account for a small portion of the total O_3 losses throughout the atmosphere [Thorne, 1980]. In the middle atmosphere, a more significant portion of the O_X is destroyed through catalytic cycles dominated by the NO_X and HO_X species [see e.g. Thorne, 1980], here symbolized with letter the X:

$$X + O_3 \rightarrow XO + O_2 \tag{2.16}$$

$$XO + O(^3P) \rightarrow X + O_2 \tag{2.17}$$

The net O_X loss reaction is of the form:

$$O_3 + O \rightarrow 2O_2 \tag{2.18}$$

Since atomic oxygen is produced by photodissociation of O_2 in the presence of sunlight, these catalytic cycles are limited during the nighttime because of low atomic

oxygen concentration in the absence of sunlight (see Figure 2.23). During daytime, at approximately 73 km, odd-oxygen loss rates are dominated by catalytic cycles involving atomic oxygen [Marsh et al., 2001].

Just after sunset, O_X loss increases briefly due to rapid conversion of atomic oxygen to O_3 and the subsequent loss through the following reaction [Marsh et al., 2001]:

$$H + O_3 \rightarrow OH + O_2 \tag{2.19}$$

The effectiveness of this loss channel, however, decreases over a few hours as atomic hydrogen is rapidly converted to OH after sunset.

During EPP not all ionization results in production of odd hydrogen as atomic oxygen can also be produced when some of the O_2^+ recombined dissociatively with electrons by several reactions [Aikin and Smith, 1999]:

$$N_2 + O_2 \rightarrow NO^+ + NO \tag{2.20}$$
$$NO^+ + e \rightarrow N + O \tag{2.21}$$
$$N^+ + O_2 \rightarrow O_2^+ + N \tag{2.22}$$
$$N_2^+ + O_2 \rightarrow O_2^+ + N_2 \tag{2.23}$$
$$O_2^+ + e \rightarrow O + O \tag{2.24}$$

However, the above reactions produce negligible atomic oxygen as compared to that produced through daytime photodissociation of O_2, implying that it does not fuel the HO_X catalytic cycles significantly.

The NO_X catalytic cycles dominate O_3 destruction in the stratosphere while the HO_X catalytic cycles are responsible for O_3 destruction in the mesosphere [Thorne, 1980]. Chlorine catalytic cycles are also known to deplete stratospheric O_3 and are responsible for the formation of the O_3 hole in spring.

2.4.3 Variability of the Tertiary Ozone Layer due to the Background Atmosphere

Observed throughout the whole winter, the magnitude and latitude extent of the tertiary O_3 layer varies significantly. The long photochemical lifetime of O_3 in the polar night below 80 km makes O_3 susceptible to both vertical and horizontal motion. Vertical motion is probably a major contributor to the observed downward displacement of the tertiary O_3 layer by several kilometers during 2004, 2006 and 2009 [see e.g Damiani et al., 2010b; Smith et al., 2009]. The downward transport of atomic oxygen (O) also plays a role in the overall amount of observed O_X. Normally during nighttime the HO_X catalytic cycles are slowed down due to lack of atomic oxygen in darkness.

The downward mean circulation and/or the downwelling associated with planetary wave activity can lead to either O_3 enhancement or decrease in the following ways

[see Smith et al., 2018]: The descending dry air from the thermosphere implies low production of HO_X species through photolysis of H_2O and therefore reduced catalytic loss of O_3, and hence high O_3 mixing ratios. On the other hand downwelling can also lead to low O_3 mixing ratios through dynamical production of OH described in subsection 2.3.1 together with the higher temperature from adiabatic warming. The OH catalytically destroys O_3 in the presence of sunlight while higher temperature also imply reduced production of O_3 through the reaction given by equation 2.4 [see Smith and Marsh, 2005]. In the presence of dynamics, low H_2O VMR (predicting low HO_X concentrations, high O_3 VMR) is normally seen in phase with high temperature (predicting low O_3 VMR). Hence, the two processes counteract each other leading a weak correlation between O_3 VMR and either H_2O VMR or temperature as seen in Figure 2.24, top panels.

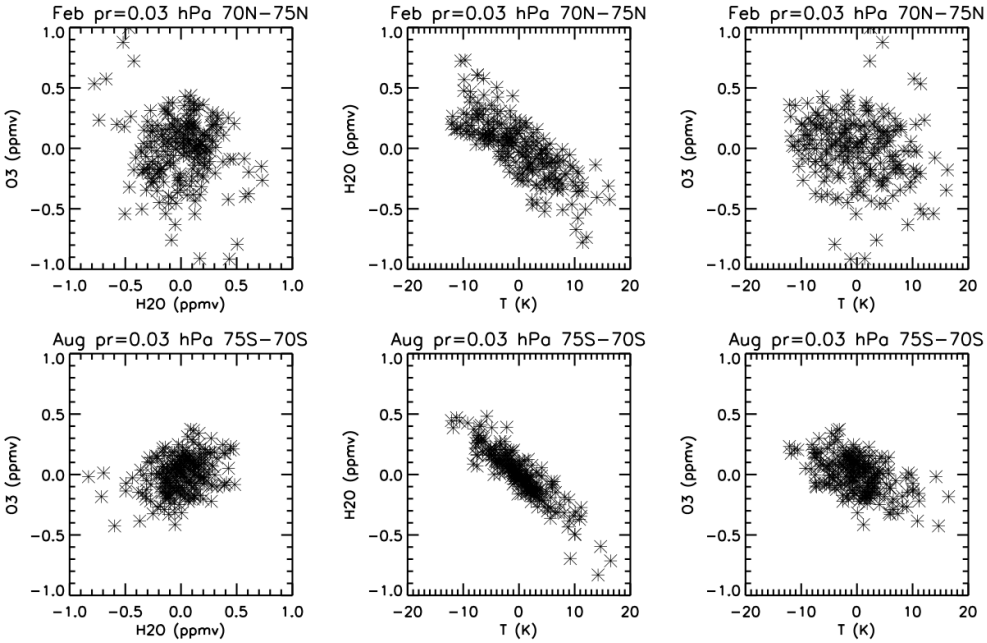

Figure 2.24: Scatter plots of the monthly average perturbations from the zonal average of nighttime ozone VMR versus H_2O VMR, H_2O VMR versus temperature, and O_3 VMR versus temperature for the latitude bands 70°–75°N in the month of February (top) and 70°–75°S in the month of August (bottom). The points in each panel include 18 longitude bins over 13 years. Taken from Smith et al. [2018].

Based on photochemistry, low temperatures implies that O_3 is more readily produced from the reaction indicated by equation 2.4 and it is destroyed more slowly by the reactions $O_3 + O \rightarrow O_2 + O_2$ and $O_3 + H \rightarrow OH + O_2$. In this case, the O_3 VMR

will exhibit a strong positive correlation with H_2O VMR as shown in Figure 2.24, bottom left panel. Because of the strong dynamical negative correlation between H_2O VMR and temperature (Figure 2.24, middle panels), O_3 VMR exhibits a corresponding negative correlation with temperature as shown in Figure 2.24, bottom right panel. For detailed studies on the variability of the nighttime O_3 layer see e.g. Damiani et al. [2010b]; Smith et al. [2018]; Sofieva et al. [2009].

2.4.4 Recent Studies: Observation of the SPEs-OH Effects on Ozone

The depletion of middle atmospheric O_3 concentrations due to SPE-induced HO_X catalytic cycles has been modeled and observed by measurements [e.g. Jackman et al., 2011, 2014; Solomon et al., 1983; Swider and Keneshea, 1973; Turunen et al., 2009]. This thesis mainly focuses on observational studies of the EEP effects on OH VMR and consequently on mesospheric O_3 VMR and the tertiary ozone layer. Consequently, in the studies reviewed here we focus mainly on EPP effects on the tertiary ozone layer.

In the first study to observe the disappearance of the tertiary O_3 layer, Seppälä et al. [2006] use O_3 VMR observations from the GOMOS instrument together with a coupled ion and neutral chemistry model to study the effects of the January 2005 SPE on the polar winter atmosphere. They use the model to infer the SPE-HO_X (and NO_X) link to O_X reduction. They find more than 70% depletion of O_3 VMR in the mesosphere between 65-80 km altitude, as also reported by Verronen et al. [2006]. They point out that for efficient loss of O_X through HO_X catalytic reactions, proton precipitation must take place in the area where the tertiary O_3 layer is observed and atomic oxygen should be available for the catalytic HO_X cycles.

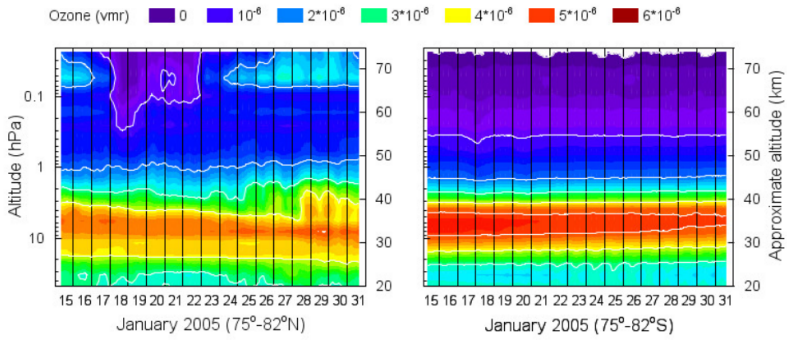

Figure 2.25: Temporal evolution of averaged values (∼75°–82°N and S) of atmospheric O_3 volume mixing ratio (VMR) for the investigated 2005 SEP events: (top) January, at North 93°<SZA<118° and at South 61°<SZA<87°. Taken from Damiani et al. [2008].

Using proton flux data from the GOES (Geostationary Operational Environmental satellites) satellite series and Aura MLS OH and O_3 observations, Damiani et al. [2008]

investigate the effects of the January, May and September 2005 SPEs on atmospheric chemistry, focusing on the relationship between O_3 and OH. They confirm that SPEs effects are different on the night and day hemispheres at high latitudes, as shown in Figure 2.25. Further their results show little response in O_3 VMR to SPEs-OH in the summer hemisphere.

Using GOMOS observations, Sofieva et al. [2009] in Figure 2.26 show a drop to values below 0.5 ppmv in the O_3 mixing ratios at the altitude of the tertiary O_3 layer compared to the pre-SPE values of approximately 2 ppmv for the SPEs in December 2006. They show that even moderate SPEs destroy the tertiary O_3 layer.

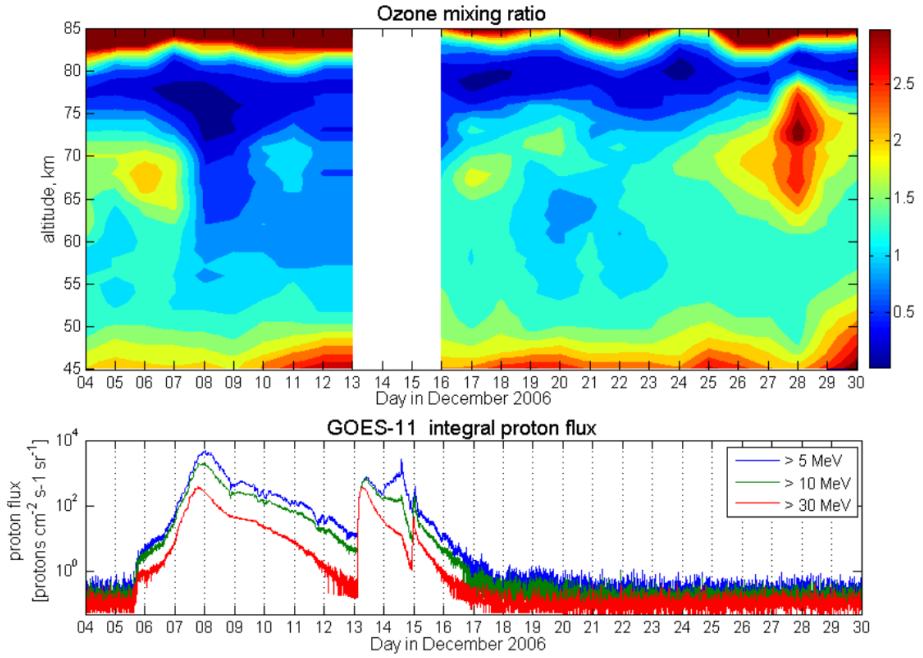

Figure 2.26: Top. Daily O_3 mixing ratios at latitudes 60-90°N in December 2006. Bottom: Proton flux measured by GOES-11. Note the destruction of tertiary O_3 layer caused by the SPE. Taken from Sofieva et al. [2009].

Verkhoglyadova et al. [2015] use particle flux measurements from GOES SEM instrument, OH from Aura MLS and O_3 from SABER to analyze the global middle atmospheric effects at local nighttime for the 7-17 November 2004 and 20-30 August 2005 SPEs. They report OH density increases during the storm main phases at latitudes $\pm$50°N/S at 65-80 km altitude corresponding to energetic proton fluxes of energy $>$10 MeV. They observe corresponding statistically significant O_3 depletions of up to 45% at latitudes 60-70°N/S. Larger relative O_3 destructions were seen in the winter hemispheres.

In a following study, Verkhoglyadova et al. [2016] use the Atmospheric Ionization Module Osnabrück (AIMOS) model to calculate the ionization rates for measured SPEs fluxes and estimate corresponding changes in OH abundances during the 7-17 November 2004 and 20-30 August 2005 SPEs. Their results show that both SPEs and precipitating electrons contribute (almost simultaneously) to the total ionization of the middle atmosphere during SPEs and concurrent geomagnetic storms, resulting in enhancement of the nighttime OH. They report that the relative contribution of electrons (compared to SPEs) could reach approximately 90% at 70-120 km altitude during the recovery phase of a geomagnetic storm, depending of the strength, duration and timing of the SPEs and the associated geomagnetic storms.

2.4.5 Recent Studies: Observation of EEP-OH Effects on Ozone

As already mentioned EPP in general can modify the distribution and concentrations of O_3 through production of HO_X in the polar night terminator region where the tertiary O_3 layer is formed. Several studies have focused on the OH induced O_3 reduction during periods of SPEs [e.g. Seppälä et al., 2006; Sofieva et al., 2009; Verkhoglyadova et al., 2015]. There is growing attention on the EEP-OH link to O_3 depletion, boosted by the availability of OH observations from the Aura MLS.

The geomagnetic storms associated with EEP tend to occur more frequently than SPEs and are predominantly recurrent during the declining phase of the solar cycle. Daae et al. [2012] infer that the frequency of such storms can lead to a significant impact on the middle atmosphere chemistry, possibly causing persistent suppression of mesospheric O_3. Turunen et al. [2016] model the effect of high-energy electron precipitation (of duration 30 min) using the SIC model and find 14% depletion of O_X at 75 km altitude. They report that the largest relative change in O_X is not seen during the actual event, but after the HO_X catalytic cycles have had an impact. They also note that pulsating aurora events occur much more frequently than SPEs and often cover large spatial regions and hence may have significant consequences on the concentrations of chemically active minor neutral constituents. Model simulations by Andersson et al. [2018] indicate average EEP (and SPEs)-induced O_3 variability of 12-24% in the mesosphere on decadal time scales, in agreement with previously published results.

The study by Andersson et al. [2014a] uses MEPED 0° electron fluxes spanning L-shells 3.0-5.5 which are corresponding to geomagnetic latitudes 55-65° and the location of the inner and parts of the outer radiation belt to study the EEP-HO_X link to O_3. For O_3, they use multiple satellite observations from Aura MLS, SABER and GOMOS (Global Ozone Monitoring by Occultation of star). With respect to a 7-days pre-storm average, their results show up to 90% short-term O_3 depletions at 75-80 km altitude, which reach down to 60 km and are comparable to the effects of the large SPEs. By

contrasting periods of maximum and minimum EEP activity, which is considered as an indication of the maximum variability over a solar cycle, they found up to 34%, 21% and 9% for SABER, GOMOS and MLS respectively, shown in Figure 2.27. The result from MLS (2005 to 2009) is less due to lower EEP forcing in 2005 compared to 2003 for SABER and GOMOS. By considering the magnitude of direct O_3 effect, they suspect that EEP could be an important contributor to the Sun-climate connection. They thus suggest that more research should be directed to better understanding of the potential effects of EEP on O_3 concentrations and its contribution in the overall solar influence on climate. This knowledge would be useful for the solar input in climate models.

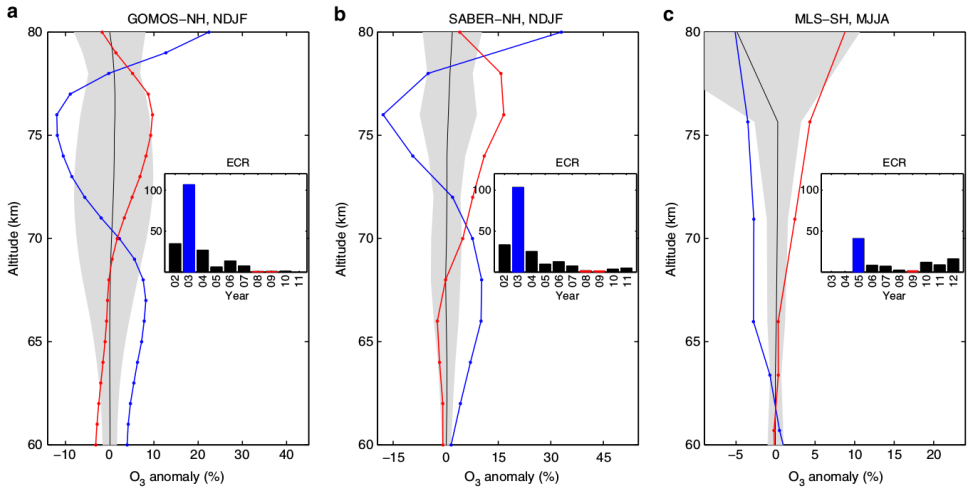

Figure 2.27: Magnitude of the long-term EEP effects on mesospheric ozone. (a–c) Ozone anomalies (% of deseasonalized daily means, averaged over the winter time. (a) November to February in the Northern hemisphere from GOMOS showing years 2003 (blue line) and 2008–2009 (red line). (b) November to February in the Northern hemisphere from SABER showing years 2003 (blue line) and 2008–2009 (red line). (c) May to August in the Southern hemisphere from MLS showing years 2005 (blue line) and 2009 (red line). Black lines: winter time climatology from 2002 to 2012; grey area: 95% confidence range of the climatological mean. Subplots: winter time average ECRs between 2002 and 2012. Taken from Andersson et al. [2014a].

2.4.6 Outstanding Questions

The study by Andersson et al. [2014a] suggests that the apparent low O_3 VMR change found in the Aura MLS observations is a result of the lower EEP forcing during the period 2005-2009. However, other conditions may also affect the O_3 VMR response to EEP-OH for example the season, time (SZA) and region of abundant O_3. The EEP-OH

impact on the tertiary O_3 layer depends on a complex combination of the intersection of a geomagnetically-oriented auroral zone and the geographically-oriented tertiary O_3 layer which varies with season and atmospheric dynamics. Further the O_3 catalytic reductions require atomic oxygen that is abundant during sunlit hours. Hence, to observe the maximum EEP-OH impact on the tertiary O_3 layer, the satellite must be in a specific local time sector to make observations of the direct EEP-OH impact on O_3 VMR. Studies investigating the EEP-OH impact need to consider the conditions and locations (in time and space) when/where EEP is important for the tertiary O_3 layer. Simultaneous observation of OH and O_3 mixing ratios is an advantage to investigate that the apparent change is truly due to OH increase and not of a dynamical origin.

Chapter 3

The Data and Methodology

This chapter gives a description of the data used in the studies included in the thesis. Emphasis is placed on the particle data which are known to possess limitations on their use. The known challenges of the particle data are pointed out together with remedies used for the corrections. It goes on to explain how the energy deposition profiles are retrieved from the corrected particle fluxes (or electron loss cone flux). This is followed by a description of the AURA MLS measurements of OH, O_3, H_2O VMR and temperature and some of the conditions under which the data can be used to accomplish the objectives of the studies in this thesis. The sources of the solar Lyman alpha radiation, solar wind parameters and magnetic indices are also briefly mentioned. The detailed explanations on how the data are applied can be found in the respective papers.

3.1 Measurement of Energetic Particles

3.1.1 NOAA/POES MEPED Observations

The Space Environment Monitor-2 (SEM-2) on board the NOAA POES satellites houses the MEPED instruments which monitor intensities of protons nominally from 30 keV to $>$ 140 MeV and electrons nominally from $>$30 keV to $>$1 MeV [Evans and Greer, 2000]. POES orbits the Earth in a polar Sun synchronous orbit at about 800 km altitude, making measurements within the same solar local time sector for all passes throughout the day. For this study we use data from NOAA-16 for year 2005 and NOAA-18 for years 2006-2009.

Channel	Energy Range [keV]
0/90 P1	30 to 80
0/90 P2	80 to 240
0/90 P3	240 to 800
0/90 P4	800 to 2500
0/90 P5	2500 to 6900
0/90 P6	$>$6900

Table 3.1: MEPED proton energy bands [Evans and Greer, 2000].

The MEPED consists of eight particle detector sys-

tems whose basic designs are described by Evans and Greer [2000]. The first set is the 0° and 90° proton solid state detector telescopes that monitor the intensity of protons in six energy bands as listed in Table 3.1. The front silicon solid-state detector in the proton telescopes is known to suffer from degradation due to radiation damage resulting in a raise of the energy thresholds to values higher than those specified in Table 3.1. In this study, the proton fluxes are corrected for degradation due to radiation damage by using correction factors derived by Sandanger et al. [2015] and Ødegaard et al. [2016].

The second set is the electron solid-state detector system which also consists of the 0° and 90° telescopes which monitor the intensity of electrons in the three energy bands listed in Table 3.2 of which the fourth energy channel is derived from relativistic electron contamination of the P6 channel [Nesse Tyssøy et al., 2016]. The electron detector telescopes are also sensitive to protons within the range 210 keV to 2700 keV as shown in Table 3.3. With the corrected proton fluxes [Ødegaard et al., 2016; Sandanger et al., 2015], the contribution of protons to the total electron telescope observations can be determined as described by Nesse Tyssøy et al. [2016].

Channel	Energy Range [keV]	Corrected Energy Range [keV]
0/90 E1	30 to 2500	>43
0/90 E2	100 to 2500	>114
0/90 E3	300 to 2500	>292
0/90 P6	>1000	>756

Table 3.2: MEPED electron energy bands and corrections [Evans and Greer, 2000; Ødegaard et al., 2017].

For the electron corrections, the Sandanger et al. [2015] and Ødegaard et al. [2016] correction factors are applied to an integral spectrum to determine the proton energy ranges measured by the telescopes. A monotonic Piecewise Cubic Hermite Interpolating Polynomial (PCHIP) is applied to the measured fluxes. The proton fluxes in the energy ranges shown in Table 3.3 are retrieved and are subtracted from the original measured electron fluxes. Hence the corrected proton fluxes are used to adjust for proton contamination in the electron data. The geometric factor for the electron detectors varies with the electron energy spectrum. Ødegaard et al. [2017], therefore, calculated new optimized geometric factors of which the associated new electron energy thresholds are >43 keV, >114 keV, >292 keV and >756 keV as shown in the third column in Table 3.2.

Channel	Proton Energies [keV]
0/90 E1	210 to 2700
0/90 E2	280 to 2700
0/90 E3	440 to 2700

Table 3.3: MEPED electron detector sensitivity to protons [Evans and Greer, 2000].

The third detector set consists of four omni-directional (dome) solid state detectors

designed to be sensitive to very energetic protons incident on the solid state detector over a wide range of angles, with a viewing axis parallel to the 0° MEPED proton and electron detector telescope units. These detectors measure proton energies in the range of >16 MeV to >140 MeV. For detailed description of the omni-directional detectors see Evans and Greer [2000].

3.1.2 Loss Cone Fluxes and Energy Deposition

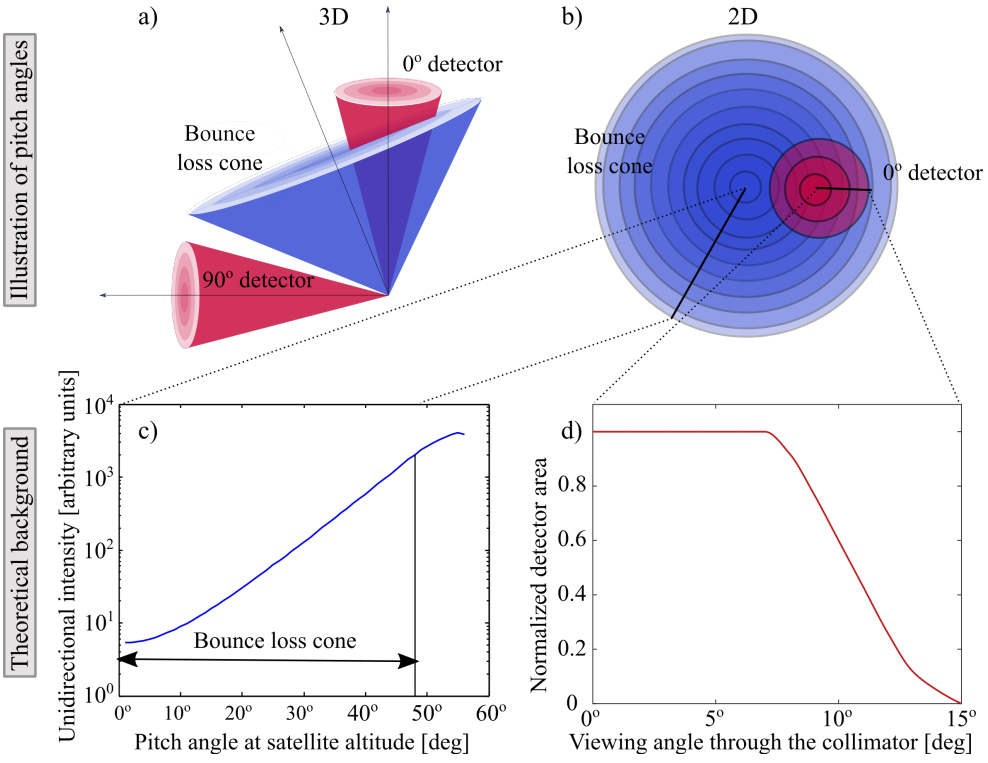

Figure 3.1: (a and b) The MEPED telescope viewing angles in respect to the loss cone exemplified for one case at high latitudes. (c) A theoretical pitch angle distribution profile based on a selected solution of the Fokker-Planck equation for particles. (d) The detector response-function for different viewing angles through the detector collimator. Taken from Nesse Tyssøy et al. [2016].

With the proton fluxes corrected for degradation due to radiation damage and the electron fluxes corrected for proton contamination, the amount of the incident energy from precipitating particle fluxes that are deposited in the atmosphere can be estimated. We use the bounce loss cone estimate described by Nesse Tyssøy et al. [2016] which is unique in comparison to previous studies. The previous studies [e.g Andersson et al., 2014a,b, 2012; Verronen et al., 2011] use electron fluxes from the NOAA POES

MEPED 0° detector telescope to estimate the fluxes of precipitating electrons. Although the 0° detector telescopes' viewing range is entirely inside the loss cone at high latitudes as illustrated in Figure 3.1, they will not view the entire bounce loss cone and hence will provide an underestimate of the precipitating fluxes [Nesse Tyssøy et al., 2016; Rodger et al., 2010]. Whereas Andersson et al. [2014a,b, 2012] and Verronen et al. [2011] use only the measurements from the 0° telescope, we use a combination of measurements from both the 0° and 90° telescopes in conjunction with pitch angle diffusion theory to construct a complete bounce loss cone for each of the new energy channels [Ødegaard et al., 2017] as described by Nesse Tyssøy et al. [2016].

Further, while previous studies [e.g. Andersson et al., 2012] use electron fluxes typically in the energy range 100-300 keV for studying the EEP effects on OH (or/and O_3), we include the P6 channel in estimating an energy spectra. In the condition that the P4 and P5 proton channels exhibit little or no response, the P6 channel plays a complementary role to the three electron channels shown in Table 3.2 in that it measures fluxes of relativistic electrons of energies $>$ 756 keV [Ødegaard et al., 2017; Yando et al., 2011]. The derivation of $>$ 756 keV electrons from the P6 channels is described by the Nesse Tyssøy et al. [2016].

Monotonic piecewise cubic Hermite interpolating polynomials (PCHIP) [Fritsch and Carlson, 1980] are fitted to the integral fluxes, which thereafter are converted into a differential electron spectrum. This in turn is used to calculate the electron energy deposition as a function of altitude. The procedure which is described in Nesse Tyssøy et al. [2016] includes calculating the number of electrons per second that pass through a horizontal surface of size 1 cm^2 at 120 km altitude. We then find the isotropic flux that gives the same number of electrons per second passing through this unit horizontal area, which we refer to as the equivalent isotropic flux level over the bounce loss cone. Each energy interval is treated separately as the level of diffusion will depend on the particle energy. The energy deposition as a function of altitude is then calculated by using results of the Rees [1989] model, taking into account the cosine factor that enters when converting from flux to particles passing through a horizontal unit surface. In these calculations we have used the COSPAR (COmmittte on SPAce research) 1986 Reference Atmosphere.

3.2 Observation/Measurement of the Atmospheric Constituents

In this thesis, we use atmospheric parameters measured by the MLS instrument on board the National Aeronautics and Space Administration (NASA) Aura satellite launched on 15 July, 2004 [Waters et al., 2006]. Aura orbit the Earth in a Sun-synchronous orbit at 705 km altitude with a period of 98.8 minutes, giving a latitude coverage of 82°N-82°S on each orbit. Hence MLS observations at any given latitude

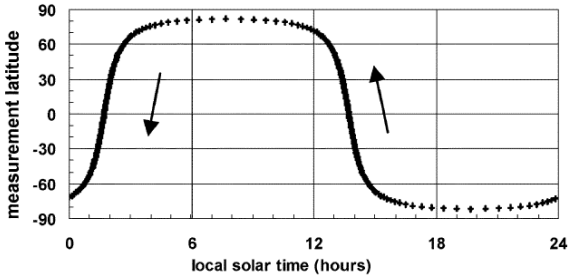

Figure 3.2: Local solar time of MLS measurements versus latitude. Crosses give the locations of profile measurements. The arrows show the direction of motion around the orbit. Taken from Waters et al. [2006].

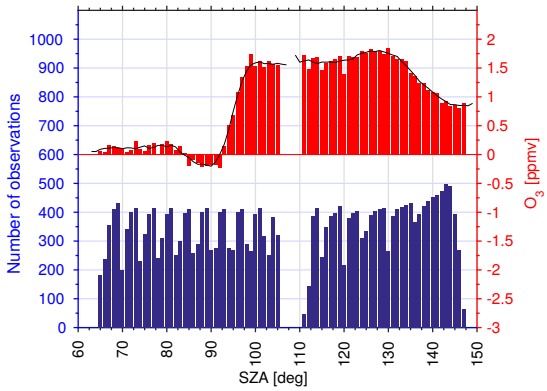

Figure 3.3: (Red): Monthly mean O_3 variation with SZA during December 2006 for the geographical latitude band of 40-80°N. The black line is the running mean of O_3 over a window of 5°. (Blue): The number of observations comprising each mean.

are taken at the same solar local time throughout the mission as shown in Figure 3.2. MLS remotely senses microwave wavelengths emissions from the limb of the Earth, and measures vertical profiles of atmospheric constituents which include: water vapor (H_2O), ozone (O_3), hydroxyl radical (OH), perhydroxyl radical (HO_2) VMR, temperature, geopotential height (GPH), among others. MLS observations give the first global measurements of odd hydrogen family species (OH and HO_2) that dominate O_3 destruction in the mesosphere. This allows for a unique opportunity to investigate the EPP impact on OH VMR and subsequently on O_3 VMR.

The data are sorted according to the instructions in the data quality manual by Livesey et al. [2015]. Since OH production from energetic particles must overcome the ambient background production from photolysis of H_2O to be visible, the studies in this thesis use nighttime observations to investigate EPP-OH changes. For nighttime conditions SZAs $>100°$ are used. However, O_3 catalytic reduction requires sunlit

conditions to take place. Therefore, for studies that include O_3, twilight-nighttime conditions are considered for which the SZAs are $>95^\circ$. The monthly mean variation of OH and O_3 with SZA for December 2006 is shown in Figure 2.16 (in subsection 2.3.4) and Figure 3.3 respectively, illustrating a typical variation of OH and O_3 with SZA during wintertime. Low OH mixing ratios are seen for SZA$>90^\circ$ and high O_3 mixing at SZA$>95^\circ$. Also shown is the number of observations included in each mean value.

3.3 The Sources of Other Parameters

3.3.1 The Solar Lyman-alpha Radiation

The Solar Extreme Ultra Violet Experiment (SEE) and the Solar Stellar Irradiance Comparison Experiment (SOLSTICE) instruments on board NASA's Thermosphere Ionosphere Mesosphere Energetics and Dynamics (TIMED) and the Solar Radiation and Climate Experiment (SORCE) spacecraft, respectively, give solar irradiance measurements within the years 2005 to 2009. These irradiance measurements are used to make composite solar Lyman-α time series that can be retrieved from the Laboratory for Atmospheric and Space Physics (LASP) Interactive Solar IRradiance Datacenter (LISIRD).

The amount of solar radiation at a specific location in latitude and altitude varies with the SZA. As such, including the SZA dependency in the the Ly-α radiation using an exponential function of the secant of the SZA yields a function of the form [see Andersson et al., 2012; Minschwaner et al., 2011]:

$$I_{\alpha}^{SZA} = I\alpha exp[-\beta sec(SZA_{min})] \tag{3.1}$$

where SZA_{min} is the minimum SZA at which the intensity of solar UV radiation is maximum at a particular altitude, location and day. β is related to the optical depth of the atmosphere at wavelengths relevant for photolysis [see Minschwaner et al., 2011]. I_α is the composite solar Ly-α radiation. In the analysis we assume β=1 since we are interested in the change of solar radiation, but not the optical properties that vary with altitude.

3.3.2 The Solar Wind Parameters and Magnetic Indices

Solar wind parameters like IMF B_Z, flow pressure and flow speed are measured by either the WIND or ACE satellites and are obtained from archives like the Coordinated Data Analysis Web (CDAweb). Magnetic activity indices are measured by ground based magnetometers, the data of which is archived and can be retrieved from the OMNI database. In this thesis, we use the Dst index, the AE index [Sugiura et al.,

1991] and the Kp index [Bartels et al., 1939] to show the level of geomagnetic disturbances. The definitions of the above mentioned indices are given in Appendix. For a review on the definitions and method of deriving the geomagnetic indices (Kp, AE and Dst) [see Rostoker, 1972]

Chapter 4

Summary and Discussion of papers

In this chapter, the summary and discussion of papers I, II and III are given. Where necessary, new analysis not included in the papers is also presented.

4.1 Longitudinal Distribution of OH

The main objectives of paper I are: to investigate the role of EEP during solar minimum, and further separate the longitudinal OH variability due to EEP and that due to atmospheric dynamics. In this paper we use solar wind parameters (flow speed, pressure and IMF B_Z) and magnetic indices (kp, Dst and AE) obtained from the OMNI database to identify two sequences of recurrent geomagnetic activity signatures in year 2008. We use nighttime (SZA$>100^\circ$) Aura/MLS observations of OH VMR, temperature, GPH and H_2O VMR, to allow for detection of EEP-related OH VMR changes. We use particle fluxes from MEPED instrument on board NOAA-18 which traverses the same local time sector as the Aura satellite, making it possible to study the local effects of EEP energy deposition on OH.

In paper I, we choose year 2008 which is deep into the solar minima, but nevertheless characterized by sequences of HSSWS which caused recurrent geomagnetic activity and subsequently recurrent EEP. By sorting the data into disturbed- and quiet-time periods based on the annual mean Dst index for the different seasons, we present results for winter in the NH and autumn in the SH as shown in Figure 4.1. Those two seasons coincided with low OH background, as well as relatively high geomagnetic activity in the respective hemispheres. On this seasonal scale EEP enhancements are seen over northern Russia and west Antarctica during disturbed conditions, which can be explained by EEP. During quiet-time, however, OH enhancements are seen over North America and still over the same region in West Antarctica, coinciding with regions with low H_2O mixing ratios and high temperatures. By fitting sinusoidal curves to the longitudinal temperature anomalies at geographic latitudes 60-70°N during winter for disturbed and quiet conditions at 75 km, planetary waves with wave numbers 1

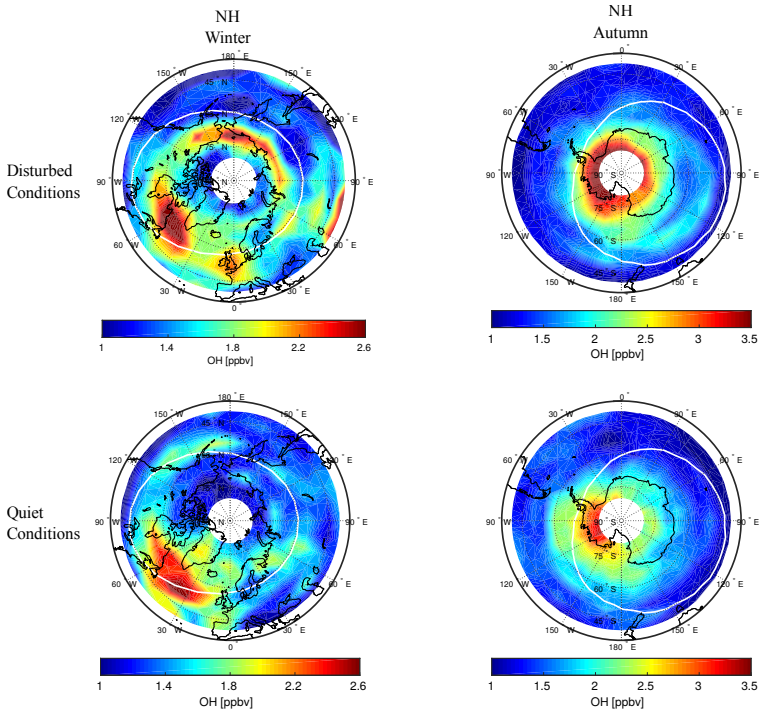

Figure 4.1: A plot taken from paper I showing mean nighttime OH during disturbed and quiet conditions in 2008 at altitudes 75–78 km for (left column) winter (January–February) at LST 2≤LST<4 in the NH and for (right column) autumn (March–May) at LST 22 $\leq$ LST $<$ 2 in the SH. Mean values were calculated for each 5° latitude by 10° longitude bin between 40° to 80°N and longitudes 180°W to 180°E. The white line shows the approximate location of 55°N/S corrected geomagnetic (CGM) latitude.

and 2 are found whose superposition seem to drive the longitudinal temperature distribution. Therefore, planetary wave activity and the associated downwelling lead to the observed OH enhancements during quiet times. The detailed mechanism of which are discussed in paper I, but are also briefly described in subsection 2.3.1.

The OH enhancement over west Antarctica, seen also during quiet time periods could possibly be also a result of a steady drizzle of radiation belt electrons due to the weak magnetic field strength in that region. The quiet time OH enhancement over North America, however, is unrelated to asymmetries in the Earth's magnetic field as it is located in a region with a high magnetic field ratio ($\frac{B_N}{B_S}$) for particle bouncing over a field line.

In paper I, the EEP-OH enhancements are of the same order of magnitude as the enhancements due to the background atmospheric conditions (see figure 4.1). This implies that we can not ignore the dynamically varying background atmosphere when assessing the EEP on the atmospheric chemistry. Therefore to separate, quantify and

understand the EEP effect on OH, we need to cater for the varying atmospheric background. This requires a method that can simultaneously account for the EEP-OH production as well as that from the background production for example through photolysis of H_2O as well as the dynamics. With this reasoning in mind, it gives the motivation for paper II.

4.2 Multiple Linear Regression: Separating the Contribution from the Different Sources

The main objectives of paper II are: to model the natural background variability of OH in order to estimate the impact of EEP on OH in a geographic and CGM coordinate system. Thus forth investigate the relative importance of SPEs and EEP during the declining phase of solar cycle 23. To study EPP effects on OH, we use MEPED NOAA POES 16 and 18 observations for years 2005 and 2009 respectively, with which we estimate precipitating particle fluxes that we use to quantify the energy deposition from energetic protons and electrons [see Nesse Tyssøy et al., 2016; Nesse Tyssøy and Stadsnes, 2015]. We use Aura MLS observations of the atmospheric constituents: temperature, GPH, H_2O and OH VMR. We also use time series of composite solar Ly-α radiation obtained from LISIRD.

The data are sorted by the geographic and CGM latitude bands of 45°-80°N and 55°-70°N respectively. Then the daily means of both the atmospheric constituents and particle energy deposition are calculated. We use triangulation based interpolation to obtain data at altitudes for which Aura MLS does retrieve observations of temperature, GPH and H_2O. The adjusted R^2 gives a measure of the amount of variation in the response variable (OH) explained by the regression models. The adjusted R^2 is used throughout the paper to show how good a model fits the observations.

We use multiple linear regression to model the background atmospheric contribution to the temporal variability of OH during the year 2005 to 2009 in the NH in both a geographic and a magnetic coordinate system. By adding the different particle energy depositions separately to the background models, models with the energy deposition are obtained.

To find out if a linear relationship exists between the response variable, OH VMR and the predictors, Pearson's correlation coefficients were calculated, which give evidence of linearity between OH VMR and the atmospheric constituents. The response variable was logarithm transformed to allow for normality of the regression residuals (error). To control for correlated predictors, first stepwise regression is used to select the predictor terms that are more relevant. Then robust weighted least squares regression is used to create models that are least affected by outliers and the effects of unequal

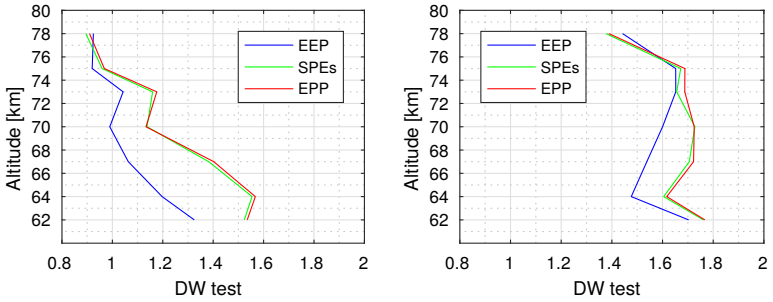

Figure 4.2: The Durbin-Watson (DW) statistic test for autocorrelation in the regression residuals for the models for which electrons (EEP), protons (SPEs) and total energy (EPP) deposition are added for the geographic (40-80°N) and corrected geomagnetic (55-70°N) latitude bands. The DW test is 2 for no autocorrelation, 0 to <2 for positive autocorrelation and >2 to 4 for negative autocorrelation. Values in the range 1.5 to 2.5 are considered relatively normal.

error variances. To cater for multicollinearity among the predictor variables, Belsley et al. [2005] collinearity diagnostics is used to identify and remove any terms whose regression coefficients are deemed to be degraded by any near dependences among predictors. Second order (quadratic) regression is opted for to cater for non-linear effects in the predictors. Centered predictor variables are used to reduce structural collinearity that may arise from inclusion of higher order terms in the regression models. In the following paragraphs, we discuss the findings and any limitations with using multiple linear regression in paper II.

Using multiple linear regression, background OH models for the geographic (40-80°N) and corrected geomagnetic (55-70°N) latitude bands are obtained at altitudes 62-78 km for years 2005 to 2009. The different particle energy depositions are added separately to the background OH model resulting in three models: background plus electron energy deposition (EEP), background plus proton energy deposition and background plus the total energy deposition (EPP). Figure 4.2 shows the Durbin-Watson (DW) statistics test for autocorrelation in the regression residuals of the EEP, SPEs and EPP models covering years 2005 to 2009 in the geographic and corrected geomagnetic (CGM) latitude bands. For models in the geographic coordinate setting, there is evidence of positive autocorrelation as is expected of time series data. For the CGM models, most of the DW test values are >1.5 except at 64 and 78 km, implying relatively normal values. Autocorrelation can, however, be catered for by autoregressive models but the lifetime of OH is less than a day in the mesosphere [see Pickett et al., 2006] and we are using data with a resolution of 1 day, therefore, it would be unrealistic to introduce lagged variables in the regression analysis. As such to better understand the causal relationship between OH and EEP, an autoregressive model is not appropriate,

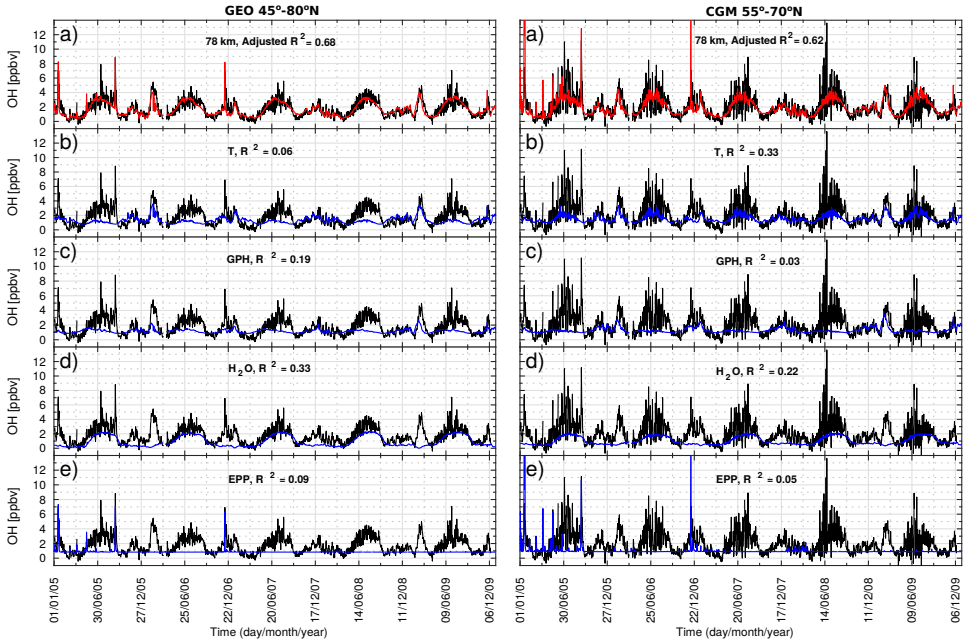

Figure 4.3: A plot taken from paper II showing the observed hydroxyl (OH) (black line) against modeled OH contribution from each of the predictors in the regression model at 78 km. The blue lines represent modeled background OH variability due to at most one predictor in the regression model. The red lines represent modeled OH which includes the background and the contribution of energetic particles (electrons and protons). The data are averaged within the geographical (GEO) latitude range of 45–80°N (left) and within a corrected geomagnetic (CGM) latitude range of 55–70°N (right).

but it could be more applicable for a predictive model.

The multiple linear regression in paper II is a mean to calculating the relative contribution from the different sources of OH variability. Figure 4.3 shows the background OH (black), modeled OH (red) and the contribution to the modeled OH from the different probable predictors at 78 km. This kind of breakdown is done for all the models in both the geographic and geomagnetic coordinate system. The results generally show the background parameters as the main contributor to temporal OH variability at altitudes above 70 km. While below 70 km, EPP dominates. Electrons contribute up to 15% at 67 km in the geographic coordinate system. In a CGM coordinate system, the electrons contribute up to 11% occurring at 75 km and at 67 km, corresponding to where 50-200 keV and >200 keV electrons respectively deposit most of their energy [see e.g. Andersson et al., 2012; Turunen et al., 2009]. Generally above 70 km the contribution from electrons is comparable to that from protons. Below 70 km, however, the proton impact is more prominent compared to the electron impact, responsible for up to 43% and 32% contribution in the geographic and CGM coordinate systems respectively. The trend of the total EPP effect is similar to that of protons in both coordinate

systems, with little difference in values.

Transforming from the geographic to the CGM coordinate system is expected to improve the impact of the electron precipitation in the regression models. This kind of behavior is only seen at 75 km where the electron contribution improves from 8% to 11% by changing from a geographic to the CGM coordinate system. The lack of improvement in the contribution from electrons at most altitudes is likely due to high short-term variability introduced in the OH data when averaged over the CGM latitude bands. These short-term variations are not captured by the regression models, hence they tend to mask the electrons contribution. Since this analysis covers the declining and minimum phase of solar cycle 23, Paper II results may be a lower estimate of the relative contribution of electrons to OH variability at long time scales.

A long time series is required to assess the contribution of EEP and SPEs to the general temporal variability of OH. During the declining and minimum phase of solar cycle 23, there were few SPEs and the EEP events there in are relatively weak. Therefore, the EEP role in general is damped (masked) by the background atmospheric variability, which is less affected by the solar cycle phases. On shorter time scales, by focusing on the more (geomagnetically) active years 2005-2006, the role of EEP in the geographic and geomagnetic latitude bands increases to $\sim$22% and $\sim$20%, respectively.

Nevertheless, it is evident that the background atmosphere governs much of the OH variability. This implies that studies concerned with the EEP-OH impact on O_3 should also carefully evaluate the background parameters, to assess whether an apparent O_3 change is truly associated with EEP-OH.

4.3 The Impact of EEP on the Tertiary Ozone Layer

The main objectives of paper III are: to investigate when and where maximum overlap between the auroral zone and the tertiary O_3 layer exists, and to identify the potential limitations of using O_3 mixing ratio observations from the Aura MLS instrument. Further, to examine the effects of two EEP events on O_3 in comparison with the effects of two SPEs within the same wintertime conditions. Hence forth check the linearity between O_3 and the parameters: AE, OH, electron energy deposition, proton energy deposition, H_2O and temperature at 73 km during January 2005 and December 2006.

In this paper, we use electron and proton energy deposition profiles obtained from particle fluxes from the NOAA-16 and -18 MEPED 0° and 90° telescopes and atmospheric observations (OH, O_3, H_2O VMR, temperature) from the Aura MLS satellite at geographic latitudes 40-80°N. We investigate when and where maximum overlap between the tertiary O_3 layer and the auroral zone (or footprint of the Earth's radiation belts) exists. We further investigate the limitations of using Aura MLS observations in studying the direct EEP- OH effects on O_3. For the first time, the EEP-OH-O_3 is

investigated by comparing two sets of SPEs and EEP events during the same winter months.

The results show that maximum overlap between the auroral zone and the tertiary O_3 layer exists during the winter months December to January for years 2005 and 2006. EEP induced OH will only effectively destroy O_3 in the presence of atomic oxygen, hence in the presence of sunlight. For SZA at twilight (95-105°) at geographic latitudes 40-80°N there are, however, generally few Aura MLS O_3 measurements (5-12% of the total observations) within the auroral zone during January and December. Figure 4.4 shows the geographic coverage of O_3 at 73 km at 5 different SZA bands in the NH, illustrating very little intersection of O_3 observations with the auroral zone at twilight (SZA 95-105°). Hence, for most SZA>95°, Aura MLS barely observes the direct EEP-OH impact on O_3, but predominately observes the lagged effect.

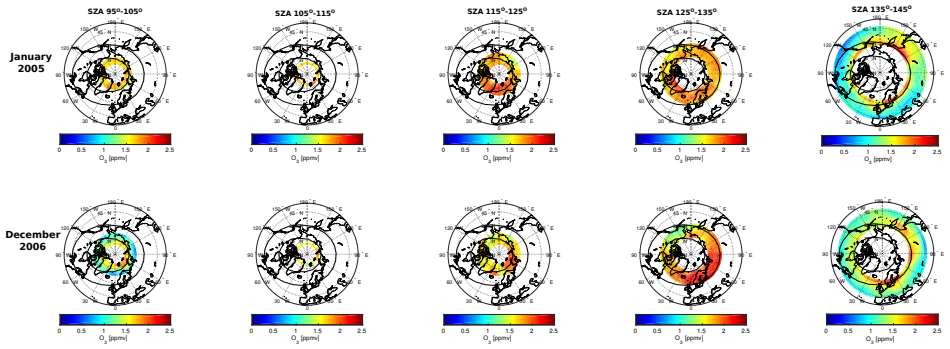

Figure 4.4: A plot taken from paper III, illustrating the geographic coverage of the mean nighttime O_3 at 73 km at different SZA bands. Mean values were calculated for each 5° latitude by 10° longitude bin between latitudes 40°-80°N and longitudes 180°W-180°E. The black oval lines show the approximate location of 55°N and 70°N CGM latitude.

Case studies of EEP and SPEs within the same wintertime conditions show that the impact region of EEP on the tertiary O_3 is much smaller than the region of overlap between the auroral zone and the tertiary O_3 layer, and also compared with the impact region of SPEs. Figure 4.5 show the mean nighttime energy deposition, OH, O_3, H_2O VMR at 73 km at geographic latitudes 40-80°N during quiet-time and particle precipitation events in December 2006. The SPE generally shows precipitation over the polar cap region with corresponding OH enhancements and O_3 depletions. The EEP-OH enhancements tend to be more intense in regions with high H_2O mixing ratios, corresponding here to longitudes 120°E-60°W. Although there is precipitation at longitudes 0-90°E, it shows no effect on OH and O_3, illustrating the impact of planetary wave in the H_2O distribution.

Further, the daily mean O_3 and the electron energy deposition at 73 km altitude ex-

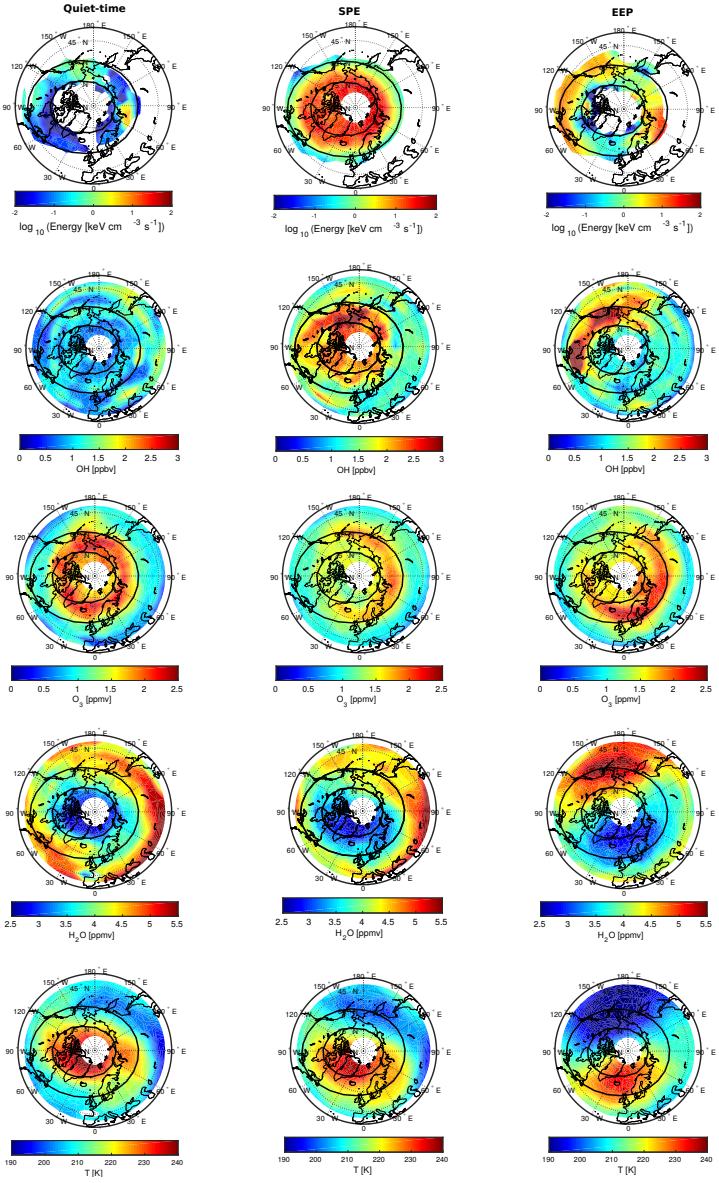

Figure 4.5: A plot taken from paper III showing the mean nighttime distribution of energy deposition, OH, O_3 and H_2O for SZA $> 95°$ at 73 km within the geographical latitude band of 40°-80°N during the months of December 2006 for quiet time (1-5 December), SPEs (6-16 December) and EEP (17-25 December) events. Mean values were calculated for each 5° latitude by 10° longitude bin between latitudes 40°-80°N and longitudes 180°W-180°E. The black oval lines show the approximate location of 55°N and 70°N CGM latitude.

hibit insignificant correlation at all the different SZAs considered (95-105°, 105-115°, 115-125°, 125-135° and 135-145°). The solar proton, however, exhibit significant correlation over a range of SZAs (95-135°) which comprises of the direct and lagged response of O_3 to SPEs. O_3 has a long recovery time (0.1-1 day) at the altitude location of the tertiary O3 layer under polar night conditions and might be subject to transport [Smith et al., 2009]. Hence a superposed epoch analysis is applied to investigate potential effects of EEP on OH and O_3 mixing ratios within the geomagnetic latitude band.

Based on the mean energy deposition, twelve EEP events are selected whose energy deposition is greater than the mean energy deposition at 73 km altitude during the winters of years 2005 to 2009 for SZAs $> 95°$ for the CGM latitude band of 55-70°N (see Table 1 in paper III). The SPEs periods with >1000 particle flux units are removed from the analysis, based on the list of SPEs (https://umbra.nascom.nasa.gov/SEP/). On performing a superposed-epoch analysis of these EEP events, the results in Figure 4.6 show a response in both OH and O_3 mixing ratios to electron precipitation after lag zero that was not revealed in simple correlation analysis. As mentioned above, the correlation between EEP/OH VMR and O_3 VMR is biased by the satellites' viewing geometry and solar local times, as catalytic reduction of O_3 is largely governed by the SZA (or sunlit conditions). However, compositing the wintertime EEP events show an appreciable reduction in O_3 VMR (up to approximately 0.35 ppmv) at 67-75 km altitudes in response to EEP-OH enhancements.

This analysis differs from that by Andersson et al. [2014a] in such a way that we are considering only EEP events during wintertime (total of 12 events) when the tertiary O_3 layer is present in the NH, while they show a superposed epoch analysis of EEP events for all seasons, strongly biased towards summer. During summer, however the tertiary O_3 layer does not exist and the O_3 mixing ratios are less than 1 ppmv. This implies that O_3 anomalies calculated for summer may potentially give large percentage changes in O_3 VMR for small changes in the absolute values of the O_3 VMR. Further, we assess both OH and O_3 together to ensure/verify that the changes observed in O_3 mixing ratios are due to OH enhancement produced by EEP but not a change related to, for example dynamics.

In summary, the limitation posed by the Aura MLS SZA/geographic coverage, the region of overlap between the auroral zone and the tertiary O_3 layer together with the background atmospheric dynamics that modulate the distribution of H_2O result in a much smaller EEP-OH impact region on the tertiary O_3 layer compared with the geographic impact of SPEs. The background dynamics could also redistribute the O_3 mixing ratio anomalies caused by the EEP-OH impact. The superposed epoch analysis indicates that there is an observable effect of EEP-OH on the O_3 mixing ratios, but to quantify the effect based on observations requires better measurement coverage as well

an overview of the background atmosphere in respect to composition and dynamics.

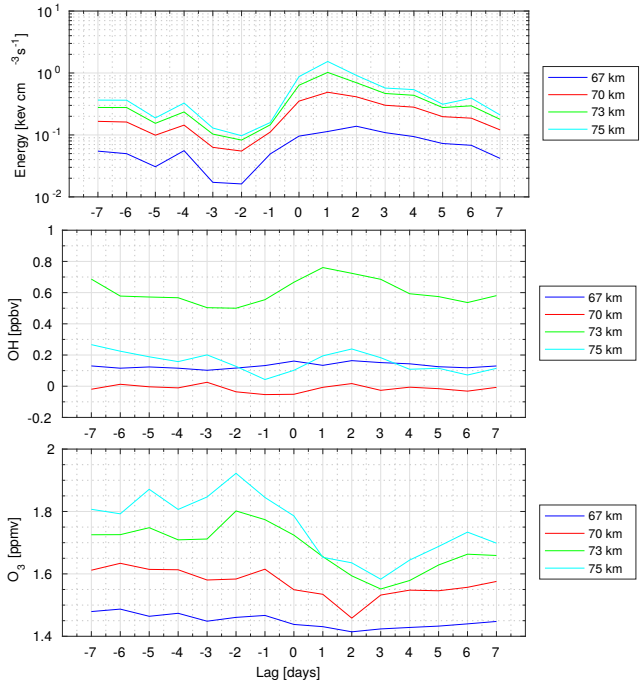

Figure 4.6: Superposed epoch analysis of the electron energy deposition, OH VMR and O_3 VMR for EEP events during the winters of years 2005 to 2009 at altitudes close to the tertiary O_3 layer (67-75 km) in the CGM latitude band of 55-70°N.

4.4 Future Prospects

Future studies should focus on investigating the contribution of electrons to OH variability over a full solar cycle or even longer than that to get a more general picture. Further, although we do not expect the general tendencies to differ, this analysis should be conducted on the SH as the offset between the magnetic and geographic pole are different. Multiple linear regression as a method might be an important research tool for tackling other scientific questions.

The SABER instrument on board the TIMED satellite gives O_3 observations with a nominal vertical resolution of 2 km. Compared to MLS which has a coarser and variable vertical resolution at mesospheric altitudes, the SABER vertical resolution is consistent and smaller. The Aura MLS O_3 observations are not suitable for scientific use for altitudes above approximately 75 km, whereas the SABER instrument provides O_3 from approximately 20 km to about 95 km during daytime to about 100-105 at night. Further the SABER measurements span over a longer period of time (from 2002) than

the Aura MLS observations (from August 2004). Therefore, with the SABER vertical resolution, altitude coverage and time span, it would be a more suitable data set for studying O_3 variability. However, SABER does not provide OH observations. In future studies, it would be more appropriate to use multiple satellite O_3 observations, together with relevant background parameters, to better understand the O_3 variability.

The outstanding questions should then be: How much of the incident energy deposition eventually affects the tertiary O_3 layer? Further, with help from models; What role does the tertiary ozone layer play in driving the mesospheric dynamics?

Abbreviations

AIMOS	Atmospheric Ionization Module Osnabrück
AU	Astronomical Unit
BLC	bounce loss cone
Bz	Northward component of the IMF
CDAweb	Coordinated Data Analysis Web
CGM	corrected geomagnetic
CIR	Corotating Interaction Region
CH	Coronal Hole
CME	Coronal Mass Ejection
COSPAR	Committee on Space Research
DEMETER	Detection of Electromagnetic Emissions Transmitted from Earthquake Regions
Dst	Storm-time Disturbance Index
DW	Durbin-Watson
ECR	electron count rate
EIT	Extreme Ultraviolet Imaging Telescope
EMIC	Electromagnetic Ion Cyclotron
EEP	Energetic Electron Precipitation
EOS	Earth Observing System
EPP	Energetic Particle Precipitation
GOES	Geostationary Operational Environmental Satellites
GOMOS	Global Ozone Monitoring by Occultation of Stars
H	atomic Hydrogen
H_2	molecular Hydrogen
HO_2	Hydroperoxy radical
HO_X	Odd Hydrogen
H_2O	Water vapor
HSSWS	High Speed Solar Wind Streams
IGRF	International Geomagnetic Reference Field
IDP	instrument for the detection of particles
IMF	Interplanetary Magnetic Field

L^*	invariant drift shell
L^*	drift shell equatorial radius
LST	Local Solar Time
LT	Local Time
MEPED	Medium Energy Proton and Electron Detector
MLS	Microwave Limb Sounder
MLT	Magnetic Local Time
NASA	National Aeronautics and Space Administration
N_2	molecular Nitrogen
NH	Northern Hemisphere
NO_X	odd Nitrogen
NOAA	National Oceanic and Atmospheric Administration
O_2	molecular Oxygen
O_3	Ozone
O_X	odd Oxygen
OH	Hydroxyl radical
POES	Polar Orbiting Environment Satellite
ppbv	parts per billion volume
ppmv	parts per million volume
SABER	Sounding of the Atmosphere using Broadband Emission Radiometry
SEM	Space Environment Monitor
SH	Southern Hemisphere
SIC	Sodankylä Ion and Neutral Chemistry
SPE	Solar Proton Event
SSC	Storm Sudden Commencement
SZA	solar zenith angle
T	Temperature
THz	Terra Hertz
ULF	Ultra Low Frequency
UV	Ultra Violet
VLF	Very Low Frequency
VMR	volume mixing ratio

Bibliography

Aikin, A. C. and Smith, H. J. P. (1999). Mesospheric constituent variations during electron precipitation events. *Journal of Geophysical Research: Atmospheres*, 104(D21):26457–26471.

Andersson, M. E., Verronen, P. T., Marsh, D. R., Seppälä, A., Päivärinta, S.-M., Rodger, C. J., Clilverd, M. A., Kalakoski, N., and van de Kamp, M. (2018). Polar ozone response to energetic particle precipitation over decadal time scales: The role of medium-energy electrons. *Journal of Geophysical Research: Atmospheres*, 123(1):607–622.

Andersson, M. E., Verronen, P. T., Rodger, C. J., Clilverd, M. A., and Seppälä, A. (2014a). Missing driver in the Sun-Earth connection from energetic electron precipitation impacts mesospheric ozone. *Nature Communications*, 5(5197).

Andersson, M. E., Verronen, P. T., Rodger, C. J., Clilverd, M. A., and Wang, S. (2014b). Longitudinal hotspots in the mesospheric OH variations due to energetic electron precipitation. *Atmospheric Chemistry and Physics*, 14(2):1095–1105.

Andersson, M. E., Verronen, P. T., Wang, S., Rodger, C. J., Clilverd, M. A., and Carson, B. R. (2012). Precipitating radiation belt electrons and enhancements of mesospheric hydroxyl during 2004-2009. *Journal of Geophysical Research: Atmospheres*, 117(D9).

Bartels, J., Heck, N. H., and Johnston, H. F. (1939). The three-hour-range index measuring geomagnetic activity. *Terrestrial Magnetism and Atmospheric Electricity*, 44(4):411–454.

Baumjohann, W. and Treumann, R. (1996). *Basic Space Plasma Physics*. Imperial College Press.

Belsley, D. A., Kuh, E., and Welsch, R. E. (2005). *Detecting and Assessing Collinearity*, pages 85–191. John Wiley & Sons, Inc.

Billings, D. E. and Roberts, W. (1964). The origin of m-region geomagnetic storms. *Astrophisica Norvegica*.

Brasseur, G. P. and Solomon, S. (2005). *Aeronomy of the Middle Atmosphere: Chemistry and Physics of the Stratosphere and Mesosphere*. Springer.

Burlaga, L. and Lepping, R. (1977). The causes of recurrent geomagnetic storms. *Planet Space Science*, 25.

Chapman, S. (1930). Xxxv. on ozone and atomic oxygen in the upper atmosphere. *Philosophical Magazine Series 7*, 10(64):369–383.

Crutzen, P. J. and Solomon, S. (1980). Response of mesospheric ozone to particle precipitation. *Planetary and Space Science*, 28(12):1147 – 1153.

Daae, M., Espy, P., Nesse Tyssøy, H., Newnham, D., Stadsnes, J., and Søraas, F. (2012). The effect of energetic electron precipitation on middle mesospheric nighttime ozone during and after a moderate geomagnetic storm. *Geophysical Research Letters*, 39(21). L21811.

Damiani, A., Funke, B., López Puertas, M., Gardini, A., von Clarmann, T., Santee, M. L., Froidevaux, L., and Cordero, R. R. (2014). Changes in the composition of the northern polar upper stratosphere in february 2009 after a sudden stratospheric warming. *Journal of Geophysical Research: Atmospheres*, 119(19):11,429–11,444.

Damiani, A., Storini, M., Laurenza, M., and Rafanelli, C. (2008). Solar particle effects on minor components of the polar atmosphere. *Annales Geophysicae*, 26(2):361–370.

Damiani, A., Storini, M., Rafanelli, C., and Diego, P. (2010a). The hydroxyl radical as an indicator of {SEP} fluxes in the high-latitude terrestrial atmosphere. *Advances in Space Research*, 46(9):1225 – 1235.

Damiani, A., Storini, M., Santee, M. L., and Wang, S. (2010b). Variability of the nighttime OH layer and mesospheric ozone at high latitudes during northern winter: influence of meteorology. *Atmospheric Chemistry and Physics*, 10(21):10291–10303.

Dungey, J. W. (1961). Interplanetary magnetic field and the auroral zones. *Physical. Review. Letters.*, 6:47–48.

Evans, D. and Greer, M. (2000). *Polar Orbiting Environmental Satellite Space Environment Monitor - 2: Instrument Descriptions and Archive Data Documentation*. Space Environment Center, Boulder, Colorado, 1.4 edition.

Feofilov, A. G. and Kutepov, A. A. (2012). Infrared radiation in the mesosphere and lower thermosphere: Energetic effects and remote sensing. *Surveys in Geophysics*, 33(6):1231–1280.

Foster, J. C., Erickson, P. J., Baker, D. N., Claudepierre, S. G., Kletzing, C. A., Kurth, W., Reeves, G. D., Thaller, S. A., Spence, H. E., Shprits, Y. Y., and Wygant, J. R. (2014). Prompt energization of relativistic and highly relativistic electrons during a substorm interval: Van allen probes observations. *Geophysical Research Letters*, 41(1):20–25.

Friedel, R., Reeves, G., and Obara, T. (2002). Relativistic electron dynamics in the inner magnetosphere — a review. *Journal of Atmospheric and Solar-Terrestrial Physics*, 64(2):265 – 282.

Fritsch, F. N. and Carlson, R. E. (1980). Monotone piecewise cubic interpolation. *SIAM Journal on Numerical Analysis*, 17(2):238–246.

Gonzalez, W. D., Joselyn, J. A., Kamide, Y., Kroehl, H. W., Rostoker, G., Tsurutani, B. T., and Vasyliunas, V. M. (1994). What is a geomagnetic storm? *Journal of Geophysical Research: Space Physics*, 99(A4):5771–5792.

Gopalswamy, N. (2008). Solar connections of geoeffective magnetic structures. *Journal of Atmospheric and Solar-Terrestrial Physics*, 70(17):2078 – 2100.

Jackman, C. H., Marsh, D. R., Vitt, F. M., Roble, R. G., Randall, C. E., Bernath, P. F., Funke, B., López-Puertas, M., Versick, S., Stiller, G. P., Tylka, A. J., and Fleming, E. L. (2011). Northern hemisphere atmospheric influence of the solar proton events and ground level enhancement in january 2005. *Atmospheric Chemistry and Physics*, 11(13):6153–6166.

Jackman, C. H., Randall, C. E., Harvey, V. L., Wang, S., Fleming, E. L., López-Puertas, M., Funke, B., and Bernath, P. F. (2014). Middle atmospheric changes caused by the january and march 2012 solar proton events. *Atmospheric Chemistry and Physics*, 14(2):1025–1038.

Kelley, M. (2009). *The Earth's Ionosphere: Plasma Physics and Electrodynamics*. International Geophysics. Elsevier Science.

Li, W., Ni, B., Thorne, R. M., Bortnik, J., Green, J. C., Kletzing, C. A., Kurth, W. S., and Hospodarsky, G. B. (2013). Constructing the global distribution of chorus wave intensity using measurements of electrons by the POES satellites and waves by the van allen probes. *Geophysical Research Letters*, 40(17):4526–4532.

Li, W., Ni, B., Thorne, R. M., Bortnik, J., Nishimura, Y., Green, J. C., Kletzing, C. A., Kurth, W. S., Hospodarsky, G. B., Spence, H. E., Reeves, G. D., Blake, J. B., Fennell, J. F., Claudepierre, S. G., and Gu, X. (2014). Quantifying hiss-driven energetic electron precipitation: A detailed conjunction event analysis. *Geophysical Research Letters*, 41(4):1085–1092.

Li, X. and Temerin, M. A. (2001). The electron radiation belt. *Space Science Reviews*, 95:569–580.

Livesey, N. J., Read, W. G., Wagner, P. A., Froidevaux, L., Lambert, A., Manney, G. L., Valle, L. F. M., Pumphrey, H. C., Santee, M. L., Schwartz, M. J., Wang, S., Fuller, R. A., Jarnot, R. F., Knosp, B. W., and Martinez, E. (2015). *Earth Observing system(EOS) Aura Microwave Limb Sounder(MLS) Version 4.2x Level 2 data quality and description document.* Jet Propulsion Laboratory, California Institute of Technology, Pasadena, California, 91109-8099, version 4.2x-1.0 edition.

Lockwood, M., Owens, M. J., and Barnard, L. (2014). Centennial variations in sunspot number, open solar flux, and streamer belt width: 1. correction of the sunspot number record since 1874. *Journal of Geophysical Research: Space Physics*, 119(7):5172–5182.

Loewe, C. A. and Prölss, G. W. (1997). Classification and mean behavior of magnetic storms. *Journal of Geophysical Research: Space Physics*, 102(A7):14209–14213.

Manney, G. L., Schwartz, M. J., Krüger, K., Santee, M. L., Pawson, S., Lee, J. N., Daffer, W. H., Fuller, R. A., and Livesey, N. J. (2009). Aura Microwave Limb Sounder observations of dynamics and transport during the record-breaking 2009 arctic stratospheric major warming. *Geophysical Research Letters*, 36(12).

Marsh, D., Smith, A., Brasseur, G., Kaufmann, M., and Grossmann, K. (2001). The existence of a tertiary ozone maximum in the high-latitude middle mesosphere. *Geophysical Research Letters*, 28(24):4531–4534.

McComas, D. J., Elliott, H. A., Gosling, J. T., Reisenfeld, D. B., Skoug, R. M., Goldstein, B. E., Neugebauer, M., and Balogh, A. (2002). Ulysses' second fast-latitude scan: Complexity near solar maximum and the reformation of polar coronal holes. *Geophysical Research Letters*, 29(9):1290.

McComas, D. J., Elliott, H. A., Schwadron, N. A., Gosling, J. T., Skoug, R. M., and Goldstein, B. E. (2003). The three-dimensional solar wind around solar maximum. *Geophysical Research Letters*, 30(10).

McComas, D. L., Ebert, R. W., Elliot, H. A., Goldstein, B. E., Gosling, J. T., Schwadron, N. A., and Skoug, R. M. (2008). Weaker solar wind from the polar coronal holes and the whole sun. *Geophysical Research Letters*, 35(L18103).

Minschwaner, K., Manney, G. L., Wang, S. H., and Harwood, R. S. (2011). Hydroxyl in the stratosphere and mesosphere - part 1: Diurnal variability. *Atmospheric Chemistry and Physics*, 11(3):955–962.

Moldwin, M. (2008). *Part II of Experimental Nuclear Physics*, volume 1, chapter The heliosphere. Cambridge University Press, New York.

Nesse Tyssøy, H., Sandanger, M. I., Ødegaard, L.-K. G., Stadsnes, J., Aasnes, A., and Zawedde, A. E. (2016). Energetic electron precipitation into the middle atmosphere-constructing the loss cone fluxes from MEPED POES. *Journal of Geophysical Research: Space Physics*, 121(6):5693–5707.

Nesse Tyssøy, H. and Stadsnes, J. (2015). Cutoff latitude variation during solar proton events: Causes and consequences. *Journal of Geophysical Research: Space Physics*, 120(1):553–563.

Neupert, W. M. and Pizzo, V. (1974). Solar coronal holes as sources of recurrent geomagnetic disturbances. *Journal of Geophysical Research*, 79(25):3701–3709.

Ødegaard, L.-K. G., Tyssøy, H. N., Sandanger, M. I. J., Stadsnes, J., and Søraas, F. (2016). Space weather impact on the degradation of NOAA POES MEPED proton detectors. *J. Space Weather Space Clim.*, 6:A26.

Ødegaard, L.-K. G., Tyssøy, H. N., Søraas, F., Stadsnes, J., and Sandanger, M. I. (2017). Energetic electron precipitation in weak to moderate corotating interaction region-driven storms. *Journal of Geophysical Research: Space Physics*, 122(3):2900–2921.

Pickett, H. M., Read, W. G., Lee, K. K., and Yung, Y. L. (2006). Observation of night OH in the mesosphere. *Geophysical Research Letters*, 33(19).

Rees, M. H. (1989). *Physics and Chemistry of the Upper Atmosphere (Cambridge Atmospheric and Space Science Series)*. Cambridge University Press.

Reeves, G. D., McAdams, K. L., Friedel, R. H. W., and O'Brien, T. P. (2003). Acceleration and loss of relativistic electrons during geomagnetic storms. *Geophysical Research Letters*, 30(10):1529.

Reeves, G. D., Spence, H. E., Henderson, M. G., Morley, S. K., Friedel, R. H. W., Funsten, H. O., Baker, D. N., Kanekal, S. G., Blake, J. B., Fennell, J. F., Claudepierre, S. G., Thorne, R. M., Turner, D. L., Kletzing, C. A., Kurth, W. S., Larsen, B. A., and Niehof, J. T. (2013). Electron Acceleration in the Heart of the Van Allen Radiation Belts. *Science*, 341(6149):991–994.

Rodger, C. J., Clilverd, M. A., Green, J. C., and Lam, M. M. (2010). Use of POES SEM-2 observations to examine radiation belt dynamics and energetic electron precipitation into the atmosphere. *Journal of Geophysical Research: Space Physics*, 115(A4).

Rostoker, G. (1972). Geomagnetic indices. *Reviews of Geophysics*, 10(4):935–950.

Sandanger, M. I., Ødegaard, L. K. G., Tyssøy, H. N., Stadsnes, J., Søraas, F., Oksavik, K., and Aarsnes, K. (2015). In-flight calibration of NOAA POES proton detectors - derivation of the MEPED correction factors. *Journal of Geophysical Research: space Physics*, 120(9):9578–9593.

Seppälä, A., Matthes, K., Randall, C. E., and Mironova, I. A. (2014). What is the solar influence on climate? Overview of activities during CAWSES-II. *Progress in Earth and Planetary Science*, 1(1).

Seppälä, A., Verronen, P. T., Sofieva, V. F., Tamminen, J., Kyrölä, E., Rodger, C. J., and Clilverd, M. A. (2006). Destruction of the tertiary ozone maximum during a solar proton event. *Geophysical Research Letters*, 33(7).

Sheeley, N. R., Harvey, J. W., and Feldman, W. C. (1976). Coronal holes, solar wind streams, and recurrent geomagnetic disturbances: 1973–1976. *Solar Physics*, 49(2):271–278.

Sinnhuber, M., Nieder, H., and Wieters, N. (2012). Energetic Particle Precipitation and the Chemistry of the Mesosphere/Lower Thermosphere. *Surveys in Geophysics*, 33.

Smith, A. K., Espy, P. J., López-Puertas, M., and Tweedy, O. V. (2018). Spatial and temporal structure of the tertiary ozone maximum in the polar winter mesosphere. *Journal of Geophysical Research: Atmospheres*, 123(0):4373–4389.

Smith, A. K., López-Puertas, M., García-Comas, M., and Tukiainen, S. (2009). SABER observations of mesospheric ozone during NH late winter 2002–2009. *Geophysical Research Letters*, 36(23). L23804.

Smith, A. K. and Marsh, D. R. (2005). Processes that account for the ozone maximum at the mesopause. *Journal of Geophysical Research: Atmospheres*, 110(D23).

Sofieva, V. F., Kyrölä, E., Verronen, P. T., Seppälä, A., Tamminen, J., Marsh, D. R., Smith, A. K., Bertaux, J.-L., Hauchecorne, A., Dalaudier, F., Fussen, D., Vanhellemont, F., Fanton d'Andon, O., Barrot, G., Guirlet, M., Fehr, T., and Saavedra, L. (2009). Spatio-temporal observations of the tertiary ozone maximum. *Atmospheric Chemistry and Physics*, 9(13):4439–4445.

Solomon, S., Reid, G. C., Rusch, D. W., and Thomas, R. J. (1983). Mesospheric ozone depletion during the solar proton event of july 13, 1982 part II. comparison between theory and measurements. *Geophysical Research Letters*, 10(4):257–260.

Solomon, S., Rusch, D., Gérard, J., Reid, G., and Crutzen, P. (1981). The effect of particle precipitation events on the neutral and ion chemistry of the middle atmosphere: II. odd hydrogen. *Planetary and Space Science*, 29(8):885 – 893.

Sonnemann, G., Grygalashvyly, M., Hartogh, P., and Jarchow, C. (2006). Behavior of mesospheric ozone under nearly polar night conditions. *Advances in Space Research*, 38(11):2402 – 2407.

Sugiura, M. (1964). Hourly values of equtorial dst for igy. In *Annals of International Geophysical Year*, pages 945–948. Pergamon Press, Oxford.

Sugiura, M., Kamei, T., Berthelier, A., and Menvielle, M. (1991). Equatorial dst index 1957-1986. In *IAGA Bulletin*, volume 40. International Association of Geomagnetism and Aeronimy.

Summers, D., Ni, B., and Meredith, N. P. (2007). Timescales for radiation belt electron acceleration and loss due to resonant wave-particle interactions: 2. evaluation for vlf chorus, elf hiss, and electromagnetic ion cyclotron waves. *Journal of Geophysical Research: Space Physics*, 112(A4).

Summers, D., Thorne, R. M., and Xiao, F. (1998). Relativistic theory of wave-particle resonant diffusion with application to electron acceleration in the magnetosphere. *Journal of Geophysical Research: Space Physics*, 103(A9):20487–20500.

Swider, W. and Keneshea, T. (1973). Decrease of ozone and atomic oxygen in the lower mesosphere during a PCA event. *Planetary and Space Science*, 21(11):1969 – 1973.

Thorne, R. (1980). The importance of energetic particle precipitation on the chemical composition of the middle atmosphere. *Pure and applied geophysics*, 118(1):128–151.

Tsurutani, B., Gonzalez, W. D., Gonzalez, A., Guarnieri, F., Gopalswamy, N., Grande, M., Kamide, Y., Kasahara, Y., Lu, G., Mann, I., McPherron, R., Soraas, F., and Vasyliunas, V. (2006). Corotating solar wind streams and recurrent geomagnetic activity: A review. *Journal of Geophysical Research*, 111(A07S01).

Turner, D. L., Angelopoulos, V., Li, W., Bortnik, J., Ni, B., Ma, Q., Thorne, R. M., Morley, S. K., Henderson, M. G., Reeves, G. D., Usanova, M., Mann, I. R., Claudepierre, S. G., Blake, J. B., Baker, D. N., Huang, C.-L., Spence, H., Kurth, W., Kletzing, C., and Rodriguez, J. V. (2014a). Competing source and loss mechanisms due to wave-particle interactions in earth's outer radiation belt during the 30 september to 3 october 2012 geomagnetic storm. *Journal of Geophysical Research: Space Physics*, 119:1960–1979.

Turner, D. L., Angelopoulos, V., Morley, S. K., Henderson, M. G., Reeves, G. D., Li, W., Baker, D. N., Huang, C.-L., Boyd, A., Spence, H. E., Claudepierre, S. G., Blake, J. B., and Rodriguez, J. V. (2014b). On the cause and extent of outer radiation

belt losses during the 30 september 2012 dropout event. *Journal of Geophysical Research: Space Physics*, 119:1530–1540.

Turner, D. L., Morley, S. K., Miyoshi, Y., Ni, B., and Huang, C.-L. (2013). Outer radiation belt flux dropouts: Current understanding and unresolved questions. In *Dynamics of the Earth's Radiation Belts and Inner Magnetosphere*, pages 195–212. American Geophysical Union.

Turner, D. L., Shprits, Y., Hartinger, M., and Angelopoulos, V. (2012). Explaining sudden losses of outer radiation belt electrons during geomagnetic storms. *Nature Publishing Group*, 8(3):208–212.

Turunen, E., Kero, A., Verronen, P. T., Miyoshi, Y., Oyama, S.-I., and Saito, S. (2016). Mesospheric ozone destruction by high-energy electron precipitation associated with pulsating aurora. *Journal of Geophysical Research: Atmospheres*, 121(19):11,852–11,861. 2016JD025015.

Turunen, E., Verronen, P. T., Seppälä, A., Rodger, C. J., Clilverd, M. A., Tamminen, J., Enell, C.-F., and Ulich, T. (2009). Impact of different energies of precipitating particles on NOx generation in the middle and upper atmosphere during geomagnetic storms. *Journal of Atmospheric and Solar-Terrestrial Physics*, 71(10-11):1176 – 1189.

Verkhoglyadova, O. P., Wang, S., Mlynczak, M. G., Hunt, L. A., and Zank, G. P. (2015). Effects of two large solar energetic particle events on middle atmosphere nighttime odd hydrogen and ozone content: Aura/mls and timed/saber measurements. *Journal of Geophysical Research: Space Physics*, 120(1):12–29.

Verkhoglyadova, O. P., Wissing, J. M., Wang, S., Kallenrode, M.-B., and P., Z. G. (2016). Nighttime mesospheric hydroxyl enhancements during sep events and accompanying geomagnetic storms: Ionization rate modeling and aura satellite observations. *Journal of Geophysical Research: Space Physics*, 121(7):6017–6030.

Verronen, P., Andersson, M., Rodger, C., Clilverd, M., Wang, S., and Turunen, E. (2013). Comparison of modeled and observed effects of radiation belt electron precipitation on mesospheric hydroxyl and ozone. *Journal of Geophysical Research: Atmospheres*, 118(19):11,419–11,428.

Verronen, P. T., Rodger, C. J., Clilverd, M. A., and Wang, S. (2011). First evidence of mesospheric hydroxyl response to electron precipitation from the radiation belts. *Journal of Geophysical Research: Atmospheres*, 116(D07307).

Verronen, P. T., Seppälä, A., Kyrölä, E., Tamminen, J., Pickett, H. M., and Turunen, E. (2006). Production of odd hydrogen in the mesosphere during the January 2005 solar proton event. *Geophysical Research Letters*, 33(24).

Wang, L. and Alexander, M. J. (2009). Gravity wave activity during stratospheric sudden warmings in the 2007–2008 northern hemisphere winter. *Journal of Geophysical Research: Atmospheres*, 114(D18).

Waters, J. W., Froidevaux, L., Harwood, R. S., Jarnot, R. F., Pickett, H. M., Read, W. G., Siegel, P. H., Cofield, R. E., Filipiak, M. J., Flower, D. A., Holden, J. R., Lau, G. K., Livesey, N. J., Manney, G. L., Pumphrey, H. C., Santee, M. L., Wu, D. L., Cuddy, D. T., Lay, R. R., Loo, M. S., Perun, V. S., Schwartz, M. J., Stek, P. C., Thurstans, R. P., Boyles, M. A., Chandra, K. M., Chavez, M. C., Chen, G.-S., Chudasama, B. V., Dodge, R., Fuller, R. A., Girard, M. A., Jiang, J. H., Jiang, Y., Knosp, B. W., LaBelle, R. C., Lam, J. C., Lee, K. A., Miller, D., Oswald, J. E., Patel, N. C., Pukala, D. M., Quintero, O., Scaff, D. M., Snyder, W. V., Tope, M. C., Wagner, P. A., and Walch, M. J. (2006). The earth observing system microwave limb sounder (EOS MLS) on the Aura satellite. *IEEE T. Geoscience and Remote Sensing*, 44(5):1075–1092.

Webb, D. (1995). Solar and geomagnetic disturbances during the declining phase of recent solar cycles. *Advances in Space Research*, 16(9):57 – 69.

Weeks, L. H., Cuikay, R. S., and Corbin, J. R. (1972). Ozone measurements in the mesosphere during the solar proton event of 2 November 1969. *Journal of the Atmospheric Sciences*, 29(6):1138–1142.

Winick, J. R., Wintersteiner, P. P., Picard, R. H., Esplin, D., Mlynczak, M. G., Russell, J. M., and Gordley, L. L. (2009). OH layer characteristics during unusual boreal winters of 2004 and 2006. *Journal of Geophysical Research: Space Physics*, 114(A2).

Yando, K., Millan, R. M., Green, J. C., and Evans, D. S. (2011). A monte carlo simulation of the NOAA POES medium energy proton and electron detector instrument. *Journal of Geophysical Research: Space Physics*, 116(A10).

Paper I

The impact of energetic electron precipitation on mesospheric hydroxyl during a year of solar minimum

A. E. Zawedde, H. Nesse-Tyssøy, R. Hibbins, P. J. Espy, L. K. G. Ødegaard, M. I. Sandanger, and J. Stadsnes

Journal of Geophysical Research: Space Physics, Vol. 121, doi:10.1002/2016JA022371, (2016)

AGU PUBLICATIONS

JGR

Journal of Geophysical Research: Space Physics

RESEARCH ARTICLE
10.1002/2016JA022371

Special Section:
Energetic Electron Loss and its Impacts on the Atmosphere

The impact of energetic electron precipitation on mesospheric hydroxyl during a year of solar minimum

Annet Eva Zawedde[1], Hilde Nesse Tyssøy[1], Robert Hibbins[1,2], Patrick J. Espy[1,2], Linn-Kristine Glesnes Ødegaard[1], Marit Irene Sandanger[1], and Johan Stadsnes[1]

[1]Birkeland Centre for Space Science, Department of Physics and Technology, University of Bergen, Bergen, Norway, [2]Department of Physics, Norwegian University of Science and Technology, Trondheim, Norway

Key Points:
- There is substantial OH production by energetic electron precipitation also during solar minimum
- To quantify the effect, the background atmospheric dynamics have to be taken into account
- It also requires detail knowledge of where and when the energetic electron precipitation occurs

Correspondence to:
H. Nesse Tyssøy,
hilde.nesse@ift.uib.no

Citation:
Zawedde, A. E., H. Nesse Tyssøy, R. Hibbins, P. J. Espy, L.-K. G. Ødegaard, M. I. Sandanger, and J. Stadsnes (2016), The impact of energetic electron precipitation on mesospheric hydroxyl during a year of solar minimum, *J. Geophys. Res., 121*, 5914–5929, doi:10.1002/2016JA022371.

Received 12 JAN 2016
Accepted 29 MAY 2016
Accepted article online 7 JUN 2016
Published online 30 JUN 2016

Abstract In 2008 a sequence of geomagnetic storms occurred triggered by high-speed solar wind streams from coronal holes. Improved estimates of precipitating fluxes of energetic electrons are derived from measurements on board the NOAA/POES 18 satellite using a new analysis technique. These fluxes are used to quantify the direct impact of energetic electron precipitation (EEP) during solar minimum on middle atmospheric hydroxyl (OH) measured from the Aura satellite. During winter, localized longitudinal density enhancements in the OH are observed over northern Russia and North America at corrected geomagnetic latitudes poleward of 55°. Although the northern Russia OH enhancement is closely associated with increased EEP at these longitudes, the strength and location of the North America enhancement appear to be unrelated to EEP. This OH density enhancement is likely due to vertical motion induced by atmospheric wave dynamics that transports air rich in atomic oxygen and atomic hydrogen downward into the middle atmosphere, where it plays a role in the formation of OH. In the Southern Hemisphere, localized enhancements of the OH density over West Antarctica can be explained by a combination of enhanced EEP due to the local minimum in Earth's magnetic field strength and atmospheric dynamics. Our findings suggest that even during solar minimum, there is substantial EEP-driven OH production. However, to quantify this effect, a detailed knowledge of where and when the precipitation occurs is required in the context of the background atmospheric dynamics.

1. Introduction

Energetic particles precipitating into the mesosphere and lower thermosphere are known to produce copious amounts of odd nitrogen (NO_X: N, NO, NO_2) and odd hydrogen (HO_X: H, HO, HO_2), which can contribute to ozone (O_3) destruction [e.g., *Jackman et al.*, 2005; *Sinnhuber et al.*, 2012]. The energetic particles (electrons, protons, and heavier ions) have different solar drivers. Coronal Mass Ejections (CMEs) associated with sunspots predominantly occur during solar maximum and are the cause of solar proton events (SPEs) which can lead to strong geomagnetic activity. The influence of the infrequent SPEs upon the middle atmosphere has been extensively studied [see, e.g., *Bates and Nicolet*, 1950; *Weeks et al.*, 1972; *Swider and Keneshea*, 1973; *Crutzen and Solomon*, 1980; *Solomon et al.*, 1981; *López-Puertas et al.*, 2005; *Damiani et al.*, 2008, 2010; *Verronen and Lehmann*, 2013; *Jackman et al.*, 2014; *Nesse Tyssøy and Stadsnes*, 2015]. The atmospheric effects of the more frequent energetic electron precipitation (EEP) events are less known and harder to detect. During geomagnetic storms energetic electrons are injected and stored in the magnetosphere where they can be accelerated to relativistic energies [*Foster et al.*, 2014] and subsequently lost to the atmosphere [*Turner et al.*, 2014]. The penetration depth varies with the particle energy, for example, a 30 keV electron will stop at ~90 km, while a 1 MeV electron penetrates to about 60 km [*Turunen et al.*, 2009]. Individually, such storms have weaker geomagnetic signatures than SPEs. It is, however, speculated that these events, because of their frequent occurrence, will have a strong impact on the atmosphere in general [*Andersson et al.*, 2014a].

Bartels [1932] identified "*M* regions" on the solar surface as the source of the sequences of recurrent geomagnetic activity that occurred during minimum solar activity. *M* regions are in fact coronal holes (CHs) and are independent of sunspot activity [*Allen*, 1943]. They are associated with open magnetic field lines and, high-speed, low-density flows in the solar wind [*Billings and Roberts*, 1964]. CHs are the source of high-speed solar wind streams (HSSWS) and subsequent recurrent geomagnetic activity [e.g., *Neupert and Pizzo*, 1974; *Burlaga and Lepping*, 1977; *Sheeley and Harvey*, 1981]. The interaction of the fast solar wind associated with

AGU Journal of Geophysical Research: Space Physics 10.1002/2016JA022371

CHs with the slow solar wind streams results in the compression of the magnetic field and plasma at their interfaces forming a corotating interaction region (CIR), which is the geoeffective structure [*Tsurutani et al.*, 2006; *Gopalswamy*, 2008]. However, the interplanetary magnetic field (IMF) associated with CIRs has a highly oscillating nature, which results in only moderate intensification of the magnetospheric currents and hence moderate geomagnetic signatures. The intensity of the resulting storm depends on the combination of solar wind speed and the direction of the B_z component [*Gopalswamy*, 2008].

Recent studies [*Verronen et al.*, 2011; *Andersson et al.*, 2012, 2014b, 2014a] provide observational evidence of radiation belt (geomagnetic latitudes 55° – 65°) electron precipitation (100 – 300 keV) affecting mesospheric (71 – 78 km) OH. Based on two case studies in the declining phase of the solar cycle, *Verronen et al.* [2011] found that 56 – 87% of the changes in OH could be explained by changes in EEP. In a follow up study, *Andersson et al.* [2012] focused on a larger part of the solar cycle from solar maximum to solar minimum. They found months of high correlation between daily zonal mean OH mixing ratios at 70 – 78 km and the flux of 100 – 300 keV electrons. The correlation coefficients were highly dependent on season and the strength of the particle precipitation. *Andersson et al.* [2014b] studied the longitudinal response of nighttime mesospheric OH to >30 keV electron precipitation, contrasting days with daily mean count rates of >100 c/s to days with <5 c/s. In total 51 days between 2005 and 2009 met the first criteria. Generally, they concluded that clear effects of EEP were seen at magnetic latitudes 55° – 72°. In the Southern Hemisphere (SH), the OH data revealed localized OH mixing ratio enhancements at longitudes between 150°W and 30°E, over West Antarctica, poleward of the South Atlantic Magnetic Anomaly (SAMA) region. In the Northern Hemisphere (NH), EEP-induced OH variations were more equally distributed with longitude; however, two potential regions of enhanced OH mixing ratio above Northern America and Northern Russia were found.

The middle atmosphere has a strong seasonal dynamical variability, including both the background meridional and zonal winds, as well as the atmospheric wave activity [see, e.g., *Shepherd*, 2000; *Kleinknecht et al.*, 2014]. For example, *Damiani et al.* [2010] have shown that during sudden stratospheric warmings (SSWs), the OH layer may show short-term variations comparable in strength to the OH increases during SPEs. *Andersson et al.* [2014b] did not include potential seasonal or meteorological factors when considering the particle impact upon the longitudinal distribution of OH, although there appears to be features less constrained to the magnetic latitudes and geomagnetic activity in both hemispheres. During strong particle precipitation events, the OH production due to background dynamics of the atmosphere might be overshadowed by the impact of energetic particle precipitation (EPP). However, during the more frequent and modest changes, the dynamical background will be of higher importance. Moreover, for the more frequent events, the magnitude of the direct EEP-induced HO_X effect on O_3 in the mesosphere is high enough to suspect that EEP could be an important contribution to the Sun-climate connection on solar cycle time scales [*Andersson et al.*, 2014a]. Assessing the impact and spatial distribution of electron forcing is, therefore, important for more accurate modeling of its atmospheric and climate effects.

The quantification of relativistic electron precipitation has, however, proved difficult due to particle detector challenges [see, e.g., *Nesse Tyssøy et al.*, 2016]. In addition, radiation belt electrons usually have strong anisotropic pitch angle distribution that needs to be accounted for when considering their impact upon the atmosphere [*Rodger et al.*, 2013; *Nesse Tyssøy et al.*, 2016]. In this study, we optimize the data from the Medium Energy Proton and Electron Detectors (MEPED) on the Polar Orbiting Environmental Satellite (POES) NOAA-18, taking into account detector degradation, proton contamination, and combining data from both the 0° and 90° telescopes to achieve a better estimate of the true loss cone fluxes. We also use electron fluxes with energy >1000 keV obtained from the proton telescopes to determine the EEP impact on OH in the middle atmosphere [*Nesse Tyssøy et al.*, 2016]. Whereas *Andersson et al.* [2014b] used all available POES satellites, we only use NOAA-18, which is traversing the same local time as the Aura satellite making it possible to study the local effects of the energy deposition by relativistic electrons on OH. The data and its application are further explained in the next section.

Since most studies have focused on geomagnetic activity during solar maximum, it is paramount to get a deeper understanding of the contribution of EEP on HO_X also during solar minimum. Therefore, we target the solar minimum year of 2008, where a sequence of weak to moderate storms triggered by HSSWS occurred. The low intensity of the recurrent storms implies that we need to carefully consider the role of the changing background dynamics upon the OH distribution. In addition to OH mixing ratios, the Aura MLS provides measurements of temperature, water vapor (H_2O), and geopotential height (GPH) which reveal the background

AGU Journal of Geophysical Research: Space Physics 10.1002/2016JA022371

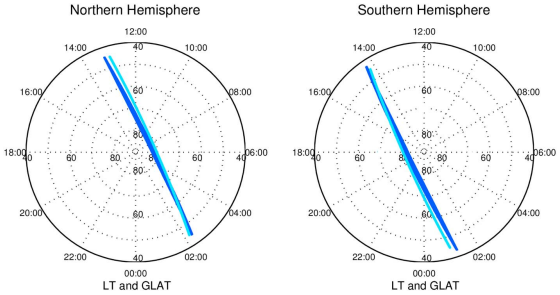

Figure 1. A plot showing the footprints of Aura (dark blue) and NOAA 18 (light blue) in local time and geographical latitudes for year 2008. Midnight is at the bottom and dusk to the left of each plot.

state of the atmosphere. Thus, extracting information on both the longitude and altitude distribution enables us for the first time, to separate the OH variability caused by EEP and by atmospheric dynamics. The resulting analysis is given in section 3, and the subsequent discussions and conclusion follows in sections 4 and 5.

2. Materials and Methods

2.1. Aura MLS Observations

The Microwave Limb Sounder (MLS) is one of the four instruments on board NASA's Aura satellite [*Schoeberl et al.*, 2006]. It is in a near-polar Sun-synchronous orbit at 705 km altitude, scanning the atmosphere up to geographic latitudes 82° N/S with about 14 orbits per day (period ~100 min). The MLS measures naturally occurring microwave thermal emissions from the limb of the Earth's atmosphere to remotely sense vertical profiles of atmospheric constituents [*Schoeberl et al.*, 2006; *Waters et al.*, 2006].

In this study we use Aura/MLS level 2 files version 4.2x for the year 2008 screened as per *Livesey et al.* [2015]. Only nighttime observations with solar zenith angle (SZA) >100° are considered to make sure no sunlight illuminates the sampled atmosphere below 100 km [*Pickett et al.*, 2006]. At night without solar radiation, the data should typically show low values of background OH, which makes the detection of OH enhancements due to EEP effects easier. In the latitude range of the radiation belts, nighttime Aura measurements occur at local solar time (LST) 02:15-03:30 in the NH during 2008. In the SH, however, Aura measurements are from LST 15:26 to 01:18. For SH nighttime observations we use LST 22:00-01:18.

The temporal resolution of Aura MLS data is ~25 s. The vertical and horizontal resolution of OH measurements is 2.5 km and 165 km, respectively, within mesospheric altitudes (60–80 km). O_3, H_2O, temperature, and GPH have coarser and variable vertical/horizontal resolutions within mesospheric altitudes [see *Livesey et al.*, 2015].

The geometric height, z, can be expressed using the pressure altitude as

$$z = -H \ln\left(\frac{P}{P_s}\right) \tag{1}$$

where H is the atmospheric scale height (~7 km) [*Brasseur and Solomon*, 2005], P_s is a reference pressure (1000 hPa) and P is the pressure level given in the MLS data.

2.2. NOAA POES MEPED Observations

In 2008, one of the five NOAA/POES satellites, NOAA 18 scanned the Earth at approximately the same local times as the Aura satellite (see Figure 1). This implies that the particle fluxes measured by MEPED/NOAA 18 deposited their energy close in both time and space to the measurements performed by Aura. Considering the short lifetime of OH below 80 km, the EEP impact on OH is considered to be a local effect.

The MEPED consists of two proton and two electron telescopes viewing almost perpendicular to each other. The electron and proton telescopes pointing radially outward are often named the 0° detectors. At high

AGU Journal of Geophysical Research: Space Physics 10.1002/2016JA022371

Table 1. MEPED Proton and Electron Energy Channels [*Evans and Greer*, 2000]

Proton Energy Channels		Electron Energy Channels	
Channel	Energy Range (keV)	Channel	Energy Range (keV)
0/90 P1	30 to 80	0/90 E1	30 to 2500
0/90 P2	80 to 240	0/90 E2	100 to 2500
0/90 P3	240 to 800	0/90 E3	300 to 2500
0/90 P4	800 to 2500		
0/90 P5	2500 to 6900		
0/90 P6	>6900		

latitudes they will view particles within the loss cone and have therefore previously been used to represent the precipitating fluxes [*Verronen et al.*, 2011; *Andersson et al.*, 2012, 2014b, 2014a]. Electrons with energies capable of precipitating into the middle atmosphere (>30 keV) have, however, often a strongly anisotropic pitch angle distribution, which decreases toward the center of the loss cone. The 0° detector looking close to the center of the loss cone will therefore provide an underestimate of the precipitating fluxes. The other electron and proton telescope, called the 90° detector, view particles near the edge or outside the loss cone. Therefore, the 90° detectors will measure higher fluxes compared to the true precipitating fluxes. To overcome this challenge, we combine data from both electron telescopes to estimate the electron fluxes over the entire loss cone. The 0° and 90° electron fluxes were fitted to the solution of the Fokker-Planck equation for pitch angle diffusion of energetic particles [*Kennel and Petschek*, 1966]. We take into account the detector sensitivity when the directional flux varies over the acceptance solid angle of the telescope [*Nesse Tyssøy et al.*, 2016]. We correct the electron data for contamination by protons [*Yando et al.*, 2011]. The degradation of the proton detector is taken into account by applying the new correction factors developed by *Sandanger et al.* [2015].

During solar minimum, when no SPEs occur, there will be insignificant high-energy proton fluxes detected by the MEPED proton telescope which can be confirmed by the P4 and P5 energy channels (see Table 1). Considering that the highest-energy channel of the proton detector (P6) is responsive to relativistic electrons, we utilize this contamination effect to get a quantitative measure of electron fluxes larger than 1 MeV [*Yando et al.*, 2011]. The particle fluxes are sampled every 2 s. However, for purposes of comparing the particle fluxes with composition data from Aura, we average the fluxes over 1° latitude bin equivalent to about 16 s.

Combining the electron and proton channels (E1, E2, E3, and P6), we achieve a differential electron spectrum covering energies from 50 to 1000 keV. We use the electron spectra to calculate the energy deposition as a function of altitude. In these calculations, we use the cosine-dependent Isotropic over the Downward Hemisphere (IDH) model of *Rees* [1989]. This is a range-energy analysis based on a standard reference atmosphere (COmmittee on SPAce Research International Reference Atmosphere 1986).

2.3. OMNI Data

In this study we use IMF and solar wind plasma parameter data for the year 2008 downloaded from the Coordinated Data analysis Web (http://cdaweb.gsfc.nasa.gov./istp-public/). We focus on the B_z, V_{SW}, and solar wind flow pressure (P_{SW}), at 1 h resolution in geocentric solar magnetospheric (GSM) coordinates. Originally, the data are measured by either WIND or the ACE satellite and time shifted to the Earth's bow shock nose. The *Dst* and *AE* indices also have a 1 h resolution, while the *Kp* index has a 3 h resolution.

3. Results

3.1. Solar Wind and Geomagnetic Conditions

In Figure 2, daily means of *Kp*, *Dst*, *AE*, B_z, V_{SW}, and P_{SW} are plotted for the whole year 2008, during which two HSSWS associated with the 27 days solar rotation period are indicated by the vertical dashed and dotted lines. The daily mean *Dst* index and IMF B_z clearly show decreases corresponding to the arrival of the HSSWS, indicating the recurrent storm activity experienced by the magnetosphere. All the storms were weak to moderate based on the *Dst* index classification by *Loewe and Prölss* [1997].

In the period January to April, both the HSSWS were geoeffective. In May, the signature of the HSSWS in the geomagnetic indices is weak. In the daily mean *Dst*, for example, this period shows $Dst > -15$ nT. Both *Kp* and *AE* also display low values in May. From June to September, one of the HSSWS becomes geoeffective again

AGU Journal of Geophysical Research: Space Physics 10.1002/2016JA022371

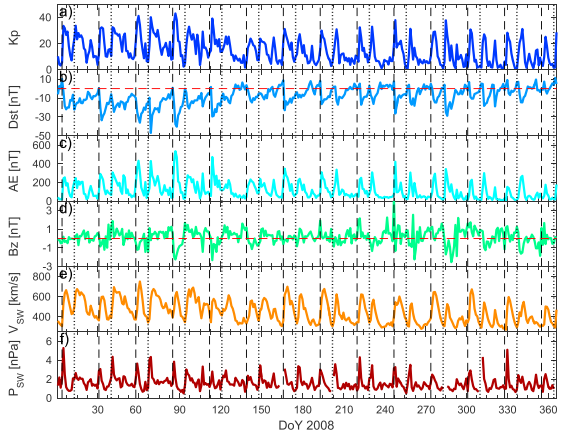

Figure 2. Daily means of *Kp*, *Dst*, *AE*, B_z, V_{SW}, and P_{SW} during 2008 from top to bottom, respectively. The black vertical dashed and dotted lines indicate the 27 days recurrent period of the HSSWS. The red dashed lines show the zero line in the *Dst* index and B_z.

(dashed vertical line). The signature from this HSSWS disappears in October. The other HSSWS (dotted vertical line) also becomes geoeffective again in September. At the end of the year, in November and December, the solar wind and geomagnetic signatures from the two HSSWS are weakened.

3.2. Longitudinal Distribution of OH

To investigate the seasonal longitudinal distribution of OH, we calculate the longitudinal OH running mean (5° longitude window) within a latitude band of 40° to 80° for altitudes 60 to 81 km in both hemispheres for winter, spring, and autumn. Note that due to the SZA selection of >100°, the data coverage for summer stops at about 65°N and 70°S. The months January and February are considered winter in the NH and summer in the SH. While the months June, July, and August are summer in the NH and winter in the SH. The other seasons follow accordingly. However, the month of December 2008 is not included in this study. The seasonal longitudinal distribution of the OH volume mixing ratio (VMR) is shown in Figure 3. All seasons show two OH maxima located at about 67 and 73 km in both hemispheres. Summer months exhibit another OH maximum located at approximately 78 km in both hemispheres. Generally, the OH VMR decreases with decreasing altitude. For winter in the NH, there is high OH VMR within longitudes 150°W–100°E for altitudes 81 km to about 76 km. In the SH winter, the high OH VMR at altitudes 76–81 km is almost homogeneously distributed but strongest within longitudes 180°W–60°W and 120°E–180°E. High OH VMR are still visible in spring within approximately the same longitude region. Autumn also shows high OH VMR within approximately the same longitudes in the NH but weaker compared to winter. In the SH, there is a stronger OH concentration within longitudes 115°–0°W than during winter, with signatures up to below 76 km. Generally, these kind of high OH concentrations at 67–81 km occurred during January, February, March, October, November, and December in the NH, while in the SH, they occurred during April to September (~autumn to winter in both hemispheres).

3.3. Longitudinal Variation of EEP Effects on OH

We present the hemispherical distribution of disturbed and quiet conditions for the energy deposition and OH during winter in the NH and autumn in the SH averaged over altitudes between 75 and 78 km in 2008. Disturbed/quiet conditions were sorted based on daily mean energy deposition by EEP at particular altitudes. Days, for which the daily mean energy deposition is greater than the annual mean energy deposition at a particular altitude range, were considered to be disturbed time. Whereas days, for which the daily mean

AGU Journal of Geophysical Research: Space Physics 10.1002/2016JA022371

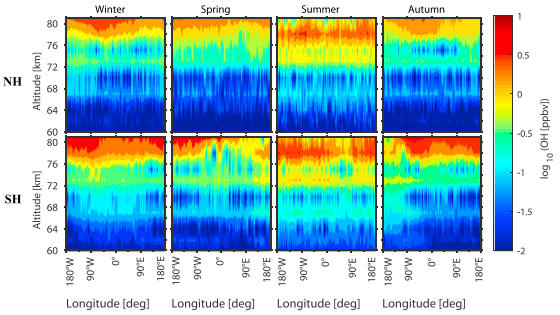

Figure 3. OH running mean (5° longitude window) for the altitude range of 60–81 km. Autumn, winter, and spring months cover a latitude band of 40° to 80°N/S for year 2008. Summer months do not extend to 80° latitude due to the SZA selection of >100°. (top row) The NH and (bottom row) the SH. (first column to fourth column) Winter, spring, summer, and autumn. The months January and February are considered winter in the NH and summer in the SH. Whereas the months Jun,e, July and August are considered summer in the NH and winter in the SH. The other seasons follow accordingly.

energy deposition is less than the annual mean energy deposition at a particular altitude range, were considered to be quiet time. The data are sorted according to geographical latitude and longitude in such a way that each 5° latitude by 10° longitude bin shows the running mean (over a window of three bins) of the energy deposition or OH/temperature/H_2O/GPH within that bin.

We present maps of an average at 75–78 km for the energy deposition and OH VMR. (For comparative studies with temperature, H_2O and GPH, we use data at 75 km.) All maps cover geographical latitudes 40°–80° N/S. The first results, sorting by season, show that winter (January and February) in the NH and autumn (March, April, and May) in the SH exhibit the longitudinal signatures in OH reported by *Andersson et al.* [2014b] more clearly than in the other seasons. This is consistent with the strength of the geomagnetic activity. Although winter is the best season to observe EEP effects in the atmospheric OH due to low background levels, EEP-related changes in OH were stronger in the SH autumn compared to winter in 2008. Consequently, we focus on the winter and autumn months for the NH and SH, respectively, as shown in Figures 4 and 5. As the maps of NH and SH cover different months, they also cover different EEP events throughout 2008.

3.3.1. Energy Deposition

Figure 4 shows the night-time mean energy deposited between 40° and 80° geographic latitudes during disturbed and quiet conditions for winter and autumn in the NH and SH, respectively. The energy data are averaged between 75 and 78 km. The storm time NH map is fairly homogeneous with maximum values covering northern Russia and part of North America at longitudes (30°E–130°W) and minimum values over Scandinavia to North America (60°W–30°E). In the SH, the energy is deposited almost homogeneously within the latitude range of the radiation belts. The energy deposition during storm times is approximately 1 order of magnitude greater than during nonstorm times in both hemispheres.

3.3.2. OH Composition

Figure 5 shows the night-time mean OH maps for disturbed and quiet conditions during winter in the NH and autumn in the SH. In the NH, OH shows clear enhancements poleward of latitude 55°N CGM during storm conditions, with local maxima within longitudes 90°–10°W and 70°E–130°W which *Andersson et al.* [2014b] refers to as the North America and northern Russia hot spots. The OH enhancement over North America is, however, also present during quiet times within longitudes 90°–0°W, and it is stronger over the North Atlantic Ocean than over North America. (There is also a region of high-OH volume mixing ratio at 60–90°E about 40–45°N ($L \sim 1.5-2$) corresponding to the inner radiation belt. As our focus is the auroral and subauroral latitudes, we consider this feature outside the scope of the current paper.)

In the SH, there appears to be a local OH enhancement over West Antarctica both during disturbed and quiet conditions which *Andersson et al.* [2014b] refers to as the Antarctic Peninsula hot spot. OH enhancement is

AGU Journal of Geophysical Research: Space Physics 10.1002/2016JA022371

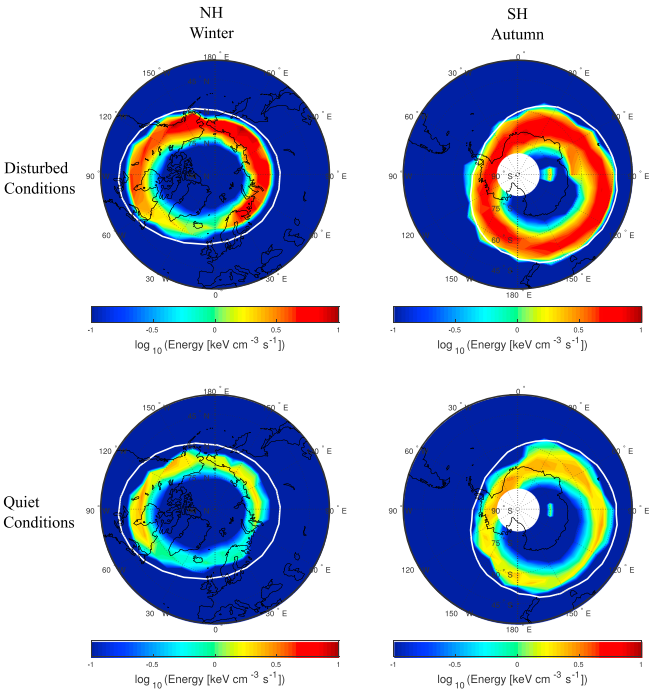

Figure 4. Mean nighttime energy deposition during (top row) disturbed and (bottom row) quiet conditions at altitudes 75–78 km for (left column) winter (January–February) at LST 2 ≤ LST < 4 in the NH and for (right column) autumn (March–May) at LST 22 ≤ LST ≤ 1 in the SH. Mean values were calculated for each 5° latitude by 10° longitude bin between 40° to 80°N and longitudes 180°W to 180°E. The white line shows the approximate location of 55°N/S CGM latitude.

seen at all longitudes during disturbed times and within longitudes 150°–0°W during quiet conditions. The West Antarctica hot spot appears, however, to be unbound by the geomagnetic location of Earth's radiation belts but seems rather to be more geographically constrained.

Note that the local OH enhancements in Figure 5 generally cover smaller longitude ranges than the hot spots seen by *Andersson et al.* [2014b] but are located within the same regions. Both the current presentation and the maps presented by *Andersson et al.* [2014b] show OH features (signatures) unconstrained to the geomagnetic latitude location (or footprints) of the Earth's radiation belts, indicating potential signatures due to the background dynamics.

3.4. Dynamical Background

We investigate the possibility that atmospheric dynamics is responsible for some of the observed OH enhancements. Figure 6 shows the temperature, H_2O and GPH (top row to bottom row) for quiet time conditions in the NH (left column) and SH (right column), respectively. In the NH, there is a temperature enhancement between longitudes 90°W and 110°E and an H_2O minimum. The temperature maximizes in

AGU Journal of Geophysical Research: Space Physics 10.1002/2016JA022371

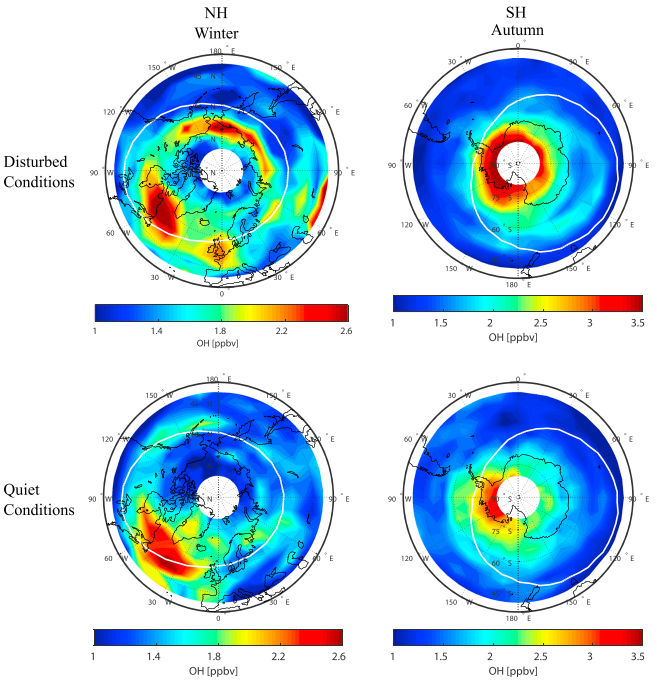

Figure 5. Mean nighttime OH during (top row) disturbed and (bottom row) quiet conditions at altitudes 75–78 km for (left column) winter (January–February) at LST $2 \leq$ LST < 4 in the NH and for (right column) autumn (March–May) at LST $22 \leq$ LST < 2 in the SH. Mean values were calculated for each 5° latitude by 10° longitude bin between 40° to 80°N and longitudes 180°W to 180°E. The white line shows the approximate location of 55°N/S CGM latitude.

approximately the same region where the North America OH maximum is located. A depression in the GPH is seen within longitudes 180°W–0°W, displaced by approximately 90° westward from the location of the temperature maximum and H_2O minimum. In the SH, the same features are seen in the temperature, H_2O, and GPH for the West Antarctica maximum, all located over approximately the same region over West Antarctica without a shift in the location of the GPH minimum. The North America and West Antarctica OH enhancements seem to follow more closely the region of intersection of the depression in the GPH with temperature maximum and H_2O minimum.

During winter time, especially in the NH, planetary wave activity is known to play an essential role in the background dynamics. To determine the role of planetary wave activity upon the OH composition, Figure 7 shows the OH (a), EEP (b), and temperature anomaly (c) in a geographic latitude band 60°–70°N for quiet (right column) and disturbed (left column) conditions. We sorted the data based on the energy deposition as in section 3.3. The temperature anomaly is the difference from the mean over the period. Then we derive the quasi-stationary planetary wave numbers 1 (S1) and 2 (S2) shown as the superposition of two sinusoidal curves fitted to the longitudinal temperature anomaly Figures 7c and 7d.

AGU Journal of Geophysical Research: Space Physics 10.1002/2016JA022371

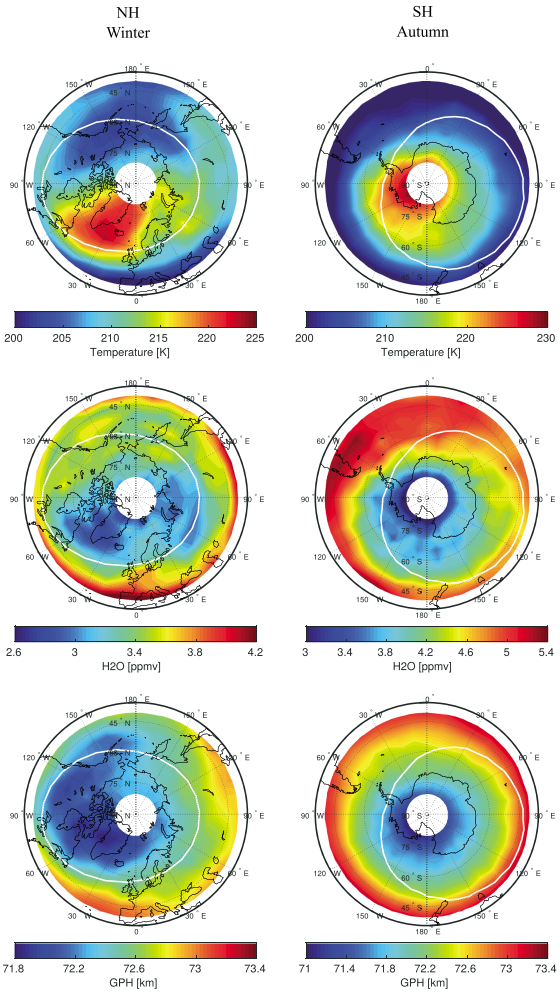

Figure 6. (top row to bottom row) Mean nighttime temperature, H_2O, and GPH during quiet conditions at altitudes 75 km for (left column) winter (January–February) at $2 \leq$ LST < 4 in the NH and for (right column) autumn at LST $22 \leq$LST< 2 in the SH during 2008. Mean values were calculated for each 5° latitude by 10° longitude bin between 40° to 80°S and longitudes 180°W to 180°E. The white line shows the approximate location of 55°N/S CGM latitude.

AGU Journal of Geophysical Research: Space Physics 10.1002/2016JA022371

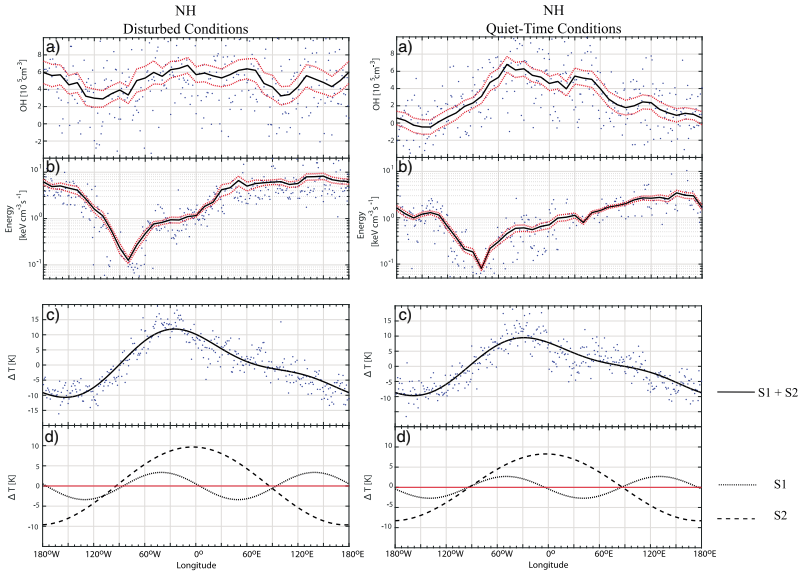

Figure 7. Longitudinal variation of OH and energy deposition averaged between altitudes 75–78 km during winter for the latitude band of 60–70°N in 2008 for disturbed and quiet time conditions. For comparison with background atmospheric dynamics, Figures 7c and 7d show the quasi-stationary planetary wave activity for wave number 1 and 2 derived from temperature between latitudes 60 and 70°N at an altitude of 75 km during winter for year 2008. (top row to bottom row) (a) OH (blue). Running mean of 30° longitude (black). (b) Energy deposition (blue). Running mean of 30° longitude (black). (c) Temperature anomaly (blue) fitted with a sinusoidal curve for the superposition of planetary waves S1 and S2 (black). (d) Sinusoidal curve fitting for planetary wave numbers 1 (S1) and 2 (S2). The red solid line is the zero line. The red dotted lines show the standard error of the mean.

During NH winter in 2008 the S1 and S2 peak around the same longitudes during both quiet and disturbed conditions. S1 has its maximum around 0°E. S2 has its maximum around 140°E and 40°W. The amplitudes are slightly higher during disturbed conditions. However, this may well be due to the random sample of days for the storm time conditions and unrelated to the EEP. During disturbed conditions S1 and S2 have an amplitude of about 19 K and 7 K, respectively. The superposition of the two waves, S1 + S2 is large at 75 km driving a longitudinal variability in temperature of around 23 K with a maximum around 25°W and a minimum close to 155°W.

The OH during disturbed conditions shows that in addition to changes correlated with the temperature variations, an additional source is present that coincides with the distribution of EEP. As Figure 4 shows, the EEP in a geographic latitude band between 60°–70°N samples only part of the auroral oval due to the offset between geomagnetic and geographical coordinates. The energy deposition shows high values (>4 keV cm^{-3}s^{-1}) between longitudes 25°E and 135°W corresponding well with the increase of OH in this region. In the region of little EEP, the OH appears to track the temperature variations as it does during quiet times. To better reveal the EEP impact on the OH density, we have subtracted the quiet time conditions from the disturbed conditions as shown in Figure 8. The longitudinal OH behavior is generally in phase with the energy deposition. The only exception is the longitude interval 30°–60°E which corresponds to regions where the auroral oval intersects a descending area of low H_2O mixing ratios (see Figure 6). Note that the negative OH values are due to the fact that some of the MLS observations are noisy in nature. Ignoring such values

AGU Journal of Geophysical Research: Space Physics 10.1002/2016JA022371

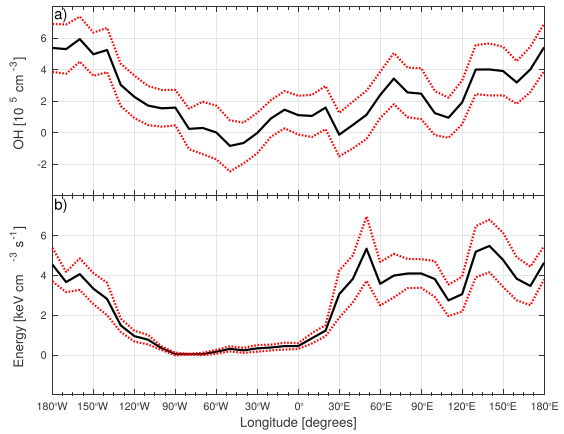

Figure 8. The difference between disturbed and quiet time at 75–78 km within a latitude band of 60–70°N for winter in 2008. The red dotted lines show the standard error of the mean. (a) Longitudinal OH (b) longitudinal energy deposition.

will automatically introduce a positive bias into any averages made of the data as part of scientific analysis [*Livesey et al.*, 2015].

4. Discussion

4.1. Is the Impact of EEP Upon the OH Production of Any Significance During Solar Minimum?

During geomagnetic storms radiation belt particles can be accelerated to high and possibly relativistic energies that precipitate deep into the atmosphere, causing enhancements of OH. EPP leads to production of HO_x species through ionization, dissociation, and dissociative ionization of the most abundant chemical species in the atmosphere (N_2 and O_2). The abundance of H_2O below 80 km facilitates the formation of large water cluster ions which recombine with electrons forming ~$2HO_x$ per ionization [*Solomon et al.*, 1981; *Sinnhuber et al.*, 2012]. EEP appears to impact the geomagnetic latitudes 55°–72° N/S CGM as illustrated by Figure 4 [see also *Andersson et al.*, 2014b].

The region of high OH VMR over northern Russia is collocated with the region of enhanced EEP energy deposition. The region of high OH VMR over North America and the North Atlantic Ocean, prominent during both disturbed and quiet conditions is not evident in the energy deposition. In the SH, we find a similar situation. The OH concentration maximizes over the West Antarctica, while the energy deposition is found to be rather homogeneously distributed with longitude. In the following, we will discuss the extent to which the local OH enhancements in the two hemispheres are related to the EEP energy deposition and the role of the background atmosphere on the longitudinal distribution of OH.

4.1.1. Longitudinal Variations of the Energy Deposition and OH in the NH

For January 2005 to December 2009, *Andersson et al.* [2014b] found two regions of high OH concentration during high EEP in the NH (51 days of data in total). These regions are the North America and northern Russia, which were attributed to EEP forcing. Our energy deposition maps based on the electron fluxes from MEPED/NOAA 18 maximizes as illustrated in Figure 4 over the northern Russia region. We do not, however, find evidence based on the energy deposition for an EEP-produced OH concentration enhancement over North America. The OH enhancement is prominent in both disturbed and quiet times. The energy deposition pattern cannot explain the distinct pattern found in the OH concentration.

AGU Journal of Geophysical Research: Space Physics 10.1002/2016JA022371

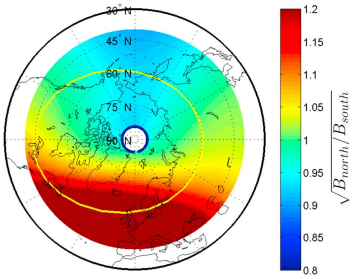

Figure 9. Ratio of magnetic field strength in the NH to the magnetic field in the SH found by magnetic field tracing using the IGRF model.

In addition to covering a shorter time period, some of the discrepancies between our energy deposition map and the map provided by *Andersson et al.* [2014b] might be due to the fact that they use the 0° detector E1 channel measuring electrons of energy larger than 30 keV. The E1 channel counts might be dominated by the lower energies that will not penetrate below 80 km. As we estimate the energy deposition at the respective heights we use the information from all the energy channels. We also limit the electron flux analysis to NOAA/POES 18 which is close in both time and space to the Aura OH retrieval. *Andersson et al.* [2014b] used multiple spacecraft at different MLT regions compared to the MLT region of the OH retrieval from Aura.

Barth et al. [2001] investigated the geomagnetic longitude dependence observed in NO_x at 106 km produced by auroral electrons. The most characteristics feature in their result is a minimum in a region above Scandinavia and Greenland. A possible candidate for these longitudinal variations in the NH is the asymmetries in the Earth's magnetic field. Electrons drifting around the Earth to the weak field associated with the SAMA are lost to the atmosphere. This depletes the electrons throughout the anomaly region. *Barth et al.* [2001], therefore, suggested that we are seeing the "normal" electron precipitation west of the weak magnetic field region but a much weakened precipitation of electrons within the weak magnetic field region itself and eastward of it. Figure 9 shows the square root ot the ratio: B_{North}/B_{South}, where B_{South} is found by magnetic field tracing using the IGRF model. Based on this theory, the low magnetic field ratio over North Asia and Alaska would imply that there will be more electron precipitation there than in the SH for particles bouncing over the same magnetic field lines. Therefore, the lower magnetic field ratio and the associated electron precipitation may explain the presence of the northern Russia hot spot. On the other hand, the magnetic field ratio is relatively higher above Scandinavia and Greenland. As the high B_{North}/B_{South} ratio overlaps with the large OH VMR, it does seem unlikely that the North America/North Atlantic OH maximum is due to EEP forcing.

4.1.2. Longitudinal Variations of the Energy Deposition and OH in the SH

In the SH autumn, there is a maximum in the OH density above West Antarctica during both disturbed and quiet conditions. The West Antarctica OH enhancement and its persistence during quiet times might be explained by the weaker magnetic field in this region that allows a steady drizzle of radiation belt electrons. Electrons that were mirroring at other longitudes could be lost here as they penetrate deeper in the atmosphere and interact with the denser atmosphere. The West Antarctica hot spot is also visible in winter and spring starting at approximately 70–73 km altitude during quiet times (not shown).

According to *Horne et al.* [2009], the effects on atmospheric chemistry due to relativistic electron precipitation (REP) are more likely to occur in the SH poleward of the SAMA region, because >1 MeV electron precipitation occur mainly in that region. However, the energy deposition seems rather uniformly distributed with geographic longitude circles as seen in Figure 4. This is also a feature in the results of *Andersson et al.* [2014b].

Although the West Antarctica OH enhancement can be explained by the weaker magnetic field in that region, its features seem more constrained by geographical rather than geomagnetic location. There is a possibility that in addition to the above mentioned causes, atmospheric dynamics may also play an active role in the formation of the West Antarctica OH maximum.

4.2. The Role of the Background Dynamics in Determining the Longitudinal OH Distribution

Elevated temperatures and dry air at 75 km appear to coexist with the longitudinal region of elevated OH VMR measured by Aura as shown in Figure 6. The high temperatures are associated with descending air motions, bringing down dry air from higher altitudes. The descent will then also bring down odd oxygen (O and O_3) and atomic hydrogen (H). Atomic oxygen has a large concentration gradient from the middle mesosphere to the mesopause, which makes the atomic oxygen highly variable in the presence of vertical motion. Even a

AGU Journal of Geophysical Research: Space Physics 10.1002/2016JA022371

small displacement can generate large changes in the mixing ratio [*Smith*, 2004]. Thus, the O_3 mixing ratio at 75 and 78 km will increase if O_3-rich air from the secondary O_3 maximum is brought down.

Winick et al. [2009] found elevated OH Meinel emissions related to the vertical displacements associated with SSWs. The vertical displacement of the OH airglow layer from 87 km to 78 km was observed at the time of major SSW from January 2009 [*Shepherd et al.*, 2010]. Assuming that this transport is fast enough to maintain an O density, it could lead to an enhanced production of vibrationally excited OH (OH*) at lower than normal altitudes [*Winick et al.*, 2009]. The pressure here will be sufficient to allow a third body reaction creating O_3:

$$O + O_2 + M \rightarrow O_3 + M \tag{2}$$

Then, O_3 will react with atomic oxygen forming OH by the exothermic reaction:

$$H + O_3 \rightarrow OH^* + O_2 \tag{3}$$

The variability of the ground state OH measured with the Aura MLS instrument during periods of SSWs by *Damiani et al.* [2010] further corroborates the interpretation by *Winick et al.* [2009]. The OH^* is deactivated either by photon emissions in the Meinel band (observed in the airglow) or by collisional quenching [*Brasseur and Solomon*, 2005]. The latter depends on the density and therefore becomes more important at lower altitudes. The enhanced level of atomic hydrogen might also contribute to the conversion of HO_2 into OH by the reaction [*Brasseur and Solomon*, 2005]:

$$H + HO_2 \rightarrow OH + OH \tag{4}$$

This potential chemical scheme seems consistent with our observation. As pointed out earlier, the quiet time longitudinal OH enhancement is only apparent above 73 km, supporting the potential effect of a steep gradient in the mixing ratios of odd oxygen. In January and February 2008 the polar vortex was displaced from its climatological position over the pole by an SSW [*Medvedeva et al.*, 2012]. There could therefore be a systematic longitudinal response associated with SSW also in our observations. However, considering the complex chemistry of the odd hydrogen family and its dependence on temperature, pressure, and mixing ratios, modeling studies and/or additional satellite data are needed in order to quantitatively assess the described features.

Also, the H_2O mixing ratios might impact the OH production efficiency. At altitudes above about 65 km, HO_x production depends on the ionization rate, and the atomic oxygen and H_2O densities [*Solomon et al.*, 1981]. The main process during the formation of HO_x due to EPP events is the uptake of H_2O, forming large cluster ions and subsequent recombination with electrons. However, if the H_2O mixing ratios are reduced by a few ppb (parts per billion), water cluster reactions may be cut off by dissociative recombination of the intermediates (e.g., O_4^+, $O^+_2 \cdot H_2O$) with electrons. In this case, even the natural electron concentration may be sufficient to reduce the efficiency of the HO_x production rate [*Crutzen and Solomon*, 1980]. This implies that the impact of EEP might also depend directly on the dynamical background as the EEP deposited over North America may be less efficient in producing OH due to the low H_2O mixing ratios compared to the EEP over northern Russia which has higher H_2O mixing ratios. This explanation also applies to Figure 8 for longitudes 30° – 60°E, and it is briefly mentioned in subsection 3.4.

Planetary waves are more prominent during wintertime, in particular in the NH. This is evident in Figure 7 which shows that the general longitudinal trend of OH VMR within a latitude band of 60° – 70°N closely follows that of the superposition of the planetary waves S1 + S2 especially during quiet time conditions. Quasi stationary planetary wave activity is of approximately the same amplitude and phase during both disturbed and quiet times (Figures 7c and 7d). Quasi-stationary planetary waves drive the background OH density with a peak that persists during both disturbed and quiet time conditions regardless of the strength of the energy deposition. The North America OH maximum which is present during both disturbed and quiet time conditions is a feature attributed to quasi-stationary planetary wave activity.

Any EEP-induced OH production will be an addition onto the already existing background OH. The OH enhancement due to EPP is visible for strong energy deposition during disturbed conditions. The visibility of the OH variability due to EEP depends on the background OH and the strength of the energy deposited. Hence, during disturbed conditions, there exist two peaks in the OH density: one due to the background dynamics and another due to EPP. Figure 7 does not show an exact one to one relationship between the

AGU Journal of Geophysical Research: Space Physics 10.1002/2016JA022371

energy deposition and the OH density in regions (longitudes 25°E–135°W) of high energy deposition where such a relationship may be expected. As already discussed, the OH production efficiency is affected by the H_2O density which may be variable over the latitude band under consideration.

Therefore, we believe that in our results for the winter 2008 NH, it is only the OH maximum over northern Russia that is attributed to EEP forcing, while the North America hot spot is mainly a consequence of a dynamical atmosphere. The West Antarctica hot spot in the SH is attributed to both EEP and atmospheric dynamics. This mechanism has not been considered by *Andersson et al.* [2014b]. Based on the increased level of OH they find over Greenland, which does not seem to be restricted in geomagnetic latitude, a planetary wave effect might be present in their data as well. Although our analysis supports the conclusion that even small storms can impact the mesospheric OH, a quantitative assessment needs to firmly establish the dynamically varying background. This could potentially be achieved by applying a multilinear regression analysis of OH with GPH, O_3, and H. The production of OH due to EEP could then be included with a potential dependency on H_2O.

5. Summary and Conclusions

OH enhancements due to EEP were seen poleward of CGM latitudes 55°N/S with regions of local maxima: the northern Russia and West Antarctica maxima. We find that the West Antarctica maximum might be explained by a combination of EEP and the weak magnetic field in this region. Even in the cases with geomagnetic quiet conditions, the weaker magnetic field in this region causes a steady drizzle of radiation belt electrons, hence causing an OH "pool" in this region. In addition, atmospheric dynamics might contribute to the formation of the West Antarctica maximum.

The North America OH maximum cannot be explained by the weaker magnetic field, since it is located in a region with relatively high magnetic field ratio. It rather appears that the North America OH maximum in 2008 is due to dynamical effects. Planetary waves in the polar winter induce downwelling of thermospheric air, bringing down dry air, atomic oxygen, and atomic hydrogen. The air density at mesospheric altitudes is sufficient to facilitate three-body reactions between atomic oxygen and O_2, which results in formation of O_3, which again reacts with atomic hydrogen forming OH. The same dynamical features may be related to the West Antarctica OH maximum. The northern Russia OH maximum, however, appears to be a feature related to EEP forcing alone.

Our findings suggest that even during solar minimum, there is substantial EEP driven OH production. To quantify this effect, the background atmospheric dynamics have to be taken into account, along with detailed knowledge of where and when the precipitation occurs. Background atmospheric dynamics are important in explaining the longitudinal distribution of OH.

Acknowledgments
This study was supported by the Research Council of Norway under contract 223252/F50. The authors thank the NOAA's National Geophysical Data Center (NGDS) for providing NOAA data (http://satdat.ngdc.noaa.gov/), WDC Geomagnetism, Kyoto, Japan, for *AE* and *Dst* indices (http://wdc.kugi.kyoto-u.ac.jp/wdc/Sec3.html), SPDF Goddard Space Flight Center for solar wind parameters (http://omniweb.gsfc.nasa.gov/), and NASA Goddard Earth Science Data and Information Services Center (GES DISC) for providing Aura/MLS data (http://mls.jpl.nasa.gov/).

References

Allen, C. W. (1943), Relation between magnetic storms and solar activity, *Mon. Not. R. Astron. Soc.*, *104*, 13–21.
Andersson, M. E., P. T. Verronen, S. Wang, C. J. Rodger, M. A. Clilverd, and B. R. Carson (2012), Precipitating radiation belt electrons and enhancements of mesospheric hydroxyl during 2004–2009, *J. Geophys. Res.*, *117*, D09304, doi:10.1029/2011JD017246.
Andersson, M. E., P. T. Verronen, C. J. Rodger, M. A. Clilverd, and A. Seppälä (2014a), Missing driver in the Sun-Earth connection from energetic electron precipitation impacts mesospheric ozone, *Nat. Commun.*, *5*, 5197, doi:10.1038/ncomms6197.
Andersson, M. E., P. T. Verronen, C. J. Rodger, M. A. Clilverd, and S. Wang (2014b), Longitudinal hotspots in the mesospheric OH variations due to energetic electron precipitation, *Atmos. Chem. Phys.*, *14*(2), 1095–1105, doi:10.5194/acp-14-1095-2014.
Bartels, J. (1932), Terrestrial-magnetic activity and its relations to solar phenomena, *Terr. Magn. Atmos. Electr.*, *37*(1), 1–52, doi:10.1029/TE037i001p00001.
Barth, C. A., D. N. Baker, K. D. Mankoff, and S. M. Bailey (2001), The northern auroral region as observed in nitric oxide, *Geophys. Res. Lett.*, *28*(8), 1463–1466, doi:10.1029/2000GL012649.
Bates, D. R., and M. Nicolet (1950), The photochemistry of atmospheric water vapor, *J. Geophys. Res.*, *55*(3), 301–327, doi:10.1029/JZ055i003p00301.
Billings, D. E., and W. Roberts (1964), The origin of *M*-region geomagnetic storms, *Astrophis. Norvegica*, *9*, 147.
Brasseur, G. P., and S. Solomon (2005), *Aeronomy of the Middle Atmosphere: Chemistry and Physics of the Stratosphere and Mesosphere*, Springer.
Burlaga, L., and R. Lepping (1977), The causes of recurrent geomagnetic storms, *Planet Space Sci.*, *25*, 1151–1160.
Crutzen, P. J., and S. Solomon (1980), Response of mesospheric ozone to particle precipitation, *Planet. Space Sci.*, *28*(12), 1147–1153, doi:10.1016/0032-0633(80)90073-2.
Damiani, A., M. Storini, M. Laurenza, and C. Rafanelli (2008), Solar particle effects on minor components of the polar atmosphere, *Ann. Geophys.*, *26*(2), 361–370, doi:10.5194/angeo-26-361-2008.
Damiani, A., M. Storini, M. L. Santee, and S. Wang (2010), Variability of the nighttime oh layer and mesospheric ozone at high latitudes during northern winter: Influence of meteorology, *Atmos. Chem. Phys.*, *10*(21), 10,291–10,303, doi:10.5194/acp-10-10291-2010.
Evans, D., and M. Greer (2000), *Polar Orbiting Environmental Satellite Space Environment Monitor—2: Instrument Descriptions and Archive Data Documentation*, 1.4 ed., Space Environment Center, Boulder, Colo.

Foster, J. C., P. J. Erickson, D. N. Baker, S. G. Claudepierre, C. A. Kletzing, W. Kurth, G. D. Reeves, S. A. Thaller, H. E. Spence, Y. Y. Shprits, and J. R. Wygant (2014), Prompt energization of relativistic and highly relativistic electrons during a substorm interval: Van allen probes observations, *Geophys. Res. Lett.*, *41*, 20–25, doi:10.1002/2013GL058438.

Gopalswamy, N. (2008), Solar connections of geoeffective magnetic structures, *J. Atmos. Sol. Terr. Phys.*, *70*(17), 2078–2100, doi:10.1016/j.jastp.2008.06.010.

Horne, R. B., M. M. Lam, and J. C. Green (2009), Energetic electron precipitation from the outer radiation belt during geomagnetic storms, *Geophys. Res. Lett.*, *36*, L19104, doi:10.1029/2009GL040236.

Jackman, C. H., M. T. DeLand, G. J. Labow, E. L. Fleming, D. K. Weisenstein, M. K. W. Ko, M. Sinnhuber, and J. M. Russell (2005), Neutral atmospheric influences of the solar proton events in October–November 2003, *J. Geophys. Res.*, *110*, A09S27, doi:10.1029/2004JA010888.

Jackman, C. H., C. E. Randall, V. L. Harvey, S. Wang, E. L. Fleming, M. López-Puertas, B. Funke, and P. F. Bernath (2014), Middle atmospheric changes caused by the January and March 2012 solar proton events, *Atmos. Chem. Phys.*, *14*(2), 1025–1038, doi:10.5194/acp-14-1025-2014.

Kennel, C. F., and H. E. Petschek (1966), Limit on stably trapped particle fluxes, *J. Geophys. Res.*, *71*(1), 1–28, doi:10.1029/JZ071i001p00001.

Kleinknecht, N. H., P. J. Espy, and R. E. Hibbins (2014), The climatology of zonal wave numbers 1 and 2 planetary wave structure in the MLT using a chain of Northern Hemisphere SuperDARN radars, *J. Geophys. Res. Atmos.*, *119*, 1292–1307, doi:10.1002/2013JD019850.

Livesey, N. J., et al. (2015), *Earth Observing System(EOS) Aura Microwave Limb Sounder(MLS) Version 4.2x Level 2 Data Quality and Description Document*, 91109–8099, version 4.2x-1.0 ed., Jet Propulsion Lab., Calif. Insti. of Tech., Pasadena, Calif.

Loewe, C. A., and G. W. Prölss (1997), Classification and mean behavior of magnetic storms, *J. Geophys. Res.*, *102*(A7), 14,209–14,213, doi:10.1029/96JA04020.

López-Puertas, M., B. Funke, S. Gil-López, T. von Clarmann, G. P. Stiller, M. Höpfner, S. Kellmann, H. Fischer, and C. H. Jackman (2005), Observation of NO_x enhancement and ozone depletion in the Northern and Southern Hemispheres after the October–November 2003 solar proton events, *J. Geophys. Res.*, *110*, A09S43, doi:10.1029/2005JA011050.

Medvedeva, I. V., A. I. Semenov, M. A. Chernigovskaya, and V. I. Perminov (2012), Studying manifestations of 2008–2011 sudden stratospheric warmings in east-Siberia and European Russia, *Geophysica*, *48*(1–2), 91–103.

Nesse Tyssøy, H., and J. Stadsnes (2015), Cutoff latitude variation during solar proton events: Causes and consequences, *J. Geophys. Res. Space Physics*, *120*, 553–563, doi:10.1002/2014JA020508.

Nesse Tyssøy, H. N., M. I. Sandanger, L. K. G. Ødegaard, J. Stadsnes, A. Aasnes, and A. E. Zawedde (2016), Energetic electron precipitation into the middle atmosphere—Constructing the loss cone fluxes from MEPED POES, *J. Geophys. Res. Space Physics*, *121*, doi:10.1002/2016JA022752, in press.

Neupert, W. M., and V. Pizzo (1974), Solar coronal holes as sources of recurrent geomagnetic disturbances, *J. Geophys. Res.*, *79*(25), 3701–3709, doi:10.1029/JA079i025p03701.

Pickett, H. M., W. G. Read, K. K. Lee, and Y. L. Yung (2006), Observation of night OH in the mesosphere, *Geophys. Res. Lett.*, *33*, L19808, doi:10.1029/2006GL026910.

Rees, M. H. (1989), Physics of the upper atmosphere, *Q. J. R. Meteorol. Soc.*, *117*, 433.

Rodger, C. J., A. J. Kavanagh, M. A. Clilverd, and S. R. Marple (2013), Comparison between POES energetic electron precipitation observations and riometer absorptions: Implications for determining true precipitation fluxes, *J. Geophys. Res. Space Physics*, *118*, 7810–7821, doi:10.1002/2013JA019439.

Sandanger, M. I., L. K. G. Ødegaard, H. N. Tyssøy, J. Stadsnes, F. Søraas, K. Oksavik, and K. Aarsnes (2015), In flight calibration of NOAA POES proton detectors—Derivation of the MEPED correction factors, *J. Geophys. Res. Space Physics*, *120*, 9578–9593, doi:10.1002/2015JA021388.

Schoeberl, M., A. Douglass, E. Hilsenrath, P. Bhartia, R. Beer, J. Waters, M. Gunson, L. Froidevaux, J. Gille, J. Barnett, P. Levelt, and P. DeCola (2006), Overview of the EOS Aura mission, *IEEE Trans. Geosci. Remote Sens.*, *44*(5), 1066–1074, doi:10.1109/TGRS.2005.861950.

Sheeley, N. R., Jr., and J. Harvey (1981), Coronal holes, solar wind streams, and geomagnetic disturbances during 1978 and 1979, *Sol. Phys.*, *70*(2), 237–249, doi:10.1007/BF00151331.

Shepherd, M. G., Y.-M. Cho, G. G. Shepherd, W. Ward, and J. R. Drummond (2010), Mesospheric temperature and atomic oxygen response during the January 2009 major stratospheric warming, *J. Geophys. Res.*, *115*, A07318, doi:10.1029/2009JA015172.

Shepherd, T. G. (2000), The middle atmosphere, *J. Atmos. Sol. Terr. Phys.*, *62*(17–18), 1587–1601, doi:10.1016/S1364-6826(00)00114-0.

Sinnhuber, M., H. Nieder, and N. Wieters (2012), Energetic particle precipitation and the chemistry of the mesosphere/lower thermosphere, *Surv. Geophys.*, *33*, 1281–1334.

Smith, A. K. (2004), Physics and chemistry of the mesopause region, *J. Atmos. Sol. Terr. Phys.*, *66*(10), 839–857, doi:10.1016/j.jastp.2004.01.032.

Solomon, S., D. Rusch, J. Gérard, G. Reid, and P. Crutzen (1981), The effect of particle precipitation events on the neutral and ion chemistry of the middle atmosphere: II. Odd hydrogen, *Planet. Space Sci.*, *29*(8), 885–893, doi:10.1016/0032-0633(81)90078-7.

Swider, W., and T. Keneshea (1973), Decrease of ozone and atomic oxygen in the lower mesosphere during a PCA event, *Planet. Space Sci.*, *21*(11), 1969–1973, doi:10.1016/0032-0633(73)90126-8.

Tsurutani, B., et al. (2006), Corotating solar wind streams and recurrent geomagnetic activity: A review, *J. Geophys. Res.*, *111*, A07S01, doi:10.1029/2005JA011273.

Turner, D. L., et al. (2014), Competing source and loss mechanisms due to wave-particle interactions in Earth's outer radiation belt during the 30 September to 3 October 2012 geomagnetic storm, *J. Geophys. Res. Space Physics*, *119*, 1960–1979, doi:10.1002/2014JA019770.

Turunen, E., P. T. Verronen, A. Seppälä, C. J. Rodger, M. A. Clilverd, J. Tamminen, C.-F. Enell, and T. Ulich (2009), Impact of different energies of precipitating particles on NO_x generation in the middle and upper atmosphere during geomagnetic storms, *J. Atmos. Sol. Terr. Phys.*, *71*(10–11), 1176–1189, doi:10.1016/j.jastp.2008.07.005.

Verronen, P. T., and R. Lehmann (2013), Analysis and parameterisation of ionic reactions affecting middle atmospheric HO_x and NO_y during solar proton events, *Ann. Geophys.*, *31*, 909–956, doi:10.5194/angeo-31-909-2013.

Verronen, P. T., C. J. Rodger, M. A. Clilverd, and S. Wang (2011), First evidence of mesospheric hydroxyl response to electron precipitation from the radiation belts, *J. Geophys. Res.*, *116*, D07307, doi:10.1029/2010JD014965.

Waters, J. W., et al. (2006), The Earth observing system microwave limb sounder (EOS MLS) on the Aura satellite., *IEEE Trans. Geosci. Remote Sens.*, *44*(5), 1075–1092, doi:10.1109/TGRS.2006.873771.

Weeks, L. H., R. S. Cuikay, and J. R. Corbin (1972), Ozone measurements in the mesosphere during the solar proton event of 2 November 1969, *J. Atmos. Sci.*, *29*(6), 1138–1142.

Journal of Geophysical Research: Space Physics 10.1002/2016JA022371

Winick, J. R., P. P. Wintersteiner, R. H. Picard, D. Esplin, M. G. Mlynczak, J. M. Russell, and L. L. Gordley (2009), OH layer characteristics during unusual boreal winters of 2004 and 2006, *J. Geophys. Res., 114*, A02303, doi:10.1029/2008JA013688.

Yando, K., R. M. Millan, J. C. Green, and D. S. Evans (2011), A Monte Carlo simulation of the NOAA POES medium energy proton and electron detector instrument, *J. Geophys. Res., 116*, A10231, doi:10.1029/2011JA016671.

II

Paper II

The Impact of Energetic Particle Precipitation on Mesospheric OH – Variability of the Sources and the Background Atmosphere

A. E. Zawedde, H. Nesse-Tyssøy, J. Stadsnes and M. I. Sandanger

Journal of Geophysical Research: Space Physics, Vol. 123, doi:10.1029/2017JA025038, (2018)

AGU100 ADVANCING EARTH AND SPACE SCIENCE

JGR

Journal of Geophysical Research: Space Physics

RESEARCH ARTICLE
10.1029/2017JA025038

Key Points:
- Linear regression can account for the background variability and Energetic Particle Precipitation (EPP) impact on mesospheric hydroxyl (OH)
- The OH variability is mainly driven by changes in temperature and H_2O above 70-km altitude and by EPP below 70-km altitude
- Protons dominate over electrons below 70-km altitude, but the electron impact is comparable to that of protons above 70-km altitude

Correspondence to:
A. E. Zawedde,
Annet.E.Zawedde@uib.no

Citation:
Zawedde, A. E., Nesse Tyssøy, H., Stadsnes, J., & Sandanger, M. I. (2018). The impact of energetic particle precipitation on mesospheric OH – Variability of the sources and the background atmosphere. *Journal of Geophysical Research: Space Physics, 123*. https://doi.org/10.1029/2017JA025038

Received 22 NOV 2017
Accepted 4 JUN 2018
Accepted article online 12 JUN 2018

The Impact of Energetic Particle Precipitation on Mesospheric OH – Variability of the Sources and the Background Atmosphere

Annet Eva Zawedde[1], Hilde Nesse Tyssøy[1], Johan Stadsnes[1], and Marit Irene Sandanger[1]

[1]Birkeland Centre for Space Science, Department of Physics and Technology, University of Bergen, Bergen, Norway

Abstract Using a new analysis technique, we estimate the precipitating particle fluxes measured by the Medium Energy Proton and Electron Detector on the National Oceanic and Atmospheric Administration Polar Orbiting Environmental Satellites. These fluxes are used to quantify the direct impact of energetic particle precipitation (EPP) on mesospheric hydroxyl (OH) measured from the Aura satellite during 2005–2009 in the Northern Hemisphere, covering the declining and minimum phase of solar cycle 23. Using multiple linear regression of nighttime OH volume mixing ratio with temperature, geopotential height, water vapor (H_2O) volume mixing ratio, Lyman-alpha (Ly-α) radiation, and particle energy deposition, we account for the background variability and hence the EPP impact independent of season and other short-term variability. We investigate the relative importance of solar proton events, energetic electron precipitation and the background to OH variability. The background dominates over EPP above 70-km altitude. Below 70 km, EPP dominates. The maximum EPP contribution is 44% and 34% in the geographic and corrected geomagnetic (CGM) settings respectively at 67 km. Protons dominate over electrons at mesospheric altitudes with maximum contributions of 43% and 32% at 67 km in the geographic and CGM settings, respectively. In a CGM setting, the electrons contribution is comparable to that of protons above 70 km, with a maximum contribution of 11% at 75 km. Since the period investigated is during relatively low solar activity, these results represent a lower estimate of the general EPP contribution to OH variability.

1. Introduction

In the mesosphere, background odd hydrogen (HO_x: H, OH, HO_2) is produced by photodissociation of water vapor (H_2O) by the reaction (Brasseur & Solomon, 2005; Solomon et al., 1981; Swider & Keneshea, 1973):

$$H_2O + h\nu \rightarrow H + OH \quad (1)$$

The photolysis of H_2O is facilitated by the Lyman-alpha (Ly-α) line (121.568 nm) for altitudes above 68 km and by Schumann-Runge band wavelengths (175–200 nm) at altitudes 60–68 km (Frederick & Hudson, 1980). The background OH production is also modified by the seasonal pole to pole circulation pattern as it affects both H_2O and temperature. Hence, the OH seasonal variability can be largely understood by considering the variations in H_2O and solar intensity (see, e.g., Canty & Minschwaner, 2002; Shapiro et al., 2012). The amount of solar radiation at a specific altitude and latitude varies with the solar zenith angle (SZA). As such the diurnal variations in OH can be described by an exponential function of the secant of the SZA (Minschwaner et al., 2011).

The wintertime OH background production is also affected by processes involving planetary wave activity, like sudden stratospheric warmings (SSWs) through an associated descent of the OH layer (see, e.g., Damiani et al., 2010; Winick et al., 2009; Zawedde et al., 2016). For example, normally OH would have a positive correlation with H_2O, and a corresponding negative correlation with temperature. However, during SSWs OH seems to have a negative correlation with H_2O and a positive correlation with temperature as elevated temperature is associated with adiabatic heating due to downwelling bringing dry air downward (see, e.g., Damiani et al., 2010). Therefore, simple correlation alone is not enough to ascertain the relation between OH and the related atmospheric constituents.

Journal of Geophysical Research: Space Physics 10.1029/2017JA025038

Energetic particle precipitation (EPP) is known to produce HO_x during solar proton events (SPEs) and energetic electron precipitation (EEP). SPEs are associated with strong geomagnetic activity driven by coronal mass ejections (CMEs) which predominantly occur during solar maximum (see, e.g., Webb, 1995). CMEs propel fast shock waves ahead of them which accelerate solar protons directly from the solar wind to very high energies capable of precipitating into the atmosphere to ~40-km altitude over the polar cap on open field lines. Depending on the particle energy, the solar protons can also penetrate closed field lines and impact the atmosphere at latitudes normally shielded from the direct solar wind impact. Monoenergetic beams of protons of energy 10-20 MeV will deposit most of their energy within the mesosphere (60-80 km) (Turunen et al., 2009). On the other hand, energetic electrons are first stored and accelerated in the Earth's radiation belts. During geomagnetic storms, electrons are accelerated to high and possibly relativistic energies before precipitating into the atmosphere (see, e.g., Li & Temerin, 2001; Reeves et al., 2013; Turner et al., 2012). Clear effects of electron precipitation on OH are seen within the latitude range of the Earth's radiation belts at magnetic latitudes 55–72° (see, e.g., Andersson, Verronen, Rodger, Clilverd, & Wang 2014). This is a small band within the atmosphere as compared to the polar cap where the protons deposit their energy. Medium energy and relativistic electrons (>100 keV) precipitate below 80 km (Turunen et al., 2009).

On interpreting the results from Weeks et al. (1972), Swider and Keneshea (1973) state that during ionization events, for every O_2^+ ion converted into an oxonium (water cluster) ion, one OH molecule is generated. An additional contribution will arise from dissociative recombination of the water cluster ions with electrons, yielding either H or OH as one of the reaction products. Therefore, the total OH + H formation rate resulting from the water cluster ion formation can be seen as $2HO_x$ (Solomon et al., 1981). Also, the behavior of the perhydroxyl radical (HO_2) is generally similar to OH (see Crutzen & Solomon, 1980). This implies that we can focus on one of the constituents in the HO_x family (i.e., OH) to study the effects of EPP on the atmospheric system.

The Aura Microwave Limb Sounder (MLS) database provides observations of both OH and HO_2, although the MLS HO_2 data are not recommended for scientific use for altitudes above 0.046 hPa (~70 km) (Livesey et al., 2015. The availability of Aura MLS OH observations sparked the genesis of several correlation studies between OH and particle fluxes. These studies have attempted to estimate how much of the mesospheric OH variability can be attributed to both SPEs and EEP. Since SPEs are strong, their effects on the atmospheric constituents are easily detected and have been extensively studied (Crutzen & Solomon, 1980; Sinnhuber et al., 2012; Solomon et al., 1981, 1983; Verronen et al., 2006, 2007, Weeks et al., 1972). Based on March 2005 and April 2006 as case studies, Verronen et al. (2011) found that 56–87% of the OH variation at 71- to 78-km altitudes can be explained by EEP. The time period of 1 month considered is rather short and will as such not reflect the general situation. Considering the period 2004–2009, Andersson et al. (2012) found a strong correlation of $r \geq 0.6$ (or $r^2 \geq 36\%$) between OH and 100- to 300-keV precipitating electrons at 70- to 78-km altitude. Although simple correlation analyses show high correlation between OH and precipitating electrons, this correlation will also be affected by OH variability from other sources, for example, photolysis of H_2O or planetary wave activity (Zawedde et al., 2016). The magnitude of this correlation may significantly change if the various probable sources of OH variability are taken into account (i.e., when other variables are held constant).

The mesospheric OH response to energetic electron energy deposition has been modeled on different time scales, for different types of events and for different geographic locations in the atmosphere (see, e.g., Aikin & Smith, 1999; Turunen et al., 2016; Verronen et al., 2013, 2015). Daae et al. (2012), Verronen et al. (2013), and Andersson, Verronen, Rodger, Clilverd, and Seppälä (2014) have discussed whether the frequent EEP events could have an impact on mesospheric OH comparable to the impact due to the infrequent SPEs over long time scales. The recurrent geomagnetic activity associated with EEP is known to vary strongly throughout a given solar cycle and will produce a continuous and significantly fluctuating source of variability in mesospheric constituents. Therefore, they suspect that on solar cycle time scales, the EEP forcing could be more important to mesospheric OH and ozone (O_3) than SPEs. Andersson, Verronen, Rodger, Clilverd, and Seppälä (2014) show that on solar cycle time scales, the direct HO_x-driven effect due to EEP causes significant variability in mesospheric O_3. They, therefore, suspect that EEP could be an important contributor to Sun-climate connection on solar cycle time scales.

In a recent study, Zawedde et al. (2016) show that during solar minimum, EEP-driven OH production is comparable with OH production due to the background atmospheric dynamics. Since EEP events are generally weak,

Journal of Geophysical Research: Space Physics 10.1029/2017JA025038

their contribution to OH variability may be masked by the seasonal trend in H_2O and solar Lyman-α radiation and shorter term variations such as SSWs. This may also depend on the altitude and the geographical location. Therefore, to quantify the EPP effect, the background atmospheric dynamics, along with detailed knowledge of where and when the precipitation occurs, needs to be taken into account. This, however, requires a method that can simultaneously take into consideration all the available sources of OH variability. This method should be able to consider the day-to-day variability in OH due to H_2O and Ly-α radiation as well as other atmospheric parameters, for example, temperature that capture the daily and seasonal variability. In addition, the contribution from energetic particles should also be accounted for. One way to achieve this goal is by using multiple linear regression to assess the contribution from a parameter when all the other parameters are held constant.

By applying a new analysis technique on measurements from the Medium Energy Proton and Electron Detector (MEPED) on the National Oceanic and Atmospheric Administration (NOAA) Polar Orbiting Environmental Satellites (POES), an estimate of the flux of precipitating electrons is obtained by measurements from both the 0° and 90° telescopes (Nesse Tyssøy et al., 2016; Ødegaard et al., 2017). An estimate of the flux of precipitating protons is obtained by combining measurements from the MEPED 0° telescope and the omnidirectional detectors (0–60°) (Nesse Tyssøy et al., 2013; Nesse Tyssøy & Stadsnes, 2015). The known challenges with NOAA POES data (see, e.g., Evans & Greer, 2000; Ødegaard et al., 2017; Sandanger et al., 2015; Yando et al., 2011) are overcome, giving a realistic estimate of the precipitating fluxes throughout the mesosphere.

It is from this perspective that we draw the objectives for this study. We use multiple linear regression to model the natural atmospheric background variability of OH in order to estimate and understand the impact of EPP on OH in general in both a geographic and magnetic coordinate system. We further investigate the relative importance of SPEs and EEP during the declining phase of solar cycle 23 (2005–2009). We analyze OH, temperature, geopotential height (GPH), and H_2O observations from the MLS instrument on board the Aura satellite and particle data from the NOAA POES satellites for the years 2005–2009. Composite solar Ly-α radiation from the Thermosphere Ionosphere Mesosphere Energetics and Dynamics (TIMED) and the Solar Radiation and Climate Experiment (SORCE) spacecrafts is also included in the analysis. In the following study, we investigate and discuss the relative contribution to OH variability from the background parameters and the solar energetic particles during the years 2005–2009.

2. Data

2.1. NOAA POES MEPED Observations

The NOAA/POES satellites provide an extensive data set of particle fluxes as measured by the MEPED 0° and 90° telescopes which are part of the Space Environment Monitor-2 instruments on board these satellites. We use particle data from NOAA-16 for year 2005 and NOAA-18 particle data for the years 2006 to 2009. The NOAA-16 and NOAA-18 particle measurements are closest in time and space to the atmospheric observations by the Aura MLS satellite.

The two MEPED electron solid-state detectors monitor the intensity of electrons in three nominal energy bands: >30, >100, and >300 keV (Evans & Greer, 2000), whose known data challenges have been catered for using the new analysis toolbox described by Nesse Tyssøy et al. (2016). In this toolbox, the proton fluxes are corrected for degradation due to radiation damage by applying correction factors derived by Sandanger et al. (2015) and Ødegaard et al. (2016). The corrected proton data are then used to correct the electron data from proton contamination. Since the geometric factor for the electron detectors varies with energy, Ødegaard et al. (2017) calculated new optimized geometric factors and the associated new energy thresholds for the electron channels are >43, >114, >292, and >757 keV. The fourth electron channel is derived from relativistic electron contamination of the p6 channel of the proton telescope detectors as described by Nesse Tyssøy et al. (2016).

If there is strong pitch angle diffusion and an isotropic distribution of the particles, the 0° and 90° telescopes give a realistic estimate of the precipitating particle fluxes. Otherwise the 0° and 90° telescopes will either underestimate or overestimate the flux of the precipitating particles, respectively, with decreasing fluxes toward the center of the loss cone (Nesse Tyssøy et al., 2016; Rodger et al., 2010, 2013). Therefore, a complete bounce loss cone flux is constructed for each of the new electron energy channels (Ødegaard et al., 2017), using measurements from both the 0° and 90° telescopes in conjunction with electron pitch angle distribution theory as described by Nesse Tyssøy et al. (2016). We convert the integral fluxes into a differential

Journal of Geophysical Research: Space Physics 10.1029/2017JA025038

electron spectrum covering energies from 43 to 757 keV, which in turn is used to calculate the energy deposition as a function of altitude. In these calculations, we use the cosine-dependent Isotropic over the Downward Hemisphere model of Rees (1989). This is a range-energy analysis based on a standard reference atmosphere (COmmittee on SPAce Research, International Reference Atmosphere 1986).

To monitor the strong solar proton precipitation, we combine the measurements from MEPED proton telescope (0°) with measurements from the MEPED omnidirectional detector system (0–60°) as described in Nesse Tyssøy et al. (2013) and Nesse Tyssøy and Stadsnes (2015). The proton telescope measures the proton fluxes in six energy bands over the range >30 to >6,900 keV, while the omnidirectional telescope measures the proton fluxes with energies >16 to >70 MeV. At high latitudes, both the 0° detector and the omnidetector measure protons in the loss cone. Under the assumption of isotropic fluxes, which is expected during SPEs, we combine the measurements from the two detector systems to obtain integral spectra by fitting monotonic piecewise cubic Hermite interpolating polynomials (Fritsch & Carlson, 1980) to the measurements. The energy deposition height profile for protons is calculated based on range energy of protons in air given by Bethe and Ashkin (1953). The atmospheric densities are retrieved from the MSIS-E-90 model (Hedin, 1991). We include the SPEs (>1,000 particle flux units) from 2005 to 2009 presented in Nesse Tyssøy and Stadsnes (2015).

2.2. Aura MLS Observations

The Aura satellite is one of the three Earth Observing System/National Aeronautics and Space Administration core platforms (Schoeberl et al., 2006). Launched in 2004, the Aura satellite focuses on observing atmospheric composition and it is dedicated to understanding the changing chemistry of our atmosphere. It is in a near polar sun-synchronous orbit at 705-km altitude, giving daily global coverage with about 14 orbits per day. The MLS is one of the four instruments on board Aura. Aura MLS measures naturally occurring microwave thermal emissions from the limb of Earth's atmosphere to remotely sense vertical profiles of atmospheric constituents, every 25 s (Schoeberl et al., 2006; Waters et al., 2006).

In this study, we use Aura/MLS Level 2 files version 4.2x data for the years 2005 to 2009. We use Northern Hemisphere (NH) nighttime data which are screened following the instructions in the data quality and description document (Livesey et al., 2015). The OH sensitivity to changes in temperature and H_2O is modest during nighttime compared to daytime, indicating a better possibility of identifying EEP effects on OH at night (Andersson et al., 2012). For the NH, considering the SZA >100° selection, approximately 97% of the MLS observations occur at solar local times 2–5 in the geographic latitude band of 45–80°N. When a corrected geomagnetic (CGM) latitude band of 55–70°N is considered, the SZA >100° selection gives solar local times 2–4. The temporal, vertical, and horizontal resolution of OH are 25 s, 2.5 km, and 165 km, respectively, within mesospheric altitudes (60–80 km). The vertical and horizontal resolutions of temperature, GPH, and H_2O are variable and coarser within the mesosphere (see Livesey et al., 2015). The pressure levels are converted into geometric height.

The local oscillator signal driving the Aura MLS 2.5-THz radiometers (from which OH measurements are derived) is provided by a methanol laser which in December 2009 began to show signs of aging and was temporarily deactivated (Livesey et al., 2015). In order to conserve the remaining lifetime of the THz instrument for valuable measurements when the Sun becomes more active, OH measurements were suspended from December 2009 to August 2011.

2.3. Solar Lyman-Alpha

The time series for the daily composite solar Ly-α radiation are retrieved from the Laboratory for Atmospheric and Space Physics Interactive Solar IRradiance Datacenter. For the years 2005–2009, the composite Ly-α times series consist of irradiance measurements from the Solar Extreme ultraviolet Experiment and the Solar Stellar Irradiance Composition Experiment instruments on board the National Aeronautics and Space Adminsitration's TIMED and SORCE spacecrafts respectively.

Since the amount of solar radiation at a certain altitude varies as a function of the SZA, applying the exponential function of the secant of the SZA to the daily composite solar Ly-α radiation yields a function of the form (see Andersson et al., 2012):

$$I_{\alpha}^{SZA} = I_{\alpha}\exp[-\beta\sec(SZA_{min})] \quad (2)$$

Journal of Geophysical Research: Space Physics 10.1029/2017JA025038

where β is a an altitude dependent fit parameter related to the optical depths of ultraviolet absorption by O_3 and molecular oxygen (O_2), SZA_{min} is the daily minimum SZA for which the intensity of solar ultraviolet radiation is maximum and I_α is the daily composite solar Ly-α radiation (approximately the Ly-α radiation at the top of the atmosphere). Assuming β to be unity gives the general daily variation in solar Ly-α radiation with SZA.

3. Methods and Results

3.1. Variation of OH

Figure 1 (top to bottom) shows the daily mean temperature, H_2O, GPH, I_α^{SZA}, electron energy deposition, proton energy deposition (for SPEs periods), and OH for years 2005 to 2009 averaged over a geographic (GEO) latitude band of 45–80° (left) and a CGM latitude band of 55–70° (right) in the NH. All averages are for 78-km altitude during nighttime except I_α^{SZA} which shows variation when β is unity during daytime. This is the case because we are only interested in the change in I_α^{SZA} and not the optical properties (optical depth) of the atmosphere which vary with altitude.

The temperature, H_2O, GPH, and I_α^{SZA} (top two panels) exhibit a strong seasonal periodic dependence for both geographic (left) and CGM (right) latitudinal averages. The seasonal behavior is such that high values of GPH, H_2O, and I_α^{SZA} correspond to low values of the temperature at 78-km altitude during summer, whereas low values of GPH, H_2O, and I_α^{SZA} are associated with high temperatures during winter. The electron energy deposition (third panels) shows a continuous signature, whereas protons show four distinct peaks for both geographic and CGM averages. Averaging over the geographic latitude band gives a strong signal of the proton energy deposition while weakening the signature from the electrons as the electrons are only deposited in a relatively small band within the geographic latitude band. Averaging over the CGM latitude range of the radiation belts covers most of the electron energy deposition resulting in a strong signature of electrons while that of the protons is less prominent as the SPEs protons will be cut off depending on their rigidity (Nesse Tyssøy & Stadsnes, 2015). As such, it is important to investigate both kinds of averages since the electrons and protons exert a somewhat different forcing in the two different latitude band averages.

The OH daily means also exhibit a seasonal variation but not as smooth and periodic as the temperature, H_2O, GPH, and I_α^{SZA}. There are distinct strong peaks in the OH daily means corresponding to the peaks in the proton energy deposition for OH averaged over the geographical latitude band. Peaks in OH corresponding to the electron energy deposition are, however, not that evident. When OH is averaged over the latitude range of the radiation belts (CGM 55–70°N), the data exhibit stronger short-term variability; hence, it is quite difficult to isolate the OH peaks that are attributed to protons as well as those due to electrons. Apart from the narrow distinct peaks associated with SPEs, OH also exhibits other relatively broader peaks during some of the winters (2006, 2007, and 2009) associated with SSWs, shown by the vertical dashed lines. For a comprehensive list of SSWs during the years 2005 to 2009 see, for example, Damiani et al. (2010). The narrow peaks associated with SPEs weaken for averages over the CGM latitude band, but the broad winter SSWs OH peaks seem to persist in both the geographic and CGM latitudinal averages.

3.2. Regression Analysis

The data are sorted by geographic coordinates; 45–80°N and by CGM coordinates; 55–70°N. Then daily averages are calculated for the respective altitudes. Triangulation-based linear interpolation is used to obtain temperature, GPH, and H_2O data at altitudes at which Aura MLS does not retrieve observations. To allow for normality of the regression models residuals, OH is transformed by taking its logarithm for all regression analyses. A constant is added to OH to ensure that the logarithms are all real.

To reduce structural collinearity, the predictors are centered by subtracting the mean from the predictor variables. Structural collinearity results from inclusion of higher-order terms like interactions and squares into the regression model. Hence, centered variables are used in the following multiple regression analysis and for the simple regression for consistency.

The adjusted R^2 (also known as the adjusted coefficient of determination) gives a measure of how much of the variation in the dependent (response) variable is explained by the regression model. The adjusted R^2 is used throughout to determine how good the models fit the observed OH at a particular altitude.

Figure 2 shows the regression workflow hereafter followed through out the methods and results. The magenta, brown, and orange arrows represent the pathways for simple linear regression, multiple linear

Journal of Geophysical Research: Space Physics 10.1029/2017JA025038

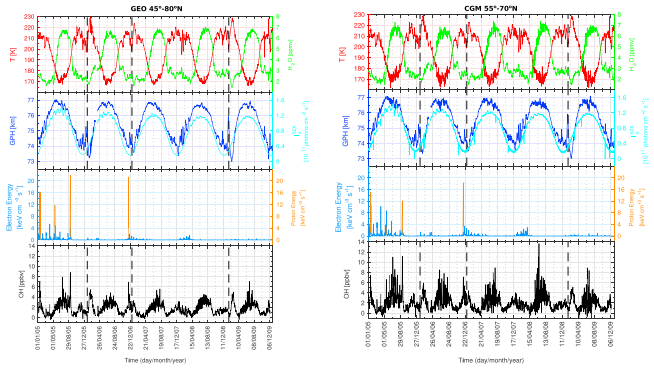

Figure 1. General view of the variation of the nighttime daily mean temperature, geopotential height (GPH), H_2O, I_α^{SZA}, energy deposition (electrons and protons), and hydroxyl (OH) during the years 2005 to 2009 averaged over a geographic latitude band of 45–80°N (left) and a corrected geomagnetic latitude band of 55–70°N (right). The temperature, GPH, H_2O, energy deposition (electrons and protons), and OH are daily averages at 78 km. Whereas I_α^{SZA} is for $\beta = 1$ (neglecting the altitude dependence in β). The vertical dashed lines denote some of the sudden stratospheric warmings for illustration.

regression for the background, and multiple linear regression of the background plus the particle energy deposition, respectively.

3.2.1. Simple Linear Regression

The top panels in Figure 3 show the Pearson's correlation performed on the OH and the proposed predictor variables: temperature, GPH, H_2O, and I_α^{SZA} separately for the years 2005 to 2009. The correlation is deemed significant for p values < 0.05 (95% confidence interval). There exists a significant correlation between OH and the proposed predictors; temperature, GPH, H_2O, and I_α^{SZA} for all altitudes except at 62 and 67 km for GPH and I_α^{SZA}. The single strongest correlation is found at 75 km followed by 78 km between OH and temperature, and OH and H_2O respectively in both the geographic and CGM framework.

Given the predictors variables; temperature, GPH, H_2O, and I_α^{SZA}, a simple linear regression model for the OH time series is given by:

$$OH(t) = C_0 + C_1 X(t) + \epsilon(t), \qquad X = T, GPH, H_2O, I_\alpha^{SZA} \tag{3}$$

where ϵ represents the random errors (or residuals) which must be normally distributed independent random variables with mean zero and constant variance (see Rawlings et al., 1998). The regression coefficients, C_0 and C_1, are listed in Table 1. For both kinds of coordinate averages, simple linear regression captures the general seasonal trend in the OH variability but fails to capture the variations due to SSWs. In order to estimate the EPP impact over the declining phase of solar cycle 23, the regression analysis must capture both long-term seasonal variation as well as short-term variability. Nevertheless, simple linear regression with H_2O gives a consistently high adjusted R^2 (>10%) for altitudes 64, 67, 73, 75, and 78 km in a geographic setting (Table 1). In a CGM setting, both temperature and H_2O give high adjusted R^2 for altitudes 73–78 km. The level of variation in OH explained by the simple linear regression models is relatively low for altitudes below 73 km.

To account for nonlinear effects in the predictors: temperature, GPH, H_2O, and I_α^{SZA}, second-order polynomial (or quadratic) regression is opted for. But in order to adhere to the *hierarchy principle*, all lower order terms are included in the model whether or not the coefficients for these effects are significant. Therefore, the second-order polynomial regression model of the response variable OH and with any of the predictor variables X is given by:

$$OH(t) = C_0 + C_{11} X(t) + C_{12} X^2(t) + \epsilon(t), \qquad X = T, GPH, H_2O, I_\alpha^{SZA} \tag{4}$$

Journal of Geophysical Research: Space Physics 10.1029/2017JA025038

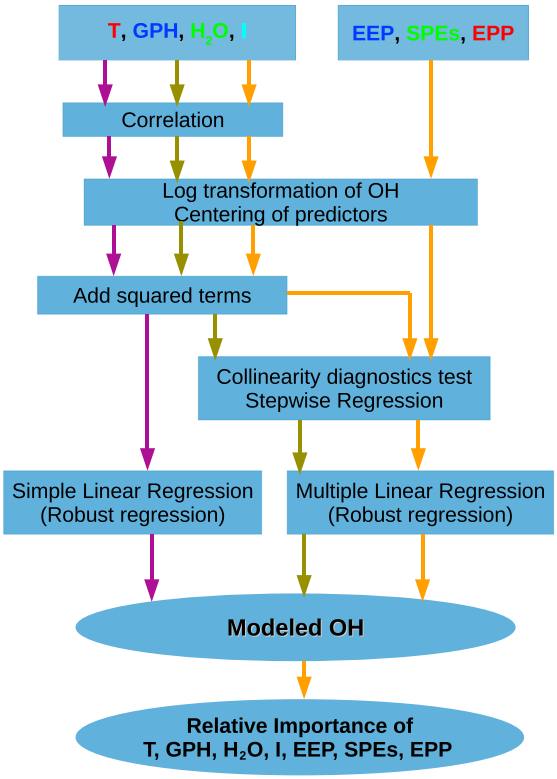

Figure 2. A flow diagram showing a summary of the workflow of methods used for linear regression analyses in this paper. The magenta arrows represent the pathway for simple linear regression. The Brown arrows represent the pathways for multiple linear regression for background hydroxyl (OH) variability. The Orange arrows represent the flowlines for multiple linear regression of the background OH variability plus the particle energy deposition. The variables OH, T, GPH, H_2O and I are: hydroxyl, temperature, geopotential height, water vapor and solar Lyman alpha radiation, respectively. The acronyms EPP, SPEs and EEP represent: energetic particle precipitation, solar proton events and energetic electron precipitation, respectively.

where C_0, C_{11}, and C_{12} are the regression coefficients also listed in Table 2 and ϵ represents the error term to account for the discrepancy between the predicted and observed response variable. Simple quadratic regression not only accounts for the nonlinear effects in the predictors but also improves the amount of variation explained by the regression models especially for altitudes above 70 km (see Figure 4a).

Temperature seems to explain more variability in OH than any of the other predictors at altitudes 75 and 78 km (see Figure 4a). The time plot of the observed and modeled OH for 2005 to 2009 from quadratic regression with temperature as the only predictor variable is shown in Figure 5. The adjusted R^2 is higher for models

Journal of Geophysical Research: Space Physics 10.1029/2017JA025038

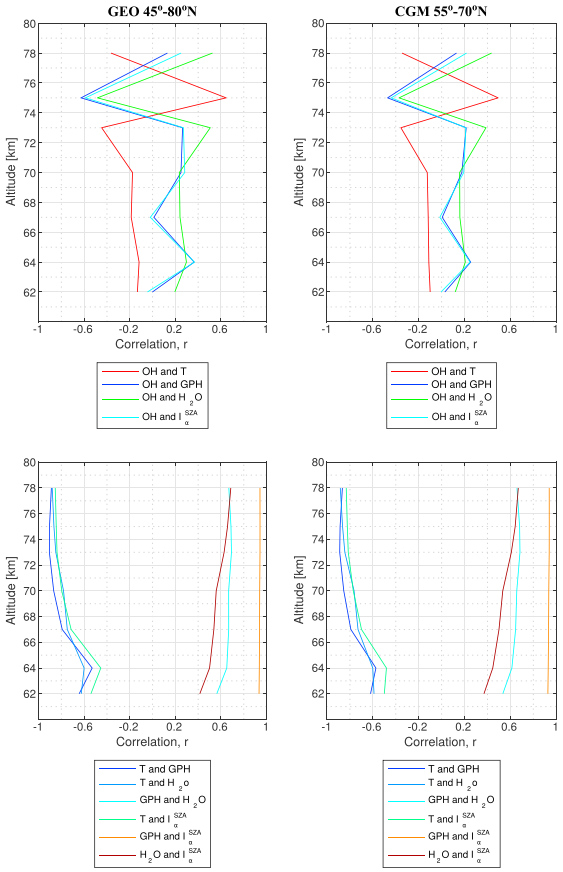

Figure 3. Top: Correlation between daily mean OH and each of the proposed predictor variables: Temperature, GPH, H_2O and I_α^{SZA}. Bottom: Correlation among pairs of predictor variables. The variables OH, GPH, H_2O and I_α^{SZA} are: hydroxyl, geopotential height, water vapor and solar Lyman alpha radiation as a function of the solar zenith angle, respectively. The acronyms GEO and CGM represent: geographic and corrected geomagnetic respectively.

for which the data are averaged over a geographical latitude band than for a CGM latitude band at the same altitude. Note that altitude 75 km displays a rather peculiar behavior in OH variability. For averages over the geographical latitude band, summers exhibit low OH volume mixing ratio (VMR) while winters exhibit high OH VMR at 75-km altitude, which behavior is reflected by the regression models. However, for averages

Journal of Geophysical Research: Space Physics 10.1029/2017JA025038

Table 1
Simple Linear Regression: Linear Regression Coefficients for Years 2005 to 2009 for a Geographic Latitude Band of 45–80° N (Left) and a CGM Latitude Band of 55–70° N (Right)

	Alt	GEO			CGM		
Var	(km)	C_0	C_1 (10^{-4})	R^2	C_0	C_1 (10^{-4})	R^2
	78	0.74	−22.88	**0.24**	0.76	−19.60	**0.12**
	75	0.56	21.93	**0.55**	0.56	26.48	**0.49**
	73	0.65	−8.94	**0.31**	0.66	−8.42	**0.18**
T	**70**	0.60	−1.67	**0.04**	0.60	−0.45	**0.03**
	67	0.61	−1.93	**0.09**	0.61	−1.35	**0.03**
	64	0.60	−0.77	**0.05**	0.60	−0.47	**0.08**
	62	0.60	−0.33	**0.02**	0.60	−0.27	**0.02**
	78	0.75	135.58	**0.03**	0.76	68.29	**0.01**
	75	0.56	−273.19	**0.46**	0.56	−317.14	**0.38**
	73	0.65	58.54	**0.11**	0.65	45.35	**0.06**
GPH	**70**	0.60	23.36	**0.11**	0.60	16.88	**0.05**
	67	0.61	1.21	**0.02**	0.61	−2.67	**0.02**
	64	0.60	11.01	**0.27**	0.60	10.49	**0.16**
	62	0.60	−0.52	**0.01**	0.60	−1.51	**0.03**
	78	0.74	300.80	**0.43**	0.76	255.21	**0.20**
	75	0.56	−172.07	**0.31**	0.57	−194.20	**0.24**
	73	0.65	93.62	**0.36**	0.66	84.59	**0.20**
H_2O	**70**	0.60	20.78	**0.08**	0.60	15.57	**0.05**
	67	0.61	14.50	**0.11**	0.61	11.57	**0.04**
	64	0.60	10.94	**0.14**	0.60	8.53	**0.10**
	62	0.60	4.55	**0.04**	0.60	3.99	**0.02**
	78	0.75	578.22	**0.07**	0.76	416.69	**0.03**
	75	0.56	−814.53	**0.40**	0.56	−954.29	**0.32**
	73	0.65	206.74	**0.11**	0.65	155.51	**0.05**
I_α^{SZA}	**70**	0.60	103.05	**0.14**	0.60	81.33	**0.07**
	67	0.61	−3.96	**0.03**	0.61	−22.47	**0.04**
	64	0.60	46.58	**0.26**	0.60	43.64	**0.15**
	62	0.60	−5.78	**0.03**	0.60	−12.16	**0.06**

Note. The response variable is $\log_{10}(\mathrm{OH} + \text{constant})$. The constant (4) is added to ensure only positive values of OH and hence only real logarithms of OH. The predictor variables are temperature, GPH, H_2O, and I_α^{SZA}. The coefficient of determination is given by the adjusted R^2. The variables OH, GPH, H_2O and I_α^{SZA} are: hydroxyl, geopotential height, water vapor and solar Lyman alpha radiation as a function of the solar zenith angle, respectively. The acronyms GEO and CGM represent: geographic and corrected geomagnetic, respectively.

over the CGM latitude band, summers exhibit some rather high variability in OH that are not reflected by the regression models. A summary of the simple linear regression workflow is shown in Figure 2 by the magenta arrows.

3.2.2. Multiple Linear Regression

Correlation between a predictor and OH may not necessarily imply causality. We wish to combine the regression analysis with all the different parameters to allow for detection of the contribution from each predictor variable when other variables are held constant. Therefore, the OH background multiple second-order polynomial regression equation for a pure quadratic model (without interaction terms) with predictors temperature, GPH, H_2O and I_α^{SZA} is of the form:

$$\mathrm{OH}(t) = C_0 + C_{j1}T(t) + C_{j2}T^2(t) + C_{k1}G(t) + C_{k2}G^2(t) + C_{l1}H(t) + C_{l2}H^2(t) + C_{m1}I(t) + C_{m2}I^2(t) + \epsilon(t) \quad (5)$$

Journal of Geophysical Research: Space Physics 10.1029/2017JA025038

Table 2
Simple Linear Regression: Second-Order Polynomial (Quadratic) Regression Model Coefficients for Years 2005 to 2009 for a Geographic Latitude Band of 45–80°N (Left) and a CGM Latitude Band of 55–70°N (Right)

	Alt	GEO				CGM			
Var	(km)	C_0	C_{11} (10^{-4})	C_{12} (10^{-4})	R^2	C_0	C_{11} (10^{-4})	C_{12} (10^{-4})	R^2
	78	0.68	−8.33	2.28	**0.56**	0.69	−7.81	2.39	**0.45**
	75	0.56	22.17	0.16	**0.54**	0.56	26.49	−0.03	**0.49**
	73	0.65	−8.05	0.40	**0.39**	0.65	−8.37	0.34	**0.26**
T	**70**	0.60	−2.04	0.21	**0.10**	0.60	−0.92	0.16	**0.06**
	67	0.61	−2.60	0.18	**0.14**	0.61	−1.78	0.10	**0.04**
	64	0.60	−0.32	−0.12	**0.08**	0.60	−0.09	−0.09	**0.09**
	62	0.60	−0.65	0.06	**0.06**	0.60	−0.70	0.07	**0.05**
	78	0.70	243.65	424.11	**0.24**	0.71	189.11	449.79	**0.18**
	75	0.57	−288.28	−50.80	**0.49**	0.57	−344.26	−72.78	**0.42**
	73	0.64	68.22	46.09	**0.20**	0.65	60.87	47.22	**0.11**
GPH	**70**	0.60	26.82	12.12	**0.15**	0.60	19.27	5.53	**0.06**
	67	0.61	1.70	1.49	**0.02**	0.61	−2.59	0.16	**0.02**
	64	0.60	11.87	2.00	**0.29**	0.60	11.46	1.45	**0.17**
	62	0.60	0.36	1.81	**0.05**	0.60	−0.04	1.97	**0.03**
	78	0.71	172.45	113.32	**0.46**	0.72	119.10	127.41	**0.25**
	75	0.58	−140.51	−47.08	**0.35**	0.58	−142.06	−68.36	**0.30**
	73	0.64	68.25	50.07	**0.50**	0.64	63.42	48.38	**0.31**
H_2O	**70**	0.60	20.80	−0.15	**0.08**	0.60	15.58	0.05	**0.05**
	67	0.61	15.14	7.14	**0.15**	0.61	12.12	3.58	**0.05**
	64	0.60	11.90	3.45	**0.17**	0.60	9.80	2.79	**0.12**
	62	0.60	4.96	1.53	**0.04**	0.60	3.94	−0.14	**0.02**
	78	0.70	892.30	2,981.60	**0.24**	0.71	819.08	3,509.60	**0.18**
	75	0.57	−885.15	−604.14	**0.43**	0.57	−1,057.70	−680.53	**0.36**
	73	0.65	251.49	480.36	**0.17**	0.65	211.37	417.30	**0.08**
I_α^{SZA}	**70**	0.60	119.46	136.78	**0.16**	0.60	100.83	124.41	**0.08**
	67	0.61	−0.99	25.71	**0.03**	0.61	−21.17	8.37	**0.03**
	64	0.60	54.94	55.76	**0.31**	0.60	56.06	61.13	**0.18**
	62	0.60	−1.27	29.88	**0.04**	0.60	−6.00	29.06	**0.04**

Note. The coefficients C_{11} and C_{12} are associated with the predictor variables temperature, GPH, H_2O, I_α^{SZA} and their squared terms, respectively. The response variable is $\log_{10}$(OH + constant). The constant (4) is added to ensure only positive values of OH and hence only real logarithms of OH. The coefficient of determination is given by the adjusted R^2. The variables OH, GPH, H_2O and I_α^{SZA} are: hydroxyl, geopotential height, water vapor and solar Lyman alpha radiation as a function of the solar zenith angle, respectively. The acronyms GEO and CGM represent: geographic and corrected geomagnetic, respectively.

where C_0, C_{j1}, C_{j2} … C_{m1}, C_{m2} are the regression coefficients (also listed in Table 3) and ϵ is the error term. Polynomial regression allows for a nonlinear relationship between the response variable and the predictors as well as maintaining a linear regression framework (linear in the regression coefficients). The coefficients for multiple linear regression without quadratic terms are also listed in Table 3 for completeness.

It is, however, evident that there is significant correlation among the predictor variables as shown in Figure 3 (bottom panels), which is strongest between GPH and I_α^{SZA}. The violation of the basic assumptions of normality, independence, and constant variance of the residuals and the predictor variables being measured without error leads to problems in least squares regression analysis (see Rawlings et al., 1998). Correlation among predictor variables, however, does not always result in collinearity. The inclusion or exclusion of a certain predictor for example H_2O may increase or decrease collinearity.

Journal of Geophysical Research: Space Physics 10.1029/2017JA025038

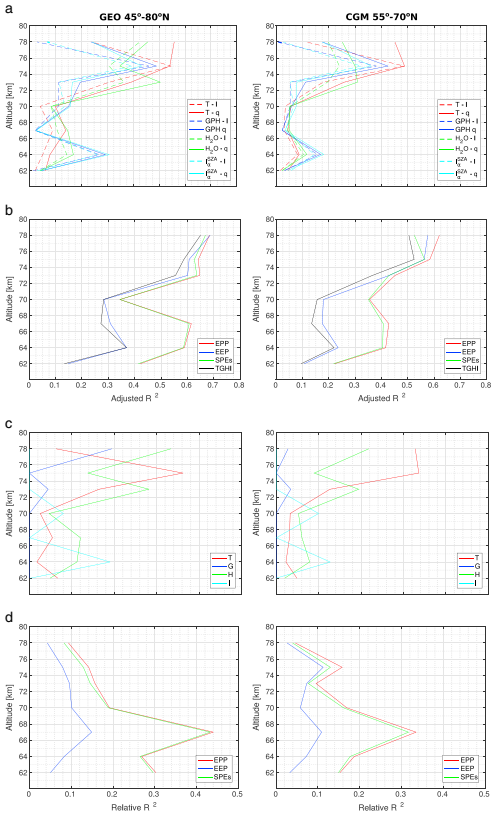

Figure 4. Line plots showing the amount of variation in OH explained by the different regression models for years 2005 to 2009. The data are averaged within the geographical (GEO) latitude range of 45 – 80°N (left) and within a corrected geomagnetic (CGM) latitude range of 55 – 70°N (right). (a) Adjusted R^2 from simple linear regression. The dotted lines represent linear (*l*) regression models, whereas the solid lines represent the quadratic (*q*) models. The colors red, blue, green, and cyan represent temperature, GPH, H_2O, and I_α^{SZA}, respectively. (b) Adjusted R^2 from multiple linear regression. The black lines represent the model of the background OH variability. The red lines represent the model of the background plus the energetic particle precipitation (electrons and protons). The blue lines represent the model with only electrons added, while the green lines represent a model for which only protons are added to the background. (c) Relative importance of temperature, GPH, H_2O, and I_α^{SZA} in a model for which the total energy (EPP) is added. (d) Relative importance of EEP, SPEs, and EPP shown by the amount variation explained by each kind of forcing at a particular altitude.

Journal of Geophysical Research: Space Physics 10.1029/2017JA025038

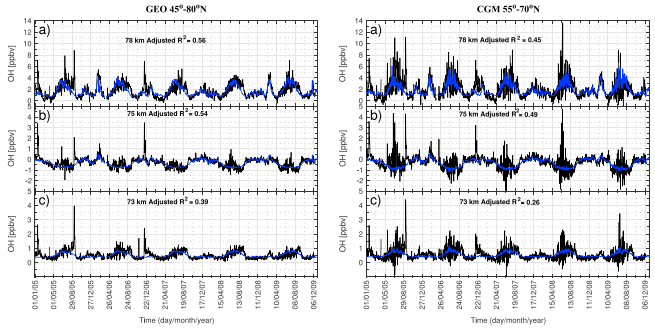

Figure 5. Simple Linear Regression: Second-order polynomial regression of the response variable hydroxyl (OH) and temperature as the predictor for years 2005–2009. The data are averaged within the geographic (GEO) latitude range of 45–80°N (left) and a corrected geomagnetic (CGM) latitude band of 55–70° N for altitudes 73, 75, and 78 km. The black line represents the OH observation, while the blue line represents the modeled OH.

Therefore, we performed Belsley et al. (2005) collinearity diagnostics that assesses the sources and the associated strength of collinearity among variables using condition indices and variance decomposition. The condition indices identify the number and strength of any near dependencies in the predictor variables. Whereas the variance-decomposition proportions identify groups of predictors involved in near dependencies, and the extent to which the dependencies may degrade the regression coefficients. The predictor terms for which the condition index is >10 and the variance decomposition is > 0.5 are deemed to degrade the regression coefficients and are therefore excluded from the regression models.

Stepwise regression is used for variable selection. Stepwise algorithm searches for and adds or removes terms until no terms can be added or removed from the model. Using the sum of squared error criterion, the stepwise algorithm adds the terms to the model if the sum of squared error of the model is smaller than 0.05 and removes terms from the model if p value of the F statistic is larger than 0.1. After finding the models' form and the relevant parameters (or terms) using stepwise regression, robust weighted least squares regression with bisquare fitting weight function was used to create models that are least affected by outliers. The models were further tested with both a quadratic (with interaction terms) and a pure quadratic (without interaction terms) models. In the following analysis we show only pure quadratic models as they were less affected by collinearity effects.

As already noted, polynomial regression (q) gives higher adjusted R^2 than linear regression for the same altitude (see, e.g., Figure 4a: the solid lines [q] against the dotted lines [l]). The multiple linear regression model further improves the description of the background variability as illustrated by the solid black lines in Figure 4b. The regression workflow for obtaining the background OH models is summarized in Figure 2 by following the brown arrows. With the background model obtained, then the different types of particle energy deposition are added to the model separately. This results in three models; a model of the background plus the electron energy deposition (EEP), a model of the background plus the proton energy deposition (SPEs), and a model of background plus the total particle energy deposition (EPP) whose coefficients are recorded in Table 4. Figure 6 shows time plots of observed (black line) and modeled OH for years 2005 to 2009 for altitudes 62 km to 78 km in the NH for the geographic latitude band. The same plots but for the CGM latitude band are shown in Figure 7. In blue are the models for the background OH variability, whereas red shows models for which the total energy deposition is included. The altitudes 75–78 km exhibit the highest adjusted R^2 for all models in the geographic and CGM latitudinal settings, respectively. Models under a geographic latitude setting give higher adjusted R^2 than their CGM latitude setting counterparts. The line plots of the adjusted R^2 from the four models is shown in Figure 4b. For the geographical latitude setting, the electron (blue) contribution to the adjusted R^2 is lower than that of the protons (green) at all altitudes except at 78 km.

Journal of Geophysical Research: Space Physics 10.1029/2017JA025038

Table 3
Multiple Linear Regression: Regression Coefficients for Linear (l) and Quadratic (q) Multiple Regression for Years 2005–2009 for a Geographic Latitude Band of 45–80°N (Left) and a CGM Latitude Band of 55–70°N (Right)

		GEO											CGM									
	Alt (km)	C_0	C_{l1} (10^{-4})	C_{k1} (10^{-4})	C_{l1} 10^{-4})	C_{m1} (10^{-4})	C_{l2} (10^{-4})	C_{k2} (10^{-4})	C_{l2} (10^{-4})	C_{m2} (10^{-4})	R^2	C_0	C_{l1} (10^{-4})	C_{k1} (10^{-4})	C_{l1} (10^{-4})	C_{m1} (10^{-4})	C_{l2} (10^{-4})	C_{k2} (10^{-4})	C_{l2} (10^{-4})	C_{m2} (10^{-4})	R^2
	78	0.74	−28.13	−479.43	238.25						**0.48**	0.76	−34.86	−1028.70	159.77	1319.80					**0.31**
	75	0.56	26.81		79.69	−80.22					**0.56**	0.56	29.10		75.90	−201.66					**0.51**
	73	0.65	−16.95	−192.89	36.70	216.21					**0.46**	0.66	−15.55	−173.95	36.23	181.86					**0.28**
l	**70**	0.60	6.07		32.70	181.76					**0.25**	0.60	6.17		32.23	156.26					**0.14**
	67	0.61	−3.30	−14.97	13.49	−21.24					**0.23**	0.61	−2.76	−13.57	12.09	−33.60					**0.11**
	64	0.60	1.36		8.92	45.58					**0.35**	0.60	1.29		8.59	45.49					**0.19**
	62	0.60	−0.36		4.96	−14.04					**0.10**	0.60	−0.34		4.06	−18.23					**0.08**
	78	0.68	17.91	48.53	351.42		1.21	236.46			**0.65**	0.69	0.81	−125.82	234.82		1.52	211.38			**0.50**
	75	0.57	27.98		96.10				−34.26		**0.59**	0.57	32.25		99.38				−42.11		**0.52**
	73	0.64	−10.74	−85.35	38.48			12.28	39.80		**0.56**	0.64	−10.02	−88.31	40.91			15.64	40.84		**0.37**
q	**70**	0.60	6.88		32.52	224.76				187.87	**0.28**	0.60	6.92		32.44	203.12				187.72	**0.16**
	67	0.61	−2.44		14.76	−76.02			8.67		**0.27**	0.61	−2.11		13.38	−87.87			7.47		**0.13**
	64	0.60	1.24		8.04	51.32				36.08	**0.37**	0.60	1.21		7.99	55.45				48.80	**0.22**
	62	0.60	−0.55		5.46	−14.37	0.04		3.03		**0.13**	0.60	−0.63		4.71	−18.42	0.04		2.41		**0.09**

Note. The coefficients $C_{l1}, \ldots, C_{m1}$ and $C_{l2}, \ldots, C_{m2}$ are associated with the predictors temperature, GPH, H_2O, β_{SZA}^{EA} and their squared terms, respectively. The response variable is $\log_{10}$(OH + constant). The constant 4 is added to ensure that the logarithms of OH are only real. The variables OH, GPH, H_2O and β_{SZA}^{EA} are: hydroxyl, geopotential height, water vapor and solar Lyman alpha radiation as a function of the solar zenith angle, respectively. The acronyms GEO and CGM represent: geographic and corrected geomagnetic, respectively.

Journal of Geophysical Research: Space Physics 10.1029/2017JA025038

Table 4
Multiple Linear Regression: Regression Coefficients for Models That Include the Energy Deposition

			GEO										CGM									
	Alt (km)	C_0	C_{f1} (10^{-4})	C_{k1} (10^{-4})	C_{f1} (10^{-4})	C_{m1} (10^{-4})	C_{n1} (10^{-4})	C_{f2} (10^{-4})	C_{k2} (10^{-4})	C_{f2} (10^{-4})	C_{m2} (10^{-4})	R^2	C_0	C_{f1} (10^{-4})	C_{k1} (10^{-4})	C_{f1} (10^{-4})	C_{m1} (10^{-4})	C_{n1} (10^{-4})	C_{f2} (10^{-4})	C_{k2} (10^{-4})	C_{f2} (10^{-4})	C_{m2} (10^{-4})	R^2
	78	0.69	18.80	37.86	377.47		445.21	1.16	250.19			**0.69**	0.70	2.23	−131.71	270.69		421.28	1.45	238.17			**0.58**
	75	0.57	29.40		115.84		309.35			−37.24		**0.61**	0.57	33.72		121.55		259.53			−48.79		**0.56**
	73	0.64	−10.32	−88.41	46.89		273.48		13.85	38.23		**0.60**	0.64	−9.34	−90.91	51.76		205.16		17.77	39.08		**0.43**
EEP	**70**	0.60	6.89		33.18	223.01	25.34				184.43	**0.28**	0.60	7.13		35.62	195.67	102.41				172.03	**0.18**
	67	0.61	−2.38		15.89	−79.27	172.14			8.99		**0.31**	0.61	−2.00		14.79	−91.08	154.24			7.71		**0.18**
	64	0.60	1.27		8.20	50.45	64.71				34.00	**0.37**	0.60	1.28		8.47	52.64	139.71				42.10	**0.24**
	62	0.60	−0.54		5.76	−15.03	90.55	0.04		3.23		**0.15**	0.60	−0.60		5.16	−19.51	68.65	0.04		2.71		**0.11**
	78	0.69	17.91	45.08	351.64		156.10	1.22	232.05			**0.67**	0.70	0.94	−122.56	236.09		215.81	1.52	208.59			**0.53**
	75	0.57	28.29		97.79		113.30			−33.88		**0.63**	0.57	32.35		99.21		162.88			−41.93		**0.56**
	73	0.64	−10.79	−86.70	38.75		70.74		11.81	40.01		**0.64**	0.64	−9.97	−89.02	41.43		78.50		14.70	41.51		**0.43**
SPE	**70**	0.60	6.86		32.58	222.91	20.01				185.77	**0.34**	0.60	6.88		32.15	200.93	54.25				181.22	**0.35**
	67	0.61	−2.44		14.76	−76.86	28.88			8.73		**0.61**	0.61	−2.10		13.36	−87.02	35.93			7.51		**0.41**
	64	0.60	1.24		7.99	50.71	18.72				35.26	**0.59**	0.60	1.18		7.82	54.25	24.96				45.75	**0.40**
	62	0.60	−0.55		5.50	−14.37	10.62	0.04		3.06		**0.41**	0.60	−0.62		4.61	−18.64	10.86	0.04		2.43		**0.22**
	78	0.69	18.44	45.55	360.98		152.03	1.20	237.13			**0.68**	0.70	1.77	−127.28	259.52		335.30	1.48	230.19			**0.62**
	75	0.57	28.91		106.05		114.71			−34.92		**0.64**	0.57	33.16		112.00		140.38			−45.94		**0.58**
	73	0.64	−10.67	−87.70	40.95		68.44		11.94	39.72		**0.65**	0.64	−9.67	−90.17	45.94		71.92		15.12	41.10		**0.45**
EPP	**70**	0.60	6.88		33.15	221.57	18.89				182.80	**0.34**	0.60	7.01		34.01	196.78	49.36				174.01	**0.35**
	67	0.61	−2.43		14.97	−77.59	28.79			8.82		**0.62**	0.61	−2.08		13.59	−87.50	36.27			7.52		**0.43**
	64	0.60	1.25		8.03	50.41	18.65				34.77	**0.59**	0.60	1.20		7.93	53.98	25.21				45.24	**0.42**
	62	0.60	−0.54		5.51	−14.44	10.71	0.04		3.08		**0.42**	0.60	−0.61		4.67	−18.89	10.83	0.04		2.48		**0.22**

Note. The response variable is $\log_{10}$(OH + constant). The constant 4 is added to ensure that the logarithms of OH are only real. The acronyms EEP, SPE, and EPP stand for the electron, protons and total (electrons plus protons) energy deposition. The coefficients C_{f1}, …, C_{n1} and C_{f2}, … C_{m2} are associated with the predictors temperature, GPH, H_2O, I_{Ly}^{ZA}, energy deposition and the squared terms of temperature, GPH, H_2O, I_{Ly}^{ZA}, respectively. The variables OH, GPH, H_2O and I_{Ly}^{ZA} are: hydroxyl, geopotential height, water vapor and solar Lyman alpha radiation as a function of the solar zenith angle, respectively. The acronyms GEO and CGM represent: geographic and corrected geomagnetic, respectively.

Journal of Geophysical Research: Space Physics 10.1029/2017JA025038

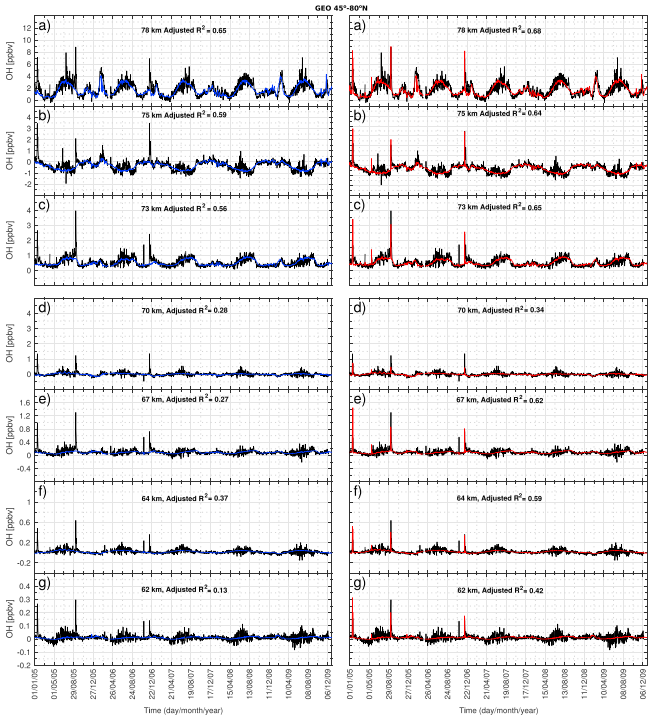

Figure 6. Multiple Linear Regression: Time plots showing observed hydroxyl (OH) (black line) against modeled OH for altitudes 62 to 78 km. The blue lines represent modeled background OH variability. The red lines represent modeled background OH including the contribution of energetic particles (electrons and protons). The data are averaged within the geographical (GEO) latitude range of 45–80°N.

In a CGM latitude setting, however, the contribution of electron energy deposition (blue) above 70-km altitude is comparable to that of protons. While the contribution of protons (green) increases with decreasing altitude and maximizes at 67 km. A summary of the regression workflow for obtaining the relative importance of the proposed predictors to the OH variability is shown in Figure 2 by the orange arrows.

3.2.3. Relative Importance

In Figure 4b we can only approximately deduce the contribution of the particle forcing to the variability in OH. In order to investigate the relative contribution of each of the predictors in the regression models, we *predict* OH using the terms for each predictor in the regression model. Then calculate the correlation coefficient, r_i between the observed and model OH, then calculate r_i^2 by squaring r_i. The total r^2_{total} is the sum of the individual r_i^2. Therefore, the contribution of each predictor to the adjusted R^2 is obtained by

$$R_i^2 = \left(r_i^2 / r^2_{\text{total}}\right) * R^2 \tag{6}$$

Journal of Geophysical Research: Space Physics 10.1029/2017JA025038

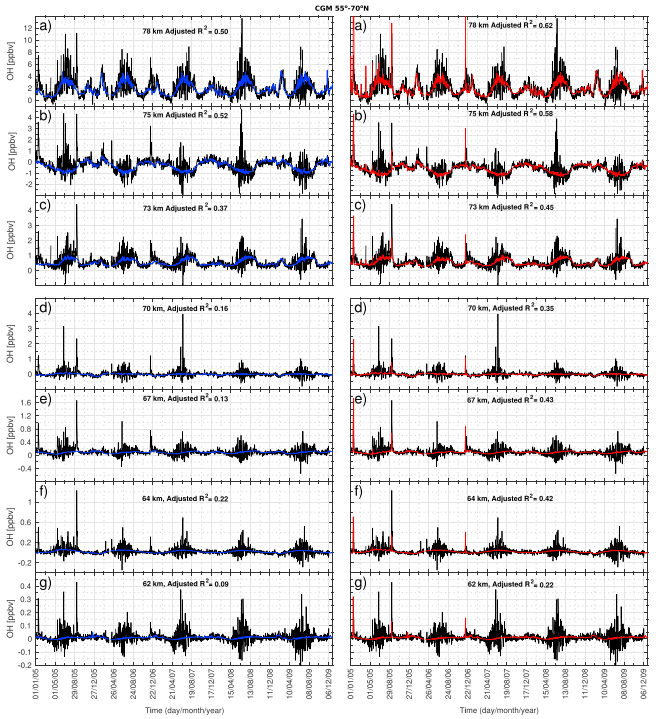

Figure 7. Multiple Linear Regression: Time plots showing observed hydroxyl (OH) (black line) against modeled OH for altitudes 62 to 78 km. The blue lines represent modeled background OH variability. The red lines represent modeled background OH including the contribution of energetic particles (electrons and protons). The data are averaged within a corrected geomagnetic (CGM) latitude range of 55 – 70°N.

where *i* represents each predictor variable including its higher-order terms if any. Figure 8 shows time plots of the contribution of each predictor variable to the adjusted R^2 for altitude 78 km in a model to which EPP is added. The figure shows the observed OH in black, modeled OH in red (part a), and the contribution of each predictor variable in blue (b – e). H_2O seems to play a dominant role in the background model, with a contribution of about 33% in the geographical setting. Whereas in a CGM setting, temperature seems to dominate with a contribution of 33% at this altitude. SSWs are well approximated by the temperature variability. The particle contribution at this altitide is about 9% and 5% in the geographic and CGM coordinate settings, respectively. This type of breakdown of the contribution of each predictor is done for electrons (EEP), protons (SPEs), and EPP for all altitudes, and the results thereof are shown in Table 5.

The breakdown of the relative importance of the background predictors in an atmosphere that is responding to the total energy deposition (EPP) is shown in Figure 4c and in Table 5. It is evident that temperature and H_2O consistently contribute to OH variability at all altitudes. The I_α^{SZA} and GPH, however, only sporadically

Journal of Geophysical Research: Space Physics 10.1029/2017JA025038

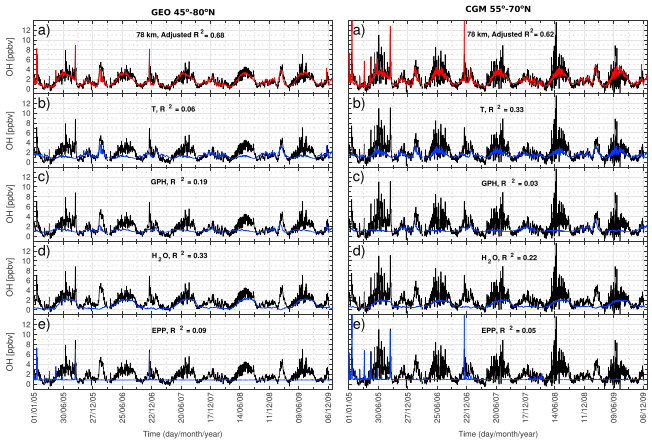

Figure 8. Multiple Linear Regression: Time plots showing observed hydroxyl (OH) (black line) against modeled OH contribution from each of the predictors in the regression model at 78 km. The blue lines represent modeled background OH variability due to at most one predictor in the regression model. The red lines represent modeled OH which includes the background and the contribution of energetic particles (electrons and protons). The data are averaged within the geographical (GEO) latitude range of 45–80°N (left) and within a corrected geomagnetic (CGM) latitude range of 55–70°N (right).

contribute to OH variability at altitudes 64–70 km and 73–78 km, respectively. Therefore, by considering temperature and H_2O only, H_2O dominates over temperature at altitudes 64–73 and 78 km in a geographic setting with a contribution of up to 33%. Also, H_2O dominates over temperature at 64–73 km in a CGM setting with a contribution of up to 22%. At 78-km altitude in a CGM setting, temperature dominates over H_2O with a contribution of 33%. The temperature gives the highest contribution with up to 36% and 34% at 75-km altitude in the geographic and CGM coordinate settings, respectively.

Furthermore, to assess the relative importance of EEP, SPEs, and EPP, a line plot of the contribution of each forcing is shown in Figure 4d. For a geographic setting, electrons contribute up to 15% at 67-km altitude. The contribution of protons increases with decreasing altitude with maximum contribution of about 43% at 67-km altitude. The trend of EPP is the same as that due to SPEs with little difference in values. In a CGM setting, the electron contribution maximizes at 67 and 75 km with a contribution of about 11%. Protons contribute up to 32% at 67 km. The trend of EPP generally follows that of SPEs at all altitudes with maximum contribution of about 34% at 67 km.

Note that there may be a discrepancy of up to $\pm 2\%$ between the total contribution from the predictors and the adjusted R^2. This is probably due to rounding off errors.

4. Discussion

4.1. Mechanisms Directly Driving OH Background Production

Nighttime mesospheric background OH has two main sources: remnants of the daytime production and the reaction of O_3 with atomic hydrogen (H). During normal, unperturbed conditions in the mesosphere, OH is mainly produced through photodissociation of H_2O by the reaction given by equation 1. The chemical lifetime of HO_x is of the order of 0.1 to 1 day in the mesosphere, allowing for the existence of the remnant of daytime OH production after sunset (see Pickett et al., 2006).

Journal of Geophysical Research: Space Physics 10.1029/2017JA025038

Table 5
Multiple Linear Regression: The Contribution of the Various Predictor to the Amount of Variation in OH Explained by the Regression Models for Altitudes 62 to 78 km in the Northern Hemisphere

	Alt	GEO						CGM					
	(km)	*T*	*G*	*H*	*I*	*E*	R^2	*T*	*G*	*H*	*I*	*E*	R^2
	78	0.06	0.21	0.38		0.04	0.69	0.31	0.03	0.21		0.03	0.58
	75	0.38		0.15		0.08	0.61	0.35		0.10		0.11	0.56
	73	0.17	0.04	0.29		0.10	0.60	0.13	0.03	0.20		0.07	0.43
EEP	70	0.03		0.06	0.10	0.10	0.28	0.02		0.03	0.07	0.06	0.18
	67	0.05		0.11	0.00	0.15	0.31	0.02		0.04	0.00	0.11	0.18
	64	0.02		0.10	0.17	0.08	0.37	0.02		0.06	0.09	0.07	0.24
	62	0.06		0.04	0.00	0.05	0.15	0.05		0.02	0.00	0.03	0.11
	78	0.07	0.19	0.32		0.08	0.67	0.28	0.02	0.18		0.04	0.53
	75	0.36		0.13		0.13	0.63	0.35		0.09		0.13	0.56
	73	0.16	0.04	0.28		0.15	0.64	0.13	0.03	0.19		0.08	0.43
SPE	70	0.03		0.05	0.08	0.19	0.34	0.03		0.05	0.10	0.16	0.35
	67	0.05		0.12	0.00	0.43	0.61	0.03		0.06	0.00	0.32	0.41
	64	0.02		0.11	0.19	0.26	0.59	0.02		0.08	0.13	0.18	0.40
	62	0.07		0.05	0.00	0.30	0.41	0.05		0.02	0.00	0.15	0.22
	78	0.06	0.19	0.33		0.09	0.68	0.33	0.03	0.22		0.05	0.62
	75	0.36		0.14		0.14	0.64	0.34		0.09		0.16	0.58
	73	0.16	0.04	0.28		0.16	0.65	0.13	0.03	0.19		0.10	0.45
EPP	70	0.03		0.05	0.08	0.19	0.34	0.03		0.05	0.10	0.17	0.35
	67	0.05		0.12	0.00	0.44	0.62	0.03		0.06	0.00	0.34	0.43
	64	0.02		0.11	0.19	0.27	0.59	0.02		0.08	0.13	0.19	0.42
	62	0.07		0.05	0.00	0.30	0.42	0.05		0.02	0.00	0.15	0.22

Note. Also shown is the adjusted R^2 for regression models for each altitude. The acronyms EEP, SPE, and EPP stand for the electron, protons, and total (electrons plus protons) energy deposition. The letters *T*, *G*, *H*, *I*, and *E* represent the contribution due to the predictors temperature, GPH, H_2O, I_α^{SZA}, and energy deposition, respectively. The variables GPH, H_2O and I_α^{SZA} are: geopotential height, water vapor and solar Lyman alpha radiation as a function of the solar zenith angle, respectively. The acronyms GEO and CGM represent: geographic and corrected geomagnetic, respectively.

The nighttime temperature, GPH, H_2O, and I_α^{SZA} shown in Figure 1 depict clear seasonal variations which are also reflected in the OH VMR, although not so distinctly. The seasonal cycle in the mesospheric temperature, GPH, and H_2O is related to the meridional circulation pattern which is characterized by upwelling at the summer pole, transport of air from the summer pole to the winter pole, causing piling of mass and descent at the winter pole. Adiabatic upward motion of air causes expansion and cooling and also brings up air rich in H_2O from lower altitudes. Adiabatic downward displacement causes compression and warming, and also the descent of dry air from thermospheric altitudes. The descent and ascent of pressure surfaces during winter and summer respectively is seen in Figure 1 in the second panels from top (i.e., GPH). Hence, during summer the mesospheric temperatures are low but the air is rich in H_2O implying more production of OH through photodissociation of H_2O by solar Ly-α radiation which is also high during summer at upper mesospheric altitudes (above 70 km). During winter, the temperatures are high but the H_2O is low, hence low background production of OH. However, the NH high-latitude winter is associated with dynamical processes involving even higher than normal winter time temperatures (>220 K) and increases in the background OH production for example during January 2006, 2007, and 2009 in Figure 1.

The temperature is dynamically connected to GPH and H_2O, and they are anticorrelated as evident in Figure 1 (top 2 panels). Temperature is also anticorrelated with I_α^{SZA}. Figure 3 (top panels) shows that generally temperature is negatively correlated with OH in the mesosphere, except at 75-km altitude. There are, however, periods in winter during which temperature shows a positive correlation with OH. One such example is January to middle March 2009 in the NH corresponding to the 2009 record breaking Arctic SSW during which the polar vortex split, resulting in a greater impact on the lower stratosphere than any other previously observed SSW

Journal of Geophysical Research: Space Physics 10.1029/2017JA025038

with no siginificant recovery of the vortex in that region (Manney et al., 2009). From Figure 1, the high temperatures also correspond to low GPH and low H_2O VMR at the same altitude. This event is preceded by a period during which the OH abundances are low, corresponding to low temperatures, high GPH, and inappreciable change in H_2O VMR.

Planetary wave activity at high latitudes during winter is associated with these temperature enhancements and are known to cause descent of thermospheric dry air, as well as atomic oxygen (O) and H to mesospheric altitudes (see, e.g., Damiani et al., 2010; Zawedde et al., 2016). The O will participate in a three body reaction with O_2, creating O_3 which reacts with H to form vibrationally excited OH (OH^*) by the reaction (Winick et al., 2009):

$$H + O_3 \rightarrow OH^* + O_2 \tag{7}$$

The OH^* is deactivated either by photon emissions in the Meinel band or by collisional quenching (Brasseur & Solomon, 2005). Therefore, in addition to photolysis of H_2O by solar radiation, SSWs and the related planetary wave activity drive mechanisms that enhance OH.

Models with only linear terms failed to capture the variability in OH due to SSWs. The linear terms in the models estimate well the OH background seasonal variability, whereas the quadratic terms estimate well the OH variability due to SSWs. Models with quadratic terms, therefore, successfully accounted for both long- and short-term variations of the background enabling the assessment of the importance of EPP-driven OH production.

4.2. EPP-Driven OH Production

Figure 1, third panels, shows the energy deposition for data averaged over a geographic latitude band of 45–80°N and a CGM latitude band of 55–70°N. The solar energetic protons would precipitate over the entire polar cap. Hence, the impact region would cover a large part of the geographical latitude band of 45–80°. Whereas the latitude range of Earth's radiation belts related to energetic electrons is well approximated by the CGM latitude band of 55–70° . Compared to the entire polar cap, the latitude range of the radiation belts is a small band within the NH. As such, the results would be biased by the dominant type of particle forcing if only one of the latitude bands is considered. Generally for modeling the background OH variability, *geographic* models seem to explain a lot more variability in OH than their *CGM* counterparts, the improvement ranging from 4% to 19% within the mesosphere by comparing Figures 6 and 7 (blue plots). This may be because the parameters responsible for OH background production are oriented in a geographic coordinate system rather than a magnetic coordinate system.

It is well known that EPP leads to production of odd hydrogen of which OH is part. With the availability of OH data from the Aura satellite, the effects of the strong infrequent SPEs have been extensively studied even over the years in question (see, e.g., Damiani et al., 2008; Verronen et al., 2006, 2007). There has also been several more recent studies on the direct EEP impact on OH (see, e.g., Andersson et al., 2012; Andersson, Verronen, Rodger, Clilverd, & Wang 2014; Verronen et al., 2011; Zawedde et al., 2016). It is, however, difficult to find convincing observational evidence of OH increases associated with precipitating electrons at altitudes below 70 km especially during solar minimum years (see, e.g., Verronen et al., 2011, 2013). With multiple linear regression, we show that there is significant and quantifiable OH changes due to EEP even below 70 km associated with relativistic electrons, which is separable from the background production. We find that in a CGM coordinate setting, for example, EEP contributes up to 11% to the OH variability at 67 km. This estimate is 0.92 times the correlation of $r \geq 0.35$ ($r^2 \geq 0.12$ or 12%) between OH mixing ratios and precipitating electrons reported by Andersson et al. (2012) for the altitude 52–70 km, that is, at altitudes affected by 100 keV–3 MeV electrons. Correlation between a single predictor and OH may, however, not necessarily imply causality and correlation analysis does not account for other sources of OH variability.

A number of publications have discussed whether precipitation of electrons from the radiation belt can have a large impact on the composition of the mesosphere comparable to SPEs (see, e.g., Andersson, Verronen, Rodger, Clilverd, & Seppälä 2014). EEP events are weaker, and their chemical response is hard to detect but occurs much more frequently than the strong sporadic SPEs. Nevertheless, the weak geomagnetic storms associated with EEP during solar minimum produce local OH enhancements that are comparable to the OH enhancements due to background atmospheric dynamics (see, e.g., Zawedde et al., 2016). In order to understand and quantify the effect of EEP on mesospheric OH, we model the background OH variability, taking into account all the possible sources of OH variability as given in Table 3. Furthermore, the contribution of each

Journal of Geophysical Research: Space Physics 10.1029/2017JA025038

predictor variable to the adjusted R^2 is estimated by equation (6) as described in subsection 3.2.3 and listed in Table 5. At 78 km for example, temperature, GPH, H_2O, I_α^{SZA}, and EPP contribute 6%, 19%, 33%, 0%, and 9% respectively for a geographic setting, with an adjusted R^2 of 68%. These numbers will slightly vary depending on the kind of particle forcing included in the regression model. It is clear that H_2O dominates the background OH production at this altitude. For a CGM setting at 78 km, temperature, GPH, H_2O, I_α^{SZA}, and EPP contribute 33%, 3%, 22%, 0%, and 5% respectively (see Figure 8).

Considering all altitudes, GPH exhibits a sporadic contribution at 73- to 78-km altitude, which weakens in a CGM setting. The I_α^{SZA} contribution though sporadic, dominates at 64- to 70-km altitude (see Figure 4c). While temperature and H_2O show consistent contribution to OH variability at all altitudes and hence are the dominant contributors. Temperature plays a dominant role at 75 km where it exhibits maximum contribution to OH variability. As mentioned earlier this altitude has a reverse seasonal behavior to that exhibited by other mesospheric altitudes. H_2O seemed to be the main contributor to OH variability at altitudes 64–73 km. Generally, temperature dominates OH variability in the upper mesosphere while in the lower mesosphere, H_2O dominates over temperature. The dominance of temperature over H_2O in the upper mesosphere (75–78) for the *CGM* models (Figure 4c, red line) is consistent with the Sodankylä Ion and Neutral Chemistry (SIC) model runs for March 2008 for altitudes 65–75 km at 60°N/S by Andersson et al. (2012) performed to verify the sensitivity of OH to H_2O and temperature. These model runs, however, do not include particle precipitation.

H_2O is important for the background OH production through photolysis, it may also be important for the dynamical OH production since it is dynamically connected to temperature. Further, H_2O is important for the EPP-OH production because it is an important constituent for formation of water cluster ions. Mesospheric HO_X, regardless of its source, can be converted to molecular hydrogen (H_2) by the reaction (Crutzen & Solomon, 1980):

$$H + HO_2 \rightarrow H_2 + O_2 \tag{8}$$

For EPP, this effect is most pronounced in the altitude range 70–85 km, thus temporarily resulting in enhanced conversion of H_2O to H_2 after an event. This results in a nonlinear relationship between OH and EPP. Therefore, with simple linear regression alone, it is not possible to clearly distinguish between the different pathways H_2O can affect the OH production.

In case of strong precipitation events, the H_2O cluster reactions which occur during EPP-HO_X production may be obstructed by dissociative recombination of the intermediate positive ions with electrons, resulting in lower HO_X production rate (<2 radicals) during periods of elevated electron concentrations (Solomon et al., 1981). This process may be expedited if the H_2O mixing ratios become less than a few parts per billion (ppb). In that case, even the natural electron concentration may considerably reduce the efficiency of HO_X production through water cluster reactions. The Solomon et al. (1981) Figure 2 shows that HO_X production rate decreases with increasing ionization rate and also decreases with increasing altitude (see also Sinnhuber et al., 2012). The decrease of EPP-HO_X production rate is hence strongly dependent on H_2O which in turn is modulated by season, latitude, and the rate of vertical transport. Therefore, it is reasonable to assume that in our regression analysis the overestimation of OH production during periods of intense precipitation events is due to this nonlinear relationship between the ionization rate and the HO_X production rate. This effect is seen in Figures 6 and 7 for the red plots especially for altitudes 75 and 78 km. At 75 km, for example, considering the January 2005 SPE, the models shown in Figures 6 and 7 overestimate the OH VMR by ~6% and ~40% for the geographic and CGM latitude bands, respectively. The peak ionization rates of 734 $cm^{-3}s^{-1}$ and 730 $cm^{-3}s^{-1}$ (not shown) associated with this event in the geographic and CGM coordinate settings are consistent with a HO_X production per ionization of ~1.7–1.8 at 75 km (see Solomon et a., 1981). These production rates are 10–15% lower than the assumed 2HO_X per ionization.

Andersson, Verronen, Rodger, Clilverd, and Seppälä (2014) argue that although the duration of the forcing for individual EEP events is only a few days, the high frequency of occurrence of EEP events is enough to cause variability in mesospheric O_3 on solar cycle time scales. For years 2005 to 2009, our results show that in the mesosphere, electrons contribute up to 11% variability in OH in a CGM coordinate setting (Figure 4d, blue), which is not directly comparable to the estimate (9%) from Andersson, Verronen, Rodger, Clilverd, and Seppälä (2014) for O_3 depletion since OH cataltytically deplets O_3. The difference might also be due the fact that we are considering a wider latitude band (55–70°) than that (55–65°) by Andersson, Verronen, Rodger, Clilverd, and Seppälä (2014). Further, Figure 4c is for the NH, while the Andersson, Verronen, Rodger, Clilverd, and Seppälä (2014) Figure 3c shows the Southern Hemisphere. They looked at the EEP impact by contrasting

Journal of Geophysical Research: Space Physics 10.1029/2017JA025038

periods of maximum and minimum EEP activity, which they considered as an indication of the maximum variability during the solar cycle, while we use multiple linear regression to investigate the contribution from a predictor variable when other variables are held constant.

The relative contribution of EEP, SPEs, and EPP is shown in Figure 4d. For the geographic setting, the relative contribution from electrons maximizes at 67-km altitude with a contribution of 15%. But still this is much lower than the maximum contribution of protons which is up to ~43% at 67 km. Protons dominate over electrons in the contribution to OH production in a geographic coordinate system setting as protons precipitate over the entire geographic band in question, whereas electrons precipitate within a limited region connected to the Earth's radiation belts (see, e.g., Andersson, Verronen, Rodger, Clilverd, & Wang 2014). In a CGM coordinate system, which follows the latitude range of Earth's radiation belts, EEP contribution to the OH variability is comparable to that of SPEs for altitudes above 70 km with a contribution of 11% at 75 km. This is consistent with 50- to 200-keV electrons which deposit most of their energy within 70–78 km (see, e.g., Andersson et al., 2012; Turunen et al., 2009). Relativistic electrons (>200 keV) deposit their energy below 70 km where the EEP impact exhibits maximum contribution of up to 11% at 67 km. Protons contribute most below 70 km with maximum contribution of 32% which also occurs at 67 km. The EPP profile generally resembles the proton profile for all altitudes with two distinct maxima at 67 and 75 km. These maxima correspond to contributions of 34% and 16%, respectively.

In general, over the declining and minimum phase of the solar cycle 23, the background parameters are responsible for most of the OH variability in the upper mesosphere above 70 km. For altitudes 62–70 km, however, EPP (and SPEs) seems to contribute more than any of the other predictors in the respective regression models (see Figures 4c and 4d). EEP dominates over the background at 67 km in both the geographic and CGM coordinate setting, respectively. Therefore, the derived effectiveness of a particle source in contributing to variability of OH depends on the type of coordinate system one is working in, as well as the energy of the incident particles which will ultimately determine the altitude at which the energy will be deposited.

4.3. On Shorter Time Scales

A long time series, including different phases of the solar cycle, is required when assessing the relative importance of EEP and SPEs upon OH in general. The lack of SPEs and the lower intensity of the EEP during solar minimum implies, however, that the role of EPP with respect to the background variability will be damped as the background variability is much less affected by the solar cycle phases. For completeness, we wish therefore to demonstrate how the methodology works on shorter time scales.

We apply the methodology in subsections 3.2.2 and 3.2.3 focusing solely on the more active years 2005–2006, where we find most of the EPP activity both in regard to SPEs and EEP. Figure 9 shows the relative contribution of EEP, SPEs, and EPP to the observed OH variability. In this case, the role of EEP in the geographic and geomagnetic latitude bands is up to ~22% and ~20%, respectively. Averaging the OH data over the CGM latitude band introduces short-term variations, most pronounced during summer, with features that are neither captured by the background variability nor by EEP. There is, nevertheless, an improvement of up to 7% in the EEP contribution at 75-km altitude due to changing to the CGM setting. It is also evident that EPP in general now is responsible for 14–60% of the OH variability between 62- and 78-km altitude.

Further, the methodology can also be used to target the relative importance of the different parameters on for example seasonal time scales. In particular, EPP-induced ozone loss during late winter and early spring has been considered as a candidate for influencing the meridional temperature change and subsequently the upward wave propagation. This could potentially impact the atmospheric dynamics from the lower mesosphere, stratosphere, and all the way to the ground (e.g., Seppälä et al., 2009, 2013). Figure 10 shows the breakdown of the contribution of the various predictors to the modeled OH variability at 78 km during February to April 2005 and 2007. The OH background level is impacted by the spring transition at the end of the periods, as well as individual EEP events. For these two case studies, EEP contributes 30–34% to the modeled OH. The contribution from EEP is more than the background contribution at 78 km. At the other altitudes, the background generally contributes more than EEP (not shown), except at 73 km for 2005.

A detailed analysis of the relative importance of EPP and the background analysis at different time scales are, however, out of scope of the current study as the main objective is to shed light on the relative importance of EEP and SPEs which requires a long time series. It demonstrates, however, the potential of a multiple linear regression model to contribute to also other important questions regarding EPP effect on OH.

Journal of Geophysical Research: Space Physics 10.1029/2017JA025038

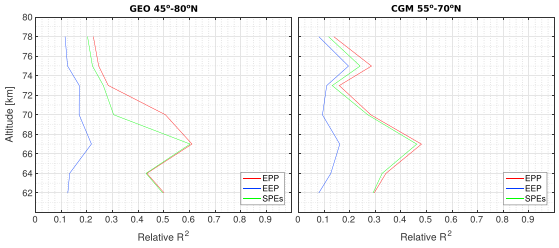

Figure 9. Multiple Linear Regression: Relative contribution of EEP, SPEs and EPP for years 2005-2006 for the geographical latitude band (45° -80° N) and CGM latitude band (55° – 70° N). The red, blue and green lines represent EPP, EEP and SPEs respectively.

4.4. Comparison to Other Studies

In one of the earliest review studies, Thorne (1980) assesses the relative contribution of certain classes of EPP to the chemical composition of the middle atmosphere. He stresses the production of odd nitrogen (NO_x) and HO_x and their subsequent role in catalytic destruction of O_3. Using the August 1972 SPE, Thorne (1980) shows that the effect of this event peaks at ∼50 km with up to 50% reduction in O_3. Such depletions of polar O_3 should cause a net reduction in the heating rate of 2.5° K/day at 60 km and 1.3° K/day at 45 km (under sunlit conditions). Thorne (1980) also combines ionization rates during two intense Relativistic Electron Precipitation events with cluster ion chemistry results to obtain profiles for mesospheric HO_x production, which he compares to the two major quiet time sources of HO_x. From that study it is evident that electron precipitation can provide an important contribution over a broad altitude range near 70 km within the mesosphere which behavior is also seen in our analysis in Figure 4d.

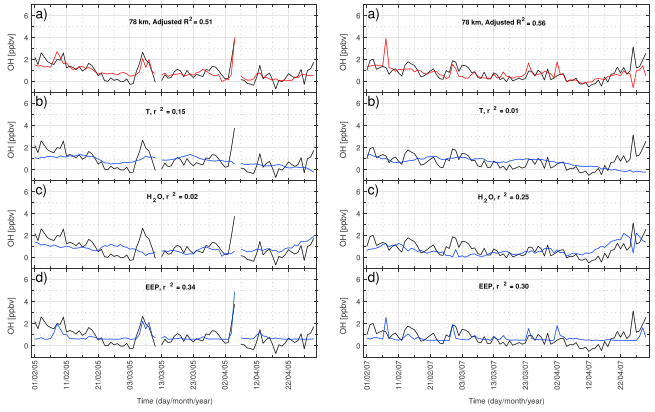

Figure 10. Multiple Linear Regression: Time plots showing observed OH (black line) against modeled OH contribution from each of the predictors in the regression model at 78 km for the spring transitions in 2005 (left) and 2007 (right). The blue lines represent modeled background OH variability due to at most one predictor in the regression model. The red lines represent modeled OH which includes the background and the contribution of energetic electron precipitation. The data are averaged within the CGM latitude range of 55° – 70°N.

Journal of Geophysical Research: Space Physics 10.1029/2017JA025038

On a diurnal scale, Aikin and Smith (1999) model the response of mesospheric constituents to EEP for two precipitation scenarios for altitudes 65, 70, and 75 km. They report that at high latitudes OH and HO_2 concentrations are enhanced by electron energy deposition with the largest difference between the background and EEP-induced OH and HO_2 occurring in the early morning hours. They stress that during the day, the extent of enhancement depends on overcoming the background production which is proportional to the ambient H_2O mixing ratio. For our study, however, we use only nighttime data for all the analysis mainly to ensure a low OH background that will enable easier detection of EEP induced OH.

Verronen et al. (2013) select the four strongest EEP events that occurred during the period 2004 to 2009: January, March; May 2005 and April 2006 and use the SIC model to study the effect of radiation belt electron precipitation on mesospheric OH and O_3 from Aura MLS. They show that the magnitude of EEP-induced OH increase depends on the SZA and the level of the background OH production with the largest OH increase seen in the winter pole at around sunrise as also reported by Aikin and Smith (1999). The OH enhancements reported in this study led to several tens of percent depletion to O_3, which was comparable to the effects previously reported in cases of large SPEs. Although the SIC model was able to reproduce the observed daily variability of OH and O_3 at 70- to 80-km altitude, they report significant differences in the absolute OH concentrations in the lower mesosphere. This implied that some correction might be needed for energies >300 keV in order to make confident conclusions at lower altitudes. With our current study, however, we have incorporated the necessary corrections for proton contamination of the electron channels and also accounted for relativistic electrons (>757 keV) which deposit their energy in the lower mesosphere as described in Nesse Tyssøy et al. (2016).

Verronen et al. (2015) use the electron concentration observations of the European Incoherent Scatter scientific Association incoherent scatter radars located in Tromsø to investigate the contribution of proton and electron precipitation to the observed electron density in the mesosphere-lower thermosphere during the October–November 2003 and September 2005 SPEs. They compare European Incoherent Scatter scientific Association measurements to the results from the SIC model, designed to separate the effects of protons and electrons. Using proton and electron ionization rates calculated from the Atmospheric Ionization Model Osnabrück v1.2, Figure 1 in Verronen et al. (2015) generally shows that protons dominate over electrons at lower altitudes (below ~72 km for September 2005 SPE) and electrons dominate at higher altitudes. This trend is also exhibited by our results in Figure 4b. Although there are similar trends for the electron and proton contribution, this differs from our study in the following ways: First as already mentioned, the source of the particle forcing differs in that we use both SPEs and EEP events for the period 2005 to 2009 in our analysis whereas Verronen et al. (2015) use two SPEs as the source of proton and electron precipitation. Then the ultimate effect and altitude of the particle precipitation is different for both studies, we are interested in effects on mesospheric chemistry, while they are interested in ionospheric effects. Furthermore, due to proton contamination of the POES MEPED electron detectors, the Atmospheric Ionization Model Osnabrück v1.2 electron ionization seems to be overestimated during SPEs forcing below 90 km where our region of interest in located. As already stated, NOAA POES data challenges are catered for as described in Nesse Tyssøy et al. (2016) for this study.

Overall, we find that in both geographic and CGM coordinate settings, the SPEs contribution to the OH variability dominates over that due to electrons for all altitudes. We find that the magnitude of the electron contribution from this study is less than that from other studies, for example, by Verronen et al. (2011) and Andersson et al. (2012) possibly due to the fact that those studies use correlation analysis without accounting for the presence of other sources of OH variability. Furthermore, some of these studies investigate case studies of very active periods which provide the short-term EEP effects on mesospheric OH and consequently on O_3. With this multiple linear regression, we investigate the relative contribution from the different available sources (or parameters) to the observed nighttime OH variability during 2005 to 2009, covering the declining and minimum phase of the solar cycle 23.

5. Summary and Conclusions

We model the natural background variability in nighttime OH using multiple linear regression, taking into account the temperature, GPH, H_2O, and I_{α}^{SZA}. Using the new MEPED analysis toolkit, we estimate the particle energy deposition in the mesosphere. We then add the different kinds of particle energy deposition (i.e., EEP, SPEs, and EPP) separately to the background regression model resulting in three types of models.

Our results show the breakdown of the contribution from the various sources to OH variability, giving the relative importance of these sources in the mesosphere.

Our models are able to capture both seasonal variations as well as short-term variability such as SSWs. Generally, temperature and H_2O seem to consistently contribute to OH variability and hence are considered the most important contributors to mesospheric background OH variability. By comparing temperature and H_2O profiles, H_2O seems to be a dominant contributor to the background OH production at altitudes 64–73 km in both coordinate settings. Temperature dominates at 75-km altitude with maximum contribution of 38% and 35% in the geographic and CGM settings, respectively.

Further, we have evaluated the role of EPP and the relative importance of EEP and SPEs over the declining and minimum phase of the solar cycle 23. However, the derived effect of energetic particles on OH depends on the applied coordinate system as well as the altitude range in consideration. In a geographic coordinate setting, protons dominate over electrons at all altitudes with a maximum contribution to OH variability of ~43% at 67 km. In a CGM coordinate setting, protons dominate over electrons only below 70 km with a maximum contribution to OH variability of ~32%. Above 70 km, the electrons contribution is comparable to the protons contribution to OH variability, with maximum contribution of ~11% at 75 km. Note that the numbers given refers to the NH. Applying the methodology in the Southern Hemisphere should, however, not impact the conclusion regarding the relative importance of SPEs and EEP. It might, on the other hand, affect relative importance of the background parameters and EPP due to a larger offset between the geographic and geomagnetic coordinate system. This should be explored in a future study.

Generally, the background dominates over the particles above 70-km altitude over the period considered. However, for altitudes below 70 km, the relative contribution from EPP is more than the relative contribution from any of the background predictors. The relative contribution of EEP and SPEs depends on the coordinate system of interest and also the energy of the incident particles which determines the altitude of the energy deposition.

The period 2005 to 2009 considered in this study coincided with the latter less active part of the declining phase of solar cycle 23. The years 2008–2009 were exceptionally quiet in regard to EPP in general. Therefore, the results from this study give a lower estimate of the relative contribution of EEP and SPEs to OH variability over the declining phase of solar cycle 23. To get a more general picture, longer time series encompassing the entire declining phase or even larger periods should be considered.

Acknowledgments
This study was supported by the Research Council of Norway under contract 223252/F50. The authors thank the NOAA's National Geophysical Data Center (NGDS) for providing NOAA POES data (https://satdat.ngdc.noaa.gov/), the LASP Interactive Solar IRradiation Datacenter (LISIRD) for providing composite solar Lyman alpha data (http://lasp.colorado.edu/lisird/lya/), and NASA Goddard Earth Science Data and Information Services Center (GES DISC) for providing Aura/MLS data (https://mls.jpl.nasa.gov/).

References

Aikin, A. C., & Smith, H. J. P. (1999). Mesospheric constituent variations during electron precipitation events. *Journal of Geophysical Research: Atmospheres*, *104*(D21), 26,457–26,471. https://doi.org/10.1029/1999JD900752

Andersson, M. E., Verronen, P. T., Rodger, C. J., Clilverd, M. A., & Seppälä, A. (2014). Missing driver in the Sun-Earth connection from energetic electron precipitation impacts mesospheric ozone. *Nature Communications*, *5*(5197). https://doi.org/10.1038/ncomms6197

Andersson, M. E., Verronen, P. T., Rodger, C. J., Clilverd, M. A., & Wang, S. (2014). Longitudinal hotspots in the mesospheric OH variations due to energetic electron precipitation. *Atmospheric Chemistry and Physics*, *14*(2), 1095–1105. https://doi.org/10.5194/acp-14-1095-2014

Andersson, M. E., Verronen, P. T., Wang, S., Rodger, C. J., Clilverd, M. A., & Carson, B. R. (2012). Precipitating radiation belt electrons and enhancements of mesospheric hydroxyl during 2004–2009. *Journal of Geophysical Research: Atmospheres*, *117*, D09304. https://doi.org/10.1029/2011JD017246

Belsley, D. A., Kuh, E., & Welsch, R. E. (2005). *Detecting and assessing collinearity* (pp. 85–191). John Wiley & Sons, Inc. https://10.1002/0471725153.ch3

Bethe, H. A., & Ashkin, J. (1953). *Part II of experimental nuclear physics, Passage of radiations through matter* (Vol. 1). New York: John Wiley & Sons.

Brasseur, G. P., & Solomon, S. (2005). *Aeronomy of the middle atmosphere: Chemistry and physics of the stratosphere and mesosphere*. Netherlands: Springer.

Canty, T., & Minschwaner, K. (2002). Seasonal and solar cycle variability of OH in the middle atmosphere. *Journal of Geophysical Research: Atmospheres*, *107*(D24), 4737. https://doi.org/10.1029/2002JD002278

Crutzen, P. J., & Solomon, S. (1980). Response of mesopheric ozone to particle precipitation. *Planetary and Space Science*, *28*(12), 1147–1153. https://doi.org/10.1016/0032-0633(80)90073-2

Daae, M., Espy, P., Nesse Tyssøy, H., Newnham, D., Stadsnes, J., & Søraas, F. (2012). The effect of energetic electron precipitation on middle mesospheric night-time ozone during and after a moderate geomagnetic storm. *Geophysical Research Letters*, *39*, L21811. https://doi.org/10.1029/2012GL053787

Damiani, A., Storini, M., Laurenza, M., & Rafanelli, C. (2008). Solar particle effects on minor components of the polar atmosphere. *Annales Geophysicae*, *26*(2), 361–370.

Damiani, A., Storini, M., Santee, M. L., & Wang, S. (2010). Variability of the nighttime OH layer and mesospheric ozone at high latitudes during northern winter: Influence of meteorology. *Atmospheric Chemistry and Physics*, *10*(21), 10,291–10,303. https://doi.org/10.5194/acp-10-10291-2010

Evans, D., & Greer, M. (2000). *Polar orbiting environmental satellite space environment monitor—2: Instrument descriptions and archive data documentation* (1.4). Boulder, CO: Space Environment Center.

Frederick, J. E., & Hudson, R. D. (1980). Atmospheric opacity in the Schumann-Runge bands and the aeronomic dissociation of water vapor. *Journal of the Atmospheric Sciences*, *55*, 301 – 327. https://doi.org/10.1175/1520-0469(1980)037<1088:AOITSR>2.0.CO;2

Fritsch, F. N., & Carlson, R. E. (1980). Monotone piecewise cubic interpolation. *SIAM Journal on Numerical Analysis*, *17*(2), 238 – 246.

Hedin, A. E. (1991). Extension of the MSIS thermosphere model into the middle and lower atmosphere. *Journal of Geophysical Research*, *96*(A2), 1159 – 1172. https://doi.org/10.1029/90JA02125

Li, X., & Temerin, M. A. (2001). The electron radiation belt. *Space Science Reviews*, *95*, 569 – 580.

Livesey, N. J., Read, W. G., Wagner, P. A., Froidevaux, L., Lambert, A., Manney, G. L., et al. (2015). *Earth Observing system(EOS) Aura Microwave Limb Sounder(MLS) Version 4.2x Level 2 data quality and description document* (91109-8099, version 4.2x-1.0). Pasadena, California: Jet Propulsion Laboratory, California Institute of Technology.

Manney, G. L., Schwartz, M. J., Krüger, K., Santee, M. L., Pawson, S., Lee, J. N., et al. (2009). Aura Microwave Limb Sounder observations of dynamics and transport during the record-breaking 2009 arctic stratospheric major warming. *Geophysical Research Letters*, *36*(12), L12815. https://doi.org/10.1029/2009GL038586

Minschwaner, K., Manney, G. L., Wang, S. H., & Harwood, R. S. (2011). Hydroxyl in the stratosphere and mesosphere — Part 1: Diurnal variability. *Atmospheric Chemistry and Physics*, *11*(3), 955 – 962. https://doi.org/10.5194/acp-11-955-2011

Nesse Tyssøy, H., Sandanger, M. I., Ødegaard, L.-K. G., Stadsnes, J., Aasnes, A., & Zawedde, A. E. (2016). Energetic electron precipitation into the middle atmosphere-constructing the loss cone fluxes from MEPED POES. *Journal of Geophysical Research: Space Physics*, *121*, 5693 – 5707. https://doi.org/10.1002/2016JA022752

Nesse Tyssøy, H., & Stadsnes, J. (2015). Cutoff latitude variation during solar proton events: Causes and consequences. *Journal of Geophysical Research: Space Physics*, *120*, 553 – 563. https://doi.org/10.1002/2014JA020508

Nesse Tyssøy, H., Stadsnes, J., Søraas, F., & Sørbø, M. (2013). Variations in cutoff latitude during the January 2012 solar proton event and implication for the distribution of particle energy deposition. *Geophysical Research Letters*, *40*, 4149 – 4153. https://doi.org/10.1002/grl.50815

Ødegaard, L.-K. G., Tyssøy, H. N., Sandanger, M. I. J., Stadsnes, J., & Søraas, F. (2016). Space weather impact on the degradation of NOAA POES MEPED proton detectors. *Journal of Space Weather and Space Climate*, *6*, A26. https://doi.org/10.1051/swsc/2016020

Ødegaard, L.-K. G., Tyssøy, H. N., Søraas, F., Stadsnes, J., & Sandanger, M. I. (2017). Energetic electron precipitation in weak to moderate corotating interaction region-driven storms. *Journal of Geophysical Research: Space Physics*, *122*, 2900 – 2921. https://doi.org/10.1002/2016JA023096

Pickett, H. M., Read, W. G., Lee, K. K., & Yung, Y. L. (2006). Observation of night OH in the mesosphere. *Geophysical Research Letters*, *33*, L19808. https://doi.org/10.1029/2006GL026910

Rawlings, J. O., Pantula, S. G., & Dickey, D. A. (1998). *Applied regression analysis: A research tool* (second ed.). New York: Springer.

Rees, M. H. (1989). Physics of the upper atmosphere. *Quarterly Journal of the Royal Meteorological Society*, *117*(498), 433 – 433.

Reeves, G. D., Spence, H. E., Henderson, M. G., Morley, S. K., Friedel, R. H. W., Funsten, H. O., et al. (2013). Electron acceleration in the heart of the Van Allen Radiation Belts. *Science*, *341*(6149), 991 – 994. https://doi.org/10.1126/science.1237743

Rodger, C. J., Clilverd, M. A., Green, J. C., & Lam, M. M. (2010). Use of POES SEM-2 observations to examine radiation belt dynamics and energetic electron precipitation into the atmosphere. *Journal of Geophysical Research*, *115*, A04202. https://doi.org/10.1029/2008JA014023

Rodger, C. J., Kavanagh, A. J., Clilverd, M. A., & Marple, S. R. (2013). Comparison between POES energetic electron precipitation observations and riometer absorptions: Implications for determining true precipitation fluxes. *Journal of Geophysical Research: Space Physics*, *118*, 7810 – 7821. https://doi.org/10.1002/2013JA019439

Sandanger, M. I., Ødegaard, L. K. G., Tyssøy, H. N., Stadsnes, J., Søraas, F., Oksavik, K., et al. (2015). In flight calibration of NOAA POES proton detectors — Derivation of the MEPED correction factors. *Journal of Geophysical Research: Space Physics*, *120*, 9578 – 9593. https://doi.org/10.1002/2015JA021388

Schoeberl, M., Douglass, A., Hilsenrath, E., Bhartia, P., Beer, R., Waters, J., et al. (2006). Overview of the EOS Aura mission. *Geoscience and Remote Sensing, IEEE Transactions on*, *44*(5), 1066 – 1074. https://doi.org/10.1109/TGRS.2005.861950

Seppälä, A., Lu, H., Clilverd, M. A., & Rodger, C. J. (2013). Geomagnetic activity signatures in wintertime stratosphere wind, temperature, and wave response. *Journal of Geophysical Research: Atmospheres*, *118*, 2169 – 2183. https://doi.org/10.1002/jgrd.50236

Seppälä, A., Randall, C. E., Clilverd, M. A., Rozanov, E., & Rodger, C. J. (2009). Geomagnetic activity and polar surface air temperature variability. *Journal of Geophysical Research: Space Physics*, *114*, A10312. https://doi.org/10.1029/2008JA014029

Shapiro, A. V., Rozanov, E., Shapiro, A. I., Wang, S., Egorova, T., Schmutz, W., et al. (2012). Signature of the 27-day solar rotation cycle in mesospheric OH and H_2O observed by the Aura Microwave Limb Sounder. *Atmospheric Chemistry and Physics*, *12*(7), 3181 – 3188. https://doi.org/10.5194/acp-12-3181-2012

Sinnhuber, M., Nieder, H., & Wieters, N. (2012). Energetic particle precipitation and the chemistry of the mesosphere/lower thermosphere. *Surveys in Geophysics*, *33*, 1281 – 1334.

Solomon, S., Reid, G. C., Rusch, D. W., & Thomas, R. J. (1983). Mesospheric ozone depletion during the solar proton event of July 13, 1982 Part II. comparison between theory and measurements. *Geophysical Research Letters*, *10*(4), 257 – 260. https://doi.org/10.1029/GL010i004p00257

Solomon, S., Rusch, D., Gérard, J., Reid, G., & Crutzen, P. (1981). The effect of particle precipitation events on the neutral and ion chemistry of the middle atmosphere: II. Odd hydrogen. *Planetary and Space Science*, *29*(8), 885 – 893. https://doi.org/10.1016/0032-0633(81)90078-7

Swider, W., & Keneshea, T. (1973). Decrease of ozone and atomic oxygen in the lower mesosphere during a PCA event. *Planetary and Space Science*, *21*(11), 1969 – 1973. https://doi.org/10.1016/0032-0633(73)90126-8

Thorne, R. (1980). The importance of energetic particle precipitation on the chemical composition of the middle atmosphere. *Pure and applied geophysics*, *118*(1), 128 – 151. https://doi.org/10.1007/BF01586448

Turner, D. L., Shprits, Y., Hartinger, M., & Angelopoulos, V. (2012). Explaining sudden losses of outer radiation belt electrons during geomagnetic storms. *Nature Publishing Group*, *8*(3), 208 – 212. https://doi.org/10.1038/nphys2185

Turunen, E., Kero, A., Verronen, P. T., Miyoshi, Y., Oyama, S.-I., & Saito, S. (2016). Mesospheric ozone destruction by high-energy electron precipitation associated with pulsating aurora. *Journal of Geophysical Research: Atmospheres*, *121*, 11,852 – 11,861. https://doi.org/10.1002/2016JD025015JD025015

Turunen, E., Verronen, P. T., Seppälä, A., Rodger, C. J., Clilverd, M. A., Tamminen, J., et al. (2009). Impact of different energies of precipitating particles on NOx generation in the middle and upper atmosphere during geomagnetic storms. *Journal of Atmospheric and Solar-Terrestrial Physics*, *71*(10-11), 1,176 – 1,189. https://doi.org/10.1016/j.jastp.2008.07.005

Verronen, P. T., Andersson, M. E., Kero, A., Enell, C.-F., Wissing, J. M., Talaat, E. R., et al. (2015). Contribution of proton and electron precipitation to the observed electron concentration in October-November 2003 and September 2005. *Annales Geophysicae*, *33*(3), 381 – 394. https://doi.org/10.5194/angeo-33-381-2015

Verronen, P., Andersson, M., Rodger, C., Clilverd, M., Wang, S., & Turunen, E. (2013). Comparison of modeled and observed effects of radiation belt electron precipitation on mesospheric hydroxyl and ozone. *Journal of Geophysical Research: Atmospheres*, *118*, 11,419–11,428. https://doi.org/10.1002/jgrd.50845

Verronen, P. T., Rodger, C. J., Clilverd, M. A., Pickett, H. M., & Turunen, E. (2007). Latitudinal extent of the January 2005 solar proton event in the northern hemisphere from satellite observations of hydroxyl. *Annales Geophysicae*, *25*(10), 2203–2215. https://doi.org/10.5194/angeo-25-2203-2007

Verronen, P. T., Rodger, C. J., Clilverd, M. A., & Wang, S. (2011). First evidence of mesospheric hydroxyl response to electron precipitation from the radiation belts. *Journal of Geophysical Research: Atmospheres*, *116*, D07307. https://doi.org/10.1029/2010JD014965

Verronen, P. T., Seppälä, A., Kyrölä, E., Tamminen, J., Pickett, H. M., & Turunen, E. (2006). Production of odd hydrogen in the mesosphere during the January 2005 solar proton event. *Geophysical Research Letters*, *33*, L24811. https://doi.org/10.1029/2006GL028115

Waters, J. W., Froidevaux, L., Harwood, R. S., Jarnot, R. F., Pickett, H. M., Read, W. G., et al. (2006). The earth observing system microwave limb sounder (EOS MLS) on the Aura satellite. *IEEE Transaction Geoscience and Remote Sensing*, *44*(5), 1075–1092. https://doi.org/10.1109/TGRS.2006.873771

Webb, D. (1995). Solar and geomagnetic disturbances during the declining phase of recent solar cycles. *Advances in Space Research*, *16*(9), 57–69. https://doi.org/10.1016/0273-1177(95)00315-6

Weeks, L. H., Cuikay, R. S., & Corbin, J. R. (1972). Ozone measurements in the mesosphere during the solar proton event of 2 November 1969. *Journal of the Atmospheric Sciences*, *29*(6), 1138–1142.

Winick, J. R., Wintersteiner, P. P., Picard, R. H., Esplin, D., Mlynczak, M. G., Russell, J. M., et al. (2009). OH layer characteristics during unusual boreal winters of 2004 and 2006. *Journal of Geophysical Research: Space Physics*, *114*, A02303. https://doi.org/10.1029/2008JA013688

Yando, K., Millan, R. M., Green, J. C., & Evans, D. S. (2011). A Monte Carlo simulation of the NOAA POES medium energy proton and electron detector instrument. *Journal of Geophysical Research: Space Physics*, *116*, A10231. https://doi.org/10.1029/2011JA016671

Zawedde, A. E., Nesse Tyssøy, H., Hibbins, R., Espy, P. J., Ødegaard, L.-K. G., Sandanger, M. I., et al. (2016). The impact of energetic electron precipitation on mesospheric hydroxyl during a year of solar minimum. *Journal of Geophysical Research: Space Physics*, *121*, 5914–5929. https://doi.org/10.1002/2016JA022371

Paper III

III

Are EEP Events Important for the Tertairy Ozone Layer?

A. E. Zawedde, H. Nesse-Tyssøy, J. Stadsnes and M. I. Sandanger

To be submitted to the Journal of Geophysical Research: Space Physics

Confidential manuscript submitted to *JGR-Space Physics*

Are EEP events Important for the Tertiary Ozone Layer?

Annet Eva Zawedde[1*] Hilde Nesse Tyssøy[1], Johan Stadsnes[1], and Marit Irene Sandanger[1]

[1]Birkeland Centre for Space Science, Department of Physics and Technology, University of Bergen, Bergen, Norway.

Key Points:

- MLS provides a unique opportunity to study the direct impact of the EPP on OH and O_3
- There is limited overlap between the auroral zone and the tertiary ozone (O_3) layer at twilight conditions
- The importance of EEP on the tertiary O_3 layer is strongly governed by the background atmosphere

*,

Corresponding author: Annet Eva Zawedde, Annet.E.Zawedde@uib.no

Abstract

Energetic particle precipitation (EPP) increases the production of odd hydrogen (HO_X) species in the mesosphere which catalytically destroy ozone (O_3) in sunlight. Hence, the EPP-HO_X impact on the tertiary O_3 layer (TOL) depends on a complex geometry of a geographic-oriented TOL, geomagnetic-oriented auroral zone, producing short-lived HO_X species, and a destruction process depending on the solar zenith angle (SZA). Particle observations from the Medium Energy Proton and Electron Detectors telescopes aboard the Polar Orbiting Environmental Satellites, and hydroxyl (OH) and O_3 mixing ratios from Aura microwave limb sounder (MLS) are used to investigate the potential limitations of using the MLS observations to study EPP-OH impact on the TOL in the northern hemisphere. Our results show limited overlap between the auroral zone and the TOL at twilight conditions. A composite analysis indicates O_3 mixing ratio decrease over the auroral zone lagged by ∼1 day compared to the maximum EEP-OH impact. Hence, MLS is predominantly observing a lagged and lower estimate of the response of O_3 to EEP-OH at SZA>95°. The energetic electron precipitation (EEP) impact region winthin the TOL is smaller than the overlap region and is strongly modulated by the background atmospheric dynamics. The results, although limited by the satellites viewing conditions, imply that the importance of EEP upon O_3 mixing ratio is strongly influenced by the atmospheric background, both in terms of chemistry and dynamics. Multi-satellite observations at different solar local times are required to separate the direct from the lagged EEP-OH impact on O_3.

1 Introduction

In the high latitude nighttime winter mesosphere, a local ozone (O_3) maximum is formed at high solar zenith angles near the polar night terminator at approximately 72 km. This maximum, *Marsh et al.* [2001] called the tertiary ozone maximum, hereafter called the tertiary O_3 layer. It owes its existence to the grazing incidence of solar radiation leading to absorption and subsequently attenuation of radiation of wavelengths below 185 nm that photodissociate water vapor (H_2O) [see also *Sonnemann et al.*, 2006]. This in turn leads to absence of odd hydrogen (HO_X) production at the polar night terminator region, slowing down the catalytic cycles that destroy O_3. O_3 production, however, continues as the atmosphere is optically thin to wavelengths that dissociate molecular oxygen (O_2) which subsequently leads to formation of O_3. The absence of HO_X together with O_3 production leads to accumulation of O_3 which persists throughout the polar night due to the long chemical lifetime of O_3 in the polar night [see *Smith et al.*, 2009].

The long chemical lifetime of O_3 during the polar night makes O_3 susceptible to dynamics. As such the temporal and spatial distribution of the tertiary O_3 layer is modulated by the meridional circulation pattern with features that vary from year to year [e.g. *Sofieva et al.*, 2009; *Smith et al.*, 2009; *Damiani et al.*, 2010; *Smith et al.*, 2018]. In particular, dynamical processes driven by planetary wave activity are known to cause downwelling of polar air which brings along O_3 together with atomic oxygen (O) which is more abundant above 80 km. The air density at mesospheric altitudes is sufficient to allow the third-body reaction that forms O_3:

$$O + O_2 + M \rightarrow O_3 + M \tag{1}$$

Hence, in addition to the descending O_3, downwelling also contributes to increased O_3 production.

Periods of strong downwelling are observed more often in the northern hemisphere (NH) winters than in the southern hemisphere (SH) winters and are associated with sudden stratospheric warmings (SSWs). The warming of the stratosphere gives a corresponding cooling in the mesosphere after which there is warming in the mesosphere due to the

adiabatic downward motions of air. The descent of the nighttime OH layer during SSWs affects the formation of the tertiary O_3 layer through HO_X, provided there is sufficient atomic oxygen to facilitate the catalytic processes [see e.g. *Damiani et al.*, 2010]. Normally under polar night conditions there is little atomic oxygen since it is mainly produced during daytime through photodissociation of O_2:

$$O_2 + h\nu \rightarrow O + O \tag{2}$$

Therefore, near the polar night terminator where the tertiary O_3 layer forms, catalytic removal of O_3 is possible if the HO_X concentrations are boosted by the downwelling processes.

The distribution of the tertiary O_3 layer is also modified by energetic particle precipitation (EPP) through solar proton events (SPEs) and energetic electron precipitation (EEP) events. Precipitating energetic particles produce odd nitrogen (NO_X) and HO_X chemical species that catalytically destroy O_3. The catalytic cycles involving HO_X species, however, predominate throughout the mesosphere while NO_X catalytic cycles are most important in the stratosphere. The EPP driven HO_X effects on mesospheric O_3 have been long studied through simulations/modeling even before observations of OH were available [e.g. *Thorne*, 1980; *Crutzen and Solomon*, 1980; *Solomon et al.*, 1983; *Seppälä et al.*, 2006; *Sofieva et al.*, 2009]. With the availability of hydroxyl radical (OH) and O_3 observations from Aura microwave limb sounder (MLS), several observational and modeling studies have confirmed the SPE-HO_X link to mesospheric O_3 depletion [e.g. *Seppälä et al.*, 2006; *Damiani et al.*, 2008; *Sofieva et al.*, 2009; *Verkhoglyadova et al.*, 2015, 2016]. With the Aura MLS, several studies have also confirmed the importance of EEP on OH [e.g. *Verronen et al.*, 2011; *Andersson et al.*, 2012, 2014a; *Zawedde et al.*, 2016, 2018]. The impact of EEP on O_3 are, however, typically investigated without simultaneous OH measurements.

Andersson et al. [2014b] points out that the EEP impact on mesospheric O_3 might be a missing parameter driving dynamics, relevant for the atmosphere and the climate system [see also *Daae et al.*, 2012]. Using O_3 observations from three different satellite instruments, *Andersson et al.* [2014b] investigates the variability of O_3 for the years 2002 to 2012, focusing on EEP related changes in O_3. They report extremely large (up to 90%) short-term (days) O_3 depletion in the mesosphere, whose magnitude is comparable to those caused by large but much less frequent solar proton events. To assess the sensitivity and robustness of the short-term variability, they show a superposed epoch analysis of the 60 largest EEP events during all seasons. Since the tertiary O_3 layer is limited to wintertime conditions, the inclusion of events from the different seasons together in an analysis may lead to biased results depending on the number of events from each season included. .

Andersson et al. [2014b] quantify and report that the long term O_3 variability as derived from MLS is low (9%) compared to that derived from Global Ozone Monitoring by Occultation of Stars (GOMOS) and Sounding of the Atmosphere using Broadband Emission Radiometry (SABER) (21% and 34% respectively) for altitudes 70-78 km, which difference they attribute to the weaker electron forcing in 2005 (for MLS) than in 2003 (for GOMOS and SABER). Apart from the EEP forcing and the highly dynamic wintertime modulating O_3, there are limitations due to chemistry in that O_3 takes place in the presence of atomic oxygen which is mainly abundant during sunlit hours when it is produced by photodissociation of O_2 [see e.g. *Thorne*, 1980; *Aikin and Smith*, 1999; *Verronen et al.*, 2013; *Turunen et al.*, 2016]. This imposes limitations on the SZA at which O_3 reduction takes place, which consequently has implication on the geographical location of the reduction. Further, the region of electron precipitation (auroral zone) should coincide with the tertiary O_3 layer. Hence, to monitor the direct EEP-OH effect on O_3, the satellite must make observations at the SZA (or local times) at twilight, either in the morning or evening when the wintertime tertiary O_3 layer exists and there is abundant

atomic oxygen to allow catalytic O_3 reduction. Observations that do not overlap with the auroral zone, tertiary O_3 layer and sunlit or twilight conditions will be affected by the lifetime of OH and recovery time of O_3. Hence, observing an O_3 decrease during nighttime implies that the catalytic reduction has taken place earlier at the polar terminator. Lack of decrease during an EPP event may indicate that the potential O_3 reduction has not yet occurred due to lack of photolysis and atomic oxygen. During daytime, however, the O_3 reduction by EPP is hard to detect as the sunlight destroys O_3 efficiently, and an additional source would not be prominent.

In contrast to GOMOS and SABER, MLS also monitors OH and hence allows for a unique opportunity to study whether the apparent O_3 changes are correlated with OH. Moreover, there are scarcely any studies that observe EEP, OH and O_3 and hence could verify that the changes observed in O_3 are due to OH enhancement produced by EEP and not a change related to for example dynamics.

In this study, we investigate when the overlap between the tertiary O_3 layer and the auroral zone exists using Aura MLS O_3 observations for years 2005-2006. We identify the time and spatial locations at which EPP, and in particular EEP, may be important for the tertiary O_3 layer. With particle observations from the National Oceanic and Atmospheric Administration/ Polar Orbiting Environmental Satellites (NOAA/POES) Medium Proton and Electron Detectors (MEPED) 0° and 90° telescopes, we further explore the effects of EEP-OH on the tertiary O_3 layer for the same period of time. By selecting two pairs of EEP events and SPEs during the same wintertime conditions (same month), we study the relative importance of EEP events and SPEs. We also use MLS H_2O mixing ratio observations to evaluate the efficiency of the EPP-OH production, as well as temperature to monitor the vertical motion of air, in correlation analysis focusing on January 2005 and December 2006. Finally, a superposed epoch analysis is applied identifying EEP events occurring exclusively in the winter months evaluating the response on OH and O_3 mixing ratios simultaneously. The aim is to understand potential cavities using the MLS observations related to the EPP-OH impact on the tertiary O_3 layer in order to better assess the potential role of EPP as a driver in the Earth's atmosphere.

2 Data

2.1 Aura MLS Observations

The MLS instrument on board the National Aeronautics and Space Administration (NASA) Aura Satellite measures naturally occurring microwave thermal radiation from the limb of Earth's atmosphere to remotely sense vertical profiles of atmospheric constituents [*Waters et al.*, 2006; *Schoeberl et al.*, 2006]. In this study, we use Aura/MLS observations of the atmospheric constituents: temperature, H_2O, OH and O_3 mixing ratios for years 2005 to 2006 in the NH, sorted as described in the data quality and description document [*Livesey et al.*, 2015].

The OH background density is low during nighttime, making EPP related changes in OH easily detectable at night. Hence, similar to *Andersson et al.* [2014b], we use SZA $> 95°$ to include also observations under twilight conditions since catalytic destruction of O_3 requires atomic oxygen that is only abundant under sunlit conditions. Moreover, the HO_X chemical life time is of the order of hours in the region of interest, the mesosphere [*Pickett et al.*, 2006], hence OH is not significantly influenced by transport. The temporal, vertical and horizontal resolution of OH in the mesosphere is 25 s, 2.5 km and 165 km respectively. For temperature, H_2O, and O_3, the vertical and horizontal resolutions are coarser and vary within the mesosphere (62-75 km) [see *Livesey et al.*, 2015].

2.2 NOAA/POES Observations

The MEPED 0° and 90° telescopes which are part of the space environment monitor-2 instruments on board the NOAA/POES satellites provide measurements of fluxes of trapped and precipitating particles. For year 2005, we use particle data from NOAA-16 while for year 2006 particle data from NOAA-18 is utilized because these two satellites measures particles that are closest in time and space to the atmospheric observations made by the Aura satellite.

The MEPED electron data is known to be contaminated by low energy protons while the solid state detectors of the proton telescope are affected by degradation due to radiation damage [*Evans and Greer*, 2000]. The procedures for correcting the MEPED electron data are described in *Nesse Tyssøy et al.* [2016]. Using the correction factors derived by *Sandanger et al.* [2015] and *Ødegaard et al.* [2016], the proton fluxes are corrected for radiation damage before they are used to correct the electron data from proton contamination. The new optimized geometric factors lead to new electron channels energy thresholds as , >43 keV, >114 keV, >292 keV and >756 keV [*Ødegaard et al.*, 2017] of which the fourth channels is obtained from relativistic electrons contamination of the P6 channel of the proton telescope detectors [*Nesse Tyssøy et al.*, 2016].

With an anisotropic distribution of particles, with decreasing fluxes towards the center of the loss cone, the 0° and 90° telescopes tend to either underestimate or overestimate the fluxes of the precipitating particles respectively[*Rodger et al.*, 2010, 2013; *Nesse Tyssøy et al.*, 2016]. Therefore, a combination of measurements from the 0° and 90° telescopes together with electron pitch angle distributions from theory of wave-particle interaction, a complete bounce loss cone flux is derived for each of the electron energy channels [*Nesse Tyssøy et al.*, 2016]. A monotonic piecewise cubic Hermite interpolating polynomials (PCHIP) [*Fritsch and Carlson*, 1980] are fittted to the the integral fluxes which thereafter are converted into a differential electron spectrum (43-756 keV). This in turn is used to calculate the electron energy deposition as a function of altitude. The procedure which is described in *Nesse Tyssøy et al.* [2016] includes calculating the number of electrons per second that passes through a horizontal surface of size 1 cm^2 at 120 km altitude. We then find the isotropic flux that gives the same number of electrons per second passing through this unit horizontal area, which we refer to as the equivalent isotropic flux level over the bounce loss cone. Each energy interval is treated separately as the level of diffusion will depend on the particle energy. The energy deposition as a function of altitude is then calculated by using results of the *Rees* [1989] model, taking into account the cosine factor that enters when coverting from flux to particles passing through a horizontal unit surface. In these calculations we have used the COSPAR (COmmittte on SPAce research) 1986 Reference Atmosphere.

Proton fluxes used are a combination of measurements from the MEPED proton 0° telescope which measures the proton fluxes with energies >30 keV to >6900 keV and the omni-directional 0-60° detectors that measures the proton fluxes with energies >16 MeV to >70 MeV [see *Nesse Tyssøy et al.*, 2013; *Nesse Tyssøy and Stadsnes*, 2015]. At high latitudes, both the 0°-detector and the omni-detector measure protons in the loss cone, and isotropic fluxes are expected during SPEs. By fitting PCHIP to the measurement from both detectors, integral spectra are obtained from which the energy deposition height profiles are calculated based on the range energy of protons in air given by *Bethe and Ashkin* [1953]. The atmospheric densities are retrieved from the MSIS-E-90 model [*Hedin*, 1991]. We include the SPEs (>1000 particle flux units) during January-March 2005 and October-December 2006 presented in *Nesse Tyssøy and Stadsnes* [2015].

3 Methods and Results

In this study we focus on twilight-nighttime O_3 mixing ratios at the altitude location (about 73 km) of the tertiary O_3 layer in the NH. The Aura/MLS instrument retrieves OH at 73 km but does not retrieve temperature, O_3 mixing ratio, H_2O mixing ratio at this altitude. Hence, triangulation-based linear interpolation is used to obtain temperature, O_3 mixing ratio and H_2O mixing ratio at 73 km using measurements at 70 km and 75 km. For all maps in this study, mean values are calculated for each 5° latitude by 10° longitude bin between latitudes 40°-80°N and longitudes 180°W-180°E. Running means are calculated for every 3 longitude bins (30°) to smooth the plots. The data set is further sorted into five classes (or bins) based on the SZA: 95°-105°, 105°-115°, 115°-125°, 125°-135° and 135°-145° in order to differentiate between the in situ and lagged O_3 impact.

3.1 When is there Overlap Between the Tertiary Ozone Layer and the Auroral Zone?

Figure 1 shows the evolution of the monthly mean nighttime O_3 at 73 km altitude throughout the year 2005 in the NH. The approximate location of the CGM latitude band 55°N-70°N where EEP is expected, is indicated by the black oval lines, here referred to as the auroral zone. O_3 mixing ratio enhancements of between approximately 1.5-2.5 ppmv around the geographic pole are seen in January to March and October to December. This is the tertiary O_3 layer. It exhibits maximum extent in latitude, extending equator-ward to latitudes below 60°N during January and December 2005 in the NH. The same months exhibit the largest region of intersection (60°-120°W) between the auroral zone and the tertiary O_3 layer at 73 km altitude. For February and November the region of intersection is less as the extent of the tertiary O_3 layer is poleward of 60°N. During March and October, the O_3 mixing ratio is lower and the region of intersection is also smaller. The SZA distribution should be symmetric around winter solstice on 21 December. This means that the month October should on average have more nights with greater SZA than the month March. From April to September, the tertiary O_3 layer does not exist. The O_3 mixing ratio is less than 1 ppmv and for large parts of the polar cap (during May-July) there are no measurements at SZA (>95°).

For precipitation to have a potential impact on the mesospheric energy budget through reduction of O_3, it should take place in a region that is abundant with O_3. Further, the catalytic reactions require the presence of sunlight that photodissociates O_2 to produce atomic oxygen. Figure 2 shows the SLT (blue) and CGM latitudes (red) at which MLS-O_3 observations are made at the five SZA bands (95°-105°, 105°-115°, 115°-125°, 125°-135° and 135°-145°) during the months of year 2005. Also shown in panel 6 is the number of observations within the auroral zone at each SZA band expressed as a percentage of the total number of observations during each month of year 2005. For the 95°-105° SZA band (black line in panel 6) which coincides with morning hours, there are few or no O_3 measurements (0-12%) taken during mid-winter months January-February and November-December within the auroral zone. This implies that Aura/MLS barely observes the in situ reduction of O_3 by HO_X during the winter months. At other months (March-September) when the tertiary O_3 layer does not form, there are more measurements (23-71%) within the precipitation zone. The same behavior is seen for the SZAs 105°-115° band (red), which is nighttime, with decreasing measurements during summer months.

Figure 3 shows the monthly mean O_3 mixing ratio at 73 km for the five SZA bands, together with the number of measurements comprising each monthly mean. For the 95°-105° SZA band, maximum O_3 mixing ratio (about 1.8 ppmv) are seen in February, followed by October-December (about 1.75 ppmv) and January (about 1.4 ppmv). There is a trough between March to September with a minimum value of about 0.6 ppmv. The

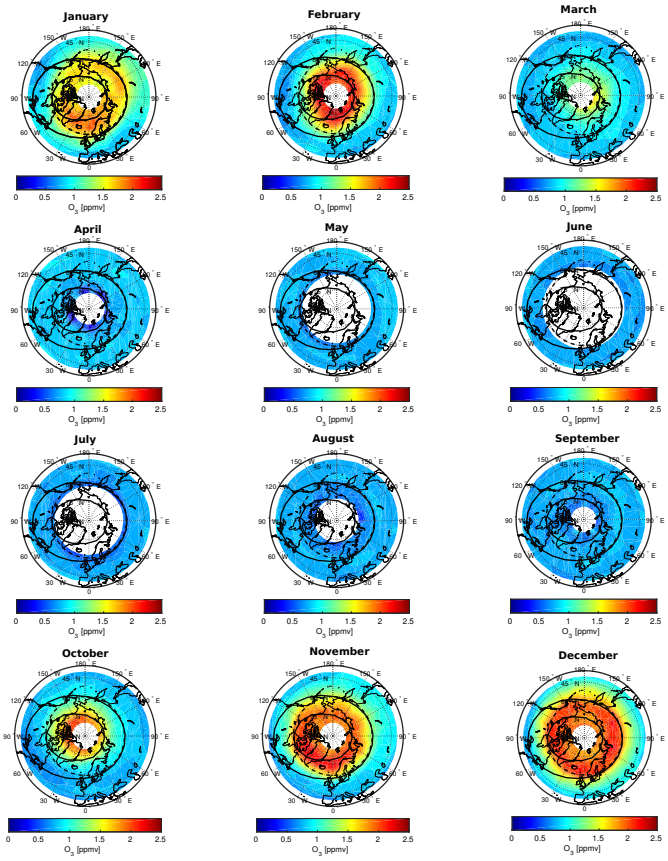

Figure 1. Overview maps showing monthly averaged nighttime O_3 at 73 km for January to December 2005 for SZA $> 95°$ in the NH. Mean values were calculated for each 5° latitude by 10° longitude bin between latitudes 40°-80°N and longitudes 180°W-180°E. The black oval lines shows the approximate locations of 55°N and 70°N CGM latitude, hence the latitude extent of the auroral zone or the footprint of the electron radiation belts. The black dashed lines represent the geographic latitude 60°N.

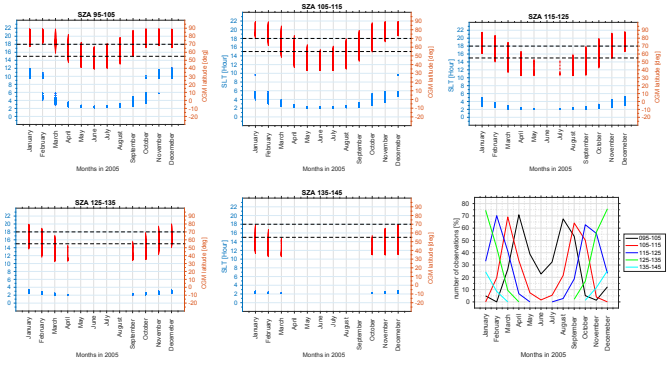

Figure 2. Panels 1-5: Plots showing the SLT and CGM latitude coverage for O_3 observations over different SZA bands for the geographical latitude band of 40°-80°N during the months of year 2005. The horizontal black dashed lines denote the CGM latitudes 55° and 70°N. **Panel 6:** The number of observations taken within the auroral zone at the different SZA bands, expressed as a percentage of the total number of observations taken within the latitude band 40°-80°N during each month of year 2005.

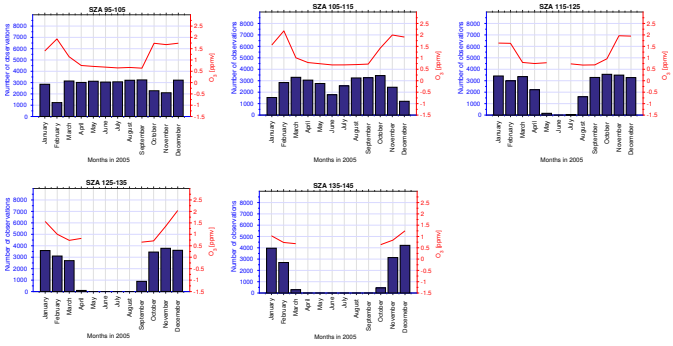

Figure 3. The red line shows the monthly averaged O_3 at 73 km over the different SZA bands for the geographical latitude band of 40°-80°N during the months of year 2005. The blue bar plots show the number of observations in each monthly mean respectively.

same kind of behavior is seen for the SZA band of 105°-115°. For the rest of the SZA bands (115°-145°), the maximum O_3 mixing ratio values during winter months progressively decrease with increasing SZA while there is progressively reducing observations during summer months as the SZA increases.

Figure 1 shows that considering all SZA >95° the tertiary O_3 layer exhibits maximum overlap with the auroral zone during the months of January and December 2005. When the data is sorted by the different SZA bands, however, the situation is quite different as there are fewer observations within the auroral zone for the SZA band of 95°-105° which corresponds to twilight hours during January and December 2005. At twilight the tertiary O_3 layer formation can take place as well as photodissociation of O_2 from which atomic oxygen forms, which is required for efficient catalytic removal of O_3. Since O_3 has a long lifetime (∼0.1-1 day) under polar night conditions at ∼73 km [*Smith et al.*, 2009], the evening twilight O_3 density will be maintained (constant) throughout the night. Since there is limited overlap between the tertiary O_3 layer and the auroral zone at twilight conditions, the MLS observations will predominantly show the premature or lagged O_3 response to EEP-OH within the auroral zone for SZAs>95°. The 95°-105° and 105°-115° SZA bands in Figure 3 show an O_3 reduction in January which is also evident in Figure 1. This O_3 reduction corresponds mainly to the January 2005 SPE [see e.g. *Seppälä et al.*, 2006; *Verronen et al.*, 2006; *Damiani et al.*, 2008]. The other SZA bands (115°-145°) which exhibit maximum overlap with the auroral zone do not exhibit a similar O_3 reduction in January.

A schematic of the geographical overlap between the tertiary O_3 layer and the auroral zone is illustrated in Figure 4 by the brown region. The magenta and red regions are parts of the tertiary O_3 layer that do not coincide with the precipitation zone while the green region is part of the oval that does not coincide with the tertiary O_3 layer. The

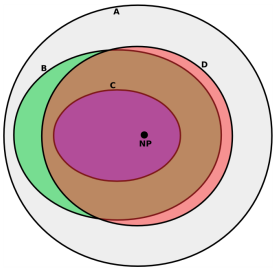

Figure 4. A schematic diagram showing the overlap between the tertiary O_3 layer and the auroral zone where electron precipitation is expected in the NH. This overlap is the region shown in color brown. The region in green represents the part of the auroral zone that does not coincide with the tertiary O_3 layer. Whereas the regions marked by red and magenta represent parts of the tertiary O_3 layer that do not coincide with the auroral zone. **A:** Outer boundary when looking down on the NH for example latitude 40°N. The acronym **NP** represents the geographic north pole. **B:** The CGM latitude 55°N. **C:** The CGM latitude 70°N. **D:** The latitude extent of the tertiary O_3 layer, defined based on the O_3 distribution of December 2005.

letters B and C represent the CGM latitudes 55°N and 70°N respectively while D is the latitude extent of the tertiary O_3 layer. The direct EEP-OH driven O_3 reduction is expected within the brown region during twilight, but measurements must also take place at the same time within that region to allow for direct observations of this effect. Otherwise, measurements taken at higher SZAs in that geographical region would detect the premature or lagged effect of EEP-OH on O_3.

3.2 The Effects of EPP-OH on the Tertiary O_3 Layer

To study the effects of EEP-OH on the tertiary O_3 layer in comparison to SPEs during wintertime conditions, the months January 2005 and December 2005 are chosen, during which there are both SPEs and EEP events. As pointed out above, these are the same months when the tertiary O_3 layer exhibits maximum overlap with the auroral zone. The SPEs periods are selected based on the list of SPEs (https://umbra.nascom.nasa.gov/SEP/) with >1000 particle flux units. EEP periods are selected based on the mean electron energy deposition at 73 km during the year 2005 to 2006. Periods with electron energy deposition above the mean value are considered EEP events, while those with electron energy deposition below the mean value are considered quiet time. This gives six and nine EEP days during January 2005 and December 2006 respectively. The quiet-time periods are each five days.

The month of January 2005 starts with EEP events (January 2-7), followed by a SPE (January 16-23) and a quiet-time period (January 25-29). The mean nighttime energy deposition, OH, O_3, H_2O mixing ratios and temperature at 73 km of which are shown in Figure 5. During these EEP events, the electron energy is deposited at all longitudes within the auroral precipitation zone, but significantly weaker in the sector 50°W-0°W. It does not show a one to one relationship with the OH enhancements. There are three apparent patches of OH enhancements within the latitude range of the radiation belts,

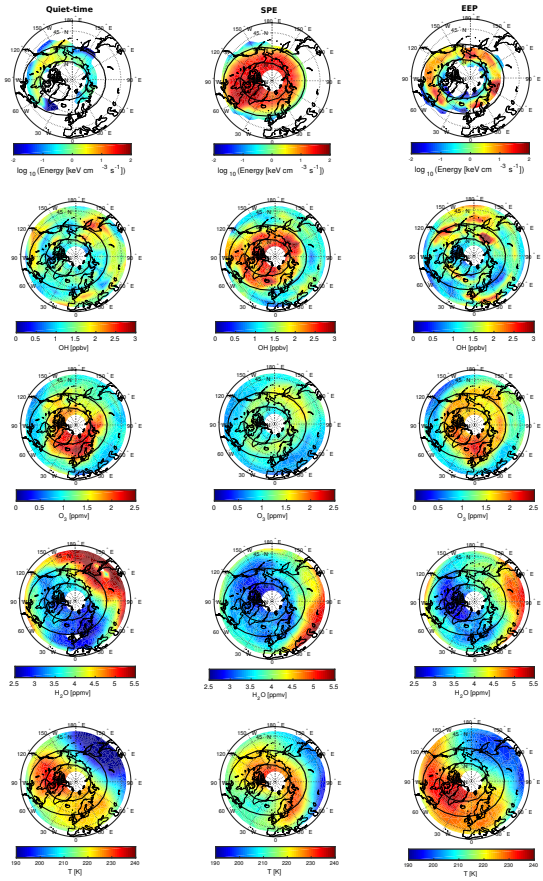

Figure 5. Mean nighttime distribution of energy deposition, OH, O_3 and H_2O for SZA $> 95°$ at 73 km within the geographical latitude band of 40°-80°N during the months of January 2005 for EEP (2-7 January), SPEs (16-23 January) and quiet time (25-31 January) periods. Mean values were calculated for each 5° latitude by 10° longitude bin between latitudes 40°-80°N and longitudes 180°W-180°E. The black oval lines show the approximate location of 55°N and 70°N CGM latitude.

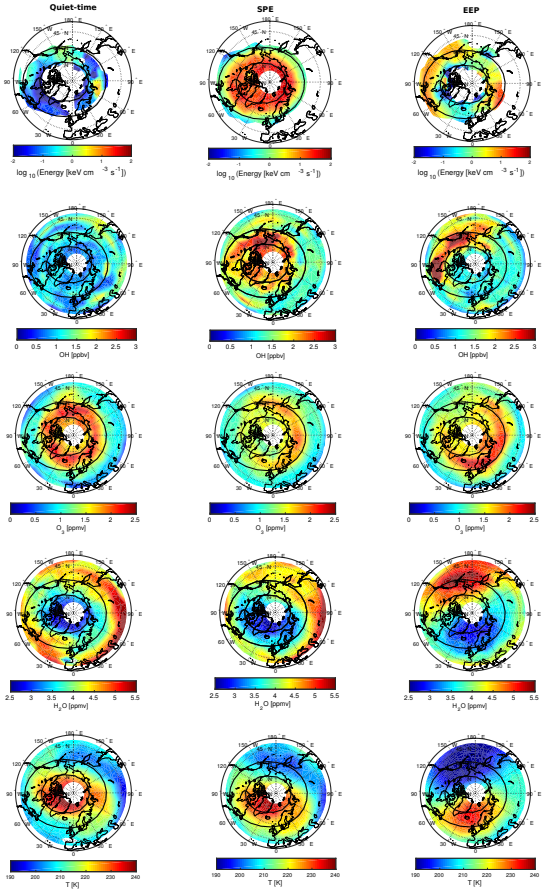

Figure 6. Mean nighttime distribution of energy deposition, OH, O_3 and H_2O for SZA $> 95^\circ$ at 73 km within the geographical latitude band of 40°-80°N during the months of December 2006 for quiet time (1-5 December), SPEs (6-16 December) and EEP (17-25 December) events. Mean values were calculated for each 5° latitude by 10° longitude bin between latitudes 40°-80°N and longitudes 180°W-180°E. The black oval lines show the approximate location of 55°N and 70°N CGM latitude.

but only one of them (90°E-180°E) seem to have a corresponding reduction in O_3, though not very distinct. This O_3 reduction occurs in the region in the auroral zone where high OH mixing ratio coincides with high H_2O mixing ratio. During the SPE, the proton energy is deposited more homogeneously within as well as poleward of the auroral zone. The corresponding OH enhancements exhibit structures that are not seen in the energy deposition. However, there is appreciable reduction in O_3 seen all over the geographic extent of the tertiary O_3 layer, corresponding with the OH enhancement all over the polar cap as well as the auroral zone. The quiet-time period exhibits some structure in OH mixing ratio within and outside the auroral zone (60°E-60°W), coinciding with the region with high H_2O mixing ratio. The geographic coverage of the tertiary O_3 layer is somewhat reduced in the quiet-time period due to seasonal effects (see Figure 1), but increased in intensity. There is also less O_3 in the region 120°E-60°W. Generally the low H_2O mixing ratios correspond to region with high temperatures, however, during quiet-time and SPE, the H_2O minima seem to be a bit out of phase with the temperature maxima.

The month of December 2006 starts with five days (December 1-5) of quiet-time period, followed by a SPE period (December 6-16) and then an EEP event (December 17-25) whose energy deposition, OH, O_3, H_2O mixing ratios and temperature maps at 73 km in the NH are shown in Figure 6. The quiet-time period in this case exhibits, lower energy deposition and lower OH mixing ratio than that during January 2005. Even in this quiet-time period, generally the region with relatively high OH mixing ratio corresponds to regions with high H_2O mixing ratio. The tertiary O_3 extends a few degrees equator-ward of the 60° latitude. During the SPE, the proton energy is deposited poleward of the 55° latitude, more intense toward the polar cap. The OH enhancement thereof is most intense within longitudes 90°E-90°W within the oval, corresponding with the region with high H_2O mixing ratio. The corresponding O_3 reduction is seen all over the tertiary layer. During EEP, the energy deposition exhibits two regions of enhanced values within longitudes 30°E-90°E and 180°E-60°W. Only the region within longitudes 180°E-60°W shows an OH enhancement, which extends to longitudes (130°E-180°E) not covered by electron precipitation. The entire region of OH enhancement (longitudes 130°E-60°W) corresponds to the region with high H_2O mixing ratio (Figure 6 right, bottom) and low O_3 mixing ratio. The energy deposited in the region within longitudes 30°E-90°E shows no OH enhancement and it corresponds to a region with low H_2O mixing ratio. The O_3 reduction seems to be modulated by EPP-OH, H_2O mixing ratio distribution and the dynamics governing the temperature at this altitude. Generally, in this case the H_2O minimum correspond to temperature maximum.

3.3 Correlation Analyses for two Winter Months

Spatially, there appears to be a negative correlation between the OH and O_3 mixing ratio during the SPE and EEP events in Figure 5 and 6. Due to the SZA dependence of OH and O_3, we proceed with correlation analysis based on the different SZA bands for January 2005 and December 2006. We calculate the daily means of the electron energy deposition, proton energy deposition, OH mixing ratio, O_3 mixing ratio, H_2O mixing ratio and temperature at 73 km for the five SZA bands: 95°-105°, 105°-115°, 115°-125°, 125°-135°, and 135°-145°. The days with SPEs are excluded from the correlation of O_3 with EEP and the AE index to exclude possible influence from SPEs. The daily mean AE index is included as a crude proxy for the EEP in case it is not captured by the single satellite measurements of the electron fluxes.

To find out if there is a linear relationship between O_3 and each of the variables: OH mixing ratio, AE, electron energy deposition, proton energy deposition, H_2O mixing ratio and temperature, we calculate Pearson's correlation coefficient, r, for all the five SZA bands at 73 km. The correlation analysis is performed on the time series for January 2005 and December 2006, the results of which are shown in Figure 7 (top) with the corresponding p-values (bottom). The correlation is deemed significant for p-value < 0.05

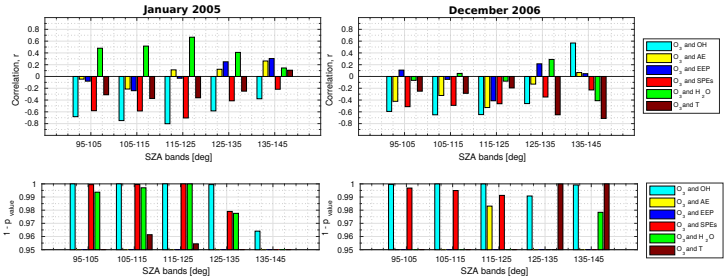

Figure 7. **Top:** Correlation between daily mean O_3 and the daily means of OH, AE index, electron energy deposition, proton energy deposition and H_2O for different SZA bands within the geographical latitude band of 40°-80°N for January 2005 (left) and December 2006 (right). The energy deposition, OH and O_3 are averages at 73 km. **Bottom:** The parameter 1-P_{value} indicates only the correlation deemed significant at 95% confidence interval (or p-value <0.05). The p-value which is the random chance probability of getting a significant correlation when the true correlation is zero.

(95% confidence interval). For January 2005, the variables OH, SPEs and H_2O exhibit significant correlation with O_3 at SZAs between 95° and 135°, with maximum correlations of -0.80, -0.70 and 0.67 occurring at the SZA band of 115-125°, corresponding to nighttime conditions. The magnitude of the respective correlations decreases for increasing or decreasing SZAs. Temperature exhibits maximum correlation of -0.37 at SZAs 135-145°. Both the AE index and EEP exhibit no significant correlation with O_3 at any of the SZAs. For December 2006, OH exhibits maximum correlation of -0.65 at SZAs 115-125°, corresponding to nighttime conditions. AE exhibits significant correlation (-0.53) only at SZAs 115-125 ° while EEP exhibits no significant correlation at any of the SZAs. SPEs exhibits maximum correlation (-0.51) at SZAs 95-105°, corresponding to twilight conditions, decreasing in magnitude as the SZA increases. While H_2O and temperature exhibit maximum correlations of -0.41 and -0.71 respectively at SZAs 135-145°.

The insignificant correlation of O_3 with EEP in both case studies may imply that EEP generally has no appreciable impact on the tertiary O3 layer. Reducing the number of observations (days) included in the correlation analysis when we remove days infested by SPEs might also play a part. The lack of correlation could, however, also be due to the viewing conditions of the MLS instrument. As shown in Figure 2, MLS is observing poleward of the auroral zone. This implies that in the twilight region where the direct O_3 reduction might occur, there is no significant electron energy deposition. If a potential O_3 reduction occurs here, it is related to EEP and OH produced in the auroral zone reducing the twilight O_3, and less O_3 is transported to these latitudes. In either case, it will not be correlated to the EEP energy deposited at these latitudes. At SZA >115° the lack of atomic oxygen prohibit EEP produced OH to effectively reduce O_3, hence there is little correlation between EEP and O_3. SPEs are not limited to the auroral zone, but impact the entire polar cap. Hence MLS will observe EEP produced OH in the presence of atomic oxygen, and subsequently the direct impact on O_3.

There are peculiar correlation tendencies seen in Figure 7 in that during winter 2005, H_2O shows positive correlation with O_3 at SZAs between 95° and 135° while during De-

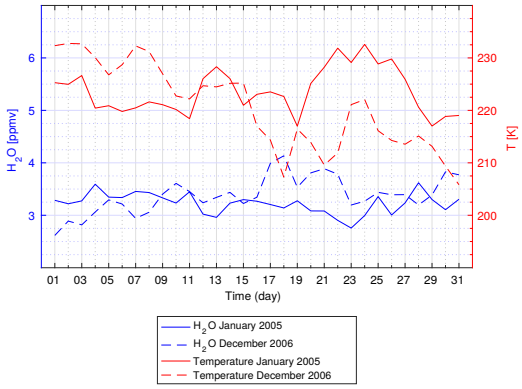

Figure 8. The daily mean H_2O (in blue) and temperature (in red) at 73 km for the SZA band of 95°-105° within the geographic latitude band of 40°-80°N. The plot for winter 2005 (January to March) is to the left while that of winter 2006 (October to December) is on the right.

cember 2006, the correlation between H_2O and O_3 is insignificant at SZAs 95° and 135°. This duality of H_2O, might reflect its role in the photochemistry and in the dynamics. On a closer inspection of the H_2O daily mean mixing ratio for the SZA band of 95°-105°, Figure 8 shows that there is less variability in H_2O and temperature (up to 0.86 ppmv and 16 K) during January 2005 as compared to December 2006 (up to 1.52 and 27 K). Low H_2O mixing ratios as seen in both January 2005 and December 2006 reflect the downward air motions associated with the mean meridional circulation during winter, bringing down dry air together with atomic oxygen and atomic hydrogen. The mesospheric air density allows atomic oxygen to participate in a three body reaction with molecular oxygen, forming O_3 by the reaction given by equation 1. At mesospheric altitudes, O_3 normally reacts with atomic hydrogen to form vibrationally excited OH (OH^*) [*Winick et al.*, 2009], which can be de-activated by either collisional quenching or by photon emission in the Meinel bands [*Brasseur and Solomon*, 2005]. In this case, in the presence of sunlight, O_3 can be reduced by the OH which will imply a positive correlation between O_3 and H_2O as seen in January 2005 [see also *Smith et al.*, 2018].

In addition, conditions of low temperature, O_3 is more readily created by the reaction in equation 1 and is destroyed more slowly through the reactions $O_3+O \rightarrow O_2+O_2$ and $O_3+H \rightarrow OH+O_2$, implying higher concentrations of O_3 [*Smith and Marsh*, 2005]. Based on photochemistry, O_3 and temperature are anti-correlated, implying that in conditions of high temperature there is less production of O_3. According to *Smith et al.* [2018, figure 13], a positive correlation is expected between O_3 and H_2O.

Based on Figure 8, there is a strong anti-correlation between H_2O and temperature in December 2006 which is consistent with a dynamical origin. In a different perspective, descending dry air implies low H_2O which in turn imply low production of HO_X species from photolysis of H_2O [see also *Smith et al.*, 2018]. Reduced production of HO_X implies reduced efficiency of the catalytic cycles that destroy O_3 leading to accumula-

Table 1. The list of EEP events based on the energy deposition at 73 km within the CGM latitude band of 55-70°N for winters of years 2005 to 2009.

Event	Date of EEP event
1	1-8 January 2005
2	11-15 January 2005
3	7-11 february 2005
4	26-28 January 2006
5	20-24 February 2006
6	18-31 December 2006
7	1-6 January 2007
8	17-28January 2007
9	29 January- 9 february 2007
10	14-29 February 2007
11	5-11 January 2008
12	12-21 January 2008

tion of O_3. In Figure 6, the H_2O minimum (predicting low HO_X, high O_3) are in phase with the temperature maximum (predicting low O_3). *Smith et al.* [2018] explains that in such a scenario the two processes counteract each other, hence the insignificant correlation for both H_2O and temperature exhibited by December 2006. Although, there are similar tendencies in January 2005, the variation in both variables is less. A difference between the two periods is also evident based on Figure 5 and 6 as the minima in H_2O and maxima in temperature are in phase in 2006, but slightly out of phase in 2005.

In summary, SPEs exhibit significant correlation with O_3 at SZAs between 95° and 135°, corresponding to nighttime-twilight conditions over a wide geographic area. The EEP events exhibit no significant correlation with O_3 at all SZAs considered, but the AE index exhibits a significant correlation at SZAs 115-125° for December 2006. This might be implying that there some small lagged response of O_3 to electron precipitation.

3.4 Superposed Epoch Analysis

Andersson et al. [2014b] applied a superposed epoch analysis of daily mean values within the CGM latitude band of 55-65°, to reveal the effect of EEP upon O_3 mixing ratio. In respect to the MLS observations, the majority of the events, however, did not include the period in time where the tertiary O3 layer exists, and has potentially strong biases due to low summer densities. Figure 9 illustrates a superposed epoch analysis of the electron energy deposition, OH and O_3 mixing ratios at altitudes close to the tertiary O_3 layer (67-75 km) for 12 winter EEP periods (listed in table 1) within the CGM latitude range of 55-70°N for years 2005 to 2009. Days for which the daily mean energy deposition is greater than the five year mean are considered EEP periods. Zero lag refer to the first day of the EEP period that exceeds the limit. The periods with SPEs are excluded from this analysis. The electron energy deposition exhibits steady rises from lag zero day, peaking at lag one day for 70-75 km altitudes, and at lag 2 days at 67 km altitude. The OH mixing ratio show a rise from lag zero to a peak at lags 1-2 days only for 70-75 km altitudes. The O_3 mixing ratio exhibits decreases at 67-75 km altitudes, with minima at lags 2-3 days. Hence there is a lag of at least a day between the EEP-OH increase and the O_3 VMR reduction [see also *Turunen et al.*, 2016]. Note, however, that there might also be a is a seasonal bias in the events as they almost exclusively occur in January and February, hence there is likely a seasonal decrease in the O_3 mixing ratio time evolution. At 73 and 75 km the O_3 reduction is up to approximately 15%.

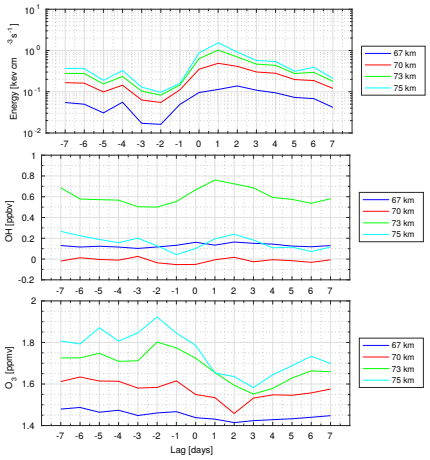

Figure 9. Superposed epoch analysis of the electron energy deposition, OH VMR and O_3 VMR for EEP events during the winters of years 2005 to 2009 at altitudes close to the tertiary O_3 layer (67-75 km) in the CGM latitude band of 55-70°N.

4 When and Where is EEP Important for the Tertiary O_3 Layer?

Aura MLS provide a unique opportunity to study if an apparent O_3 change is associated with OH produced by EEP. In this paper we investigate time and spatial locations at which the EEP-OH effects on the tertiary O_3 layer can be observed in order to better assess the EPP role on O_3 variability. We focus on the conditions and possible limitations of using Aura MLS O_3 observations in assessing the EEP-OH impact on O_3.

4.1 The General Formation and Sunrise behavior of O_3 Mixing Ratios Observed by Aura/MLS

The tertiary O_3 layer is formed near the winter polar night terminator (twilight conditions) at ∼72 km at latitudes close to 60°, extending poleward covering the polar cap. At sunset, solar Ly-α radiation that is responsible for photolysis of H_2O is cut off first due to the grazing incidence (large SZA) of solar radiation near the polar night terminator, making the atmosphere opaque to Ly-α radiation. Therefore, production of HO_X species is cutoff. The solar radiation in the Schumann-Runge bands have a much smaller O_2 absorption cross section than Ly-α has for H_2O [see *Sonnemann et al.*, 2006]. Thus, the production of atomic oxygen and hence O_3 increases in the absence of HO_X species. The high O_3 mixing ratios seen at SZA approximately >95° in Figure 10, very prominent during quiet-time, represent the tertiary O_3 layer at 73 km within the latitude band 40°-80°N during January 2005 (top) and December 2006 (bottom). At SZA approximately >130°, although still nighttime, the observations are progressively taken equator-ward, away from the latitude range of the tertiary O_3 layer as can be seen in Figure 11 (ex-

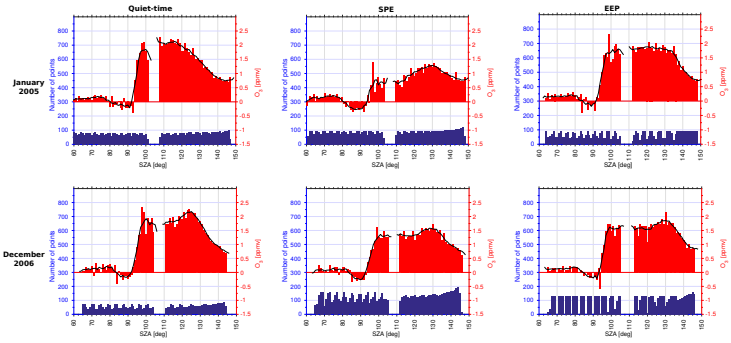

Figure 10. The variation of O_3 with SZA at 73 km within the geographical latitude band of 40°-80°N for January 2005 (top) and December 2006 (bottom). The red bars represent O_3 averages per SZA, calculated over the days during quiet-time, SPEs and EEP periods. The black line represents the running mean of O_3 mixing ratios, averaged over a window of 5°. The blue bars represent the number of observations involved in the averages.

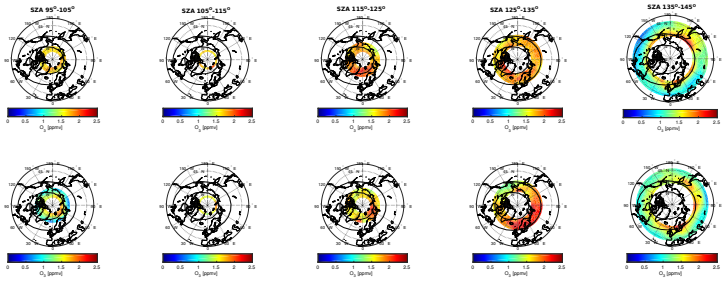

Figure 11. Monthly mean nighttime distribution of O_3 mixing ratio at 73 km for SZA bands between 95° and 145° within the geographical latitude band of 40°-80°N during January 2005 (top) and December 2006 (bottom). Mean values were calculated for each 5° latitude by 10° longitude bin between latitudes 40°-80°N and longitudes 180°W-180°E. The black oval lines shows the approximate location of 55°N and 70°N CGM latitude.

treme right). This explains the low O_3 mixing ratios for SZA approximately >130° in Figure 10.

At sunrise, rapid photodissociation of O_3 by sunlight causes a rapid decreases in O_3 density. As solar ultraviolet radiation of wavelengths greater than the Schumann-Runge absorption of O_2 (200nm< $\lambda \leq$240nm) penetrates, the O_3 mixing ratio increases [*Aikin and Smith*, 1999]. Although atomic oxygen is produced during this period, the efficiency of the catalytic cycles is low since production of HO_X species through photolysis of H_2O is reduced, hence the O_3 rise. Later as Ly-α radiation starts penetrating mesospheric altitudes, H_2O photolysis produces HO_X which catalytically destroys O_3 which is evident in Figure 10 at 80° <SZA<100°. Rapid photolysis of O_3 leads to low concentrations during daytime (SZA<80°).

4.2 The Conditions and Limitations for Observation of EEP-OH Effects on O_3

In Figure 4, the expected region of intersection between the precipitation zone and the tertiary O_3 layer is represented by the brown region, which may vary in latitude coverage depending on the strength of the event and the seasonal extent of the tertiary O_3 layer. The O_3 reduction occurs efficiently in the presence of abundant atomic oxygen which is required for the catalytic cycles. Although atomic oxygen is produced during EPP events, the amount formed by increased ionization is small compared to that produced by photodissociation [see e.g. *Aikin and Smith*, 1999; *Seppälä et al.*, 2006]. Therefore, sunlit conditions are required for effective catalytic O_3 reduction [*Turunen et al.*, 2016].

From Figure 1 it is clear that the maximum overlap between the oval and the tertiary O_3 layer occurs during December-January in the NH winter. When the data is sorted by the five SZA bands, O_3 reduction is seen in the month of January 2005 for SZA bands 95°-105° and 105°-115° in Figure 3. In December 2006, O_3 reduction extends from 95°-105° to 115°-125° (not shown). There is, however, very limited overlap between the O_3 measurements and the auroral zone during January and December for the SZA bands 95°-105° and 105°-115° as seen in Figure 2. The intersection of the auroral zone with O_3 observations increases by the SZA of 115°-125° and increases further with increasing SZA.

The Aura/MLS instrument mainly takes observations in the morning sector (LST 2-13), covering the morning twilight within the geographic location 40°-80°N [see also *Waters et al.*, 2006]. For the January 2005 and December 2006 SPEs shown in Figure 10, reduction in nighttime O_3 is seen starting at SZA ∼<135° as compared to the respective quiet-time periods. More reduction is seen at SZA ∼<120°. This kind of behavior is also seen for the December 2006 EEP event, but not distinctly for the January 2005 EEP event. Since there is O_3 reduction prior to morning twilight conditions, it implies that an EPP source was active at or before evening twilight although the satellite was not at this location at evening twilight. Hence, MLS is observing a lagged effect of a potential EEP-OH O_3 reduction.

MLS is observing in the morning twilight conditions for the SZA band of 95°-105° in the NH. In this SZA band, however, there is limited overlap between the oval and the tertiary O_3 layer as shown in Figure 2 and 11. In Figure 11 O_3 reduction at SZA 115°-125° within longitudes 100°E-160°E for the January 2005 EEP event (top). The same feature is seen at 125°-135° within longitudes 170°E-120°W for the December 2006 EEP event (bottom). There appears to be O_3 reduction associated with these two EEP events, whose measurements are taken at larger SZA within the precipitation zone. This implies that the observations at these large SZA are showing a lagged effect of EEP-OH on O_3. This could be the case since O_3 has a long recovery time [see *Smith et al.*, 2009]. To observe the direct and hence maximum effect of EEP-OH on O_3, observations should be

taken at twilight conditions, within the auroral zone during EEP events during wintertime when the tertiary O_3 layer forms.

Further, based on Figure 5 and 6, it appears that electron precipitation are more effective in a region that is abundant in H_2O. In fact for the December EEP event, there is no apparent OH enhancement observed in the region within longitudes 0°E-90°E despite the energy deposited there. H_2O is required for the formation of water cluster ions which are required in the process of EPP-OH formation [*Solomon et al.*, 1981]. The O_2^+ ion formed by ionization reacts with O_2, forming O_4^+ which uptakes H_2O, forming progressively larger water cluster ion at each stage of the reaction. The water cluster ions later dissociatively recombine with electrons forming H and OH ($\sim$2 HO_X per ionization). If the water cluster reactions are cut off by dissociative recombination with intermediates like O_4^+, then less than 2 HO_X per ionization are produced. This can occur if the H_2O mixing ratios reduce by a few ppb, then the natural electron concentrations may reduce the efficiency of EPP-HO_X production [*Solomon et al.*, 1983]. In recent study, *Zawedde et al.* [2018] report that H_2O is responsible for approximately 20% variability of OH mixing ratio at 73 km within geomagnetic latitudes 55-70°N (auroral zone) for year 2005 to 2009 whereas the EEP contribution is 7%.

4.3 Observation of the Tertiary O_3 Layer Within the Auroral Zone

Figures 5 and 6 show that during SPEs there is proton precipitation over the polar cap, extending to the auroral zone depending on the rigidity of the precipitating protons. There is corresponding OH enhancement, but most intense in regions with high H_2O mixing ratio which in turn is modulated by planetary wave activity [see e.g *Zawedde et al.*, 2016]. O_3 reduction is seen all over the latitude extent of the tertiary O_3 layer. *Zawedde et al.* [2018] show that SPEs contributes approximately 8% to the OH variability at 73 km within geomagnetic latitudes 55-70°N (auroral zone) for year 2005 to 2009. In the same Figures 5 and 6, electron precipitation seems to affect OH distribution and consequently O_3 more in regions rich in H_2O. Planetary wave activity seems to be modulating the longitudinal distribution of H_2O at 73 km, hence modulating the longitudinal distribution EPP-OH which in turn modulates the distribution of O_3. In this case we do not see the *Winick et al.* [2009] dynamical production of OH at this altitude, but the planetary wave modulates the distribution of H_2O which is required for the formation of water cluster ions from which OH and H, eventually form through dissociative recombination with electrons [see e.g *Solomon et al.*, 1981].

Taking a closer look on the EEP events, in Figure 5, the January EEP events seem to exhibit almost homogeneous energy deposition within the auroral zone. The respective OH production is, however, sparsely distributed within the oval with three patches of OH enhancement, with a less evident response in the O_3. The planetary wave in the H_2O distribution seems to place a trough in H_2O mixing ratios over much of the region of intersection between the auroral zone and the tertiary O_3 layer. For the January 2005 EEP event, *Andersson et al.* [2014b, Figure 2c] show up to approximately 35% O_3 loss at 70-75 km in the SH. During January, however, it is summer in the SH implying low O_3 mixing ratio during nighttime at mesospheric altitudes. Figure 1 shows that generally O_3 mixing ratios are <1 ppmv during summer. Therefore a reduction of for example 35% would imply approximately a change of <0.35 ppmv, implying that although the percentage may seem large, the actual values are really small compared with wintertime conditions. As such it would be more meaningful to perform the analysis in the winter hemisphere where there is abundant O_3 during nighttime as well as optimum intersection between the auroral zone and the tertiary O_3 layer [see also *Damiani et al.*, 2008, Figure 2].

Further during summer there is also restricted coverage by Aura MLS at high latitudes, also covering parts of the auroral zone as shown in Figure 1. In this case small

changes in the O_3 mixing ratio may result in large percentages that may portray a non realistic picture in regard to the EEP-OH impact on the tertiary O_3 layer. Therefore in a statistical study, if there are more events during summer than during winter, the results normally expressed as anomalies may be biased by the summer large percentages. In the *Andersson et al.* [2014b] super epoch analysis, only 6 of the 28 EEP events in the NH and 11 out of the 27 EEP events in the SH are from winter when the tertiary O_3 layer is present.

The December EEP events in Figure 6 exhibits OH mixing ratio enhancement in regions with high H_2O mixing ratio (longitudes 150°E-90°W). But still only a portion of the region of OH enhancement coincides with the latitude coverage of the tertiary O_3 layer. In this case, we see that part of the electron energy deposition (at longitudes 30°-90°E) has no response on OH mixing ratios and subsequently not on O_3 mixing ratio. Of the EEP-OH formed, still only a portion lies within the geographic location of the tertiary O_3 layer, and can have an effect on O_3 in the presence sunlight. Therefore for this case we see that only a very small portion of the energy deposition eventually could have effect on the O_3 mixing ratios.

Although the impact region may seem rather small, it is important to find out if the frequently occurring EEP events would have a significant impact on nighttime O_3, where it is abundant and hence potentially important for the energy budget. Figure 7 shows the correlation of O_3 with the variables OH, AE, electron energy deposition (EEP), proton energy deposition (SPEs), H_2O and temperature separately for January 2005 and December 2006. The SZAs 95-105° are considered to be under morning twilight conditions, therefore the EEP-OH that has accumulated over a few hours and the direct EEP-OH will have drastic impact on the O_3 mixing ratios through catalytic cycles. This is possible when solar radiation that photodissociates O_2 penetrates the atmosphere to mesospheric altitudes. A modeling study by *Turunen et al.* [2016] also shows that for EEP occurring before sunrise, the largest relative change in O_X species is not seen during the electron forcing, but after the HO_X catalytic cycles have had an impact in the morning.

EEP and AE exhibit insignificant correlation with O_3 at all SZAs considered except at 115-125° when the AE exhibits a significant correlation of -0.53 (r^2=28%) for December 2006. This significant correlation at nighttime SZAs indicates the possibility of a relationship between electron precipitation and lagged O_3. The lack of correlation between O_3 and EEP may be a result of the very little overlap between the auroral zone (region of electron precipitation) and the tertiary O_3 layer (see Figure 11), together with the modulation of H_2O distribution by planetary waves [see e.g. *Zawedde et al.*, 2016]. H_2O in turn modulates the production of EPP- HO_X by water cluster reactions [*Solomon et al.*, 1981]. The correlation analysis results are in line with the small impact area by electron precipitation already discussed, implying that EEP may actually have little impact on the tertiary O_3 layer. To investigate the direct effect, there is need for observations at twilight conditions within the auroral zone. The Aura MLS instrument barely makes observations at twilight within the auroral zone.

Therefore, by considering all SZA>95°, most of the O_3 reduction we see for example in Figure 6 is predominantly that which was reduced at evening twilight and has not yet recovered. With Aura MLS, we can only observe very little of the EEP-OH direct effect on O_3. This kind of limitation may also be present in some of the studies that have made the same SZA selection to study the EEP-OH direct effect. For example *Andersson et al.* [2014b] select SZA>95° for Aura MLS O_3 observations. In that case some portion of the O_3 anomaly reported might actually not be the direct EEP-OH effect on O_3 variability since O_3 takes some time to recover under polar night conditions [see *Smith et al.*, 2009].

The limitations are not as strict with SPEs since they precipitate over the entire polar cap, covering almost the entire geographic extent of the tertiary O_3 layer. Differ-

ent studies show that the January 2005 and December 2006 SPEs had a strong effect on the tertiary O_3 layer. *Seppälä et al.* [2006] report that the SIC model predicted >70% O_3 loss between 70-80 km during the January 2005 SPE. Whereas *Sofieva et al.* [2009] report a drop in O_3 mixing ratios at 65-70 km from ∼2 ppmv before the SPE to <0.5 ppmv after storm onset (>75%). These results are a bit higher than our results which show correlations of -0.58 and -0.41 (r^2 = 34% and 17%) for January 2005 and December 2006 SPEs respectively at SZAs 95-105° (twilight conditions). At larger SZAs (115-125°), however, our results for the January 2005 SPE show a higher correlation of -0.70 (49%).

The lack of correlation between EEP and O_3 mixing ratio reduction, might be due to the viewing conditions of the MLS. The superposed epoch analyses shows, however, a lagged O_3 mixing ratio reduction in response to EEP and OH enhancement. A lagged response was also shown in the study by *Turunen et al.* [2016]. Further, the distribution of the tertiary O_3 layer is influenced by planetary waves leading to longitudinal variations [*Smith et al.*, 2018]. more prominent in the NH winter. This makes it hard to see the direct impact of EEP on the tertiary O_3; the O_3 observed might not yet have been reduced, or might have already partly recovered. The planetary waves/dynamics tend to transport the O_3 away from the auroral zone, leading to mixing. Nevertheless, the superposed epoch analysis including both OH and O_3 implies that there is evidence for a subtle impact of EEP on the tertiary O_3 layer.

Therefore, for EEP to have an impact on O_3, it depends on a complex combination of the geographic intersection of the region of particle precipitation with the tertiary O_3 layer, the distribution of the background atmospheric constituents, planetary waves, and time of precipitation. The combination of all these factors results in a much smaller impact on O_3 from EEP than from SPEs. To quantitatively assess how much of the energy deposition actually affects O_3 requires a combination of particle observations from different satellites observing at different local times together with O_3 observations from different satellites at local times covering twilight conditions.

5 Summary and Conclusions

MLS is the only satellite-born instrument that simultaneously measures OH and O_3, and hence allows to study if the apparent O_3 changes are correlated with OH. There are very few studies that observe EEP, OH and O_3 and therefore are able to verify that the changes observed in O_3 are dues to OH enhancement produced by EEP and is not a change related to for example dynamics.

In this study we investigate when maximum overlap between the auroral zone and observation of the tertiary O_3 exists. We further investigate when in time and where in location EEP is important for the variability in the tertiary O_3 layer. By sorting the MLS data into 5 SZA bands, we use correlation analysis to find out the relationship between the variables OH, AE, energy deposition (protons and electrons), H_2O and temperature in the different SZA bands of Aura MLS.

Our results show that maximum overlap between the auroral zone and the tertiary O_3 layer exists during winter: January and December in the NH. In the periods considered, the months January 2005 and December 2006 are active with both SPEs and EEP events. Generally there is limited overlap between the auroral zone where EEP is expected and the location of the tertiary O_3 layer which varies in size in the different winter months. Furthermore, there is limited overlap between the oval and the tertiary O_3 layer when Aura MLS is observing in the SZA band of 95°-105° at which morning twilight conditions are expected.

Therefore, for SZA>95° in the NH the Aura MLS barely observes the direct EEP-OH effect on the tertiary O_3 layer. Within the auroral zone, the MLS instrument pre-

dominantly observes the O_3 that was impacted at evening twilight and it is yet to recover from the impact. This makes it tricky to make confident deductions on the EEP-OH impact on the tertiary O_3 layer.

The case studies considered show that only a portion of the electron energy deposition will result in OH formation, as it appears to be strongly depending on the geographic distribution of H_2O. Further, only a portion of the EEP-OH formed will be able to impact the tertiary O_3 layer at twilight conditions depending on its geographic extent. This results in a much smaller EEP impact region within the geographic extent of the tertiary O_3 layer as compared with the impact region of SPEs which cover almost the entire extent of the tertiary O_3 layer. The correlation analysis also shows no significant relationship between electron precipitation and the tertiary O_3 layer, but an indication of possible relationship with lagged O_3 at nighttime SZAs. The superposed epoch analysis, however, indicates O_3 mixing ratio decrease over the auroral zone lagged by 1 day compared to the maximum EEP-OH impact. This implies that the importance of EEP upon the O_3 mixing ratio is strongly influenced by the atmospheric background both in terms of chemistry and dynamics.

A quantitative assessment needs multi satellite measurements of both O_3 and EEP at different solar local times, covering evening to morning twilight conditions, to separate the direct EEP-OH effect on O_3 from the delayed effect. In the same respect, to quantify how much of the electron precipitation eventually affects O_3, observations at twilight conditions are required. It is also necessary to account for the variability due to the background atmospheric dynamics as they affect the O_3 distribution through H_2O and temperature, and redistributes the O_3 anomalies.

Acknowledgments

This study was supported by the Research Council of Norway under contract 223252/F50. The authors thank the NOAA's National Geophysical Data Center (NGDS) for providing NOAA data (https://satdat.ngdc.noaa.gov/), and NASA Goddard Earth Science Data and Information Services Center (GES DISC) for providing Aura/MLS data (https://mls.jpl.nasa.gov/).

References

Aikin, A. C., and H. J. P. Smith (1999), Mesospheric constituent variations during electron precipitation events, *Journal of Geophysical Research: Atmospheres*, *104*(D21), 26,457–26,471, doi:10.1029/1999JD900752.

Andersson, M. E., P. T. Verronen, S. Wang, C. J. Rodger, M. A. Clilverd, and B. R. Carson (2012), Precipitating radiation belt electrons and enhancements of mesospheric hydroxyl during 2004-2009, *Journal of Geophysical Research: Atmospheres*, *117*(D9), doi:10.1029/2011JD017246.

Andersson, M. E., P. T. Verronen, C. J. Rodger, M. A. Clilverd, and S. Wang (2014a), Longitudinal hotspots in the mesospheric OH variations due to energetic electron precipitation, *Atmospheric Chemistry and Physics*, *14*(2), 1095–1105, doi:10.5194/acp-14-1095-2014.

Andersson, M. E., P. T. Verronen, C. J. Rodger, M. A. Clilverd, and A. Seppälä (2014b), Missing driver in the Sun-Earth connection from energetic electron precipitation impacts mesospheric ozone, *Nature Communications*, *5*(5197), doi:10.1038/ncomms6197.

Bethe, H. A., and J. Ashkin (1953), *Part II of Experimental Nuclear Physics*, vol. 1, chap. Passage of radiations through matter, John Wiley & Sons, New York.

Brasseur, G. P., and S. Solomon (2005), *Aeronomy of the Middle Atmosphere: Chemistry and Physics of the Stratosphere and Mesosphere*, Springer.

Crutzen, P. J., and S. Solomon (1980), Response of mesopheric ozone to particle precipitation, *Planetary and Space Science*, *28*(12), 1147 – 1153, doi:10.1016/0032-0633(80)90073-2.

Daae, M., P. Espy, H. Nesse Tyssøy, D. Newnham, J. Stadsnes, and F. Søraas (2012), The effect of energetic electron precipitation on middle mesospheric nighttime ozone during and after a moderate geomagnetic storm, *Geophysical Research Letters*, *39*(21), doi:10.1029/2012GL053787, L21811.

Damiani, A., M. Storini, M. Laurenza, and C. Rafanelli (2008), Solar particle effects on minor components of the polar atmosphere, *Annales Geophysicae*, *26*(2), 361–370, doi:10.5194/angeo-26-361-2008.

Damiani, A., M. Storini, M. L. Santee, and S. Wang (2010), Variability of the nighttime OH layer and mesospheric ozone at high latitudes during northern winter: influence of meteorology, *Atmospheric Chemistry and Physics*, *10*(21), 10,291–10,303, doi:10.5194/acp-10-10291-2010.

Evans, D., and M. Greer (2000), *Polar Orbiting Environmental Satellite Space Environment Monitor - 2: Instrument Descriptions and Archive Data Documentation*, Space Environment Center, Boulder, Colorado, 1.4 ed.

Fritsch, F. N., and R. E. Carlson (1980), Monotone piecewise cubic interpolation, *SIAM Journal on Numerical Analysis*, *17*(2), 238–246.

Hedin, A. E. (1991), Extension of the MSIS thermosphere model into the middle and lower atmosphere, *Journal of Geophysical Research: Space Physics*, *96*(A2), 1159–1172, doi:10.1029/90JA02125.

Livesey, N. J., W. G. Read, P. A. Wagner, L. Froidevaux, A. Lambert, G. L. Manney, L. F. M. Valle, H. C. Pumphrey, M. L. Santee, M. J. Schwartz, S. Wang, R. A. Fuller, R. F. Jarnot, B. W. Knosp, and E. Martinez (2015), *Earth Observing system(EOS) Aura Microwave Limb Sounder(MLS) Version 4.2x Level 2 data quality and description document.*, Jet Propulsion Laboratory, California Institute of Technology, Pasadena, California, 91109-8099, version 4.2x-1.0 ed.

Marsh, D., A. Smith, G. Brasseur, M. Kaufmann, and K. Grossmann (2001), The existence of a tertiary ozone maximum in the high-latitude middle mesosphere, *Geophysical Research Letters*, *28*(24), 4531–4534, doi:10.1029/2001GL013791.

Nesse Tyssøy, H., and J. Stadsnes (2015), Cutoff latitude variation during solar proton events: Causes and consequences, *Journal of Geophysical Research: Space Physics*, *120*(1), 553–563, doi:10.1002/2014JA020508.

Nesse Tyssøy, H., J. Stadsnes, F. Søraas, and M. Sørbø (2013), Variations in cutoff latitude during the January 2012 solar proton event and implication for the distribution of particle energy deposition, *Geophysical Research Letters*, *40*(16), 4149–4153, doi:10.1002/grl.50815.

Nesse Tyssøy, H., M. I. Sandanger, L.-K. G. Ødegaard, J. Stadsnes, A. Aasnes, and A. E. Zawedde (2016), Energetic electron precipitation into the middle atmosphere-constructing the loss cone fluxes from MEPED POES, *Journal of Geophysical Research: Space Physics*, *121*(6), 5693–5707, doi:10.1002/2016JA022752.

Ødegaard, L.-K. G., H. Nesse Tyssøy, M. I. J. Sandanger, J. Stadsnes, and F. Søraas (2016), Space weather impact on the degradation of NOAA POES MEPED proton detectors, *J. Space Weather Space Clim.*, *6*, A26, doi:10.1051/swsc/2016020.

Ødegaard, L.-K. G., H. Nesse Tyssøy, F. Søraas, J. Stadsnes, and M. I. Sandanger (2017), Energetic electron precipitation in weak to moderate corotating interaction region-driven storms, *Journal of Geophysical Research: Space Physics*, *122*(3), 2900–2921, doi:10.1002/2016JA023096.

Pickett, H. M., W. G. Read, K. K. Lee, and Y. L. Yung (2006), Observation of night OH in the mesosphere, *Geophysical Research Letters*, *33*(19), doi:10.1029/2006GL026910.

Rees, M. H. (1989), *Physics and Chemistry of the Upper Atmosphere (Cambridge Atmospheric and Space Science Series)*, Cambridge University Press.

Rodger, C. J., M. A. Clilverd, J. C. Green, and M. M. Lam (2010), Use of POES SEM-2 observations to examine radiation belt dynamics and energetic electron precipitation into the atmosphere, *Journal of Geophysical Research: Space Physics*, *115*(A4), doi:10.1029/2008JA014023.

Rodger, C. J., A. J. Kavanagh, M. A. Clilverd, and S. R. Marple (2013), Comparison between POES energetic electron precipitation observations and riometer absorptions: Implications for determining true precipitation fluxes, *Journal of Geophysical Research: Space Physics*, *118*(12), 7810–7821, doi:10.1002/2013JA019439.

Sandanger, M. I., L. K. G. Ødegaard, H. Nesse Tyssøy, J. Stadsnes, F. Søraas, K. Oksavik, and K. Aarsnes (2015), In-flight calibration of NOAA POES proton detectors - derivation of the MEPED correction factors, *Journal of Geophysical Research: space Physics*, *120*(9), 9578–9593, doi:10.1002/2015JA021388.

Schoeberl, M., A. R. Douglass, E. Hilsenrath, P. K. Bhartia, R. Beer, J. W. Waters, M. R. Gunson, L. Froidevaux, J. C. Gille, J. J. Barnett, P. F. Levelt, and P. DeCola (2006), Overview of the EOS Aura mission, *Geoscience and Remote Sensing, IEEE Transactions on*, *44*(5), 1066–1074, doi:10.1109/TGRS.2005.861950.

Seppälä, A., P. T. Verronen, V. F. Sofieva, J. Tamminen, E. Kyrl, C. J. Rodger, and M. A. Clilverd (2006), Destruction of the tertiary ozone maximum during a solar proton event, *Geophysical Research Letters*, *33*(7), doi:10.1029/2005GL025571.

Smith, A. K., and D. R. Marsh (2005), Processes that account for the ozone maximum at the mesopause, *Journal of Geophysical Research: Atmospheres*, *110*(D23), doi:10.1029/2005JD006298.

Smith, A. K., M. López-Puertas, M. García-Comas, and S. Tukiainen (2009), SABER observations of mesospheric ozone during NH late winter 20022009, *Geophysical Research Letters*, *36*(23), doi:10.1029/2009GL040942, l23804.

Smith, A. K., P. J. Espy, M. López-Puertas, and O. V. Tweedy (2018), Spatial and temporal structure of the tertiary ozone maximum in the polar winter mesosphere, *Journal of Geophysical Research: Atmospheres*, *123*(0), 4373–4389, doi:10.1029/2017JD028030.

Sofieva, V. F., E. Kyrölä, P. T. Verronen, A. Seppälä, J. Tamminen, D. R. Marsh, A. K. Smith, J.-L. Bertaux, A. Hauchecorne, F. Dalaudier, D. Fussen, F. Vanhellemont, O. F. d'Andon, G. Barrot, M. Guirlet, T. Fehr, and L. Saavedra (2009), Spatio-temporal observations of the tertiary ozone maximum, *Atmospheric Chemistry and Physics*, *9*(13), 4439–4445, doi:10.5194/acp-9-4439-2009.

Solomon, S., D. Rusch, J. Gérard, G. Reid, and P. Crutzen (1981), The effect of particle precipitation events on the neutral and ion chemistry of the middle atmosphere: II. odd hydrogen, *Planetary and Space Science*, *29*(8), 885 – 893, doi:10.1016/0032-0633(81)90078-7.

Solomon, S., G. C. Reid, D. W. Rusch, and R. J. Thomas (1983), Mesospheric ozone depletion during the solar proton event of july 13, 1982 part II. comparison between theory and measurements, *Geophysical Research Letters*, *10*(4), 257–260, doi:10.1029/GL010i004p00257.

Sonnemann, G., M. Grygalashvyly, P. Hartogh, and C. Jarchow (2006), Behavior of mesospheric ozone under nearly polar night conditions, *Advances in Space Research*, *38*(11), 2402 – 2407, doi:10.1016/j.asr.2006.09.011.

Thorne, R. (1980), The importance of energetic particle precipitation on the chemical composition of the middle atmosphere, *Pure and applied geophysics*, *118*(1), 128–151, doi:10.1007/BF01586448.

Turunen, E., A. Kero, P. T. Verronen, Y. Miyoshi, S.-I. Oyama, and S. Saito (2016), Mesospheric ozone destruction by high-energy electron precipitation associated with pulsating aurora, *Journal of Geophysical Research: Atmospheres*, *121*(19),

11,852–11,861, doi:10.1002/2016JD025015, 2016JD025015.

Verkhoglyadova, O. P., S. Wang, M. G. Mlynczak, L. A. Hunt, and G. P. Zank (2015), Effects of two large solar energetic particle events on middle atmosphere nighttime odd hydrogen and ozone content: Aura/mls and timed/saber measurements, *Journal of Geophysical Research: Space Physics*, *120*(1), 12–29, doi:10.1002/2014JA020609.

Verkhoglyadova, O. P., J. M. Wissing, S. Wang, M.-B. Kallenrode, and G. P. Zank (2016), Nighttime mesospheric hydroxyl enhancements during sep events and accompanying geomagnetic storms: Ionization rate modeling and aura satellite observations, *Journal of Geophysical Research: Space Physics*, *121*(7), 6017–6030, doi:10.1002/2015JA022217.

Verronen, P., M. E. Andersson, C. J. Rodger, M. A. Clilverd, S. Wang, and E. Turunen (2013), Comparison of modeled and observed effects of radiation belt electron precipitation on mesospheric hydroxyl and ozone, *Journal of Geophysical Research: Atmospheres*, *118*(19), 11,419–11,428, doi:10.1002/jgrd.50845.

Verronen, P. T., A. Seppälä, E. Kyrölä, J. Tamminen, H. M. Pickett, and E. Turunen (2006), Production of odd hydrogen in the mesosphere during the January 2005 solar proton event, *Geophysical Research Letters*, *33*(24), doi:10.1029/2006GL028115.

Verronen, P. T., C. J. Rodger, M. A. Clilverd, and S. Wang (2011), First evidence of mesospheric hydroxyl response to electron precipitation from the radiation belts, *Journal of Geophysical Research: Atmospheres*, *116*(D07307), doi:10.1029/2010JD014965.

Waters, J. W., L. Froidevaux, R. S. Harwood, R. F. Jarnot, H. M. Pickett, W. G. Read, P. H. Siegel, R. E. Cofield, M. J. Filipiak, D. A. Flower, J. R. Holden, G. K. Lau, N. J. Livesey, G. L. Manney, H. C. Pumphrey, M. L. Santee, D. L. Wu, D. T. Cuddy, R. R. Lay, M. S. Loo, V. S. Perun, M. J. Schwartz, P. C. Stek, R. P. Thurstans, M. A. Boyles, K. M. Chandra, M. C. Chavez, G.-S. Chen, B. V. Chudasama, R. Dodge, R. A. Fuller, M. A. Girard, J. H. Jiang, Y. Jiang, B. W. Knosp, R. C. LaBelle, J. C. Lam, K. A. Lee, D. Miller, J. E. Oswald, N. C. Patel, D. M. Pukala, O. Quintero, D. M. Scaff, W. V. Snyder, M. C. Tope, P. A. Wagner, and M. J. Walch (2006), The earth observing system microwave limb sounder (EOS MLS) on the Aura satellite., *IEEE T. Geoscience and Remote Sensing*, *44*(5), 1075–1092, doi:10.1109/TGRS.2006.873771.

Winick, J. R., P. P. Wintersteiner, R. H. Picard, D. Esplin, M. G. Mlynczak, J. M. Russell, and L. L. Gordley (2009), OH layer characteristics during unusual boreal winters of 2004 and 2006, *Journal of Geophysical Research: Space Physics*, *114*(A2), doi:10.1029/2008JA013688.

Zawedde, A. E., H. Nesse Tyssøy, R. Hibbins, P. J. Espy, L.-K. G. Ødegaard, M. I. Sandanger, and J. Stadsnes (2016), The impact of energetic electron precipitation on mesospheric hydroxyl during a year of solar minimum, *Journal of Geophysical Research: Space Physics*, *121*(6), 5914–5929, doi:10.1002/2016JA022371.

Zawedde, A. E., H. NesseTyssøy, J. Stadsnes, and M. I. Sandanger (2018), The impact of energetic particle precipitation on mesospheric oh - variability of the sources and the background atmosphere, *Journal of Geophysical Research: Space Physics*, *0*(ja), doi:10.1029/2017JA025038.

Appendix

Some Definitions

AE index is intended to put a measure on the maximum auroral activity.

Dst index is intended to give a measure of the strength of the ring current by measuring the negative excursion in the horizontal component of the Earth's magnetic field.

kp index is intended to be a measure of the global level of geomagnetic activity.

Adiabatic invariants are quantities that can be treated as characteristics constants of a particle, which may change but only slowly compared with the respective time scales (or some typical periodicities of the particle motion) [Baumjohann and Treumann, 1996]. For example the three basic particle motions are associated with adiabatic invariants that are conserved for slowly changing magnetic fields within their respective timescales.

The first adiabatic invariant (ϕ_μ) is associated with the magnetic flux within a gyro period given by [Baumjohann and Treumann, 1996]:

$$\phi_\mu = \frac{2\pi m}{q^2}\mu = constant \tag{1}$$

where ϕ_μ is the magnetic flux, m is the particle mass, q is the charge and μ is the magnetic moment. It implies that as a particle moves into a region of stronger magnetic field, the gyro-radius of the particle will get increasingly smaller, so that the magnetic flux encircled by the orbit remains constant.

The second adiabatic invariant (J). As a particle gyrating over a magnetic field line moves into the converging field at either hemispheres, it will be reflected in the region of high magnetic field at the mirror points and it can bounce between the mirror points at a bounce frequency ω_b such that: [Baumjohann and Treumann, 1996].

$$J = \oint m v_{||}\, ds \tag{2}$$

where V|| is the parallel particle velocity, ds is an element of the guiding center path. J is conserved for electromagnetic variations with frequency $\omega < \omega_b$ if the changes in the field are slow.

The third adiabatic invariant (ϕ). If $\omega <$ the drift frequency (ω_d), the magnetic flux enclosed by the drift orbit is given by [Baumjohann and Treumann, 1996]:

$$\phi = \frac{2\pi m}{q^2} M = constant \tag{3}$$

where M is the magnetic moment of the antisymmetric magnetic field.
$\mathbf{L}^*$ is the equatorial distance in Earth radii (R_E) from the center of the Earth to a drift shell if the Earth is considered a dipole.

$$L^* = \frac{2\pi M}{\phi R_E} \tag{4}$$

L-shell is the equatorial distance to a magnetic field line measured in Earth radii.
Pitch angle (α) is the angle between the particle's velocity vector and the local magnetic field line:

$$\alpha = tan^{-1} \frac{v_\perp}{v_\parallel} \tag{5}$$

where v_{perp} and $v_{parallel}$ are the perpendicular and parallel components of the particle velocity.
Relative sunspot number (R) is a measure of the number or groups of sunspots visible on the solar surface, according to the formula [see e.g. Lockwood et al., 2014]:

$$R = \kappa(10N_g + N_s) \tag{6}$$

where N_s in the number of individual spots, N_g is the number of sunspot groups and κ is a parameter that varies with location and observing instrument.

Graphic design: Communication Division, UiB / Print: Skipnes Kommunikasjon AS

uib.no

ISBN: 978-82-308-3600-2